



## Durham E-Theses

---

*Temporal analysis of the least energetic events in  
pulsar data from observations with the high energy  
stereoscopic system*

Aristeidis Noutsos,

### How to cite:

---

Aristeidis Noutsos, (2006) *Temporal analysis of the least energetic events in pulsar data from observations with the high energy stereoscopic system*, Durham theses, Durham University. Available at Durham E-Theses Online: <http://etheses.dur.ac.uk/2696/>

### Use policy

---

The full-text may be used and/or reproduced, and given to third parties in any format or medium, without prior permission or charge, for personal research or study, educational, or not-for-profit purposes provided that:

- a full bibliographic reference is made to the original source
- a [link](#) is made to the metadata record in Durham E-Theses
- the full-text is not changed in any way

The full-text must not be sold in any format or medium without the formal permission of the copyright holders.

Please consult the [full Durham E-Theses policy](#) for further details.

# Temporal Analysis of the Least Energetic Events in Pulsar Data from Observations with the High Energy Stereoscopic System

— Volume 2 —

by

Aristeidis Noutsos

The copyright of this thesis rests with the author or the university to which it was submitted. No quotation from it, or information derived from it may be published without the prior written consent of the author or university, and any information derived from it should be acknowledged.



Submitted in conformity with the requirements  
for the degree of Doctor of Philosophy

Department of Physics  
University of Durham  
South Road  
Durham. UK.

**09 JUN 2006**

Copyright © 2006 by Aristeidis Noutsos



# Contents

<b>5</b>	<b>Temporal Analysis of <math>\gamma</math>-ray Pulsar Data</b>	<b>244</b>
5.1	Introduction . . . . .	244
5.2	Definitions . . . . .	246
5.2.1	Time Definitions . . . . .	246
5.2.2	Analysis Definitions . . . . .	250
5.3	Data Extraction and Reduction . . . . .	259
5.3.1	Software Operation Checks . . . . .	259
5.3.2	Timestamp Extraction . . . . .	261
5.3.3	Verification of the Barycentring Routine . . . . .	263
5.3.4	Extraction of Low-Energy Events . . . . .	273
5.4	Uniformity Tests . . . . .	278
5.4.1	Pearson's $\chi^2$ -test . . . . .	282
5.4.2	The Rayleigh Test . . . . .	295
5.4.3	The $H$ -test . . . . .	302
5.4.4	The $C_m$ ("Cosine") Test . . . . .	304
5.5	The Helene Method for Upper Limit Estimation . . . . .	309
5.5.1	Method Performance and The Feldman–Cousins Approach . . . . .	311
5.6	The Independent Fourier Spacing . . . . .	317
5.7	Simulations . . . . .	320
5.7.1	Monte Carlo Pulse Generator . . . . .	320
5.7.2	Uniformity Tests: Operation and Performance . . . . .	323
5.7.3	Effective Area . . . . .	337
5.7.4	Energy versus Image Amplitude . . . . .	339
<b>6</b>	<b>Observations and Results</b>	<b>344</b>
6.1	Introduction . . . . .	344

6.2	Pulsar Observations . . . . .	344
6.3	Three Pulsars Under the Microscope: Periodic Analysis and Upper Limits . . . . .	348
6.3.1	The Crab Pulsar: Standard Candle? . . . . .	348
6.3.2	PSR B1706–44: A Young, Promising Candidate . . . . .	356
6.3.3	PSR B1259–63: SS 2883’s Closest Companion . . . . .	359
6.3.4	Upper Limits on the Flux . . . . .	375
6.3.5	Upper Limits on the Cut-off Energy of Exponential and Super-Exponential Spectra . . . . .	389
<b>7</b>	<b>Summary and Future of H.E.S.S. Pulsar Observations</b>	<b>396</b>
7.1	Summary of Results . . . . .	396
7.2	A Brighter Future: H.E.S.S. Phase II . . . . .	398
7.2.1	H.E.S.S. Phase II Detection Rates . . . . .	403
7.3	Potential Improvements on the Present Analysis Methods . . . . .	408
7.3.1	Introduction . . . . .	408
7.3.2	Improving the Statistics . . . . .	410
7.3.3	Optimising the Image Amplitude Cut: The $Q$ -factor . . . . .	415
7.4	Beyond H.E.S.S. . . . . .	420

## Chapter 5

# Temporal Analysis of $\gamma$ -ray Pulsar Data

### 5.1 Introduction

The H.E.S.S. analysis software is based on CERN's ROOT format [370]. Each Cherenkov shower deposits an amount of light on the telescope, whose distribution across the camera is recorded in ROOT binary files. These files contain information on the individual pixel intensities as well as each event's arrival time, called a *timestamp*: the latter is recorded by the GPS clock. As mentioned earlier, each observation night with all 4 H.E.S.S. telescopes in operation can produce 100 GB worth of raw data. Clearly, such a large amount of information is difficult to handle, especially if one is to analyse months of data taking. A more flexible format is the ROOT DST (Data Storage Tree) format, which is derived from raw files but is  $\sim 10\%$  smaller in comparison. DST files contain all the necessary information for the analysis of Cherenkov events; but in contrast to raw files, a DST file contains only the number of ph.e., for each pixel, that remain after the pedestal has been removed.

Each observation run is contained in a single DST file regardless of the type of observation (single-telescope or stereoscopic). For ON/OFF observations, the ON and OFF portions of the observation are stored in separate DST files. Wobble-mode observations are also stored in separate files according to the declination offset, which can be either  $+0.5$  or  $-0.5$ . Besides other operations, the H.E.S.S. software is capable of parametrising the shapes of Cherenkov images, based on the pixel

information that is stored in DST files. In other words it generates Hillas parameters for each image. However, generation of the entire set of image parameters is not guaranteed for all images, as faint or dispersed images on the camera might not satisfy the requirements for a reliable fit. Nevertheless, in the case of successful generation of Hillas parameters, the analysis proceeds with the selection of those events that pass the image cuts. The selection of image cuts for a particular data set depends upon the user, and it is usually optimised with simulations that take into account various observing parameters. These parameters can be the Z.A. of observation, the mode of observation (i.e. whether the source is observed with one, two, three or four telescopes), the assumed spectral index of the source, etc. The image cuts are applied to both on- and off-source observations, and the surviving number of events are compared with each other to deduce the signal excess in the on-source portion of the observation. Provided there is a persistent  $\gamma$ -ray signal in the on-source data, its significance is given by Eq. 3.29. In the case of stereoscopic DSTs (i.e. data files from simultaneous observations of a source with more than one telescope), each event's parameters are calculated based on the pixel information from all participating telescopes (i.e. CT1–CT4). In particular, the arrival times of stereoscopic events are determined by the central trigger, which assigns a single timestamp to each event. These timestamps correspond to the event arrival time at the central trigger unit (CT0).

Using the arrival times of Cherenkov events, we have performed a temporal analysis on pulsar data that were collected with H.E.S.S. in the period 2002–2004. The selected targets were the Crab pulsar, PSR B1706–44 and PSR B1259–63, which were considered appropriate for a number of reasons:

To begin with, the double-peaked profile of the Crab pulsar, which appears consistently throughout the EM spectrum, is considered well suited to the sensitivity of statistical tests like the  $\chi^2$  and the  $C_m$ . On the other hand, the broad profile of PSR B1706–44 is more easily detectable with the Rayleigh test. Finally, PSR B1259–63, which has not been observed with EGRET, poses a challenge to the  $H$ -test, which is an overall good test for pulses of unknown shape and position.

In terms of visibility from the H.E.S.S. site, PSR B1706–44 could have hardly been in a more favourable position, since it can be observed at Z.A.s as small as  $20^\circ$  during culmination. Crab, on the other hand, is not at an

optimal position relative to the H.E.S.S. site and constantly culminates below  $45^\circ$  above the horizon. However, one cannot ignore the fact that this pulsar is considered the standard candle in all wavelengths.

PSR B1259–63 is an opportunity to study a binary system and perform the relevant corrections to the orbital focus, in addition to the standard barycentric corrections (see section 5.2.2). This opportunity arose from this pulsar’s periastron passage, which occurred after H.E.S.S. Phase I had been completed. Although the collection of these data was mainly aiming at the detection of PSR B1259–63’s DC emission — which arises from its interaction with the companion star — we hastily took advantage of the opportunity to check for pulsed emission directly from the pulsar.

The following sections describe the methods of temporal analysis which were performed on the data. Their application to the above three cases is presented in the next chapter, where we discuss the results and their implications.

## 5.2 Definitions

To facilitate a better understanding of the pulsed analysis’ details, a number of definitions is presented in the following sections.

### 5.2.1 Time Definitions

#### Solar and Sidereal Time (ST)

One apparent solar day is the time interval between two culminations of the Sun as viewed from a given location on Earth. However, because the Earth revolves around the Sun at a variable orbital velocity throughout the year, and because the axis of its diurnal rotation is not perpendicular to the ecliptic, this time interval varies over the course of one year. On the other hand, the mean solar day assumes an *imaginary* Sun that moves across equator (not the ecliptic) at a uniform rate. By definition, one mean solar day is equal to 24 h. The difference between the apparent and the mean solar day is given by the equation of time and can be as large as 15 min during the year.

The Sidereal Time provides a measure of the Earth’s rotation with respect to the stars rather than the Sun. It is equal to the hour angle between the meridian of a given location and the vernal equinox. Due to its orbital motion around the

Sun, the Earth has to rotate by an additional angular increment before the Sun returns to its zenith position between successive culminations. This interval varies throughout the year and corresponds, on average, to  $\approx 4$  min. On the other hand, the impact of the Earth's orbital motion on the apparent positions of the stars in the sky is insignificant. Hence, the interval between two successive culminations for a given star is fixed. Therefore, one Sidereal Day is shorter than the mean solar day by 4 min.

The ST — measured at Greenwich — can have the form of apparent or mean ST depending on whether one considers the true or mean position of the vernal equinox, respectively. The Greenwich Apparent Sidereal Time (GAST) takes into account the instantaneous position of the vernal equinox, which includes the various nutations of the Earth's axis: i.e. the polar motions. On the other hand, the Greenwich Mean Sidereal Time (GMST) is based on a uniform precession of the vernal equinox, i.e. without accounting for nutations. The time difference between GAST and GMST is given by the equation of equinoxes and can be as large as 1.2 s [371].

Finally, the mean ST at any geographical location, namely the Local Mean Sidereal Time (LMST), can be calculated from GMST by adding the longitudinal offset of the location from Greenwich after it has been converted to a sidereal offset. The conversion accounts for the difference between the mean solar and sidereal day, and the conversion factor is  $t_{ST}/t_{MS} \approx 0.997$ . Having LMST, the calculation of the Local Apparent Sidereal Time is done through the equation of equinoxes, like in the case of Greenwich.

### **Julian Date (JD)**

The Julian Date represents the decimal-integer count of mean solar days, starting at 12:00 (noon), on 1 January 4713 BC. For example, the J2000 reference co-ordinate system (Julian epoch), which specifies the positions and orbital elements of celestial objects at 12:00, on 1 January 2000, corresponds to 2451545.0 Julian days. The previous reference epoch, B1950 (Besselian epoch), corresponds to  $JD=2433282.42345905$ .

### **Modified Julian Date (MJD)**

In order to comply with the civil usage of time and make JD more convenient, the Modified Julian Date (MJD) was defined. MJD is an equivalent time format to



JD, but instead it begins at 00:00 (midnight) rather than 12:00. The reference date for MJD is 17 November 1858, that corresponds to  $JD=2400000.5$ . Hence, MJD is defined as

$$MJD = JD - 2400000.5 \quad (5.1)$$

### Universal Time (UT)

The original definition of Universal Time was given as the mean solar time of the Greenwich meridian, starting each day at 00:00. Since 1982, however, UT has been connected to GMST through the conventional relationship [372]

$$\begin{aligned} \text{GMST}(0 \text{ h UT}) = 24110.54841 + 8640184.812866 \times T_U + \\ + 0.093104 \times T_U^2 - 0.0000062 \times T_U^3 \text{ s} \end{aligned} \quad (5.2)$$

which gives the GMST seconds at 00:00 UT.  $T_U = (JD - 2451545.0)/36525$  is the number of Julian centuries that have elapsed since 12:00 UT, on 1 January 2000.

### International Atomic Time (TAI)

The TAI time-scale was initially based on the first  $^{55}\text{Cs}$  atomic clock, which started in 1955. TAI values have always been the result of a statistical combination of an ensemble of atomic clocks kept across the world. On 1 January 1958, TAI was defined equal to UT.

### Terrestrial Time (TT)

The Terrestrial time does not have a single realisation, but it can be defined based on various time-scales. TT has been in the ephemerides since 2001. The time rate of TT is the same as that of clocks on the rotating Earth, but it represents the time in the reference frame that moves with the Earth's geocentre. Therefore TT is a linear transformation of the geocentric time-scale, TCG (see next paragraph). The most practical realisation of TT is through TAI by using the relationship

$$TT = \text{TAI} + 32.184 \text{ s} \quad (5.3)$$

One of the proposed realisations of TT is based on pulsar timing.

### Geocentric Co-ordinate Time (TCG)

The Geocentric Co-ordinate Time corresponds to the time measured in a frame that moves with the geocentre, but unlike TT TCG takes into account the Earth's gravitational well which causes time to flow differently on the surface and at the geocentre. For that reason TCG clocks tick faster than clocks on the Earth's surface. The rate difference between UTC and TCG is roughly  $20 \text{ ms y}^{-1}$  [371].

### Co-ordinated Universal Time (UTC)

The Co-ordinated Universal Time, or just UTC, has been through many phases since its first definition in 1963. It is the basis of radio broadcasts of time around the world. Its definition requires that UTC always maintains an integer amount of seconds difference from TAI, which results in occasional 1-s adjustments, called leap seconds.

UTC is always kept within 0.9 s of UT. The latter time-scale is, as mentioned, associated with the Earth's rotation. Over the past 30 years, the Earth's crust rotation has accelerated, which resulted in a 7-year gap between 1998 and 2005, during which there have not been leap seconds [373]. However, the International Earth Rotation and Reference Systems Service (IERS) will introduce a positive leap second at the end of December 2005 [374].

### Barycentric Dynamical Time (TDB)

TDB is the appropriate time-scale for calculations of celestial motions in the solar system. The TDB rate flows uniformly at the solar system barycentre but deviates significantly from atomic clocks — on the Earth's surface — over annual time-scales. The difference is especially notable close to the perihelion and aphelion positions of the Earth's orbit, where relativistic effects make TT flow slower and faster than TDB, respectively. The difference between TT and TDB depends only on periodic terms and it is given approximately by [375]

$$\text{TDB} - \text{TT} = 0.001658 \sin g + 0.000014 \sin(2g) \text{ s} \quad (5.4)$$

where  $g = 356^\circ.53 + 0^\circ.9856003 \cdot (\text{JD} - 2451545.0)$ .

Over longer periods, the average TDB rate is equal to that of Earth clocks.

## 5.2.2 Analysis Definitions

### Event Folding

Pulsar lightcurves can be reproduced from the event arrival times via *event folding*. By that term we mean the assignment of a specific phase to all pulsar events. Since a pulsar rotates constantly, the phase,  $\varphi$ , is a monotonic function of time: i.e.  $\varphi = \varphi(t)$ . The phase of an event that was generated at time  $t$  is equal to the number of rotations that the pulsar has completed between a reference time 0 and time  $t$ . The reference phase,  $\varphi(0)$ , is usually chosen arbitrarily, although it typically corresponds to the pulsar's angular position where the maximum radiation intensity is observed.

Despite the fact that the phase can include the integer number of pulsar rotations since  $t = 0$  plus the fraction of a full cycle, because in every cycle each phase is associated with exactly the same orientation as in any other cycle, the fractional part is the most interesting: it shows the angular position of the pulsar with respect to  $\varphi(0)$ ; and if  $\varphi$  is expressed in radians, this fraction is given by

$$\phi = \frac{\varphi}{2\pi} - \left\lfloor \frac{\varphi}{2\pi} \right\rfloor \quad (5.5)$$

where  $\lfloor x \rfloor$  is the floor function of a variable  $x$  [376]. Therefore,  $\phi \in [0, 1)$ .

The average frequency of a pulsar,  $\langle f \rangle$ , is defined as the number of cycles per time interval. Therefore it corresponds to how many times a specific phase, say  $\varphi = 0$ , occurs in that interval. For an infinitesimal amount of time,  $dt$ , the instantaneous frequency at time  $t$  is defined as  $f(t) = d\varphi(t)/dt$ . Hence, knowing the frequency function, one can integrate to derive the phase function and assign a phase to events that occurred at  $t$ . More specifically,

$$\varphi(t) = \int f(t) dt \quad (5.6)$$

The frequency function can be defined through its frequency derivatives at a reference time  $t_0$ , which are known for a number of pulsars and are provided by precise radio observations in pulsar ephemerides. In theory, the frequency at an arbitrary time  $t$  is defined exactly by all its derivatives as

$$f(t) = \sum_{n=0}^{\infty} \frac{f^{(n)}(t_0)(t - t_0)^n}{n!} \quad (5.7)$$

In practice, only the first few derivatives are available from observations and there-

fore this function can be approximated as

$$f(t) = f(t_0 + (t - t_0)) \approx f(t_0) + \dot{f}(t_0)(t - t_0) + \frac{1}{2}\ddot{f}(t_0)(t - t_0)^2 \quad (5.8)$$

Substituting this expression in Eq. 5.6, we get

$$\varphi(t_0 + (t - t_0)) \approx \int [f(t_0) + \dot{f}(t_0)(t - t_0) + \frac{1}{2}\ddot{f}(t_0)(t - t_0)^2]d(t - t_0) \quad (5.9)$$

performing the integration we come to the final expression for  $\varphi(t)$ :

$$\varphi(t_0 + (t - t_0)) \approx \varphi_0 + f(t_0)(t - t_0) + \frac{1}{2}\dot{f}(t_0)(t - t_0)^2 + \frac{1}{6}\ddot{f}(t_0)(t - t_0)^3 \quad (5.10)$$

where  $\varphi_0$  is the phase at the reference time  $t_0$ .

The occurrence of pulsar glitches and other timing irregularities [184] can cause a disruption to the otherwise stable evolution of the frequency function and render a set of ephemeris values invalid. By the term *invalid* we mean that the provided values are unsuitable for extrapolation beyond a certain time. The reason for that can be the timing irregularities, or simply the fact that the above approximation of  $f(t)$  starts to deviate from the actual frequency value after long periods of time. Thus, the ephemerides are kept up-to-date by frequent, in some cases monthly, measurements of the parameters. Provided there is no glitch, etc. between measurements, the extrapolated values from the  $t_0$  of one ephemeris to those of its successor should match. The degree to which the successive ephemerides are consistent with each other can be expressed by means of a statistical error, which can be calculated from the errors of the parameters, at  $t_0$ , via Gaussian error propagation [377]. Hence, the error on the frequency at time  $t$  can be calculated from the expression

$$\begin{aligned} \sigma_f^2(t) = \sigma_f^2(t_0) + \sigma_{\dot{f}}^2(t_0)(t - t_0)^2 + \frac{1}{4}\sigma_{\ddot{f}}^2(t_0)(t - t_0)^4 + \\ + \left[ \dot{f}(t_0) + \ddot{f}(t_0)(t - t_0) \right]^2 \sigma_{(t-t_0)}^2 \end{aligned} \quad (5.11)$$

where  $\sigma_{(t-t_0)}$  is the accuracy of the time measurements.

Using equations 5.10 and 5.5 together with a valid ephemeris, one can calculate the phase of any event given its arrival time.

### The Poisson Process and Distribution

$\gamma$ -ray astronomy has poor statistics compared to other branches of astronomy, like radio astronomy. The  $\gamma$ -ray signals are typically characterised by photon rates  $\sim 1 \text{ min}^{-1}$ . Such statistics are best described by counting distributions, like the Poisson distribution. The Poisson distribution can be defined as the limiting case of the binomial distribution, where the number of independent trials,  $n$ , per unit time,  $\delta t$ , is very large (i.e.  $n \rightarrow \infty$ ), and the probability of a single trial being positive (say a successful detection) tends to zero (i.e.  $pr \rightarrow 0$ ). Hence, the number of positive occurrences,  $\mu$ , expected in  $\delta t$  is  $\mu = n \cdot pr \ll n$ . In Cherenkov experiments, for example, the number of detected events (independent trials) per unit time — which corresponds to the trigger rate — is very high compared to the fraction of detected  $\gamma$  rays. The probability for each detected event to be a  $\gamma$  ray is very small, but the trigger rate is high enough so that a number of  $\gamma$  rays is actually detected.

The probability of having  $k$  positive occurrences during an experiment which yields on average  $\mu$  positive events per unit time,  $\delta t$ , is given by the Poisson probability function:

$$pr(k; \mu) = \frac{\mu^k e^{-\mu}}{k!}, \quad \mu \in \mathbb{R}, \quad k \in \mathbb{I} \quad (5.12)$$

Hence, the Poisson distribution requires only the mean number of positive occurrences,  $\mu$ , to describe how probable a given number of positive occurrences,  $k$ , is in a fixed amount of time,  $\delta t$ .

The variance,  $\sigma^2$ , of the Poisson distribution is equal to the expected mean, and the standard deviation is  $\sigma = \sqrt{\mu}$ . The usefulness of  $\sigma$  is evident in  $\gamma$ -ray observations: an average number of events,  $N_c$ , which is detected from a Poissonian cosmic-ray background implies  $\sigma = \sqrt{N_c}$ ; and if an on-source observation yields  $N_\gamma$   $\gamma$  rays, then the significance of the signal can be quantified in terms of the number of Poissonian standard deviations,  $n$ , above the expected background:

$$n = \frac{N_\gamma}{\sqrt{N_c}} \quad (5.13)$$

In practice, the on-source and off-source observations are executed separately, which results in having two, independent data sets with  $N_{\text{ON}}$  and  $N_{\text{OFF}}$  events. These data sets define two different Poissonian distributions with expected means equal to the corresponding events in each set. The number of  $\gamma$  rays is then calculated from the difference between the two data sets: i.e.  $N_\gamma = N_{\text{ON}} - N_{\text{OFF}}$ . The resulting data

set from the subtraction also defines an independent Poissonian distribution, which is different to the previous two. Since this data set is derived from both on-source and off-source distributions, it contains their Poissonian fluctuations (i.e. deviations from the mean). Hence, its variance,  $\sigma^2$ , is equal to the sum of the variances of the component distributions. Its standard deviation is therefore

$$\sigma^2 = \sigma_{\text{ON}}^2 + \sigma_{\text{OFF}}^2 \Rightarrow \sigma = \sqrt{N_{\text{ON}} + N_{\text{OFF}}} \quad (5.14)$$

The significance of the  $\gamma$ -ray signal can now be estimated to

$$n = \frac{N_\gamma}{\sigma} = \frac{N_{\text{ON}} - N_{\text{OFF}}}{\sqrt{N_{\text{ON}} + N_{\text{OFF}}}} \quad (5.15)$$

It is not unusual for experimenters to require a detection significance of  $5\sigma$  before they report it. An estimate of the probability that corresponds to that significance level can be given based on the Gaussian approximation of the Poisson distribution, which holds for large  $\mu$  ( $\gtrsim 10$ ). Then, the translation from Poissonian standard deviations to probability levels is just a matter of look-up tables. Taking the natural logarithm of both sides of Eq. 5.12, we have

$$\ln pr(k; \mu) = \ln \left( \frac{\mu^k e^{-\mu}}{k!} \right) \quad (5.16)$$

We can substitute the denominator of the RHS fraction using the Stirling approximation for large  $\mu$ :

$$\ln pr(k; \mu) \approx \ln \left( \frac{\mu^k e^{-\mu}}{k^k e^{-k} \sqrt{2\pi k}} \right) \quad (5.17)$$

After expanding the logarithm on the RHS and contracting the resulting logarithmic terms, we get

$$\ln pr(k; \mu) = k \ln \frac{\mu}{k} + (k - \mu) - \ln \sqrt{2\pi k} \quad (5.18)$$

At this point we set  $\epsilon = k - \mu \ll \mu$ ; but we will justify the inequality graphically later (see Fig. 5.1). The above equation now becomes

$$\ln pr(k; \mu) = -(\mu + \epsilon) \ln \left( 1 + \frac{\epsilon}{\mu} \right) + \epsilon - \ln \sqrt{2\pi(\mu + \epsilon)} \quad (5.19)$$

We can approximate the first logarithmic quantity on the RHS using  $\ln(1 + \epsilon) \approx \epsilon - \epsilon^2/2 + \epsilon^3/3 - \dots$  and keeping only the first- and second-order terms. The result

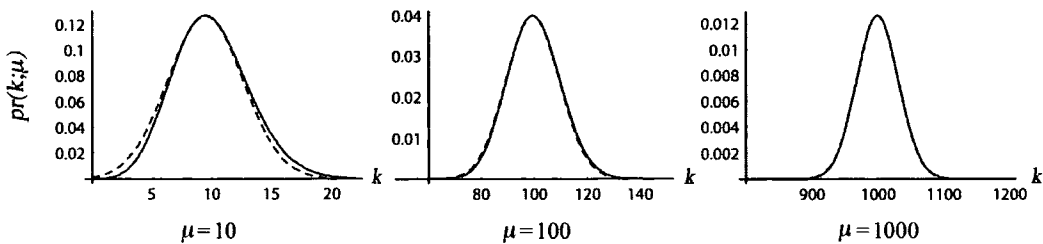


Figure 5.1: (from [378]) The Poisson probability function and its Gaussian approximation for three values of the mean,  $\mu$ . It is clear that the approximated Gaussian function deviates for  $\mu = 10$  but becomes practically indistinguishable from the Poisson function for  $\mu = 1,000$ . This similarity for large means can be used to translate Poissonian standard deviations,  $\sigma$ , into Gaussian probability levels.

is

$$\ln pr(k; \mu) \approx -\frac{\epsilon^2}{2\mu} - \ln \sqrt{2\pi(\mu + \epsilon)} \approx -\frac{\epsilon^2}{2\mu} - \ln \sqrt{2\pi\mu} \quad (5.20)$$

Finally, by exponentiating both sides we obtain the approximated probability function:

$$pr(k; \mu) \approx \frac{1}{\sqrt{2\pi\mu}} e^{-(k-\mu)^2/(2\mu)} \quad (5.21)$$

which is a Gaussian distribution centred on  $\mu$ .

Fig. 5.1 shows the Poisson probability function (solid curve) and its approximated Gaussian version (dashed curve) for  $\mu = 10, 100$  and  $1,000$ . Firstly, it can be seen that the two functions become practically indistinguishable for  $\mu = 1,000$ . Secondly, one can see that for large  $\mu$  the width of the distribution becomes an insignificant part of the mean: in the case of  $\mu = 1,000$ , the distribution covers the values  $900 < k < 1,100$ , and therefore the maximum  $\epsilon$  value is  $\approx 100$ .

The practical match between the Poisson distribution and its Gaussian approximation for large means can be used to translate the number of standard deviations of a  $\gamma$ -ray signal above the mean into one-tail Gaussian probability levels. Table 5.1 can be used for such a conversion, for signals with an excess of up to  $5\sigma$ .

$n\sigma$	$pr(k > n\sigma, \mu)$
$0\sigma$	$5 \times 10^{-1}$
$0.5\sigma$	$3.085 \times 10^{-1}$
$1\sigma$	$1.587 \times 10^{-1}$
$1.5\sigma$	$6.681 \times 10^{-2}$
$2\sigma$	$2.275 \times 10^{-2}$
$2.5\sigma$	$6.21 \times 10^{-3}$
$3\sigma$	$1.35 \times 10^{-3}$
$3.5\sigma$	$2.33 \times 10^{-4}$
$4\sigma$	$3.17 \times 10^{-5}$
$4.5\sigma$	$3.4 \times 10^{-6}$
$5\sigma$	$2.87 \times 10^{-7}$

Table 5.1: One-tail Gaussian probability levels for the value of  $k$  to exceed  $n$  standard deviations above the mean  $\mu$ . For large  $\mu$  ( $\gtrsim 10$ ), this table becomes also valid for Poissonian standard deviations.

### Barycentring

During the continuous monitoring of a pulsar from a fixed position on Earth, the pulsed signal has to travel through different path lengths as the Earth revolves and rotates. This causes continuous variations in the signal frequency, which do not reflect those in the pulsar's inertial frame. We will display the reason for those variations for the orbital motion of the Earth, although the same principle can be applied to the rotational motion as well. In reality, the actual variation is a combination of both.

Fig. 5.2 shows a section of the Earth's annual orbit around the Sun. An observer fixed at the geocentre, which happens to lie in the path of the beamed emission of a pulsar, will record a succession of wave packets that are generated at the pulsar's frequency,  $f_0$ . As the Earth moves along its orbit, the distance traversed by the photons from the pulsar to the Earth changes continuously. Consequently, this affects the observed frequency of the pulsations. In the figure, we have assumed that when the Earth is in position A, a wave packet is recorded at the Earth's position, and a successive wave packet is trailing the first one at distance  $c/f_0$  away. If the Earth were stationary with respect to the pulsar, the second wave packet would have arrived after  $1/f_0$  s at Earth. However, the Earth is travelling with velocity  $v = \Delta x/\Delta t$  towards the pulsar, and therefore it meets with the wave packet



at an earlier time:  $t_2 = (1/f_0) - \Delta t$ , at position B. If we set the time when the first wave packet is recorded to zero (i.e.  $t_1 = 0$ ), then the apparent frequency of the signal as seen by the observer is the reciprocal of  $t_2 - t_1$ :

$$\frac{1}{f} = \frac{1}{f_0} - \frac{\Delta x}{v} \quad (5.22)$$

where we replaced  $\Delta t$  with  $\Delta x/v$ . During  $\Delta t$ , the wave packet travelling with the speed of light traversed distance  $c/f_0 - \Delta x$ , whereas the Earth travelling with speed  $v$  towards the pulsar traversed distance  $\Delta x$ . Hence,

$$\Delta t = \frac{\Delta x}{v} = \frac{1}{f_0} - \frac{\Delta x}{c} \quad (5.23)$$

Combining Eq. 5.22 and Eq. 5.23, we get

$$f = f_0 \left(1 + \frac{v}{c}\right) \quad (5.24)$$

This result is an example of the famous Doppler–Fizeau effect, which in our case leads to an increased frequency compared to the source's. The opposite occurs when the Earth is receding from the source.

In order to reflect the actual frequency variations that occur in a pulsar's reference frame, the recorded event times have to be transformed to a reference frame in which the pulsar has zero acceleration. Clearly, this transformation requires accurate knowledge of the relative motion between the Earth and the pulsar. A good choice, for which we have accurate positional and temporal information, is the reference frame that moves with the Solar System Barycentre (SSB). Available ephemerides provide accurate and up-to-date information of the Earth's position relative to the SSB. Moreover, the use of the well-defined TDB time-scale for events arriving at the SSB provides a uniform timeflow which is unaffected by the variations of the gravitational potential that exist on the Earth.

### Ephemeris Formats

The most commonly used ephemeris formats, which provide updated values of pulsar frequencies and their derivatives, as well as other pulsar properties, are two: the one generated by the Jodrell Bank radio observatory in the U.K., and the GRO format, which — as its name suggests — was widely used in the *CGRO* community. The latter is also the format that is used by the Australia Telescope National Facility

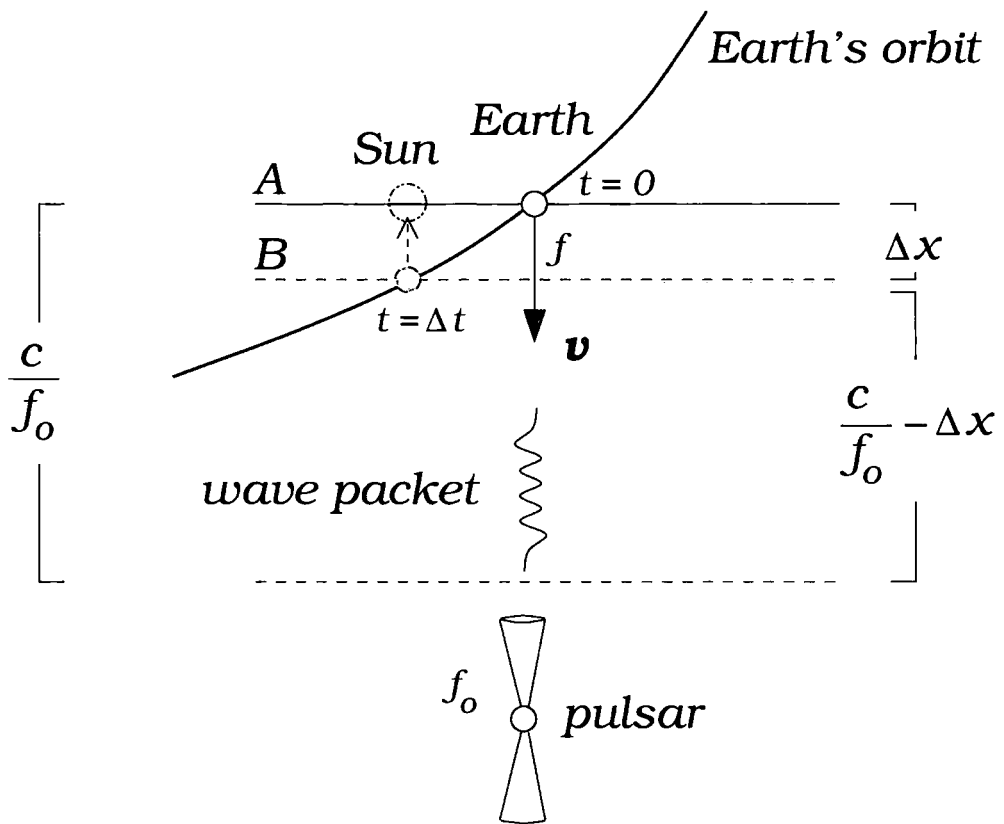


Figure 5.2: Schematic representation of the Doppler-Fizeau effect on the pulsar signals arriving at Earth.

(ATNF) and their popular pulsar-timing software, TEMPO. (The distribution of TEMPO along with the accompanying reference manual is maintained by Princeton University [379].) The above two formats are described in the next paragraphs, together with examples:

### Jodrell Bank Ephemeris

The Jodrell Bank radio observatory in Manchester, U.K., maintains an accurate monthly ephemeris for the Crab pulsar. The provided parameters are contained in lines that correspond to each month (Fig. 5.3). Each line contains the arrival time of the pulse,  $t_0$ , which is given as an integer number of Modified Julian days plus a small time interval,  $t_{\text{MIT}}$  or  $t_{\text{JPL}}$ : this interval corresponds to the arrival time of the first main pulse after midnight, at the SSB. The time-scale used is TDB and the phase at  $t_0$  is defined equal to 0. The calculation of the arrival times is based on either the Jet Propulsion Laboratory (JPL) planetary ephemeris [380], DE200, or the Massachusetts Institute of Technology (MIT) ephemeris, PEP311 — which however extends only until February 1990.

The ephemeris provides the frequency,  $f_0$ , and its first derivative,  $\dot{f}_0$ , at  $t_0$ , as they are calculated at the SSB. Also stated are the errors on  $f_0$  and  $\dot{f}_0$ , as well as the pulsar dispersion measure, DM, together with the time delay due to interstellar scattering. Since the measurements take place monthly, each line can be safely assumed to be valid during the preceding and successive half month. However, the ephemeris comes with detailed notes of timing irregularities, when required. In such cases, measurements are performed in shorter periods to account for the irregular changes in the pulsar's timing behaviour, and the validity ranges are mentioned accordingly.

### GRO Ephemeris

The GRO pulsar ephemeris format is the most popular amongst the astronomical community. For isolated pulsars, all the provided parameters are included in single lines, as in the Jodrell Bank format. For binary pulsars there is an additional line which contains the orbital parameters of the binary system (see Fig. 5.4). All parameters correspond to an MJD epoch when the measurement took place, and each measurement is provided with a validity range that is defined by a starting and ending MJD. The arrival times of the pulses are

Date	MJD	$t_{MRT}$ sec	$t_{JPL}$ sec	$t_{acc}$ $\mu$ sec	$\nu$ Hz	$\sigma_\nu$	$\dot{\nu}$ $10^{-15} \text{ sec}^{-2}$	$\sigma_{\dot{\nu}}$	DM $\text{pc cm}^{-3}$	$\tau_{208}$ $\mu$ sec
15 MAY 88	47296	0.007050	0.032072	200	29.9843723662	4	-378616.35	1.24	(56.859)	100
15 JUN 88	47327	0.010773	0.002803	200	29.9833582852	5	-378586.88	1.89	(56.859)	100
15 JUL 88	47357	0.012682	0.005060	300	29.9823770003	2	-378574.13	0.61	(56.859)	100
15 AUG 88	47388	0.021515	0.014156	300	29.9813631037	5	-378527.08	1.53	56.894	100
15 SEP 88	47419	0.013883	0.006608	250	29.9803492921	7	-378504.96	1.95	(56.894)	100

Figure 5.3: (from [357]) The Jodrell Bank ephemeris for the Crab pulsar. The first 4 columns show the date that corresponds to the calculated parameters of the respective ephemeris line. Columns 1–3 show this date in human-readable, Gregorian format, and column 4 contains the same date in MJD format. Columns 5 and 6 contain the small time amount (TDB format) that has elapsed between midnight of the aforementioned date and the arrival of the first main pulse. This calculation is based on either the JPL DE200 (column 6), or the Massachusetts Institute of Technology, PEP311 planetary ephemerides (column 5). Column 7 shows the error in the determination of the arrival times,  $t_{acc}$ , which represents the accuracy of the calculation for the whole calendar month. The next four columns contain the frequency and the frequency derivative of Crab’s pulses together with the corresponding standard deviations of the measurements. Finally, the last two columns contain the dispersion measure (DM) of the source at the time of the measurement and the introduced signal delay due to interstellar scattering.

calculated at the geocentre. Each arrival time is expressed as the fraction of a UTC Julian day after the TDB epoch that corresponds to the calculated frequency values of the respective ephemeris line. The ephemeris provides values for the frequency, and the first and second derivatives of the frequency (i.e.  $f$ ,  $\dot{f}$  and  $\ddot{f}$ ). All frequency values are calculated at the SSB. A short description of each field is presented in Table 5.2.

## 5.3 Data Extraction and Reduction

### 5.3.1 Software Operation Checks

Prior to our main searches for pulsed emission in pulsar data, it was considered appropriate to check the correct function of our software, with data from the well-established Crab nebula. Its DC emission had already been detected at the significance of  $\sim 50 \sigma$  by other collaborators [382]. We tried to match the result with our version of the software.

Character Range	Parameter	Description
Line 1		
1–8		Pulsar name (truncated if a J2000 name)
10–21		J2000 right ascension (hh mm ss.sss)
23–34		J2000 declination (–dd mm ss.ss)
36–40		Start of validity range (MJD)
42–46		End of validity range (MJD)
48–62	$t_0$	TDB epoch of pulse frequencies and infinite frequency UTC pulse TOA at geocentre (MJD)
64–80	$f_0$	Pulse frequency at the Solar System Barycentre (Hz)
82–93	$\dot{f}_0$	First time derivative of barycentric pulse frequency (Hz s <sup>−1</sup> )
96–104	$\ddot{f}$	Second time derivative of barycentric pulse frequency (Hz s <sup>−2</sup> )
106–109		RMS residual of fit in milliperiods
111–111		Letter code indicating origin of data (A = Australia)
115–119		Planetary system ephemeris used for barycentre correction
121–130		Full J2000 pulsar name
Line 2		
1–8		Pulsar name (truncated if a J2000 name)
10–25	$P_b$	Orbital period (at the Solar system barycentre) (s)
26–37	$a$	Semi-major axis of pulsar orbit (s)
39–48	$e$	Orbital eccentricity
50–63	$T_0$	TDB epoch of periastron passage (MJD)
65–74	$\omega$	Longitude of periastron (deg)
76–82	$\dot{\omega}$	Rate of periastron advance (deg y <sup>−1</sup> )
84–91	$\gamma$	Time dilation and gravitational redshift term (gamma) (s)
93–102	$\dot{P}_b$	First time derivative of orbital period
104–104		Letter code indicating origin of data (A = Australia)

Table 5.2: (from [381]) Description of the individual fields in the GRO pulsar ephemeris format. An example of the format for the binary pulsar PSR B1259–63 is shown in figure 5.4. The orbital parameters of Line 2 will be defined in section 6.3.3 where the binary motion of this pulsar is explained in detail.

```

Index: 123456789012345678901234567890123456789012345678901234
Line 1: 1302-635 13 02 47.660 -63 50 8.70 53099 53176 53137.000000545
Line 2: 1302-635 106852894.76599 1296.3837509 0.86990542 48124.35237650
-----
Index: 5678901234567890123456789012345678901234567890123456789
Line 1: 20.9366848577709 -1.00171E-12 -1.87E-21 1.8 A * DE200 1302-6350
Line 2: 138.668020 0.00000 0.000000 0.00E+00 A
-----

```




Figure 5.4: (from [381]) The structure of the GRO pulsar ephemeris format for the binary pulsar PSR B1259–63. The ephemeris consists of the two lines between the separators, whereas the top line is inserted here as an index to the character positions. Here, we have split the lines into two sections in order to fit the information across the page. An explanation for each field is given in Table 5.2.

In order for the comparison to be sensible, we had to make sure that the data runs matched those analysed by the other collaborators. The chosen data set consisted of 10 runs from the Crab nebula, which were produced with a 3-telescope stereo observation. The total exposure time was  $\approx 4$  h. Another factor that had to be kept the same between the analyses was the applied cuts to the data. In both cases, the *standard* H.E.S.S. cuts for the Crab nebula<sup>1</sup> were used (see Table 5.3). The standard cuts have been derived from simulations of the  $\gamma$ -ray emission from a source with an assumed DC spectrum that matches the Crab nebula’s. The spectrum of the Crab’s nebular emission had already been measured, before H.E.S.S., with experiments like H.E.G.R.A. and Whipple [383],[32]. Furthermore, the large Z.A. of Crab observations ( $\sim 45^\circ$ ) was also taken into account in those simulations. Using the standard cuts on the 4-h data set, we managed to reproduce the high significance mentioned above [382].

### 5.3.2 Timestamp Extraction

The search for periodicities in the data requires the extraction of the event timestamps which are stored in DST files. Each event is assigned a timestamp using the GPS clock of the Central Trigger System, which provides absolute UTC time with an accuracy of  $1 \mu\text{s}$ . We used H.E.S.S. routines to express the arrival times as UTC seconds since the standard epoch J2000. This choice is the natural one, since the celestial co-ordinates that correspond to the J2000 epoch offer higher posi-

<sup>1</sup>Following Crab nebula’s characterisation as the “standard candle”, the optimised set of image cuts is also referred to as standard.

Parameter	min	max	
<i>length</i>	1.8	5.2	mrاد
<i>width</i>	0.45	1.25	mrاد
<i>distance</i>	0	18	mrاد
<i>LoverS</i>	0	0.018	mrاد ph.e. <sup>-1</sup>
<i>alpha</i>	0	7	deg
Image Cleaning ( <i>p',q'</i> )	(5,10)		(pixels,ph.e.)

Table 5.3: (from [384]) A variant of the standard cuts for single-telescope observations of the Crab nebula. This set of cuts aims at the optimisation of the significance of the Crab’s DC signal. Note that the *LoverS* carries an implicit cut on the *Image Amplitude*, requiring it to be above 100 ph.e. The bottom row shows the additional (to the hardware one) restriction imposed on the image-cleaning thresholds (see section 4.3.1), which is set in the software and is used together with the standard H.E.S.S. cuts.

tional accuracy at our observation dates than those based on the B1950 epoch. This time format is sufficient for the study of local events: e.g. those generated by the flat-fielding device, since both the source and the detector belong to the same reference frame. However, the temporal study of astronomical objects from the Earth’s surface requires the measurement of time in a different time format, as well as the transformation of the event times to a more appropriate reference frame.

Using the `Pulsar.GetArrivalTimeAtSolarSystemBarycenter(UTC,location)` function of the H.E.S.S. software, we converted the UTC timestamps at Namibia to TDB timestamps at the SSB. This function requires, as input, the UTC times of the events at a selected `location` on Earth and uses the JPL DE200 planetary ephemeris to calculate the TDB arrival times of the events from a Pulsar’s direction. The resulting values were expressed as TDB seconds since J2000.

The pulsar co-ordinates are retrieved automatically from a database, which also contains information on the type of observation that corresponds to the particular run which is being analysed. For example, during a wobble observation, the offset by  $\pm 0.5^\circ$  R.A. of the source position, relative to the camera centre, is taken into account. Any positional image cuts applied to the data are also offset accordingly.

Despite the straightforward operation of the H.E.S.S. routines, the whole process of timestamp extraction was not hassle-free. A number of data runs from observations of PSR B1259–63 contained repetitive events: i.e. the same timestamp was subsequently repeated in the data [385]. We haste to make the point that such events

cannot be real, as that would imply a dead-time between subsequent events that is  $< 1 \mu\text{s}$ . As mentioned earlier, the H.E.S.S. DAQ can manage a dead time that is at least  $5.5 \mu\text{s}$  (see section 4.3.1). The offending runs were early-produced DSTs of PSR B1259–63 and were corrected and reproduced at a later time, past which the data from this pulsar were re-analysed. However, as a safety measure, we modified the time-extraction routine in order to skip follow-up events with timestamps equal to their predecessors. Not only does this process filter out the spurious events, but most importantly it prevents them from misleading our sensitive temporal analysis. The effect of their presence will be mentioned later, when we discuss the results from PSR B1259–63.

### 5.3.3 Verification of the Barycentring Routine

It is hard to exaggerate the importance of barycentring. Especially in pulsar observations where the signals have periods of the order of ms, the corrections have to guarantee that the pulses arrive in phase with each other. For example, if an observation began when the source was overhead, then after 6 h the source will be on the horizon, and the light-travel time will have increased by approximately  $R_{\oplus}$ . This introduces a delay of  $\Delta t = R_{\oplus}/c \approx 21 \text{ ms}$ , which means that, in the case of the Crab pulsar ( $f = 30 \text{ Hz}$ ), the pulses are now arriving with a phase difference  $\Delta\phi \approx f\Delta t = 0.6$ . Hence, the phases of all events that were emitted from the pulsar when it had the exact same orientation relative to our line-of-sight will not line up in a phasogram, and the lightcurve will appear dispersed and potentially unrecognisable. Therefore, it was regarded essential to cross-check the barycentring routine. This was done via the two different routes described below.

#### Experimental Method

The first method was to acquire optical data from the Crab pulsar and try to reconstruct the familiar double-peaked lightcurve, at the correct phase positions. Approximately 100 s worth of optical data were collected with the PMT that is mounted on the camera lid of the H.E.S.S. telescopes (see section 4.3.2). Each optical event was characterised by a UTC timestamp and an amount of d.c. corresponding to the number of ph.e. of the event. Using the H.E.S.S. barycentring routine, the event times were converted into TDB arrival times at the SSB. In addition, the TDB times were folded into phases using a contemporaneous GRO ephemeris for the Crab pulsar.



The GRO ephemeris format provides the frequency values at the SSB, which correspond to a reference time of a pulse arriving at the geocentre; also, this reference time is given in UTC format. Hence, a specialised routine was used, which converts the GRO reference times,  $t_0$ , to TDB times at the SSB,  $t$  [386]. Moreover, because the frequency values are calculated at time  $t_0$ , they had to be carried forward based on the frequency derivatives and the time difference,  $t - t_0$ , between the arrival time at the geocentre and that at the SSB (see Eq. 5.8). Having the transformed values at the SSB, we wrote a simple event-folding routine, based on Eq. 5.10, to get the event phases for each event. In addition, because of the high amount of NSB in the data, we determined the NSB pedestal and subtracted it from each event's d.c. contribution. The way this was achieved with the code is the following:

The NSB triggers are expected to contribute an amount of d.c. for each event,  $N_i$ , which is randomly distributed around the mean,  $\langle N \rangle$ , according to Poissonian statistics. Hence, one expects that, for noise, the deviations from the mean are within  $1 \sigma$ : i.e.  $\sqrt{\langle N \rangle}$ . Moreover, the value of  $\langle N \rangle$  also varies with time but over time-scales that are substantially longer than the signal's period. In our data set this variation is shown in Fig. 5.5, where we used coarse binning ( $6 \times 10^4$  events  $\equiv 2$  s) to represent the slow variation of the mean across 100 s.

When a pulsed event is recorded, its d.c. contribution is added to that of the NSB, and so the resulting events which contain both the NSB and the optical pulse will naturally show an excess of d.c. from the background. However, this excess is a tiny fraction of  $\langle N \rangle$  and can be less than  $\sqrt{\langle N \rangle}$  for a single event. If the event folding is carried out correctly, i.e. it is based on a valid and accurate ephemeris, the optical events should all be bunched in phase. In other words, we expect the binning of all the events according to their phase to result in the events containing the signal being concentrated in a number of phase bins that correspond to the peaks of the Crab pulsar's emission. By subtracting the average NSB from every event contribution, the majority of events that contain the signal will have positive residuals, whereas the residuals from the rest are expected to be randomly distributed around zero, according to Poisson. However, due to the slow variation of the average NSB contribution across our data set, it is more accurate to calculate the average pedestal over *short* intervals compared to the total length of the data

set and subtract it from the event contributions contained in the corresponding data segment. Hence, we decided to split the data into segments containing 1,000 successive events and calculate the value of  $\langle N \rangle$ , which is expected to be practically constant over such short intervals ( $\Delta t \approx 40$  ms).

Finally, by adding all the residuals in a phase bin, the d.c. from the events containing the signal are expected to add up proportionally to the number of events in the whole data set,  $n$ , whereas the contributions from the background events should add up proportionally to only  $\sqrt{n}$ . Therefore, given the large amount of data analysed ( $n \sim 3 \times 10^5$ ), we expected the signal to stand out against the background fluctuations.

In order to display the integrated lightcurve, we plotted the histogram that shows which phase regions are more prominent during one full rotation of the Crab pulsar. Such histograms that plot pulsar intensity variations during one period, in discrete phase steps (phase bins) are called *phasograms*. We divided Crab's period into 20 such bins, which corresponds to intervals of  $\approx 1.5$  ms. This decision was based on the duty cycles of the components in Crab's double-peaked lightcurve, which occupy  $\approx 10\%$  of the period. The chosen bin width was considered adequately narrow for the pulse shape to be revealed. Since we were only interested in the average d.c. contribution per bin — which corresponds to the average signal intensity during 1.5 ms — we divided the sum of the d.c. residuals in each bin by the number of events in the bin. The bottom of Fig. 5.6 shows the resulting phasogram from our analysis, compared to the  $\gamma$ -ray profile of the Crab pulsar above 100 MeV as was derived from EGRET observations [22]. The Crab pulsar's profile does not change significantly across the EM spectrum, so a side-by-side comparison between the two profiles is expected to result in a positional coincidence. Within the temporal uncertainties imposed by the resolution of our phasogram, the match between the two profiles of Fig. 5.6 is evident.

### Analytical Method

In addition to the above experimental cross-check, a second, analytical method was followed. This time, we tried to match the results from the code using first principles and the ephemeris information from *The Astronomical Almanac, 2003*, of the U.S. Naval Observatory [387]. We calculated the barycentric correction for a hypothetical event from the direction of the Crab pulsar, whose arrival time (hereafter

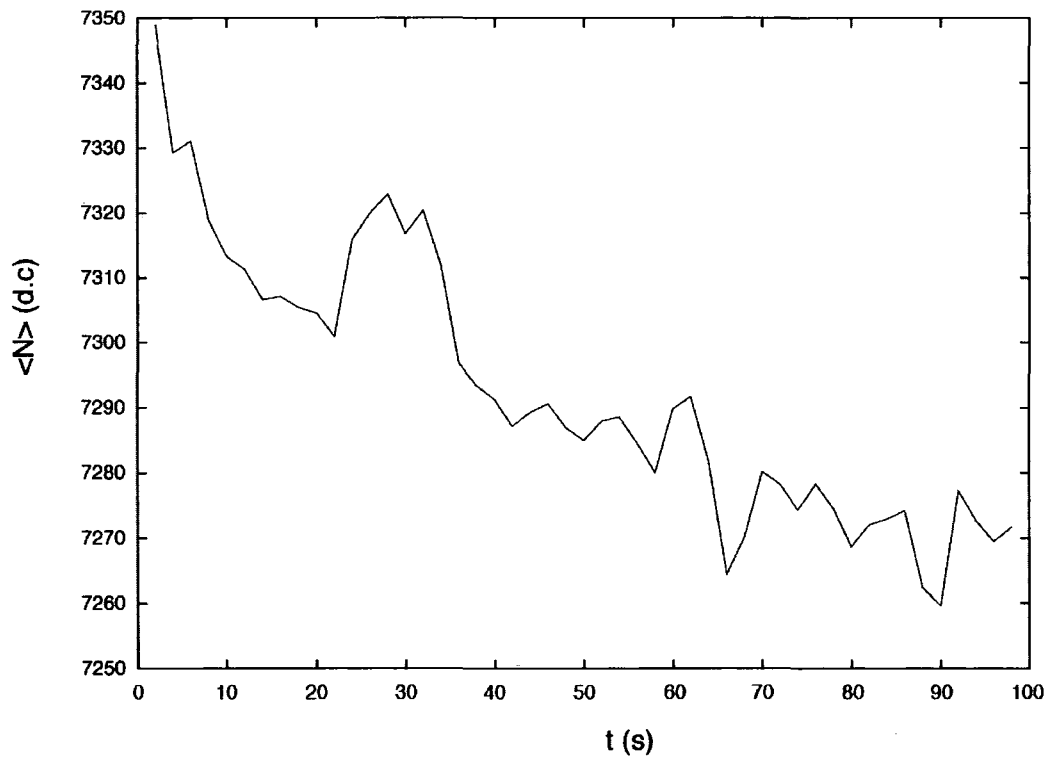


Figure 5.5: The variation of the average NSB pedestal across 100 s of optical data from Crab pulsar's observations with a single PMT. Each average value in this plot was calculated from the contributions of  $6 \times 10^4$  successive events corresponding to approximately 2 s exposure time.

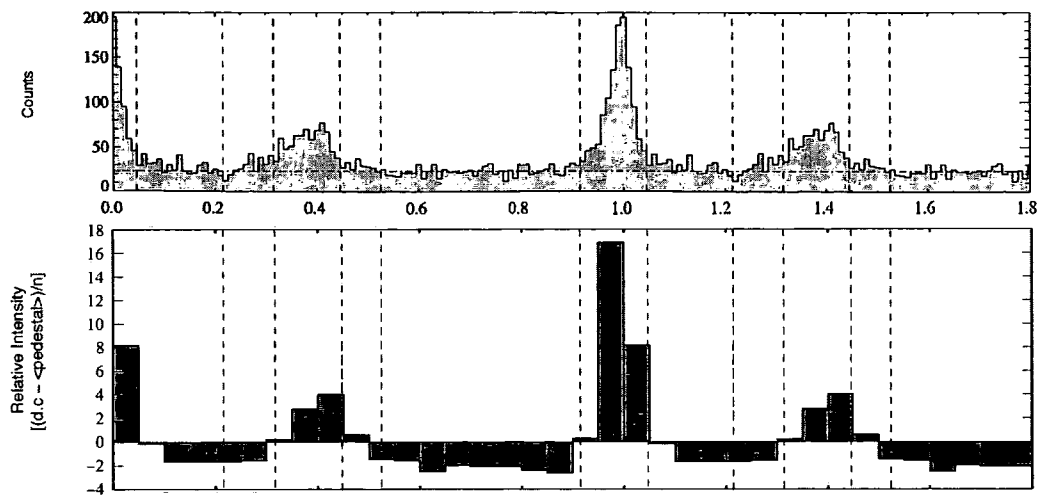


Figure 5.6: Comparison of the Crab pulsar's optical lightcurve (bottom phasogram), as was derived from our analysis using the GRO ephemeris, with the  $\gamma$ -ray pulse (top phasogram), as was measured with EGRET above 100 MeV [22]. The height of each bin in our phasogram is equal to the *average* d.c. excess from the NSB pedestal, of all events with phases contained in the bin. The latter was calculated by averaging over segments of 1,000 successive events, but without excluding those containing contributions from the pulsed signal. Therefore, it is biased towards higher values than the true value of the background. As a result, the bins outside the peak areas show a negative excess, on average. Although the temporal resolution of the optical plot ( $\approx 1.5$  ms) is lower than the  $\gamma$ -ray phasogram's ( $\approx 0.3$  ms), the positional coincidence of the peaks between the two profiles is evident.

<i>observatory</i>	Namibia
latitude ( $\phi$ )	$-23^{\circ}.27166667$
longitude ( $\theta$ )	$-16^{\circ}.5$
<i>source</i>	Crab pulsar
Right Ascension ( $\alpha$ )	05 h 34 m 31.95 s
declination ( $\delta$ )	$22^{\circ} 00' 52''.2$
<i>date</i>	00:00 UT, 0 January 2003

Table 5.4: The assumed values for the H.E.S.S. site location and the Crab pulsar, which were used to calculate the barycentric correction of an event with arrival time at 00:00 UT, on 0 January 2003.

*date*) in Namibia was at 00:00 UT, on 0 January 2003. The precise values used throughout our analysis are presented in Table 5.4.

The correction of the event's arrival time from Namibia to the SSB was done in two steps: first, we calculated the correction from the *observatory* to the geocentre and then the correction from the geocentre to the SSB; finally, we combined the corrections, while taking into account their sign, and compared the result with that generated by `Pulsar.GetArrivalTimeAtSolarSystemBarycenter`. The exact process is presented in the following sections.

### Geocentre–Namibia Correction

The calculation of the event's Local Apparent Sidereal Time (LAST) that corresponds to *date* (see Table 5.4) requires knowledge of the Greenwich Mean Sidereal Time (GMST), tabulated in the almanac. From that, we subtract the equation of equinoxes at *date*, and the result is the Greenwich Apparent Sidereal Time (GAST), also tabulated. Finally, we add the East longitude (or subtract the West longitude) of the *observatory* to get LAST. Hence,

$$\begin{array}{rcl}
 \text{GMST} & = & 06 \text{ h } 36 \text{ m } 60.3987 \text{ s} \\
 & & -0.9472 \text{ s} \\
 \text{GAST} & = & 06 \text{ h } 36 \text{ m } 59.4514 \text{ s} \\
 & & - 1 \text{ h } 06 \text{ m} \\
 \hline
 \text{LAST} & = & 05 \text{ h } 30 \text{ m } 59.4514 \text{ s}
 \end{array}$$

The next step is to find the Z.A.,  $z^{\circ}$ , of the *source* at *date*. For that, we need the hour angle ( $H^{\circ}$ ) of the *source*, which we calculate by subtracting its Right Ascension

( $\alpha$ ) from LAST. Therefore,

$$H^\circ = \text{LAST} - \alpha = -0^\circ.885410838 \quad (5.25)$$

The Z.A. can be calculated now from the spherical triangle which is defined by the north celestial pole, the *observatory* and the *source* (see Fig. 5.7):

$$\begin{aligned} \cos z &= \sin \delta \sin \phi + \cos \delta \cos \phi \cos H^\circ = 0.703464606 \Rightarrow \\ &\Rightarrow z = 45^\circ.294365 \end{aligned} \quad (5.26)$$

At this point we need to calculate the Earth radius  $R_\oplus(\phi)$  at the *observatory*, which should be between the maximum value on the equator ( $\phi = 0^\circ$ ) and the minimum on the poles ( $\phi = 90^\circ$ ). Our calculations are based on the values of the WGS 84 (World Geodetic System 1984) reference spheroid [388], with flattening

$$f = \frac{R_\oplus(0^\circ) - R_\oplus(90^\circ)}{R_\oplus(0^\circ)} = 0.003352811 \quad (5.27)$$

The following equation relates the radius of the Earth  $R_\oplus(\phi)$  with  $\phi$  and  $f$  [389]:

$$\begin{aligned} R_\oplus(\phi) &= R_\oplus(0^\circ) \left\{ 1 - f \sin^2 \left[ \tan^{-1} \left[ \frac{R_\oplus^2(90^\circ)}{R_\oplus^2(0^\circ)} \tan \phi \right] \right] \right\} \Rightarrow \\ \Rightarrow R_\oplus(\phi) &= 6374836.581 \text{ m} \end{aligned} \quad (5.28)$$

Finally, the barycentric correction can be calculated from the scalar product between the vector pointing to the *source* and the Earth radius vector connecting the centre of the Earth to the *observatory*. The angle between them is  $z^\circ$ . Thus,

$$\delta t_{\text{eo}} = \frac{1}{c} \mathbf{R}_\oplus \cdot \hat{\mathbf{s}} = \frac{1}{c} R_\oplus \cos z^\circ = 0.014958588 \text{ s} \quad (5.29)$$

### Conversion between UT and TDB

The barycentric correction from the geocentre to the SSB requires the position and velocity of the Earth at *date*. Although this is tabulated in the almanac, the time-scale used is the Barycentric Dynamical Time (TDB). Our *date* is in Universal Time (UT), so a conversion must be made. The conversion from Terrestrial Time (TT) to TDB for 2003 is given in the almanac [387] and for 00:00, 0 January 2003, it yields

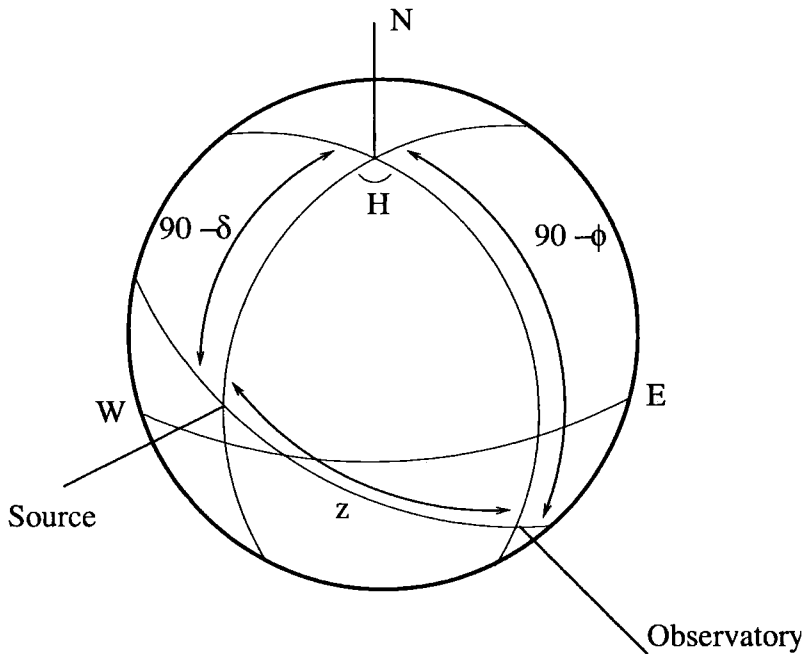


Figure 5.7: 3-dimensional projection of the observed source and observatory positions on the celestial sphere. The source's declination is denoted as  $\delta$  and the observatory's latitude, as  $\phi$ . Furthermore, in this representation, the hour angle that separates the two positions is letter-coded as  $H$  and the Z.A. of the source, as  $z$ . The celestial equator is the line that connects East (E) and West (W), whereas the north celestial pole is defined by the letter N.

$$\begin{aligned} \text{TDB} - \text{TT} &= 0.001658 \sin g + 0.000014 \sin 2g \text{ s} \Rightarrow \\ \Rightarrow \text{TDB} - \text{TT} &= -1.096785457 \times 10^{-4} \text{ s} \end{aligned} \quad (5.30)$$

where  $g = 356^\circ.27 + 0^\circ.98560028d$ , with  $d$  being the day number counting from 1 (1 January 2003) to 365 (31 December 2003). Application of this formula to our *date* corresponds to  $d = 0$ . The conversion from TT to UT requires the tabulated value of  $\Delta T = \text{TT} - \text{UT}$ , which we can use to obtain the time difference between TDB and UT at *date*. Hence,

$$\begin{aligned} \text{UT} = \text{TT} - \Delta T &= \text{TDB} - \Delta T + 1.096785457 \times 10^{-4} \text{ s} \Rightarrow \\ \Rightarrow \text{TDB} - \text{UT} &= 64.99989396 \text{ s} \end{aligned} \quad (5.31)$$

This means that the tabulated parameters that are given in the almanac with reference to 00:00 TDB should be extrapolated forward by 64.99989396 s to give the parameter values corresponding to *date*.

### Extrapolation of the Earth's Position

The almanac gives the position and velocity of the Earth with respect to the SSB at 00:00 TDB. We have derived the difference between TDB and UT, and so we can calculate the corresponding values at 00:00 UT using the equation

$$\mathbf{R}' = \mathbf{R} + \mathbf{V} \cdot \Delta t \quad (5.32)$$

where  $\mathbf{R}$  and  $\mathbf{V}$  are the tabulated Cartesian position and velocity vectors in au and  $\text{au d}^{-1}$ , respectively.  $\Delta t$  is the time difference between TDB and UT, as previously noted. Substituting for the values to be extrapolated, we get

$$\begin{aligned} \mathbf{R}' &= \begin{pmatrix} -0.153910449 \\ 0.886499068 \\ 0.384340387 \end{pmatrix} \text{ au} + \begin{pmatrix} -17268248 \\ -2545393 \\ -1103033 \end{pmatrix} \times 10^{-9} \frac{\text{au}}{\text{d}} \times \\ &\quad \times \frac{\Delta t}{86400} \text{ d} = \begin{pmatrix} -0.15392344 \\ 0.886497153 \\ 0.384339557 \end{pmatrix} \text{ au} \end{aligned} \quad (5.33)$$



**SSB–Geocentre correction**

In order to correct for the revolution of the Earth around the Sun, we have to transform the *source* position vector into the equatorial rectangular co-ordinate system with reference to the SSB [387]. In the latter, we find the relationship between  $(\alpha, \delta)$  and  $(x, y, z)$  to be

$$\begin{aligned}\hat{\mathbf{s}} = (x_s, y_s, z_s) &= (\cos \alpha \cos \delta, \sin \alpha \cos \delta, \sin \delta) \Rightarrow \\ \Rightarrow \hat{\mathbf{s}} &= (0.102808958, 0.92137092, 0.374841226) \text{ au}\end{aligned}\quad (5.34)$$

Having the two vectors,  $\mathbf{R}'$  and  $\hat{\mathbf{s}}$ , we can now take their scalar product prior to calculating the Sun–Earth barycentric correction  $\delta t_{se}$ . So,

$$\begin{aligned}\delta t_{se} &= \frac{\mathbf{R}' \cdot \hat{\mathbf{s}}}{c} = \frac{1}{c}(X' \cos \alpha \cos \delta + Y' \sin \alpha \cos \delta + Z' \sin \delta) \Rightarrow \\ \Rightarrow \delta t_{se} &= 471.5765905 \text{ s}\end{aligned}\quad (5.35)$$

where  $X', Y', Z'$  are the Cartesian co-ordinates of  $\mathbf{R}'$ . Furthermore, the angle  $\theta_{se}$  between  $\mathbf{R}'$  and  $\hat{\mathbf{s}}$  is given by

$$\theta_{se} = \cos^{-1} \left( \frac{c \cdot \delta t_{se}}{R'} \right) = 15^\circ.00845579 \quad (5.36)$$

**Total Barycentric Correction**

The total correction from the *observatory* to the SSB is given by some linear combination of  $\delta t_{eo}$  and  $\delta t_{se}$ . In our case, because both  $\theta_{se}$  and  $z^\circ$  are acute, the corrections add up to give a  $\delta t_{tot}$  delay (see Fig. 5.8). In fact, for night-time observations like those of Cherenkov astronomy, this is the only feasible scenario. However, in radio astronomy where observations during daylight are possible, the above individual corrections could add up to a negative delay (obtuse angles), or subtract to give either a negative or a positive delay (only one obtuse). Furthermore, if both  $\mathbf{R}'$  and  $\mathbf{R}_\oplus$  form right angles with  $\hat{\mathbf{s}}$ , then no correction is needed. Nevertheless, in the present case we have

$$\delta t_{tot} = \delta t_{eo} + \delta t_{se} = 471.5915491 \text{ s} \quad (5.37)$$

This correction represents the light-travel time as it was calculated using UT values for the arrival times of the events at the *observatory*. Therefore, the above amount of time has to be added to the UT seconds since JD2000 of an event that had arrived at 00:00 UT, on 0 January 2003, in order to calculate the UT seconds of the same event when it was at the SSB. Note that this correction is independent of the time-scale used.

By running `Pulsar.GetArrivalTimeAtSolarSystemBarycenter` with input `UTC=94564800.816` s, which corresponds to the date under test, we got the barycentred time to be `TDB=94565336.591047972` s in the TDB time-scale. In order to compare the barycentred with the UTC timestamp, we expressed them into the same time-scale using the formula

$$\begin{aligned} \text{UTC} = \text{TDB} - 0.001658 \sin g - 0.000014 \sin(2g) - \\ - \Delta\text{AT} - 32.184 \text{ s} \end{aligned} \quad (5.38)$$

where  $\Delta\text{AT} = \text{TDT} - \text{UTC} - 32.184$  s, and its value for 2003 is tabulated in the almanac. After substituting for the values that correspond to our case, Eq. 5.38 takes the simpler form

$$\text{UTC} = \text{TDB} - 64.183890321 \text{ s} \quad (5.39)$$

Finally, the difference between the two computed timestamps, either in the UTC or TDB time-scale, is

$$(\Delta\text{UTC})_{\text{H.E.S.S.}} = (\Delta\text{TDB})_{\text{H.E.S.S.}} = 471.591157652 \text{ s} \quad (5.40)$$

which is different by only 0.000391448 s from the one calculated from first principles (see Eq. 5.37). This amount corresponds to  $\approx 1\%$  of the Crab pulsar's period, and therefore our result can be considered satisfactory.

### 5.3.4 Extraction of Low-Energy Events

#### Motivation

Pulsed emission from  $\gamma$ -ray pulsars has been seen with EGRET to extend up to at least 20 GeV (see e.g. Fig. 3.22). The Vela and Geminga pulsars show evidence of a sharp cut-off within EGRET's energy range, but they are expected according to

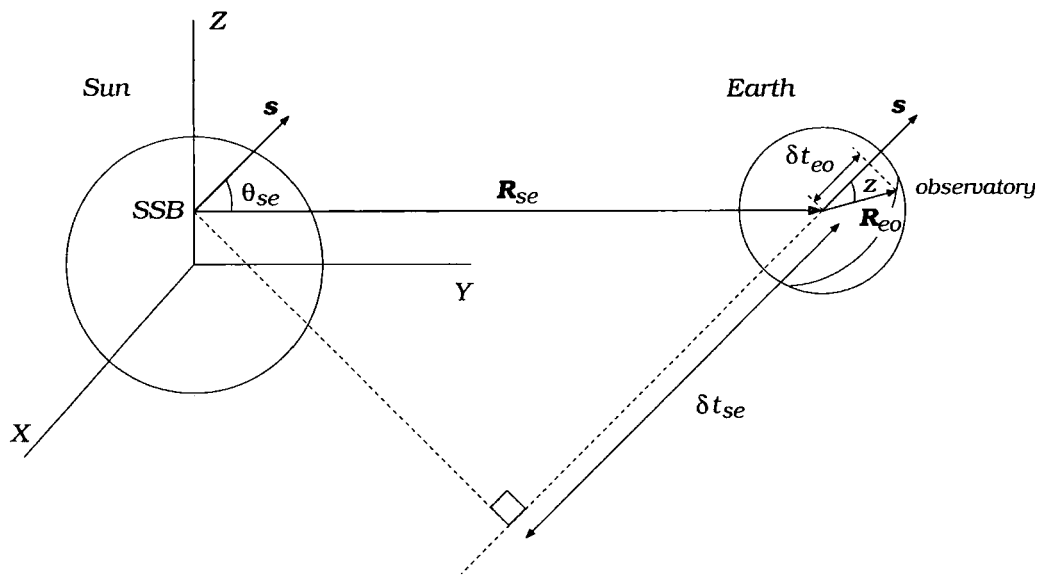


Figure 5.8: The Earth-Sun-Observatory configuration for the case where the Earth-Sun and Earth-Observatory barycentric corrections are positive increments to the event arrival times at the Observatory.

the Outer Gap models to have a significant pulsed component in TeV energies (see e.g. Fig. 3.23): for the Vela pulsar, the integral flux of the TeV component ( $\gtrsim 100$  GeV) is roughly 7 orders of magnitude lower than that observed with EGRET above 100 MeV. On the other hand, pulsars like PSR B1706–44 retain their power-law spectra up to the top energy bin of EGRET, but they have not been detected by VHE experiments in the TeV range. Clearly, a cut-off must exist somewhere above 20 GeV. The predicted Outer Gap flux for PSR B1706–44 above the energy threshold of H.E.S.S. is negligible: almost 10 orders of magnitude lower than the EGRET one. However, the sensitivity of the H.E.S.S. telescopes above 100 GeV is at least 3 orders of magnitude higher than EGRET’s at a few GeV energies, which makes it possible to detect luminous TeV components from pulsars like Vela. On the other hand, all EGRET pulsars exhibit bright GeV components whose flux is well within H.E.S.S.’s grasp, but whose cut-offs are steep, and even the most optimistic Outer Gap scenarios restrain the emission below the imaging threshold of H.E.S.S. ( $\gtrsim 100$  GeV). Fig. 5.9 summarises all of the above in the sensitivity plot for H.E.S.S. Phase I, which shows the minimum required integral flux for a  $5\text{-}\sigma$  detection after 50 h of exposure time, as a function of photon energy. For the sake of comparison, we have included EGRET’s sensitivity after 1 year of observations. Both sensitivity curves correspond to observations of steady sources. In addition, the plot includes the predicted integral fluxes as a function of the photon energy, from a Vela- and PSR B1706–44-type Outer Gap accelerator.

In the context of this thesis, we are interested in the low-energy synchro-curvature emission, part of which has been detected with EGRET, and which is also consistent with the Polar Cap and Outer Gap acceleration mechanisms. One can hope to detect the steep GeV cut-offs by selecting the least energetic events detected with H.E.S.S. from pulsar observations. These events are likely to lie below the detector’s threshold, for which enhancement using shape parameters fails due to the inadequate number of pixels in the shower image. These events do not generally pass the shape and orientation cuts, i.e. *length*, *width*, *alpha*, etc. Their positional information, however, requires only a few bright pixels per event, and hence the application of appropriate *IA* and *distance* cuts to the data guarantees their survival, while at the same time provides a rejection of unwanted high-energy events. The reasoning behind our specific cut selection is presented in the following paragraph.

Unfortunately, the advantage of background rejection is lost with this analysis strategy. The advantage is recovered with the use of sensitive pulsed-analysis

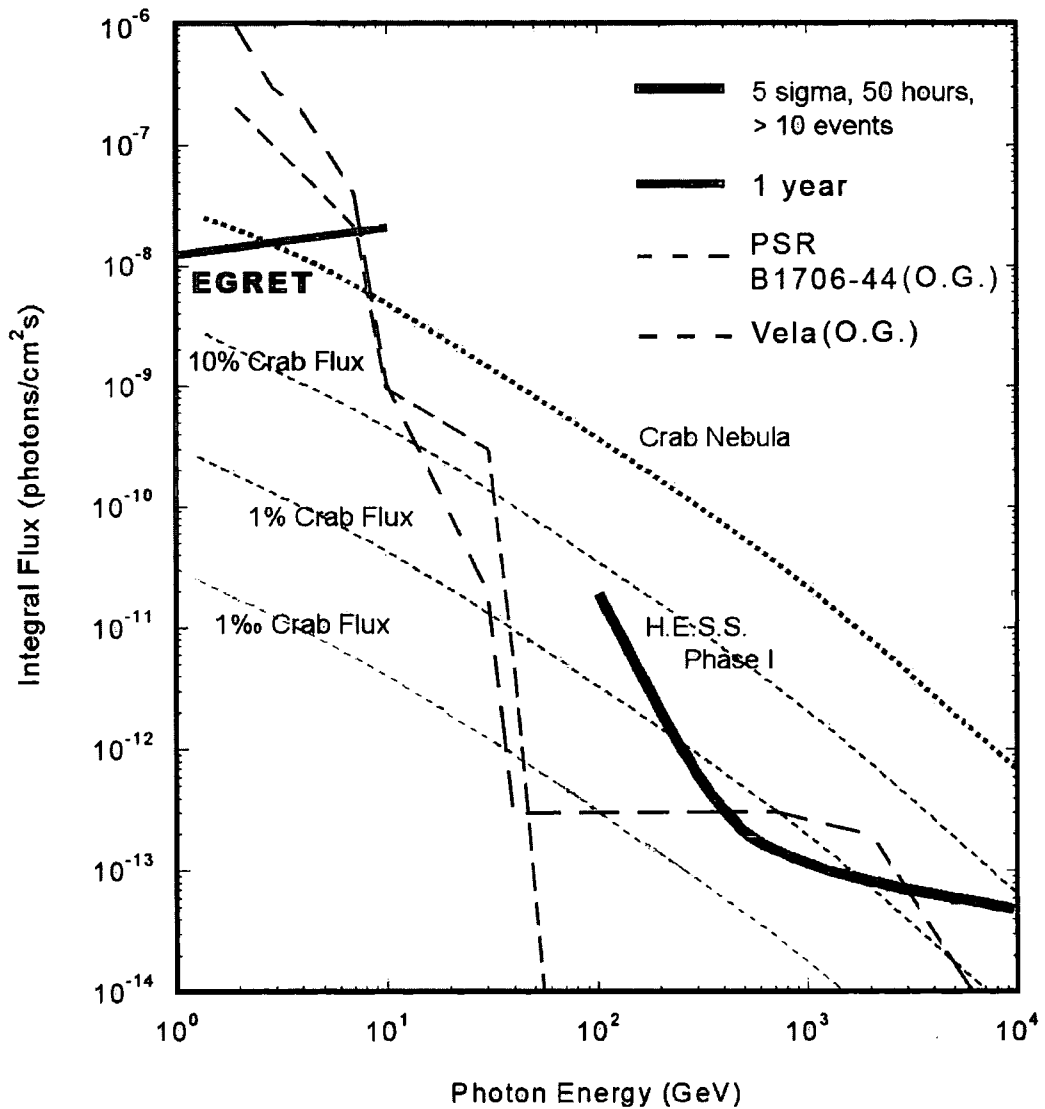


Figure 5.9: Comparison plot between the sensitivity of H.E.S.S. Phase I above 100 GeV [390] and EGRET's, above 100 MeV [391]. Also included are the predicted Outer Gap integral fluxes as a function of energy, from Vela (dashed black line) and PSR B1706-44 (dashed grey line). The calculations were based on Outer Gap spectra by Hirotani [296].

methods, which provide the means for a signal detection, even below the detector threshold. These methods are discussed in section 5.4. Another critical parameter of the low-energy analysis is the number of events which the H.E.S.S. telescopes are capable of detecting below their threshold, given a source's  $\gamma$ -ray spectrum. The answer to that question requires the simulation of the detector's effective area as a function of the energy. A detailed description of how this was done is given in section 5.7.

### Image Cut Selection

In addition to the cuts on the Hillas parameters (see Table 5.3), the standard cuts apply a stricter sector ( $p'$ ) and pixel ( $q'$ ) criterion to the data (see 4.3.1). Clearly, this can only discard events further, as the hardware values,  $q$  and  $p$ , had already been in effect during the observations. A choice of  $(p', q') = (5, 10)$  is typically made, which can be considered conservative compared to the hardware setting of  $(p, q) = (4, 6)$  for single-telescope observations and  $(p, q) = (3, 5)$  for stereo ones [335].

The standard cuts are not suitable for the analysis of the lowest event energies possible. Instead, their purpose is to reject the maximum amount of cosmic rays ( $\sim 99.98\%$ ), while retaining a statistically significant amount of  $\gamma$  rays ( $\sim 30\%$ ). Unfortunately, the two key parameters towards this goal, i.e. shower imaging and telescope sensitivity, do not serve well for our purpose: the former improves with increasing energy, above 100 GeV, whereas the latter peaks at TeV energies. For example, a set of cuts that is similar to the one of Table 5.3 was applied to 4.5 h of Crab nebula data [334] and resulted in a  $20\text{-}\sigma$  detection. However, the energy threshold after the application of the cuts was estimated to be  $\approx 800$  GeV. Hence, the restriction to only low-energy events has to invoke a different set of cuts.

Our selection of an appropriate low-energy set of cuts was derived from the optimised *IA* range — which is implicit in the standard cuts — rather than from a series of Monte Carlo simulations. More specifically, if we consider the above set of standard cuts (say C1), then we can deduce from it a set of cuts (say C2) which will focus on energies below those covered by C1: the minimum and maximum values of *LoverS* in C1 are  $LS_{\min} = 0$  and  $LS_{\max} = 0.018$  mrad ph.e.<sup>-1</sup>, respectively; likewise, for the *length* cut we have  $L_{\min} = 1.8$  and  $L_{\max} = 5.2$  mrad. Fig. 5.10 shows a graphical representation of the region that is covered by C1, in the *length-size* parameter space. Since the low-energy events are associated with small events

on the camera, one should aim, as a first step, at the lowest possible *size* values. Hence, by setting our upper limit on the *size*,  $S_{\max}^{\text{C2}}$ , equal to the minimum implicit *size* of C1,  $S_{\min}^{\text{C1}}$ , we concentrated only on the smallest events that passed the trigger criteria. Using the values of C1 and Fig. 5.10, we have

$$S_{\max}^{\text{C2}} = \frac{L_{\min}}{LS_{\max}} = 100 \text{ ph.e.} \quad (5.41)$$

Bearing in mind that the smallest camera events are unlikely to have all their Hillas parameters reconstructed, we let all the shape and orientation parameters without restrictions. Nevertheless, for reasons that were explained earlier (see section 4.2.5), we decided to apply a cut to the *distance* of the events from the expected source position on the camera: following the standard analysis, we restricted the *distance* parameter below 18 mrad. However, realising the importance of keeping only those events that are small and central, we applied a second set of cuts to the data, which restricts the *distance* even further. The chosen upper limit on the *distance* was 12.7 mrad, which constrains the sample of events to an area on the camera exactly half compared to that from the standard cuts: i.e.  $\pi(12.7)^2 = \pi(18)^2/2$  (mrad)<sup>2</sup>. The H.E.S.S. array achieves an angular resolution of  $0.1^\circ$  ( $\sim 1.7$  mrad) per event. Hence, our *distance* cut restricts the event positions within a well-defined area on the camera: i.e. below  $12.7 \pm 1.7$  mrad.

For the image-cleaning parameters,  $p'$  and  $q'$ , we chose to compromise between the values used in the standard analysis,  $(p', q') = (5, 10)$ , and the hardware setting for stereo observations,  $(p', q') = (3, 5)$ . So, a loose criterion with  $(p', q') = (3, 7)$  was used, which would guarantee the registration of the smallest detectable events, but also reduce slightly the amount of NSB recorded in the DSTs: it has been reported that for DC signals the gain from reducing the threshold from (5,10) to (4,7) would lead to a  $\sim 15\%$  improvement in significance [384].

The two sets of low-energy cuts that were used during the extraction of the data are shown in Table 5.5. Only the timestamps of the events passing those cuts were considered in our follow-up temporal analysis.

## 5.4 Uniformity Tests

In 1969, Beran derived a complete class of uniformity tests on the circle [392]. Given a set of arrival times  $t_i$  ( $i = 1, 2, 3, \dots, n$ ), one can fold  $t_i$  into phases,  $\phi_i$ , with an assumed frequency,  $f_i$ . The circular tests of uniformity give an estimate of the

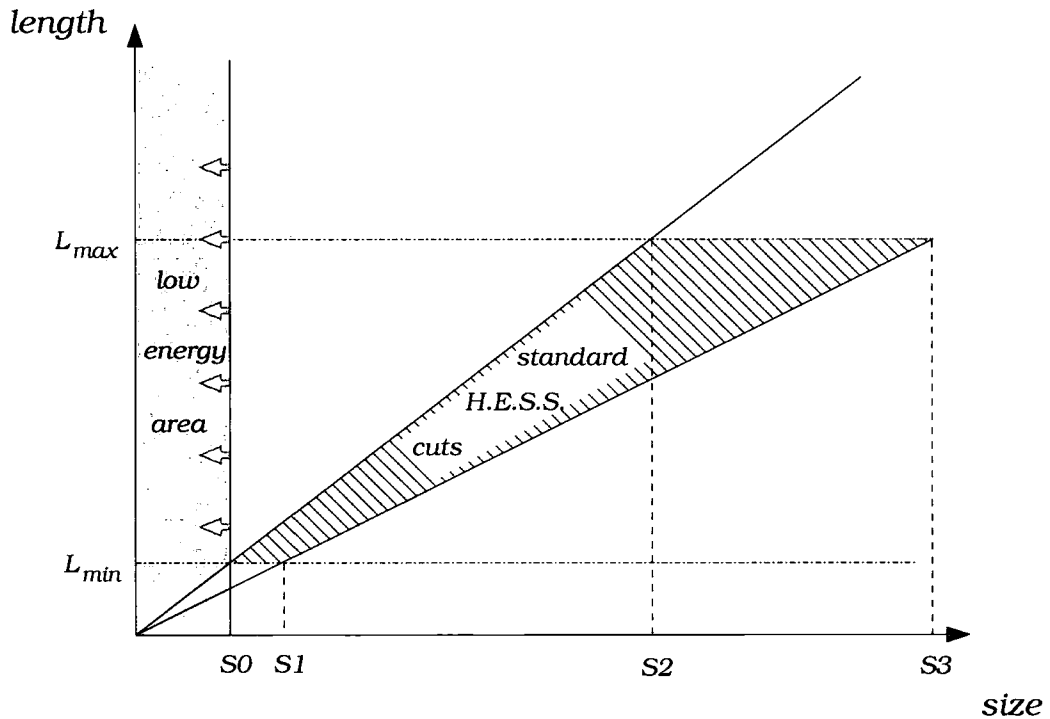


Figure 5.10: This plot shows the constraints imposed by the standard *length* and *LowerS* cuts on the image size, in the *length*–*size* parameter space. Application of these cuts also implies that the *size* would have to be between a minimum ( $S_0$ ) and a maximum ( $S_3$ ) value. This allows us to create a set of cuts which is optimised for low-energy events, by setting  $S_0$  as our maximum. In this figure, the line-filled area corresponds to the standard-cuts selection area, which is normally optimised for  $\sim$  TeV energies. The region with *size*  $< S_0$  (grey-shaded) defines a selection of events with low ph.e. content. An additional cut on the *distance* of those events refines our sample to low-energy events.



Parameter	<i>Standard</i>		<i>Central</i>		
	min	max	min	max	
<i>length</i>	0	$\infty$	0	$\infty$	mrاد
<i>width</i>	0	$\infty$	0	$\infty$	mrاد
<i>distance</i>	0	18	0	12.7	mrاد
<i>size</i>	0	100	0	100	ph.e.
<i>alpha</i>	0	$\infty$	0	$\infty$	
Image Cleaning ( $p',q'$ )	(3,7)		(3,7)		(pixels,ph.e.)

Table 5.5: Our two sets of low-energy image cuts. The *standard* set is based on the standard cuts of Table 5.3, whereas the *central* set is aimed towards small and more centralised events on the camera.

probability of the phases being distributed uniformly in the phase parameter space, from  $[0, 2\pi)$  (see Fig. 5.11). The basic assumption of all such tests is the absence of directional preference in the data: i.e. that there is no bunching in phase. Hence, high probability levels dictate uniformity, whereas low probability levels could be an indicator of signal presence. The assumption of uniformity is referred to as the *null hypothesis*,  $H_0$ , and can be formulated as follows:

$$H_0 : g(\phi) = 1/(2\pi); \quad \phi \in [0, 2\pi) \quad (5.42)$$

where  $g(\phi)$  is the probability density function (p.d.f.) that describes the true intensity variations of the signal as a function of phase: i.e. the true lightcurve. Under  $H_0$  this function is constant across one period, which means that the probability of finding an event at a specific phase is the same as finding it at any other. Such lightcurves describe the uniform background in  $\gamma$ -ray data.

Alternatively, the rejection of the null hypothesis leads to the confirmation of signal presence at a certain level of significance, which is estimated by the uniformity test. This alternative hypothesis,  $H_A$ , can be described by a p.d.f. that is a linear function of the uniform p.d.f. mentioned above, and a periodic p.d.f.,  $g_s(\phi)$ , which represents the pulsed signal undiluted by background: its form is

$$H_A : g(\phi) = pg_s(\phi) + (1 - p)/(2\pi) \quad (5.43)$$

where  $p$  is the pulsed fraction of the total number of events in the lightcurve,  $N = N_{\text{pulsed}} + N_{\text{unpulsed}}$ : i.e.

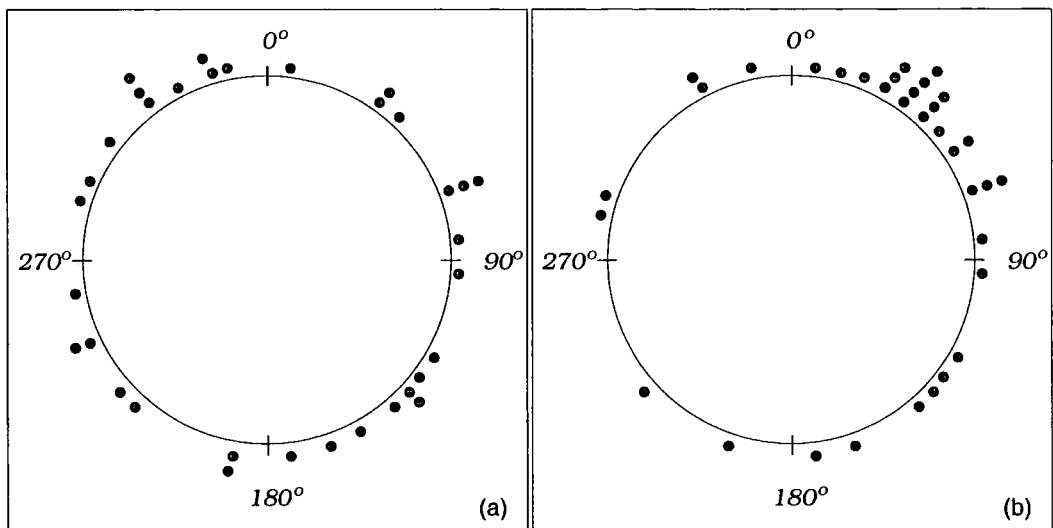


Figure 5.11: Testing for uniformity on the circle. Circular tests of uniformity estimate the degree to which the distribution of event phases (black bullets) across the phase parameter space,  $[0, 2\pi)$ , is bunched around specific phase positions. For example, case (a) in this figure shows that there is almost negligible bunching in phase, and hence the distribution can be considered uniform. On the other hand, (b) shows clearly a preferred phase direction around  $30^\circ$ .

$$p = \frac{N_{\text{pulsed}}}{N_{\text{pulsed}} + N_{\text{unpulsed}}} \quad (5.44)$$

The function  $g_s$ , which is also called *source function* in the bibliography (see e.g. [393]), is generally unknown. In addition, the signal strength — which is expressed through the pulsed fraction — is also unknown. The form of  $g(\phi)$  can only be discerned through observations, but the true lightcurve can only be obtained after an infinite amount of events have been recorded. As this is not feasible, one can only approximate  $g(\phi)$  by constructing various experimental functions, called *density estimators*, using the phases of the recorded sample of events. A density estimator,  $\hat{g}(\phi; \phi_i)$ , has the property

$$g(\phi) \equiv \lim_{n \rightarrow \infty} \hat{g}(\phi; \phi_i) \quad (5.45)$$

where  $i = 1, 2, 3 \dots, n$ .

De Jager *et al.* have investigated the application of certain density estimators to  $\gamma$ -ray data [394], some of which are presented in the following sections. Based on these estimators, one can construct *test statistics*, which are parameters that quantify the degree of uniformity in the data. The capabilities and power of various tests for uniformity are dependent on their associated statistics. A general expression for these statistics has the form

$$B = 2\pi N \psi(\hat{g}) = \int_0^{2\pi} [\hat{g}(\phi; \phi_i) - 1/(2\pi)]^2 d\phi \quad (5.46)$$

Basically,  $\psi(\hat{g})$  provides a measure of the deviation of the density estimator,  $\hat{g}(\phi)$ , from the uniform distribution, for a given data set. In all uniformity tests, the larger the  $\psi(\hat{g})$ , the more unlikely the  $H_0$ .

In the following paragraphs, we will describe four uniformity tests that were used in our periodicity searches.

### 5.4.1 Pearson's $\chi^2$ -test

#### General

The  $\chi^2$ -test has been successfully used in X-ray astronomy, where data are a lot richer compared to those from  $\gamma$ -ray observations [395],[396]. This test is a special case of the general class of Beran's tests, and the  $\chi^2$ -test statistic can be derived from Eq. 5.46 using a Histogram density Estimator (HE) [394]. The general form of

the statistic is [397]

$$\chi_{k-1}^2 = \sum_{j=1}^k \frac{(N_j - N_{\text{expected}})^2}{\sigma_{\text{expected}}^2} = \sum_{j=1}^k \frac{(N_j - N/k)^2}{N/k} \quad (5.47)$$

where  $N_j$  is the number of observed events contained in each phase bin,  $j$ , and  $k$  is the total number of bins;  $N_{\text{expected}} = N/k$  is the expected number of events in each bin, assuming a flat distribution, with  $N$  being the total number of events in the histogram. The standard deviation of  $N_{\text{expected}}$  is  $\sigma_{\text{expected}} = \sqrt{N_{\text{expected}}}$ , if one assumes a Poissonian distribution for the number of counts.

Note that the  $\chi_{k-1}^2$  statistic is quoted with the parameter  $k - 1$ . This parameter corresponds to the *degrees of freedom* (df) involved in the construction of the histogram from which the statistic is derived. The df in every problem that is defined by a set of parameters is equal to the number of parameters in a subset, whose values are independent of any other parameter in the set. The construction of a histogram with  $k$  bins, in particular, requires the knowledge of the contents of only the  $k - 1$  bins. For a fixed number of events,  $N$ , the values in the  $k - 1$  bins can be chosen independently of any other bin, but the content of the  $k^{\text{th}}$  bin is restricted by the total number of events to the value  $N_k = N - \sum_{j=1}^{k-1} N_j$ . Hence, the df in the  $\chi_{k-1}^2$ -test are always one less than the number of bins.

This helps us define the reduced  $\chi_{k-1}^2$  statistic, which is the version normalised to the number of df and is given by

$$\chi_{k-1}^2/(k-1) = \frac{1}{k-1} \sum_{j=1}^k \frac{(N_j - N/k)^2}{N/k} \quad (5.48)$$

Generally, the  $H_0$  is accepted for values of  $\chi_{k-1}^2/(k-1) \sim 1$ . The presence of a signal in the data yields high values of the reduced  $\chi_{k-1}^2$ , whereas  $\chi_{k-1}^2/(k-1) \ll 1$  reveals an unphysical data origin: e.g. a flat distribution with unrealistically low fluctuations.

### The Choice of Bins

Clearly, the value of  $\chi^2$  depends on the number of phase bins,  $k$ , in which the lightcurve has been divided. Therefore, the results from the  $\chi^2$ -test are *binning-dependent*, which introduces a bias associated with user choice. Choosing the bin number,  $k$ , affects the bin width,  $1/k$ . The *true* intensity variations of pulsar emis-

sion can only be represented with a phasogram if  $k \rightarrow \infty$ , but that would require an equally infinite number of photons. In reality, the amount of collected  $\gamma$  rays is very limited: EGRET collected only  $\sim 100$  pulsed  $\gamma$  rays above 1 GeV, after observing the Crab pulsar for 3 months (Fig. 5.12). If a narrow peak ( $\delta < 1/k$ ) in a pulsar's profile occurs at a phase which happens to lie on the common border between two bins, then the number of events corresponding to the peak is split across these bins, and the signal excess from the mean is reduced. However, an identical lightcurve shifted by half a bin's width, i.e.  $\Delta\phi = 1/(2k)$ , would place the narrow peak within one bin and maximise the significance of the excess (Fig. 5.13). Hence, the  $\chi^2$ -test depends on rotations, and therefore, in bibliographical terms, it is not a *rotation invariant*.

On the other hand, if the choice of  $k$  is such that every peak is resolved by a high number of bins, then there is danger of running out of statistics, since each bin is likely to contain a very low percentage of the overall counts. Again, this could lead to a flat profile with low significance. In this latter case, the choice of  $k$  is also limited by the temporal resolution of the instrument, although this upper limit is not a useful one, since modern VHE experiments, like H.E.S.S., have resolutions that are up to 3 orders of magnitude higher than most pulsed profiles require. For example, the EGRET profile of the Crab pulsar above 1 GeV (Fig. 5.12) was divided into 50 bins, each one representing a time step of  $33/50 \approx 0.7$  ms in the pulsar's rotation; and with a temporal resolution of  $\sim 1 \mu\text{s}$ , the profile could have been split, in principle, into 33,000 bins; then, the 60  $\gamma$  rays of the main peak would have had to be distributed amongst  $\approx 4,500$  bins, most of which would have been empty.

It becomes evident that the  $\chi^2$ -test is sensitive to the selection of bins and that this affects the significance of the result. Unfortunately, there is no hard-and-fast rule for choosing the optimal  $k$  which will maximise the test sensitivity, and the final choice depends on the expected profile in each case. Since no pulsar has been detected in VHE, the  $\gamma$ -ray profiles are unknown *a priori*. The Crab pulsar may be the only exception, as its profile remains consistent throughout the EM spectrum. For all the rest we can only assume that the EGRET profiles are similar in the VHE regime. In general, it seems appropriate to choose  $k = 1/\delta$  in order to include the FWHM of the peaks in single bins.

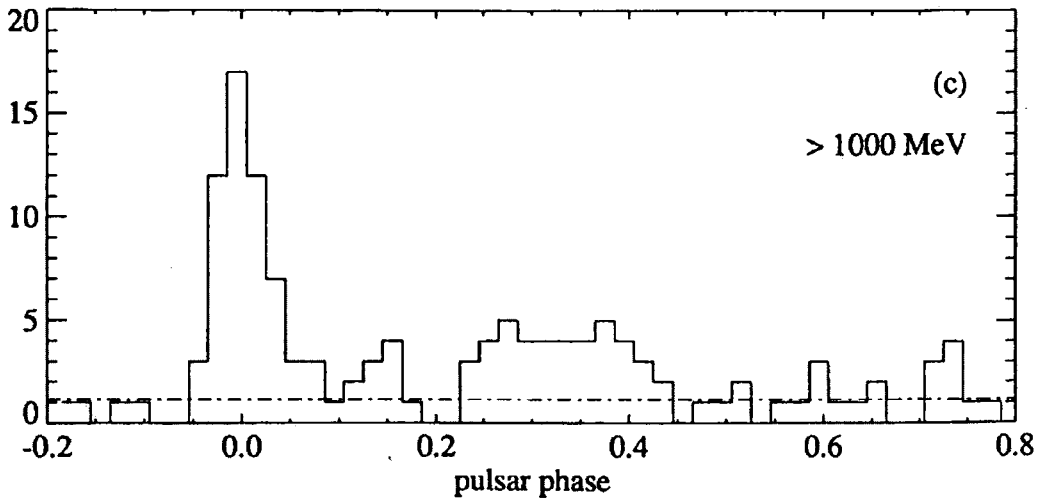


Figure 5.12: (from [22]) The Crab pulsar's  $\gamma$ -ray phasogram above 1 GeV, from observations that took place from April to June 1991, with EGRET. The main peak of the profile at phase 0 is resolved by a mere 60 photons divided amongst 7 bins.

### Test Sensitivity

Leahy *et al.* [398] have performed a number of checks which show that the  $\chi^2$ -test becomes increasingly sensitive with decreasing duty cycles,  $\delta$ . They plotted the *test power* as a function of the signal duty cycle,  $\delta$ , assuming  $k = 16$  bins and  $p = \text{const.}$  In their work, the test power is expressed as the percentage of successful detections of a square pulse of known period, at a given probability level. However, this definition of test power is not unique and varies amongst authors. Fig. 5.14 shows the resulting function, which is based on individual calculations of  $\chi^2$  for square pulses of known period and varying  $\delta$ . It can be seen that the power of the  $\chi^2$ -test is very sensitive to the width of the signal and that it varies by a factor of  $\approx 20$  across the duty cycle range.

Using simpler arguments, it was possible to derive an analytical expression for the value of  $\chi^2$  as a function of  $\delta$  and the pulsed fraction,  $p$ . Like Leahy *et al.*, we assumed a square pulse superimposed on a Poissonian background with standard deviation  $\sigma_c = \sqrt{N_c}$ , where  $N_c$  is the collected number of cosmic-ray photons in exposure time  $T$ . The pulsed component consists of  $N_\gamma$  photons distributed across  $m$  bins, with the total number of bins being  $n > m$ ; hence the duty cycle is  $\delta = m/n$ . Having chosen a square pulse, we assumed that the fluctuations of the pulsed component

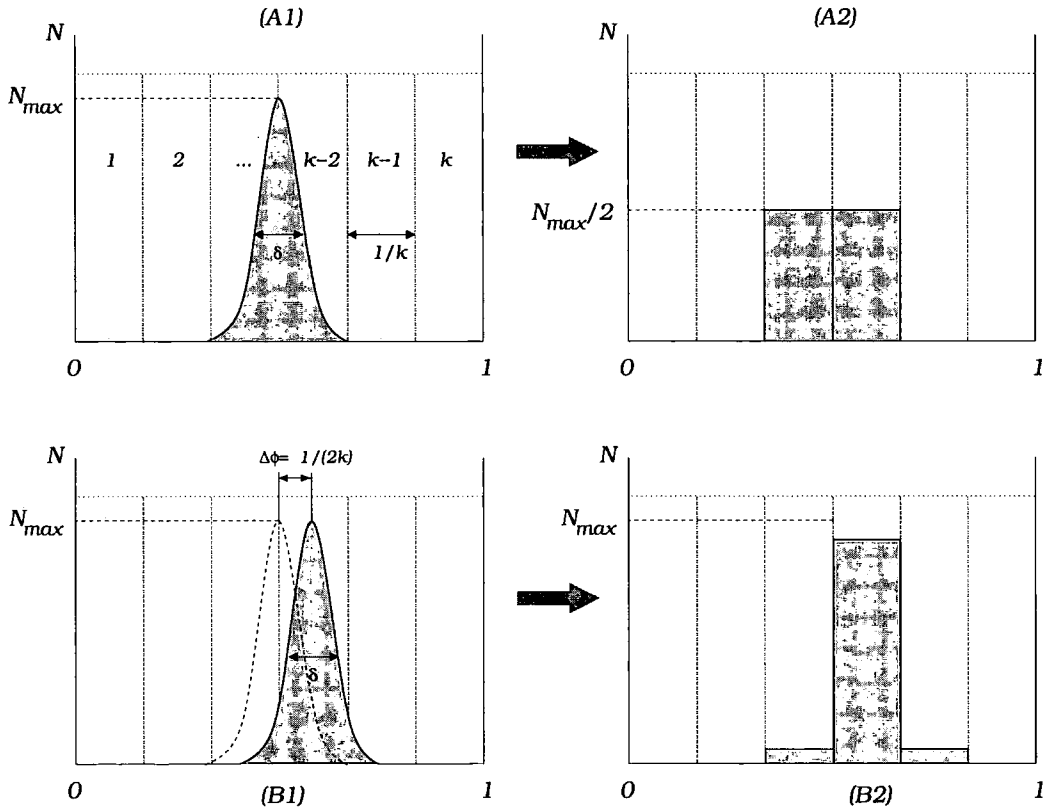


Figure 5.13: A schematic representation of the  $\chi^2$ -test dependence on rotations. Phasogram A1 shows the true lightcurve of a pulsar, which contains a single, narrow peak of duty cycle  $\delta$ . The calculation of  $\chi^2$  requires a binning decision. A choice of  $k$  bins whose width is large enough to contain the entire peak could optimise the significance. However, in the absence of *a priori* knowledge of the peak position, the binning process could split the peak into two bins (phasogram A2), each one containing half the number of counts with respect to the true maximum,  $N_{\max}$ . Hence, the signal excess, as calculated with the  $\chi^2$ -test, is reduced compared to the actual. A shift of all the event phases by  $1/(2k)$ , which corresponds to half a bin's width, fits almost all the pulsed photons into a single bin (phasogram B1). Consequently, the resulting phasogram (B2) becomes a faithful representation of the true lightcurve, and the significance is maximised. The dependence of the calculated  $\chi^2$  values on such shifts (or rotations) is a major disadvantage compared to rotation-invariant tests, like the Rayleigh test (see next section).

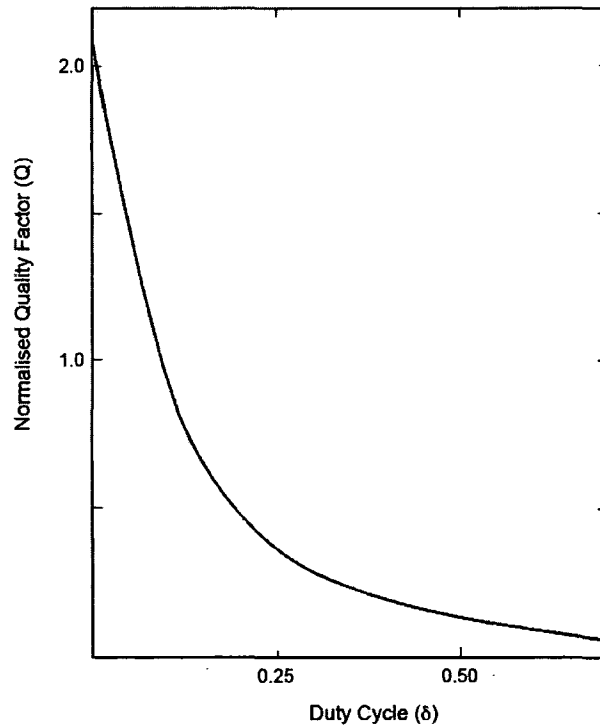


Figure 5.14: (from [398]) The power of Pearson's  $\chi^2$ -test, in arbitrary units, as a function of the duty cycle of the pulsed signal,  $\delta$ . The values of the  $y$  axis correspond to a normalised quality factor — defined in Leahy *et al.*'s publication [398] — which is related to the percentage of successful detections of the tested pulse, at a 90% confidence level: for  $Q = 1$ , the pulse is detected 50% of the time. Leahy *et al.* used square pulses of known period and variable  $\delta$  and calculated  $\chi^2_{15}$  for each individual signal. The signal strength,  $p$ , was fixed in all tests.



are zero, and therefore every one of the  $m$  bins contains  $N_\gamma/m$   $\gamma$  rays. Fig. 5.15B shows the assumed phasogram.

Using this phasogram, one can calculate the reduced  $\chi^2$  value, which is generally given by Eq. 5.48. In our case, the expected number of events in each bin is  $(N_\gamma + N_c)/n$ , where  $N_c + N_\gamma$  is the total number of events in the phasogram. Hence, the null hypothesis corresponds to those events being uniformly distributed across the entire phase range. We would like to calculate  $\chi_{n-1}^2/(n-1)$  for the case where there is significant excess in  $m$  contiguous bins of the phasogram, as a result of pulsed emission occurring in a specific phase range.

If  $N_i$  is the *observed* number of events in the  $i^{\text{th}}$  bin, then the general form of the reduced  $\chi_{n-1}^2$  statistic is

$$\chi_{n-1}^2/(n-1) = \frac{1}{n-1} \frac{\sum_{i=1}^n \left( N_i - \frac{N_\gamma + N_c}{n} \right)^2}{(N_\gamma + N_c)/n} \quad (5.49)$$

Outside the pulse region the phasogram contains only background events, whereas the pulse consists of background and pulsed events. We can split this sum into these two regions. Hence,

$$\chi_{n-1}^2/(n-1) = \frac{1}{n-1} \left[ \frac{\sum_{i=1}^m \left( \frac{N_\gamma}{m} + N_i - \frac{N_\gamma + N_c}{n} \right)^2}{(N_\gamma + N_c)/n} + \frac{\sum_{i=1}^{n-m} \left( N_i - \frac{N_\gamma + N_c}{n} \right)^2}{(N_\gamma + N_c)/n} \right] \quad (5.50)$$

where we have separated the known pulsed component,  $N_\gamma/m$ , from the unknown background component,  $N_i$ .

At this point we will make an effort to estimate the quantity  $N_i - N_c/n$ , which is the fluctuation of every bin's background component around the average background events in a bin. This can be done by assuming the phasogram of Fig. 5.15a, which contains  $N_c$  events distributed uniformly across the entire phase range. Hence, the phase distribution in this phasogram is consistent with the  $H_0$ . As a consequence, a calculated value for the reduced  $\chi_{n-1}^2$  should be roughly equal to 1. Based on that, we can write

$$\chi_{n-1}^2/(n-1) = \frac{1}{n-1} \frac{\sum_{i=1}^n \left( N_i - \frac{N_c}{n} \right)^2}{N_c/n} \approx 1 \quad (5.51)$$

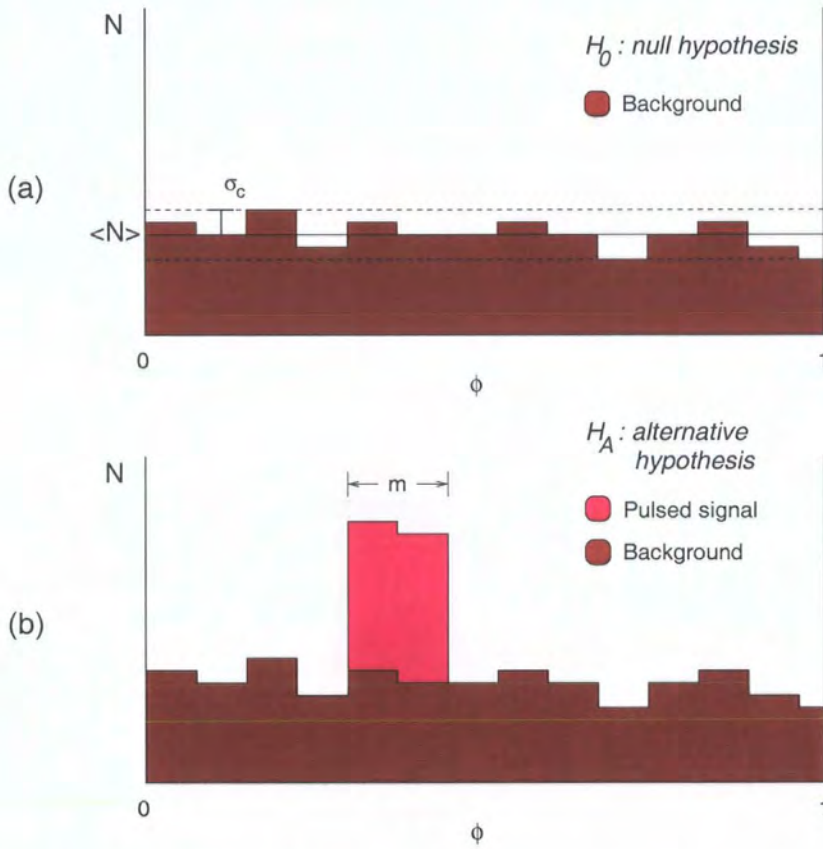


Figure 5.15: Assumed phasograms for the analytical calculation of  $\chi^2$ . (a) Phasogram consistent with the null hypothesis ( $H_0$ ), where all the event phases are uniformly distributed across one period, and the number of events per bin fluctuates by  $\sigma_c$  around the mean,  $\langle N \rangle$ . (b) Phasogram that contains a uniform background component plus a pulsed component that extends over  $m$  bins. The presence of a signal in the data is consistent with the alternative hypothesis ( $H_A$ ).

A further assumption is that all bins fluctuate around the mean by the same amount, in which case the above equation becomes

$$\left(N_i - \frac{N_c}{n}\right)^2 \approx \frac{n-1}{n^2} N_c \quad (5.52)$$

We can now substitute the squared quantity in the sums of Eq. 5.50, bearing in mind that its value can be either positive or negative. Thus,

$$\begin{aligned} \chi_{n-1}^2/(n-1) &\approx \frac{n}{(n-1)(N_\gamma + N_c)} \times \\ &\times \left[ \sum_{i=1}^m \left( \frac{N_\gamma}{m} - \frac{N_\gamma}{n} \pm \frac{\sqrt{n-1}}{n} \sqrt{N_c} \right)^2 + \sum_{i=1}^{n-m} \left( -\frac{N_\gamma}{n} \pm \frac{\sqrt{n-1}}{n} \sqrt{N_c} \right)^2 \right] \end{aligned} \quad (5.53)$$

After summing up the events in the two regions and some algebra, we arrive at an analytical expression for  $\chi_{n-1}^2/(n-1)$

$$\begin{aligned} \chi_{n-1}^2/(n-1) &= \\ &= (1-p) \left[ 1 + \frac{1}{n-1} \left( \frac{1-\delta}{\delta} \right) \left( \frac{p}{1-p} \right)^2 N_c \right] \pm 2(1-\delta)p \sqrt{\frac{N_c}{n-1}} \end{aligned} \quad (5.54)$$

where we have invoked the duty cycle,  $\delta = m/n$ , and the pulsed fraction,  $p = N_\gamma/(N_\gamma + N_c)$ . The last term on the RHS of this equation expresses the uncertainty in the calculation of the  $\chi^2$  value, which arises from the uncertainty in the direction of the fluctuation of the background component in the bins. These fluctuations exist, of course, both inside and outside the phase range of the pulsed emission. In the above equation we assumed that in those two phase regions the fluctuations are in the same direction, in order to estimate the maximum value of  $\sigma_{\chi^2} = 2(1-\delta)p\sqrt{N_c/(n-1)}$ . That leads to the factor 2 involved in this term. Since  $\sigma_{\chi^2} \propto \sqrt{N_c}$ , its value is — in most cases — negligible compared to  $\chi^2 \propto N_c$ . Therefore, it will be ignored in our qualitative study that follows.

We can now set a lower limit on the exposure time,  $T$ , which is needed to achieve a specific level of significance (in terms of a probability equivalent to the value of  $\chi_{n-1}^2/(n-1)$ ) given that the background and  $\gamma$ -ray event rates remain constant during  $T$ . If these rates are  $R_\gamma$  and  $R_c$ , respectively, then Eq. 5.54 becomes

$$\chi_{n-1}^2/(n-1) = (1-p) \left[ 1 + \frac{1}{n-1} \left( \frac{1-\delta}{\delta} \right) \left( \frac{p}{1-p} \right)^2 R_c T \right] \quad (5.55)$$

One remark to be made here is the polynomial dependence of  $\chi^2$  on the signal strength (i.e. the pulsed fraction). This is shown more clearly if we expand the term containing  $p$ , so that

$$\chi_{n-1}^2/(n-1) = 1 - p + \frac{R_c T}{n-1} \left( \frac{1-\delta}{\delta} \right) p^2 (1 + p + p^2 + \dots) \quad (5.56)$$

which contains all powers of  $p$ . In the case of weak signals — abundant in  $\gamma$ -ray astronomy — a useful approximation for  $p \ll 1$  yields

$$\chi_{n-1}^2/(n-1) \approx 1 + \frac{R_c}{n-1} \left( \frac{1-\delta}{\delta} \right) p^2 T \quad (5.57)$$

Finally, Eq. 5.55 can be solved for  $T$  to give an estimate of the required exposure for, say, a  $5\text{-}\sigma$  detection. Hence,

$$T_{5\sigma} = \frac{n-1}{R_c} \left( \frac{\delta}{1-\delta} \right) \left( \frac{1-p}{p} \right)^2 \left[ \frac{\chi_{n-1}^2(5\sigma)/(n-1)}{1-p} - 1 \right] \quad (5.58)$$

which becomes

$$T_{5\sigma} \approx \frac{n-1}{p^2 R_c} \left( \frac{\delta}{1-\delta} \right) [\chi_{n-1}^2(5\sigma)/(n-1) - 1] \quad (5.59)$$

for weak signals.

A very important property of Eq. 5.58 is that in the presence of a signal, the minimum required time for a  $5\text{-}\sigma$  detection is proportional to the quantity  $\delta/(1-\delta)$ . In Fig. 5.16 we have plotted the required exposure time for a  $5\text{-}\sigma$  detection with a  $\chi_{19}^2$ -test against the duty cycle,  $\delta$ . The selected values for the pulsed fraction and the event rate are also shown in this plot. It can be seen that between sources of equal flux,  $\langle F \rangle$ , those with narrow pulse profiles are more easily detectable. In those cases, Eq. 5.58 can be approximated with

$$\begin{aligned} T_{5\sigma} &= \frac{n-1}{R_c} \delta (1 + \delta + \delta^2 + \dots) \left( \frac{1-p}{p} \right)^2 \left[ \frac{\chi_{n-1}^2(5\sigma)/(n-1)}{1-p} - 1 \right] \approx \\ &\approx \frac{n-1}{R_c} \delta \left( \frac{1-p}{p} \right)^2 \left[ \frac{\chi_{n-1}^2(5\sigma)/(n-1)}{1-p} - 1 \right] \end{aligned} \quad (5.60)$$

which means that for practically all pulsar signals known so far ( $\delta < 0.5$ ), the detection time increases proportionally to  $\delta$ . Moreover, if we only consider weak narrow signals, then the above expression takes the simple form

$$T_{5\sigma} \approx (n-1) \frac{\delta}{p^2 R_c} \cdot \chi_{n-1}^2(5\sigma)/(n-1) \quad (5.61)$$

We can now support our assertion regarding the increased sensitivity of periodicity searches for weak signals compared to the standard DC analysis. Crab's nebular emission, for example, is phase-independent, which would correspond to  $\delta = 1$  according to the above. Therefore, as expected, uniformity tests are insensitive to such signals, since  $T \rightarrow \infty$  for  $\delta \rightarrow 1$ . The analytic expression that relates the exposure time with the detection significance for DC signals (Eq. 3.29) was mentioned in chapter 3. By invoking the above definition of  $p$ , we can directly compare Eq. 3.29 with Eq. 5.58. Of course,  $p$  corresponds now to the fraction of DC  $\gamma$  rays in the data. Thus the minimum exposure time for a 5- $\sigma$  detection of a DC signal now becomes

$$T_{5\sigma} = \frac{(1-p)(2-p)}{p^2} \frac{1}{R_c} \cdot \sigma_{\text{DC}}^2 \quad (5.62)$$

where  $\sigma_{\text{DC}} = 5$ . Fig. 5.17 shows  $T_{5\sigma}$  as a function of  $p$ , for DC and pulsed emission. It is evident that weak periodic signals are more easily detectable than DC signals of the same strength. However, the gap between the sensitivity of the pulsed and DC detection methods is practically eliminated for  $p \gtrsim 0.1$ .

In the above formulation, the quantity  $p\sqrt{N_c/(1-p)} = p\sqrt{N}$ , where  $N$  is the total number of events in the phasogram, appears in all tests for uniformity and it is usually referred to, in the bibliography, as the *fundamental scaling parameter*. This parameter is associated with the source's physical parameters as well as with the characteristics of the detector. More specifically, if the average pulsed flux over exposure time  $T$  was  $\langle F \rangle$ , then a detector with effective area  $A$  would collect  $N_\gamma = \langle F \rangle AT$   $\gamma$  rays. So, we can write

$$p\sqrt{N} = \frac{\langle F \rangle AT}{\sqrt{N}} = \langle F \rangle A \left( \frac{T}{\langle R \rangle} \right)^{1/2} \quad (5.63)$$

where  $\langle R \rangle$  is the average trigger rate over exposure time  $T$ .

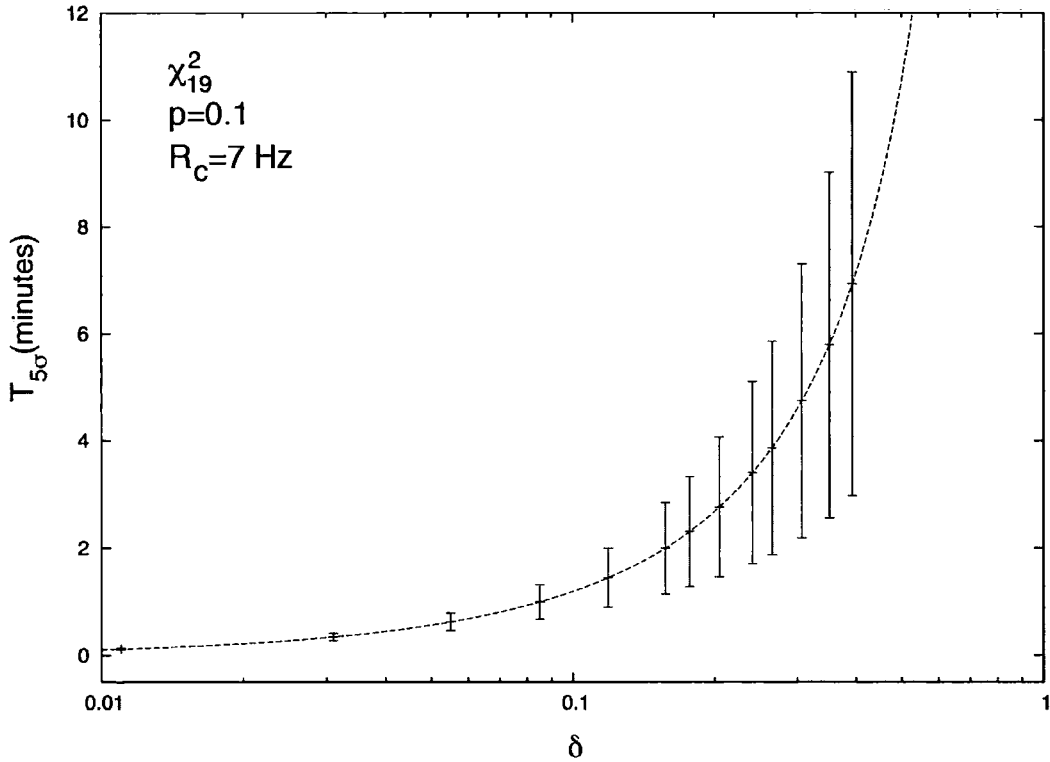


Figure 5.16: Plot of the dependence of the minimum exposure time for a 5- $\sigma$  detection with the  $\chi^2_{19}$ -test, on the duty cycle of the pulsed signal,  $\delta$ . This plot was generated using Eq. 5.58 with the pulsed fraction equal to  $p = 0.1$  and a background event rate equal to  $R_c = 7$  Hz. For  $\delta < 0.5$ , which applies to all pulsar profiles observed so far, the test is evidently more sensitive than for wider profiles. Finally, as expected for all uniformity tests, the sensitivity of the  $\chi^2$ -test tends to 0 (i.e.  $T \rightarrow \infty$ ) as  $\delta \rightarrow 1$ .

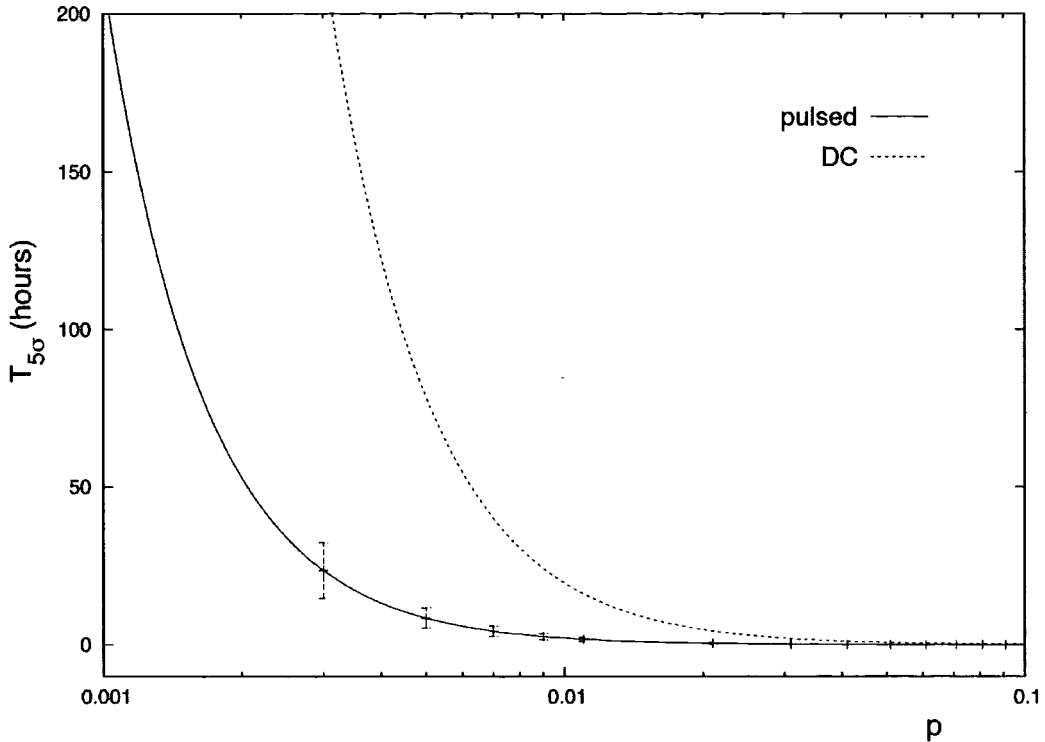


Figure 5.17: Graphical comparison between the sensitivity of the  $\chi^2$ -test in periodicity searches (solid line) and that of a standard DC analysis for steady signals (dotted line), as a function of the signal strength. Here, the sensitivity is expressed as the minimum required exposure time for a  $5\text{-}\sigma$  detection with a  $\chi^2_{19}$ -test (pulsed) and an ON/OFF DC analysis (see sections 3.2.3 and 4.3.3). Also, the signal strength is represented by  $p = R_\gamma / (R_\gamma + R_c)$ , where  $R_\gamma$  is equal to the pulsed or DC  $\gamma$ -ray rate, respectively. The plotted functions correspond to the analytical expressions of equations 5.58 and 5.62, for the pulsed and DC emission, respectively. In both cases, we selected  $R_c = 7$  Hz for the background event rate, whereas the pulsed emission was assumed with duty cycle  $\delta = 0.1$ . It can be seen that weak, pulsed signals ( $p \lesssim 0.01$ ) are more easily detectable with uniformity tests than DC signals of the same strength, with a traditional ON/OFF method. Nevertheless, the detection methods become equally sensitive for stronger signals ( $p \gtrsim 0.1$ ).

### 5.4.2 The Rayleigh Test

The Rayleigh test is a special case of the  $Z_m^2$  test, which was extensively used by the *COS-B* collaboration with pulsar data [399]. The  $Z_m^2$  statistic can be derived from the general Beran's class of uniformity tests assuming a Fourier Series Estimator (FSE) with  $k$  harmonics [394]. The statistic is defined as

$$Z_m^2 = 2N \sum_{k=1}^m \left[ \left( \frac{1}{N} \sum_{i=1}^N \cos k\phi_i \right)^2 + \left( \frac{1}{N} \sum_{i=1}^N \sin k\phi_i \right)^2 \right] \quad (5.64)$$

where  $N$  is the total number of events in the data series and  $\phi_i$ , as before, the event phases after folding. The quantities  $\hat{\alpha}_k = (1/N) \sum_{i=1}^N \cos k\phi_i$  and  $\hat{\beta}_k = (1/N) \sum_{i=1}^N \sin k\phi_i$  are the *trigonometric moments* of the FSE. In that sense, the Rayleigh test is a  $Z_1^2$  test: i.e. a  $Z_m^2$  test with  $m = 1$  harmonic. Hence, the Rayleigh statistic is given by

$$2NR^2 = 2N (\hat{\alpha}^2 + \hat{\beta}^2) = \frac{2}{N} \left[ \left( \sum_{i=1}^N \cos \phi_i \right)^2 + \left( \sum_{i=1}^N \sin \phi_i \right)^2 \right] \quad (5.65)$$

Clearly, the Rayleigh statistic does not depend on binning, unlike the  $\chi^2$ -test, which gives it an advantage over the latter. However, the assumption of an FSE with only the first harmonic makes this test more sensitive to broad, sinusoidal profiles, as we will see later. In addition, the lack of higher order harmonics makes this test insensitive to bimodal lightcurves, since their components cancel each other and pass by unnoticed.

The probability distribution of the Rayleigh test statistic matches that of the  $\chi^2$  with 2 df, provided  $N > 100$  [400]. The latter deviates from the Rayleigh distribution for lower values of  $N$  (see Fig. 5.18). Given a data set with  $N$  events, which yields a certain value of the Rayleigh statistic (say  $2NR_0^2$ ), the probability of  $H_0$  being true for that data set is given by

$$pr(> NR_0^2 | H_0) = \exp(-NR_0^2) \quad (5.66)$$

where the quantity  $NR_0^2$  is mentioned in the bibliography as the Rayleigh power [401]. Eq. 5.66 also corresponds to the probability of finding values of  $NR^2$  greater than  $NR_0^2$ , in the absence of a pulsed signal. In a data set containing random



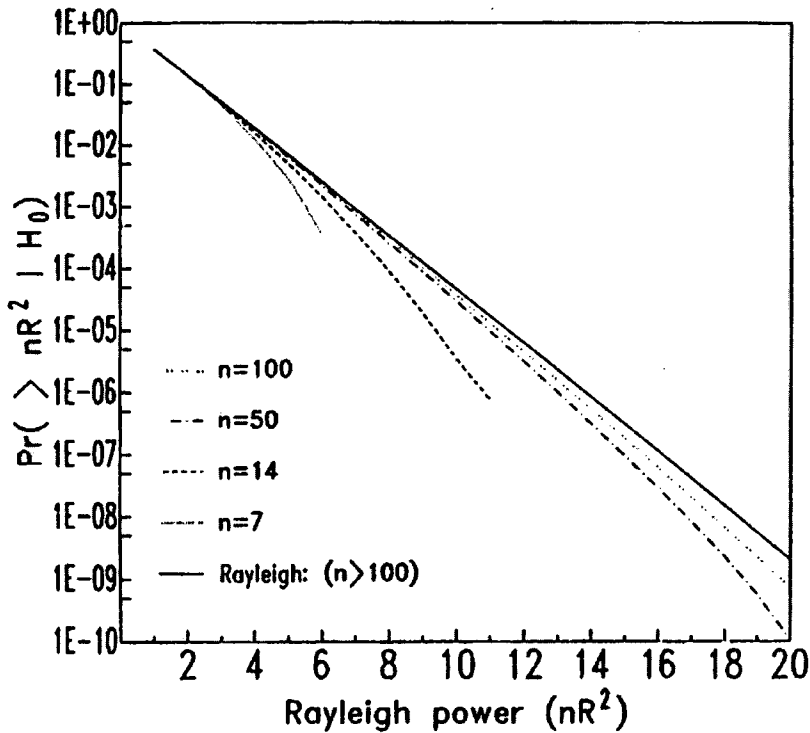


Figure 5.18: (from [400]) The probability distribution of the Rayleigh powers for various values of  $N$  (dotted lines). The solid line corresponds to the probability distribution of the Rayleigh powers, which was calculated using Eq. 5.66 with  $N > 100$ , which matches the  $\chi^2$  distribution with 2 df.

Poissonian noise, only the most probable Rayleigh powers are likely to occur, which are the values of  $NR^2$  that are close to zero. The occurrence of large values of  $NR^2$  in such a data set implies that a significantly large number of events have phases that belong to a tightly bunched phase region. Although this is possible to occur by chance with a probability  $\exp(-NR^2)$ , it is more probable that it originates from a focused emission and, thus, the presence of a signal.

We will show now that the Rayleigh power, too, is a function of the scaling parameter  $p\sqrt{N}$ , and we will proceed with the calculation of an upper limit on the pulsed fraction  $p$ , given a value of the Rayleigh power corresponding to  $pr(> NR^2)$ . We assume that a data set with  $N$  event phases is composed of a Poissonian background component with  $N_c$  random phases and a pulsed component with  $N_\gamma$  phases that are bunched in phase space. Then, the expression of the Rayleigh power

for this particular data set is

$$NR^2 = \frac{1}{N} \left[ \left( \sum_{i=1}^{N_\gamma} \cos \chi_i + \sum_{j=1}^{N_c} \cos \psi_j \right)^2 + \left( \sum_{i=1}^{N_\gamma} \sin \chi_i + \sum_{j=1}^{N_c} \sin \psi_j \right)^2 \right] = \dots \quad (5.67)$$

where  $\chi_i$  are the event phases of the bunched emission and  $\psi_j$  those of the random background emission.

By expanding the terms in the square brackets, we get

$$\begin{aligned} &= \frac{1}{N} \left[ \left( \sum_{i=1}^{N_\gamma} \cos \chi_i \right)^2 + \left( \sum_{j=1}^{N_c} \cos \psi_j \right)^2 + 2 \left( \sum_{i=1}^{N_\gamma} \cos \chi_i \right) \left( \sum_{j=1}^{N_c} \cos \psi_j \right) \right] + \\ &+ \frac{1}{N} \left[ \left( \sum_{i=1}^{N_\gamma} \sin \chi_i \right)^2 + \left( \sum_{j=1}^{N_c} \sin \psi_j \right)^2 + 2 \left( \sum_{i=1}^{N_\gamma} \sin \chi_i \right) \left( \sum_{j=1}^{N_c} \sin \psi_j \right) \right] \end{aligned} \quad (5.68)$$

At this point we can make use of the mathematical identity

$$\begin{aligned} \sum_{i=1}^n x_i \sum_{j=1}^m y_j &= (x_1 + x_2 + \dots + x_n)(y_1 + y_2 + \dots + y_m) = \\ &= x_1 y_1 + x_1 y_2 + \dots + x_2 y_1 + x_2 y_2 + \dots + x_n y_m = \sum_{i=1}^n \sum_{j=1}^m x_i y_j \end{aligned} \quad (5.69)$$

which is valid for all  $x_i, y_j \in \mathbb{R}$  and  $n, m \in \mathbb{I}$ . Hence, Eq. 5.67 becomes

$$\begin{aligned} NR^2 &= \frac{1}{N} \left[ \left( \sum_{i=1}^{N_\gamma} \cos \chi_i \right)^2 + \left( \sum_{j=1}^{N_c} \cos \psi_j \right)^2 + 2 \sum_{i=1}^{N_\gamma} \sum_{j=1}^{N_c} \cos \chi_i \cos \psi_j \right] + \\ &+ \frac{1}{N} \left[ \left( \sum_{i=1}^{N_\gamma} \sin \chi_i \right)^2 + \left( \sum_{j=1}^{N_c} \sin \psi_j \right)^2 + 2 \sum_{i=1}^{N_\gamma} \sum_{j=1}^{N_c} \sin \chi_i \sin \psi_j \right] \end{aligned} \quad (5.70)$$

In order to proceed, we have to consider the distributions of  $\chi_i$  and  $\psi_j$ : the latter is uniform across  $[0, 2\pi)$ , whereas the former is narrower, with all its phases concentrated in a subset of  $[0, 2\pi)$ , say  $\Theta$ . Hence,

$$\psi_j \in [0, 2\pi) \quad (5.71)$$

$$\chi_i \in \Theta \subset [0, 2\pi) \quad (5.72)$$

Furthermore, we use the trigonometric identity

$$\cos \chi_i \cos \psi_j + \sin \chi_i \sin \psi_j = \cos(\chi_i - \psi_j) = \cos \omega_{ij} \quad (5.73)$$

where we have defined the 2-dimensional matrix  $\omega_{ij} = \chi_i - \psi_j$ ; and  $\omega_{ij} \in [0, 2\pi)$ , since  $\Theta \cup [0, 2\pi) \equiv [0, 2\pi)$ .

Finally, we can use the expressions for the trigonometric moments  $\hat{\alpha}_{\gamma,c}$  and  $\hat{\beta}_{\gamma,c}$ , for the pulsed and background components, in order to simplify the summation terms in Eq. 5.70. Note that  $\hat{\alpha}$  and  $\hat{\beta}$  express the average values of the  $\cos(\dots)$  and  $\sin(\dots)$  terms, respectively. More specifically,

$$\hat{\alpha}_{\gamma} = \frac{1}{N_{\gamma}} \sum_{i=1}^{N_{\gamma}} \cos \chi_i = \langle \cos \chi_i \rangle \quad (5.74)$$

$$\hat{\beta}_{\gamma} = \frac{1}{N_{\gamma}} \sum_{i=1}^{N_{\gamma}} \sin \chi_i = \langle \sin \chi_i \rangle \quad (5.75)$$

$$\hat{\alpha}_{c} = \frac{1}{N_c} \sum_{j=1}^{N_c} \cos \psi_j = \langle \cos \psi_j \rangle \quad (5.76)$$

$$\hat{\beta}_{c} = \frac{1}{N_c} \sum_{j=1}^{N_c} \sin \psi_j = \langle \sin \psi_j \rangle \quad (5.77)$$

Hence, Eq. 5.70 now becomes

$$\begin{aligned}
 NR^2 &= \\
 &= \frac{1}{N} \left[ (N_\gamma \langle \cos \chi_i \rangle)^2 + (N_\gamma \langle \sin \chi_i \rangle)^2 \right] + \frac{1}{N} \left[ (N_c \langle \cos \psi_j \rangle)^2 + (N_c \langle \sin \psi_j \rangle)^2 \right] + \\
 &+ \frac{1}{N} \left[ 2 \sum_{i=1}^{N_\gamma} \sum_{j=1}^{N_c} \cos(\chi_i - \psi_j) \right] = \\
 &= \frac{N_\gamma^2}{N} (\langle \cos \chi_i \rangle^2 + \langle \sin \chi_i \rangle^2) + \frac{N_c^2}{N} (\langle \cos \psi_j \rangle^2 + \langle \sin \psi_j \rangle^2) + \\
 &+ 2 \frac{N_\gamma N_c}{N} \langle \cos \omega_{ij} \rangle
 \end{aligned} \tag{5.78}$$

For large  $N_c$ , the quantities  $\langle \cos \psi_j \rangle$ ,  $\langle \sin \psi_j \rangle$  and  $\langle \cos \omega_{ij} \rangle$  are approximately zero due to the uniform distribution of  $\psi_j$ . Therefore, the Rayleigh power is equal to

$$NR^2 \approx \frac{N_\gamma^2}{N} (\langle \cos \chi_i \rangle^2 + \langle \sin \chi_i \rangle^2) = (p\sqrt{N})^2 \tag{5.79}$$

### Test Sensitivity

It was mentioned that the Rayleigh test is sensitive to broad profiles, whereas the  $\chi^2$ -test is sensitive to narrow ones. Leahy *et al.* performed analytical calculations for both tests [398] assuming a square pulse profile of known period. The resulting performance of the  $\chi^2$ -test was shown in Fig. 5.14. Fig 5.19 shows the performance of both tests for pulsed signals with various duty cycles,  $\delta$ , and under the assumption of a constant pulsed fraction,  $p$ . It can be seen that above  $\delta \approx 13\%$  the sensitivity of the Rayleigh test can be up to twice the  $\chi^2$ -test's, whereas for shorter duty cycles the  $\chi^2$ -test becomes clearly dominant. In general, it appears from this plot that the power of the Rayleigh test is not as dependent on the duty cycle as the  $\chi^2$ -test's is, varying only by a factor  $\approx 5$  across the  $\delta$  range. For large duty cycles,  $\delta \rightarrow 1$ , both tests become insensitive, which is expected for all uniformity tests.

Based on Eq. 5.79 we can now perform a similar calculation to that which led to Eq. 5.58, but instead of constraining the exposure time we will set an upper limit on the pulsed fraction,  $p$ . The Rayleigh probability levels for large  $N = N_\gamma + N_c$  are given by Eq. 5.66. We have shown that

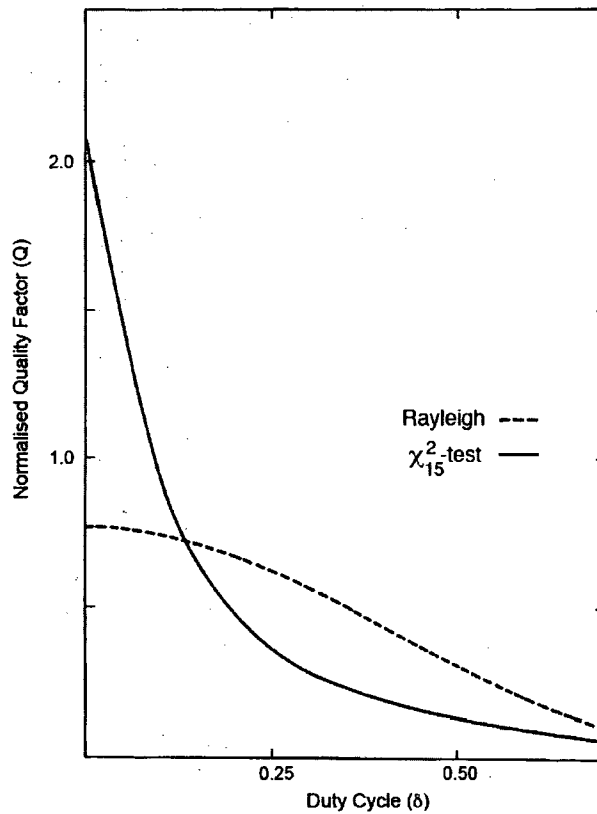


Figure 5.19: (from [398]) The power of the Rayleigh test (dotted line) compared with that of a  $\chi^2$ -test with 15 df (solid line), as a function of the duty cycle of the pulsed signal,  $\delta$ . The plotted function was calculated by Leahy *et al.* using square pulses of known period and variable  $\delta$ . The values of  $NR^2$  and  $\chi^2$  were calculated for each individual signal. In this plot, the test power is expressed as the fraction of successful detections of the tested pulses, at a 90% confidence level. The quality factor,  $Q$ , is constructed from this fraction (see [398]). When the pulse is detected half the time, then  $Q = 1$ .

$$(N_\gamma + N_c) R_0^2 = \frac{N_\gamma^2}{N_\gamma + N_c} \quad (5.80)$$

where  $NR_0^2$  is the Rayleigh power that corresponds to  $pr(> NR_0^2) = \exp(-NR_0^2)$ . We can rewrite this equation introducing  $p$ :

$$(N_\gamma + N_c) R_0^2 = \frac{p^2}{1-p} N_c \quad (5.81)$$

We would like to calculate the maximum value of  $p$  that would have resulted in a detection, to a probability level  $s$  under the  $H_0$ , of a pulsed signal containing  $N_\gamma$  events, with the Rayleigh test. Assuming that the Rayleigh test did not detect the signal to that probability level,  $s$ , the yielded Rayleigh probability under the  $H_0$  must have been

$$pr \geq s \Rightarrow \exp\left(-\frac{p^2}{1-p} N_c\right) \geq s \Rightarrow \frac{p^2}{1-p} \leq -\frac{\log s}{\log e} \frac{1}{N_c} \geq 0 \quad (5.82)$$

where equality corresponds to the upper limit,  $p_{\text{ul}}$ . By setting the RHS quantity of the last inequality equal to  $x$  and considering only the equality, we form the quadratic equation

$$p_{\text{ul}}^2 + xp_{\text{ul}} - x = 0 \quad (5.83)$$

The root with physical meaning is

$$p_{\text{ul}} = \frac{1}{2}x \left( \sqrt{1 + \frac{4}{x}} - 1 \right) = \frac{1}{2}\sqrt{x} (\sqrt{x+4} - \sqrt{x}) \quad (5.84)$$

However, for large  $N_c$  and typical values of  $s$ , we can approximate with  $x \ll 1$ . For example, a data set with  $N_c = 1,000$  yields  $x \sim 0.01$  by requiring a 5- $\sigma$  confidence level. Hence, Eq. 5.84 becomes

$$p_{\text{ul}} \approx \sqrt{-\frac{\log s}{\log e} \frac{1}{N_c}} \quad (5.85)$$

Using the above value for the background counts and setting  $s \sim 10^{-7}$  — which corresponds roughly to 5  $\sigma$  — this equation yields an upper limit of  $\approx 13\%$  of the background: i.e. 130  $\gamma$  rays.

### 5.4.3 The $H$ -test

In 1989, de Jager, Swanepoel and Raubenheimer (hereafter DSR) introduced the  $H$ -test [393] as a general test for uniformity which performs, on average, better than other known tests, regardless of pulse shape and position. The  $H$ -test is an optimised and rescaled version of the  $Z_m^2$  test. It is based on the  $Z_m^2$  statistic, like the Rayleigh test, but it possesses two important qualities that make it a better overall test compared to the  $Z_m^2$  test.

Firstly, it does not require from the user to select a single value for  $m$ , but it selects only that harmonic,  $M$ , which maximises the quantity

$$\max_{1 \leq m < \infty} (Z_m^2 - 4m + c) = Z_M^2 - 4M + c \quad (5.86)$$

where  $c$  is an integer constant. This determination procedure is called Hart's rule [402] and the choice  $c = 0$  leads to the optimised-by-Hart's-rule  $Z_m^2$  statistic, with  $m = M$ , also known as the  $Z^2$  statistic. We will not get into further detail regarding the principle on which Hart's rule operates, but in rough terms Hart's rule maximises the performance of the FSE for a given data set. More information can be found in [400].

Secondly, the integer constant  $c$  can be, in general, different from zero. A second optimisation compared to the general  $Z_m^2$  test comes from power studies, where the conclusion is that a value  $c = 4$  provides the best omnibus statistic. DSR defined this statistic as

$$H \equiv \max_{1 \leq m \leq 20} (Z_m^2 - 4m + 4) = Z_M^2 - 4M + 4 \quad (5.87)$$

where the maximum number of harmonics considered, i.e.  $m = 20$ , was chosen by the authors both because of the limited statistics from simulations, but also because the truncation of Eq. 5.86 at higher harmonics does not change the power of the  $H$ -test significantly [393]. In [400], de Jager reported that the probability of finding  $M = 20$  in noise data is only  $2 \times 10^{-5}$ .

Similarly to the  $\chi^2$  and Rayleigh tests discussed here, the  $H$ -test rejects uniformity for large values of the statistic. The probability of accepting the  $H_0$  is derived from the distributions of the  $H$  statistic for the individual values of  $m$ . This would normally require simulations for each number of harmonics — involving the aforementioned computational obstacles — and construction of probability tables, as in

$m$	$\theta(m)$	$r(m)$	$m$	$\theta(m)$	$r(m)$
1	0.522	1.065	11	0.343	2.171
2	0.495	1.981	12	0.329	2.114
3	0.453	2.117	13	0.327	2.149
4	0.425	2.166	14	0.322	2.131
5	0.402	2.177	15	0.298	1.984
6	0.385	2.172	16	0.285	1.957
7	0.375	2.190	17	0.292	2.026
8	0.353	2.125	18	0.308	2.239
9	0.352	2.144	19	0.308	2.150
10	0.364	2.272	20	0.231	1.744

Table 5.6: (from [400]) The critical parameters for the calculation of the probability levels from the  $H_m$  distribution. The parameter values were derived from  $10^7$  noise simulations, which were enough for the determination of the probability distributions with  $\leq m \leq 20$ .

the case of the  $\chi_{k-1}^2$  statistic. Fortunately, de Jager was able to parametrise the distributions of the  $H$  statistic by fitting 20 simulated distributions of  $H$  to an equal number of  $\Gamma$  distributions, using the parameters

$$\begin{aligned}\theta(m) &= \frac{\langle H_m \rangle}{\sigma_m^2} \\ r(m) &= \frac{\langle H_m \rangle^2}{\sigma_m^2}\end{aligned}\tag{5.88}$$

where  $\langle H_m \rangle$  and  $\sigma_m^2$  are the mean and the variance of each of the 20 probability distributions. The values of  $\theta(m)$  and  $r(m)$  have been calculated by the author from  $10^7$  simulations of random noise [400]. Table 5.6 presents these values for  $m \leq 20$ .

Based on the above parametrisation, de Jager provided an analytical expression for calculating the probability of accepting the  $H_0$ , given a value of  $H$  found at a specific harmonic  $m$ . This expression is [400]

$$pr(> H_m | H_0) = \int_x^\infty \frac{t^{r(m)-1} \exp(-t)}{\Gamma[r(m)]} dt\tag{5.89}$$

where  $x = \theta(m)H_m$  and  $\Gamma[r(m)]$  is the  $\Gamma$  function to which the probability distribution for  $m$  harmonics was fitted.

Eq. 5.89 was verified by the author after  $10^5$   $H_m$  values were calculated from



300 uniformly distributed phases and the resulting probability levels were converted into Rayleigh powers,  $NR^2$ , using Eq. 5.66. The distribution of the Rayleigh powers was well fitted with the expected exponential function  $\exp(-NR^2)$  [400].

### Test Sensitivity

In terms of performance, the  $H$ -test is known to be powerful for a broad range of possible pulse profiles. Fig. 5.20 shows a comparison plot between the power of various tests for uniformity which are used in  $\gamma$ -ray astronomy. From this plot, it is clear that the overall performance of the  $H$ -test is better than the rest. Its only competitor, for  $\delta > 0.2$ , seems to be Watson's test, whose statistic is

$$U^2 = 2N \sum_{k=1}^{\infty} \frac{1}{(2\pi k)^2} (\hat{\alpha}_k^2 + \hat{\beta}_k^2) \quad (5.90)$$

However, the  $H$ -test has a computational advantage over Watson's test since it only requires  $\sim 40N$  steps for the calculation of  $H$  from Eq. 5.87, whereas the latter test's steps are of the order of  $N^2$  [393]. Hence, for large amounts of data, the  $H$ -test is much faster.

The calculation of upper limits on the pulsed fraction,  $p$ , with the  $H$ -test depends on the complexity of the lightcurve, i.e. unimodal, bimodal, etc., and requires Monte Carlo simulations for the individual cases. Nevertheless, for single pulses this calculation has been parametrised by fitting an analytical expression to the Monte Carlo results [403]. Since our upper limit calculations, presented herein, were performed at the C.L. of  $3\sigma$ , we provide here the relevant expression that constrains the scaling parameter,  $p\sqrt{N}$ , within an upper value,  $p_{3\sigma}\sqrt{N}$ , at that C.L. Therefore, given a calculated value of  $H$  for a data set with  $N$  events, the  $3\sigma$  upper limit on the scaling parameter for single pulse profiles is given by

$$p_{3\sigma}\sqrt{N} = (1.5 + 10.7\delta)(0.174H)^{0.17+0.14\delta} \times \exp(0.08 + 0.15\delta) \log^2(0.174H) \quad \text{where } H > 0.3 \quad (5.91)$$

#### 5.4.4 The $C_m$ ("Cosine") Test

The appearance of this uniformity test in the available bibliography has been relatively recent, and a brief explanation of its properties can be found in [403]. As a result, it has not been widely used by the astronomical community. The  $C_m$  test

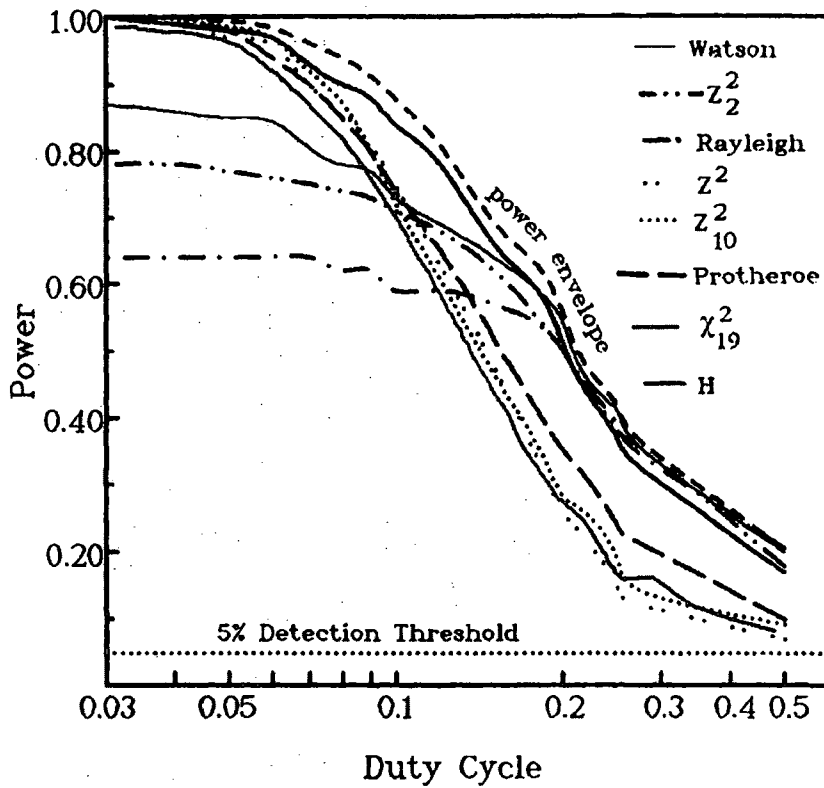


Figure 5.20: (from [393]) Test power versus duty cycle,  $\delta$ , for various tests for uniformity. The simulated signal, which the power of each test was tested against, had a single Gaussian profile with  $p = 0.1$  and  $N = 300$ . The detection threshold,  $\alpha$ , corresponds to the maximum acceptable probability outcome, from any test, that rejects  $H_0$ ; and here, it was chosen equal to 0.05. The dense, dashed line corresponds to the power envelope which represents the power of the optimal test choice for each duty cycle. This curve has been derived from Beran's work. Clearly, the utilisation of this optimised power curve requires *a priori* knowledge of the duty cycle, which is rarely available.

can be considered as a short version of the  $Z_m^2$  test, but it is more specialised with regard to single pulses of known position. In principle, the power of this test lies in the symmetry of the cosine trigonometric moment for minor deviations from a specific phase, where the pulse is located, say for  $\phi = \mu$ . By centring all event phases around the expected pulse position,  $\mu$ , the quantities  $\cos(\phi_i - \mu)$  will always be positive around the pulse, i.e. when  $\mu' = |\phi_i - \mu| < \delta$ , whereas the corresponding sine moments will have opposite signs on opposite sides of the pulse position. Hence, the  $C_m$  test statistic is constructed by adding only the centred  $\hat{\alpha}_k$  trigonometric moments for all harmonics,  $m$ : i.e.

$$C_m = \left(\frac{2N}{m}\right)^{1/2} \sum_{k=1}^m \hat{\alpha}_k = \left(\frac{2N}{m}\right)^{1/2} \sum_{k=1}^m \sum_{i=1}^N \cos k(\phi_i - \mu) \quad (5.92)$$

and the corresponding  $S_m$  statistic, which sums only the sine trigonometric moments is

$$S_m = \left(\frac{2N}{m}\right)^{1/2} \sum_{k=1}^m \hat{\beta}_k = \left(\frac{2N}{m}\right)^{1/2} \sum_{k=1}^m \sum_{i=1}^N \sin k(\phi_i - \mu) \quad (5.93)$$

The test relies on the assumption that the pulse profile is symmetric around the expected phase: like a Gaussian profile centred on  $\mu$ , for example. In that case,  $C_m$  will be a large positive number, and  $S_m$  will be close to zero due to the equal event numbers with opposite sine values on either side of the Gaussian. It is the exclusion of those sine terms from the statistic that gives  $C_m$  test the advantage over the  $Z_m^2$  test, in terms of test power.

Nevertheless, it is not always feasible to pinpoint the peak phase  $\mu$ , or it is equally likely that the profile is not completely symmetric. In the case of the Crab pulsar, for example, the profile remains constant throughout the EM spectrum, and it is reasonable to assume that the profile seen with EGRET will be the same in the VHE region, too. That is to say, “phase locking” should hold true. However, if the peak phase slips from the expected position, the  $C_m$  test provides the means of tracing such incident via the  $S_m$  statistic: the asymmetry introduced by the phase-slipping results in the increase of the latter quantity’s absolute value, i.e.  $|S_m|$ . The reason is that, now,  $S_m$  also contains information on the pulsed phases, which are distributed unequally around  $\mu$ . The probability distribution of both  $C_m$  and  $S_m$  for noise is the  $N(0, 1)$ : i.e. the normal distribution with mean 0 and variance 1. In such case one should calculate  $C_m \approx S_m \approx 0$ . Therefore, in the presence of a signal at the

expected phase, the value of  $C_m$  can be directly translated into Gaussian standard deviations.

Finally, there remains a question of the optimal choice for  $m$ . Numerical inspection of the behaviour of  $C_m$  against Gaussian and square pulse profiles has shown that beyond an optimal number of harmonics,  $m^*$ , the inclusion of further harmonics does not contribute to the significance of the detection but, instead, it reduces it because of the dependence of  $C_m$  on  $1/m^{1/2}$ . A general expression for  $m^*$  was then given as [403]

$$m^* \sim \frac{1}{2\delta} \quad (5.94)$$

### Test Sensitivity

It has been mentioned that the Rayleigh test is the best option for sinusoids and that it does not require *a priori* knowledge of the pulse position. On the other hand, application of the  $C_m$  test to sinusoids, i.e. profiles with  $m = 1$ , requires knowledge of the peak phase. Moreover, a  $C_1$  test takes into account only the  $\hat{\alpha}$  trigonometric moment, whereas the Rayleigh statistic depends on both  $\hat{\alpha}$  and  $\hat{\beta}$ . Therefore, it becomes an interesting task to compare these two tests in terms of performance.

In  $C_m$  test's explanatory publication [403], de Jager showed a plot of the test power as a function of the scaling parameter for both tests. For those tests, he used a sinusoid of known phase position (see Fig. 5.21). The test power was quantified in terms of the probability of detecting a signal with either test, at the significance level of  $> 3\sigma$ . In other words, it represents the fraction of the total number of trials in which the  $H_0$  was rejected at the minimum level of  $3\sigma$ , for a range of signal strengths. The plot shows that detections throughout the tested range of  $p\sqrt{N}$  occur more often with the  $C_1$  test. Hence, the  $C_1$  test is more powerful at detecting sinusoids of known position.

Like the rest of the tests examined here, the  $C_m$  test also provides an analytical formula for upper limit estimation. Given the calculated value of  $C_m$  for a data set, the  $z$ - $\sigma$  upper limit on the pulsed fraction,  $p$ , can be approximated with [403]

$$p \approx \left(\frac{m}{2N}\right)^{1/2} \frac{C_m + z}{\sum_{k=1}^m \alpha_s(k)} \quad (5.95)$$

where  $\alpha_s(k)$  are the cosine trigonometric moments of the source function,  $g_s(\phi)$ . Since the true source function is unknown,  $g_s(\phi)$  can be approximated with one of

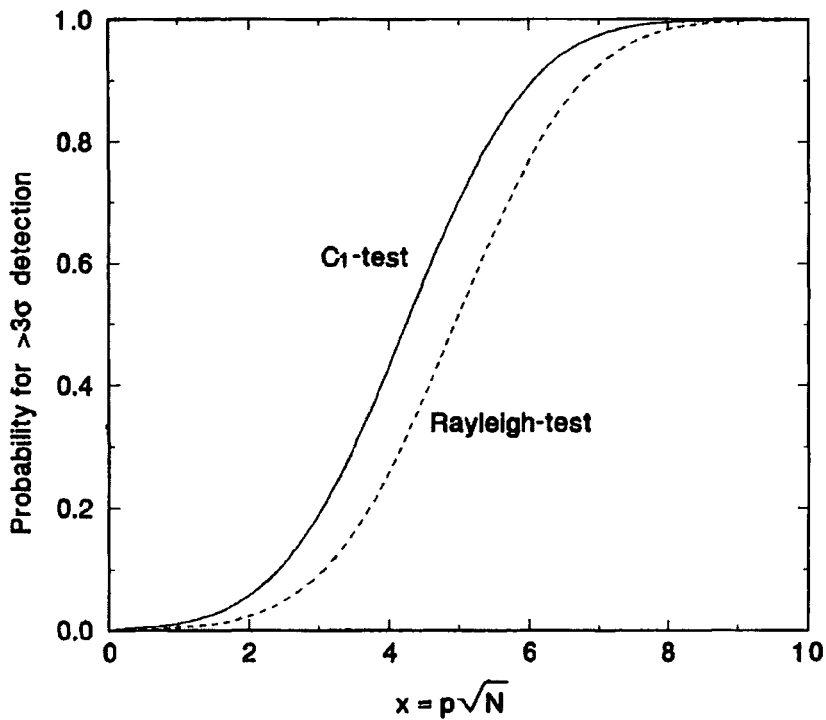


Figure 5.21: (from [403]) Power curves for the Rayleigh (dotted line) and  $C_1$  tests (solid line). In this plot, the test power is represented as the probability of each test detecting a sinusoidal pulse profile of known phase position, at the minimum significance level of  $3\sigma$ , for a range of signal strengths. The signal strength is expressed as the scaling parameter,  $p\sqrt{N}$ . It can be seen that for most of the signal strengths tested, the  $C_1$  test performs better.

the known distributions: i.e. Gaussian, sinusoidal, square, etc. In this work, we have chosen to simulate profiles using a Gaussian distribution (see section 5.7). The relevant trigonometric moment,  $\alpha_s(k)$ , in Eq. 5.95 is then given by [403],[404]

$$\alpha_s(k) = \exp\left(-\frac{1}{2}k^2\sigma^2\right) \cos k\mu' \quad (5.96)$$

which corresponds to a Gaussian with variance  $\sigma^2 = (2.668\delta)^2$  and mean  $\mu'$ . In the case where phase locking is held throughout the data set, i.e.  $\mu' = 0$ , Eq. 5.96 becomes

$$p \approx \left(\frac{m}{2N}\right)^{1/2} \frac{C_m + z}{\sum_{k=1}^m \exp\left(-\frac{1}{2}k^2\sigma^2\right)} \quad (5.97)$$

For detectable signals, i.e. those that lead to a value of  $C_m$  that exceeds a specified number of standard deviations, Eq. 5.97 can be used for the estimation of the pulsed fraction, if  $z = 0$  is set. In that case, the  $\pm 1$ - $\sigma$  confidence interval (C.I.) is calculated by setting  $z = \pm 1$ . Then, one can be confident to 67% that the true value of  $p$  lies within that interval.

## 5.5 The Helene Method for Upper Limit Estimation

The Helene method [405] was initially used in spectroscopy: as in the determination of  $\gamma$ -ray spectra from radioactive elements, for example. It was used to set an upper limit on the number of counts that a spectral peak must contain, in the expected energy range, following a non-detection. However, the method can be used in any experiment involving a statistical background and a contribution due to a possible source in an expected region, called *peak area*. The region which is expected to contain the signal can be defined in terms of an energy or phase range, or some other suitable parameter, depending on the nature of the signal. The total number of counts in the peak area, i.e. background plus possible signal, is usually denoted by  $C$ , whereas the number of counts from the average background contribution in the same area is denoted by  $B$ . The latter is typically calculated by averaging all data outside the peak area. The Helene method provides the means of calculating the upper limit on the number of signal counts in the peak area, usually denoted by  $A$ , and the error probability of the affirmation,  $\alpha$ . Then, the C.L. of the upper limit is automatically  $(1 - \alpha)\%$ .

The principle on which the Helene method operates for the calculation of the

above is simply based on the estimation of the probability,  $\alpha$ , of having a measured value of signal counts,  $x > A$ , in a series of  $n$  identical experiments. The probability of occurrence of a specific value of  $x$ , i.e. the number of times it will turn up in  $n$  experiments, is described by the p.d.f. of  $x$ , say  $g(x)$ . If  $x$  is a physical quantity, e.g. flux, for  $n \rightarrow \infty$  all physically allowed values of  $x$  will occur. In that case, the true value of  $x$  can be represented by the mean of the p.d.f.,  $\langle x \rangle$ .

Hence, by fixing  $\alpha$  to a desired probability level, the  $(1 - \alpha)\%$  upper limit on the number of counts is derived from

$$\alpha = \int_A^\infty g(x) dx \quad (5.98)$$

where  $g(x)$  is the normalised-to-unity p.d.f. of the true number of signal counts. Clearly,  $A$  cannot be calculated analytically from this equation — except for the simplest forms of  $g(x)$  — and numerical computation is required.

It can be proven, by means of Bayesian statistics [406], that given a measurement of  $C$  and  $B$ , the p.d.f. of the signal counts,  $x$ , has the Poissonian form

$$g(x) = N_1 \frac{(x + B)^C \exp[-(x + B)]}{C!} \quad (5.99)$$

where  $N_1$  is a normalisation constant which secures that

$$\int_0^\infty g(x) dx = 1 \quad (5.100)$$

For  $C \gg 1$ , which is the case for VHE  $\gamma$ -ray astronomy, the above p.d.f. can be approximated with a Gaussian distribution with mean  $\langle x \rangle = C - B$  and variance  $\sigma^2 = C$ . So that

$$g(x) \approx N_2 \frac{1}{\sqrt{2\pi C}} \exp\left[-\frac{(x - \langle x \rangle)^2}{2C}\right] \quad (5.101)$$

where  $N_2$  is the normalisation constant for the Gaussian p.d.f.

Equations 5.99 and 5.101 assume that the background is exactly known (i.e.  $\sqrt{B} \approx 0$ ), which is however not true in VHE data, as the fluctuations of the background are most of the time larger than the pulsed signal itself; in which case the latter is not detectable. Therefore, one has to consider a Poissonian background in Eq. 5.101, which now becomes

$$g(x) \approx N_3 \frac{1}{\sqrt{2\pi(B+C)}} \exp \left[ -\frac{(x - \langle x \rangle)^2}{2(B+C)} \right] \quad (5.102)$$

where, as before,  $N_3$  is the normalisation constant.

Using Eq. 5.99 in Eq. 5.98, Helene plotted  $A$  as a function of  $B$  for various values of the peak area counts, by setting the C.L. to 95% or, equivalently, to  $\sim 1.5 \sigma$  (see Fig. 5.22). Nevertheless, for large values of  $C (\gg 1)$  — which is relevant to our research — one can use Eq. 5.102. For such cases, there exists a suitable analytical expression for  $\alpha$ , which is then given by [405]

$$\alpha = \operatorname{erfc} \left( \frac{A - \langle x \rangle}{\sqrt{B+C}} \right) / \operatorname{erfc} \left( \frac{-\langle x \rangle}{\sqrt{B+C}} \right) \quad (5.103)$$

where  $\operatorname{erfc}(z)$  is the complementary error function [407]

$$\operatorname{erfc}(z) = \sqrt{\frac{2}{\pi}} \int_z^\infty e^{-\frac{1}{2}t^2} dt \quad (5.104)$$

Since  $A$  is a monotonic function of  $B$  for all  $C$ , one can use numerical methods to calculate the upper limit that corresponds to a certain value of  $\alpha$ , given the value of the background and the peak area counts.

### 5.5.1 Method Performance and The Feldman–Cousins Approach

The Helene method is a specialised method for producing upper limits for any data set, even when the signal *can* be measured. Therefore, it does not provide a useful discriminant between data sets with measurable signals and those for which only upper limits can be derived. Hence, the decision for using the method appropriately is a responsibility of the user.

In addition, the Helene method always assumes positive values for the true number of counts in the signal,  $\langle x \rangle$ , a fact which can be inferred from Eq. 5.100. In the case of a Gaussian distribution this means that  $\langle x \rangle = C - B$  is always assumed positive. However, VHE  $\gamma$ -ray astronomy is plagued with large backgrounds and weak signals, and therefore it happens often that  $\langle x \rangle < 0$ .

As a result, the Helene method does not take into account all possible cases, and it can be said that it suffers from “wrong coverage”. Excluding the possibility of negative signals leads to confidence intervals that do not contain the true signal at the stated confidence level (measurement error) but, instead, contain it at a higher or lower C.L., depending on the signal strength. For weak signals the stated error



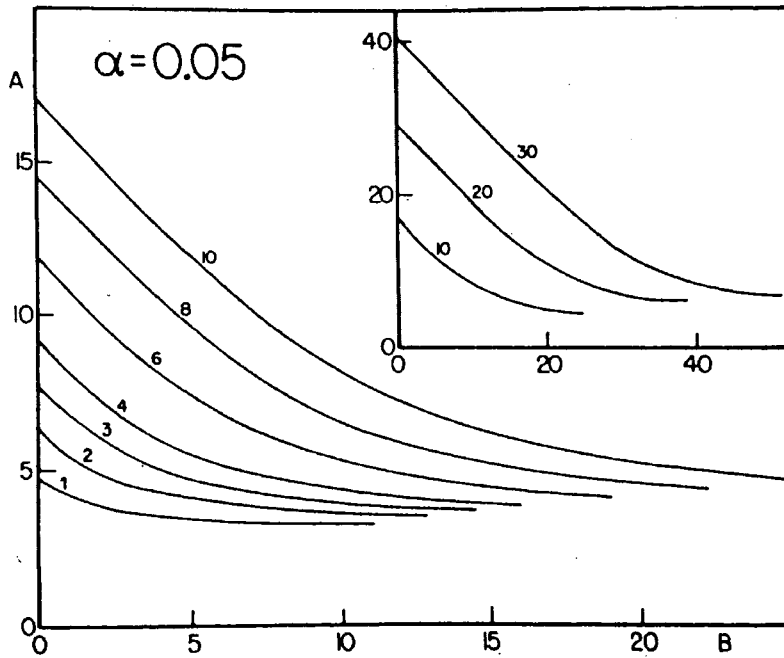


Figure 5.22: (from [405]) Upper limit on the signal counts of the peak area,  $A$ , against the background counts,  $B$ , for various values of the total counts in the peak area,  $C$ . All upper limit curves correspond to a C.L. of  $(1 - \alpha)\% = 95\%$ .

tends to be higher than the actual, which reduces the power of the method and makes it conservative. In those cases, it is said that the stated confidence intervals “overcover”. In contrast, measurable signals, i.e. above a set detection threshold, lead to “undercoverage”, which means that the stated errors are underestimated: this results in optimistic error values and should be avoided at all cost.

By simulating a series of fictitious signals which were distributed around a mean,  $\langle x \rangle$ , it was shown that if  $\langle x \rangle \ll 3\sigma$ , then the reported 90% upper limit is actually larger than the signal strength,  $x$ , in  $> 90\%$  of the cases. Doing the same for  $\langle x \rangle \gg 3\sigma$ , it was shown that the reported 90% confidence interval contains the true signal in  $< 90\%$  of the cases, and hence the reported error on the signal strength is unrealistically small [256],[408]. Fig. 5.23 compares the actual coverage of the Helene method with the stated C.L., for various values of  $\langle x \rangle$  (translated into standard deviations), after a series of repetitions of a simulated experiment.

To correct for the wrong coverage of the C.I., Feldman and Cousins [409] made use of a method for the construction of the correct C.I., called the Neyman’s construction [410]. In the context of our analysis, we have not used the Feldman–Cousins approach, but a brief description is provided here for completeness.

Neyman’s construction defines an interval of acceptable values for  $x$ , which belong, with a probability  $\alpha$ , to a distribution with mean value  $\langle x \rangle$ . By defining such intervals, i.e.  $[x_{1i}, x_{2i}]$ , for a range of mean values,  $\langle x \rangle_i$ , one can construct *confidence belts* like the one shown in Fig. 5.24. The individual lengths,  $x_{2i} - x_{1i}$ , of those acceptance intervals can be defined by fixing  $\alpha$  for all  $\langle x \rangle_i$  and including only the values of  $x$  that fulfil the following condition:

$$\int_{x_{1i}}^{x_{2i}} g(x; \langle x \rangle_i) dx = 1 - \alpha \quad (5.105)$$

where  $g(x; \langle x \rangle_i)$  is the p.d.f. of  $x$  that is distributed according to some function around the mean  $\langle x \rangle_i$ . It is not uncommon to assume a Gaussian distribution for  $g(x; \langle x \rangle_i)$ .

In order to define the intervals  $[x_{1i}, x_{2i}]$  in a unique way, one has to include some extra conditions for  $g(x; \langle x \rangle_i)$ . A classic choice for those conditions has the form

$$\int_{-\infty}^{x_{1i}} g(x; \langle x \rangle_i) dx = \alpha \quad (5.106)$$

which leads to UL satisfying  $pr(\langle x \rangle_i > A_{(1-\alpha)\%}) = \alpha$ , where  $A_{(1-\alpha)\%}$  is the upper limit at a C.L. of  $(1 - \alpha)\%$ . Additionally,

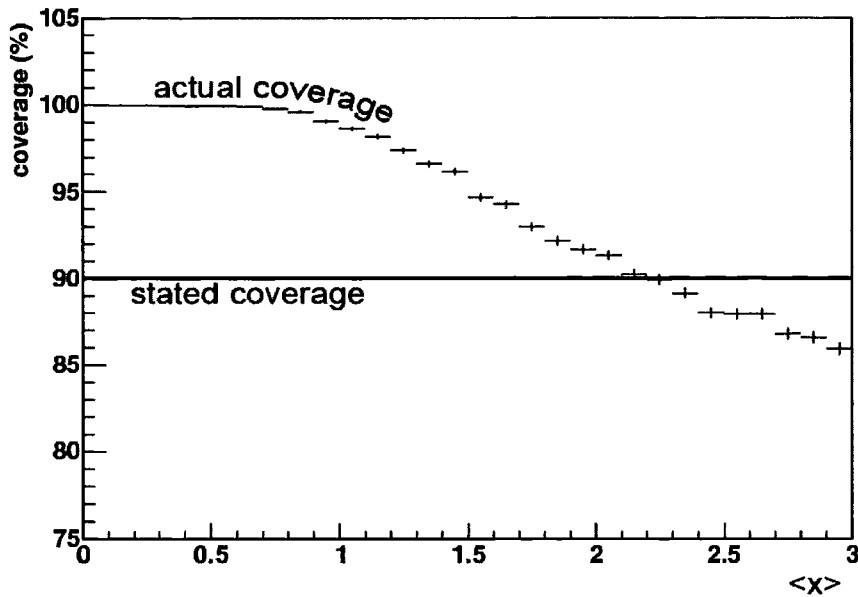


Figure 5.23: (from [408]) Comparison between the stated and actual coverage of the Helene method as a function of signal strength,  $\langle x \rangle$ , which is expressed in this plot in standard deviations. By setting the detection threshold to  $3\sigma$ , a number of fictitious signals were simulated for each value of  $\langle x \rangle < 3\sigma$ . The fraction of signals with strength below the 90% upper limit from the Helene method was calculated. In addition, for all  $\langle x \rangle > 3\sigma$  the fraction of simulated signals with signal strengths inside the Helene, 90% confidence interval was estimated. Both fractions should be consistent with the stated 90% C.L. However, it is clear that for weak signals, i.e.  $\langle x \rangle < 2.2$ , the method reports a 90% UL, where in reality more than 90% of the signals have strengths below the Helene UL. For  $\langle x \rangle > 2.2$  the opposite occurs, and the signals with strength inside the stated confidence interval make up for  $< 90\%$  of the population: this means that the error on the measured value, as stated with this method, is optimistic.

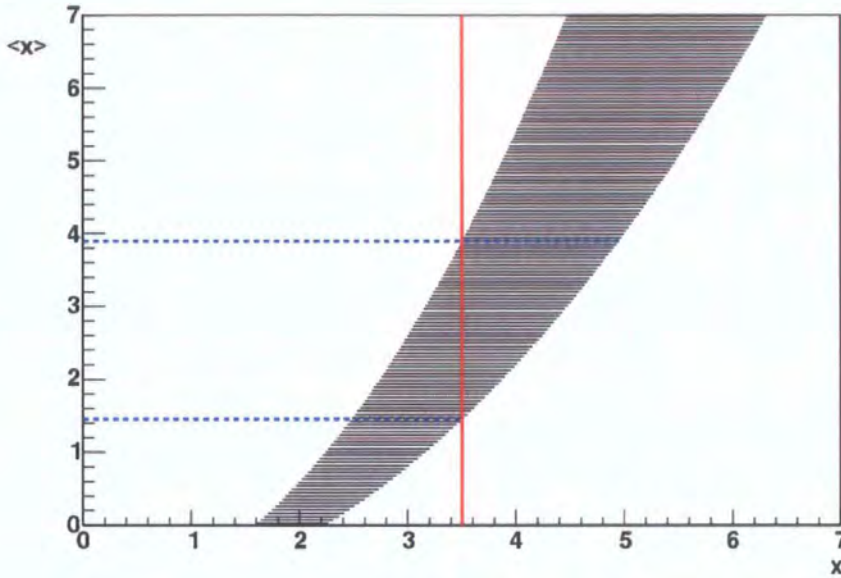


Figure 5.24: (from [256]) The Neyman's Construction of C.I. in the Feldman–Cousins approach. The confidence belt shown corresponds to the choice of a single probability level,  $\alpha$ . The horizontal lines of the belt contain  $(1 - \alpha)\%$  of all the values of  $x$  that comprise the individual distributions with mean values  $\langle x \rangle$ . By drawing a vertical line at a measured value of  $x$  — in this figure  $x = 3.5$  — one can construct the C.I. for the true value  $\langle x \rangle$ , which should be contained within the intersection points of the line and the belt borders, at a  $(1 - \alpha)\%$  C.L. For low values of  $x$  — here below  $x = 2.2$  — one can only calculate the  $(1 - \alpha)\%$  UL, which is the value of  $\langle x \rangle$  that corresponds to the non-zero intersection point.

$$\int_{-\infty}^{x_{1i}} g(x; \langle x \rangle_i) dx = \int_{x_{2i}}^{\infty} g(x; \langle x \rangle_i) dx = \frac{\alpha}{2} \quad (5.107)$$

which leads to C.I. satisfying  $pr(\langle x \rangle_i < \mu_1) = pr(\langle x \rangle_i > \mu_2) = \alpha/2$ , where  $[\mu_1, \mu_2]$  is the C.I. at a C.L. of  $(1 - \alpha)\%$ . Furthermore, Feldman and Cousins introduce the likelihood ratio

$$R(x) = \frac{g(x; \langle x \rangle_i)}{g(x; \langle x \rangle_{\text{opt}})} \quad (5.108)$$

where  $\langle x \rangle_{\text{opt}}$  is the physically allowed value of  $\langle x \rangle$  that maximises  $g(x; \langle x \rangle_i)$ . In brief,  $R(x)$  makes sure that the most probable values of  $x$  that are also physically allowed have priority in the construction of the acceptance intervals.

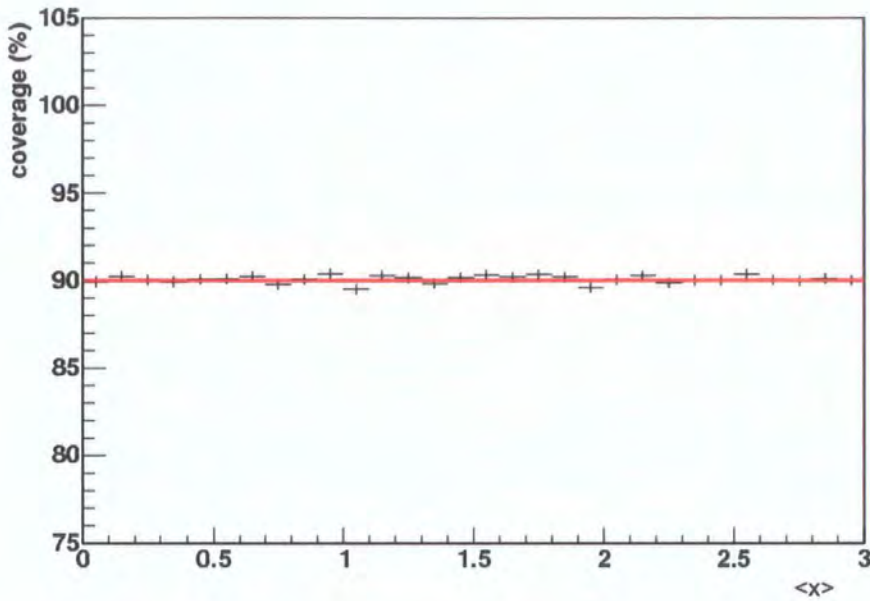


Figure 5.25: (from [408]) Comparison plot between the stated coverage (90%) of the Feldman–Cousins method (solid line) and the actual coverage of Monte Carlo simulations (crosses).

The constructed confidence belt for a specific  $\alpha$  can be used to define the C.L. for values of  $x$  below the detection threshold, and the C.I. for those above; the transition between the two is smooth. Fig. 5.24 shows how this is done. Given a measured value of  $x$ , one can draw a vertical line at this value. The intersection points between this line and the borders of the confidence belt define the C.I. for the values of  $\langle x \rangle$ , with a probability of  $1 - \alpha$ . As can be seen in the same figure, for weak signals (i.e. low values of  $x$ ) the intersection gives only an upper limit on  $\langle x \rangle$ , since the lower boundary is zero.

Since Feldman and Cousins construct the acceptance intervals for  $x$  based on all the physically allowed values of  $\langle x \rangle$ , the method’s coverage is guaranteed to be compatible with the stated C.L. Fig. 5.25 shows a coverage plot for the Feldman–Cousins approach (compare with Fig. 5.23), in which the stated C.L. (solid line) for UL or C.I. is compared with Monte Carlo simulations (crosses). It can be seen that, within statistical errors, the simulated coverage matches the value stated by the method.

## 5.6 The Independent Fourier Spacing

Despite the wealth of available ephemerides for most pulsars — mainly through radio observations — there are cases where VHE pulsar observations do not take place contemporaneously with a valid radio ephemeris. Hence, if one uses an invalid ephemeris, there is a risk of folding the data using the wrong frequency, since the cumulative error, as given by Eq. 5.11, may be unacceptable at the time of the data set. The threshold beyond which the departure of the used frequency from the actual one can be considered unacceptably large is quantified in terms of the Independent Fourier Spacing (IFS). To assist a more specific definition of the IFS, one can imagine a time-sorted data set of total exposure time  $T = t_1 - t_0$ , containing the arrival times of all the pulsed events from a pulsar, during  $T$ . If the pulsar frequency,  $f(t)$ , which is naturally a function of time (see Eq. 5.8), is such that  $1/f(t) \ll T \quad \forall t \in [t_0, t_1]$ , then the following definition can be given:

One IFS is equal to the frequency interval,  $\Delta f(t_0)$ , by which the pulsar's actual frequency at the time of the data set's first event should be shifted, so that the resulting phase shift of the last folded event, in that data set, is exactly 1.

The phase shift is gradual and increases monotonically with time within the data set's duration, so that for any event with  $t = t_i \in [t_0, t_1]$  it is equal to

$$\Delta\phi(t_i) = \Delta f(t_0)(t_i - t_0) \quad (5.109)$$

where we assumed that all frequency derivatives remain constant throughout the data set. Hence, for the last event, the definition of one IFS yields

$$\Delta f(t_0)T = 1 \Rightarrow \text{IFS} = \Delta f(t_0) = \frac{1}{T} \quad (5.110)$$

Clearly, in a data set with a large number of pulsed events, the individual phase shifts,  $\Delta\phi(t_i)$ , will vary continuously across  $[0, 1)$ . Therefore, upon folding with frequency  $f(t_0) + \text{IFS}$ , a narrow peak in a pulsar's profile will appear completely smeared (see Fig. 5.26). Consequently, the two lightcurves that were produced by folding the events using  $f_0$  and  $f_0 + \text{IFS}$  are independent from each other, and it can be said, in general, that all frequencies separated from each other by one IFS or more are, by definition, *independent*.

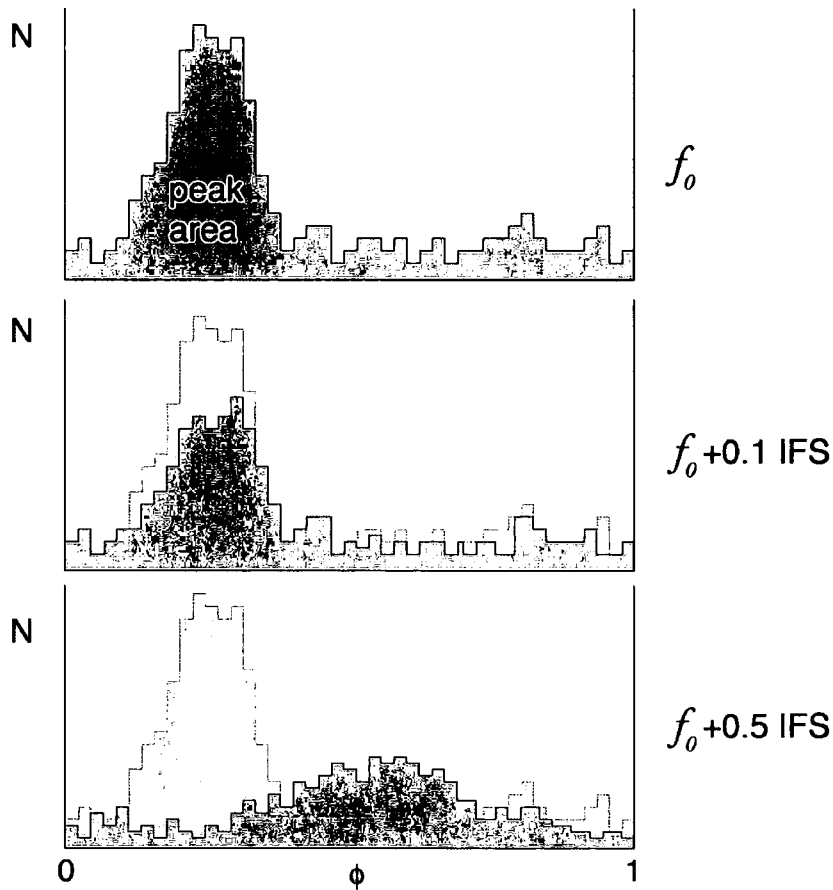


Figure 5.26: The effect of pulse smearing when folding pulsar data. The top phasogram shows an example lightcurve, which resulted from folding the data with the pulsar frequency,  $f_0$ . Provided the folding is carried out using the correct frequency for all events in the data, the pulsed events should all be grouped inside the peak area. If, instead, one uses a slightly shifted frequency to construct the phasogram, the event folding will introduce a corresponding phase shift to the phases of the pulsed events, which depends on each event's timestamp (Eq. 5.109). This will cause the events to depart from the peak area by different phase amounts, which smears the original pulse. The middle phasogram shows the resulting lightcurve after folding the events with the pulsar frequency shifted by 1/10 of the Independent Fourier Spacing. The smearing of the actual pulse, which is dimmed out for comparison, is more evident in the bottom plot, where the frequency used was  $f_0 + 0.5 \cdot \text{IFS}$ .

In order to avoid smearing a potential signal by choosing the wrong frequency, one can search through a number of IFSs on either side of the suspected frequency. However, the freedom to browse a range of frequencies until the right one is found comes at a cost: each independent frequency searched contributes to the increase of the number of independent trials, which is equal to the number of free, independent parameters in our search. In other words, each additional IFS searched increases the df by one. As a consequence, the probability,  $pr(> Z|H_0)$ , of accepting  $H_0$  using a statistic, say  $Z$ , is increased to its *effective* value,  $pr'(> Z|H_0) \geq pr(> Z|H_0)$ . To make this clearer, one can imagine the extreme case where a search for a signal is conducted by applying a uniformity test to an infinitely wide range of independent frequencies. In that case, all the values of the test statistic,  $Z$ , will come up at least once, and the number of occurrences for each  $Z$  will follow the p.d.f. of  $Z$ , say  $g(Z)$ . Thus, the significance of any outcome from such a test is zero, or equivalently  $pr'(> Z|H_0) = 1 \quad \forall Z$ .

In practice, where the range of frequencies is finite, the effective probability,  $pr'(> Z|H_0)$ , is a function of the number of IFSs in the searched range. More specifically, if the resulting probabilities after searching through  $x$  IFSs of a data set are  $pr_i$ , where  $i = 1, 2, 3 \dots x$  is the index number of the independent trials, then the effective probabilities that take into account the df of the search are given by [400]

$$pr'_i = 1 - (1 - pr_i)^x \quad (5.111)$$

and because in the case of a signal detection we are usually dealing with very low probabilities, i.e.  $pr \sim 10^{-7}$ , this expression can be approximated with the simpler

$$pr'_i \approx xpr_i \quad (5.112)$$

For example, if a uniformity test on a data set resulted in the rejection of  $H_0$  at the  $5\text{-}\sigma$  level, after scanning through  $x \sim 500$  IFSs, then the effective significance of the result would be only  $3.5 \sigma$ . Had the same result been achieved using an accurate ephemeris whose error on the frequency throughout the data set was less than 1 IFS, the significance stated by the uniformity test would have reflected reality. Therefore, it is suggested that periodicity searches through frequency ranges covering more than 1 IFS should only be conducted when the analysis lacks of an accurate ( $\sigma_f < \text{IFS}$ ) and contemporaneous ephemeris.



## 5.7 Simulations

### 5.7.1 Monte Carlo Pulse Generator

In order to check that the code for the uniformity tests functions properly, it was considered suitable to generate simulated signals that would be used as our test-bench. We coded a Monte Carlo pulse generator that simulates a pulsed signal of custom shape, superimposed on a Poisson-distributed background. Here, we set forth only the key points of our code.

Before the simulation begins, the user has the choice between a unimodal (single peak) or bimodal (double peak) lightcurve for the pulsed component. In addition, the properties of the signal need also be specified. The pulse duty cycle(s),  $\delta$ , and the peak phase position(s),  $\mu$ , are some of the required parameters; others include the pulsed fraction,  $p$ , as well as the signal frequency and its derivatives ( $f$ ,  $\dot{f}$ , etc.).

The code tries to mimic a real observation by simulating both signal and background for a user-defined amount of time,  $\Delta t = T$ , equivalent to the exposure time of an observation. Starting from  $t_0 = 0$ , the routine increments time in steps (bins) of  $dt$ , which have customisable temporal width. Our choice was to have bins equal to  $1/50$  of the signal's period, which was proven to be an adequate temporal resolution, but also resulted in acceptable computation times. For each time bin, the code assigns a phase to the contemporary value of  $t = t_0 + k \cdot dt$  — where  $k$  is an integer — based on the values of  $f$ ,  $\dot{f}$ , etc. Then it calculates the average number of events that each bin contains, using a custom p.d.f. for the phase distribution from  $0$  to  $2\pi$  and the user-defined event rates for the background ( $R_c$ ) and the signal ( $R_\gamma$ ). As mentioned earlier, our choice was a Gaussian source function of the form [394]

$$g_s(\phi; \mu, \delta) = \frac{1}{\sqrt{2\pi\sigma^2}} \sum_{l=-\infty}^{\infty} \exp \left[ -\frac{(\phi - \mu + 2\pi l)^2}{2\sigma^2} \right] \quad (5.113)$$

where  $\sigma = 2.668\delta$  radians. Using this function in Eq. 5.43 results in the p.d.f. that defines the probability of having an event at phase  $\phi$ . For the given total event rate  $R = R_\gamma + R_c$ , the average number of events in an interval  $dt$  is given by

$$\langle N \rangle = R \cdot dt \cdot \left[ pg_s(\phi; \mu, \delta) + \frac{1-p}{2\pi} \right] \quad (5.114)$$

which is a real number. Based on this average, the code calculates the integer number of events for each bin using a non-uniform random number generator [411],

which, in our case, follows a Poissonian distribution with mean  $\langle N \rangle$  (see Eq. 5.12).

Having filled each bin with a number of events, the procedure has to assign a timestamp to each one of them; this is done with a Mersenne generator [412], which is a uniform random-number generator that obeys a flat p.d.f. Each event receives a timestamp which is equal to the contemporary  $t$  plus a random fraction of  $dt$ . Finally, the timestamps of all events in every bin, within exposure time  $T$ , are written out on a file whose format is identical to that produced from the timestamp extraction process with real data.

### Example Pulse Profiles

Since we had control over parameters like pulse width, position and modulation, it was considered appropriate to simulate the morphology of the EGRET pulse profiles for the Crab pulsar and PSR B1706–44, which were our analysis targets. This way we could test the correct function of our uniformity tests as well as their sensitivity using the expected pulse shapes (see next paragraph).

The Crab pulsar's profile is bimodal with the main peak being  $\approx 5$  times more intense than the second one. They are located at phase  $\mu_1 = 0$ , for the main peak, and  $\mu_2 = 0.38$ , for the second peak. Moreover, their duty cycles are  $\delta_1 \approx 0.1$ , for the main, and  $\delta_2 \approx 0.11$ , for the second peak [289]. In order to simulate the Crab pulsar's bimodal profile, the following p.d.f. was used (compare with Eq. 5.43):

$$g(\phi) = p_1 g_s(\phi; \mu_1, \delta_1) + p_2 g_s(\phi; \mu_2, \delta_2) + \frac{1 - p_1 - p_2}{2\pi} \quad (5.115)$$

where  $p_1$  and  $p_2$  are the pulsed fractions corresponding to the main and second peak, respectively [394]. In our simulation we used a  $\gamma$ -ray event rate equal to 1 Hz, for the main, and 0.2 Hz for the second peak; and the background rate was set to 11 Hz: 10 Hz cosmic rays plus 1 Hz DC  $\gamma$  rays. The resulting integrated lightcurve over  $T = 16.6$  min is shown in Fig. 5.27a. In the same figure, we have also included the phasogram of the average counts,  $\langle N \rangle$ , which was produced using with Eq. 5.114 and is shown for two periods. It can be seen that the integrated lightcurve possesses only one significant peak ( $\sim 5 \sigma$ ), whereas the second peak is too weak to be resolved from the background.

In addition, we simulated a broad, Gaussian profile, similar to that of PSR B1706–44. The central phase of the profile's peak is known to be shifted with respect to the radio pulse by about 0.4 and has a duty cycle,  $\delta$ , roughly equal to

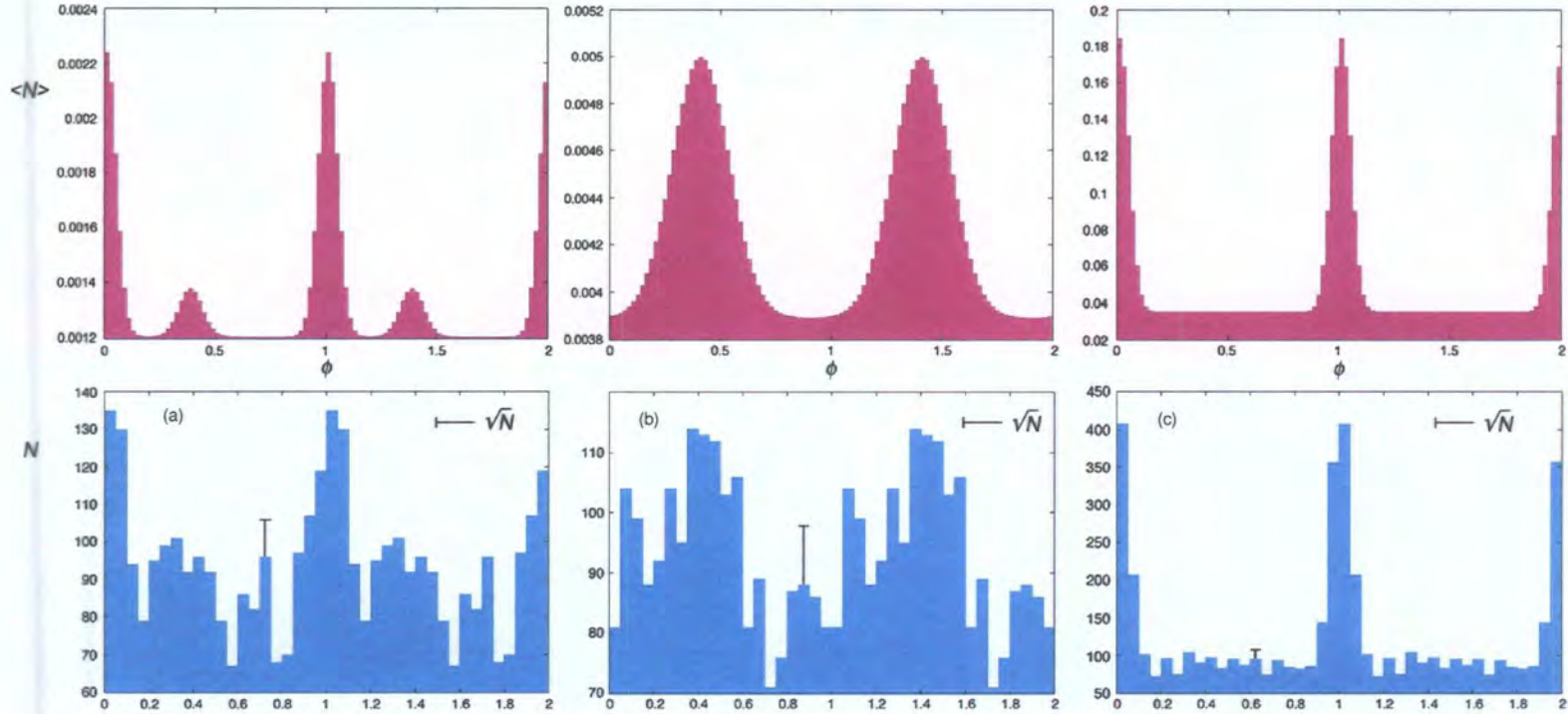


Figure 5.27: The simulated lightcurves for (a) the Crab pulsar and (b) PSR B1706–44. In addition, we simulated a narrow, single-peaked profile to be used as a test bench (c). The top row of plots shows the p.d.f.s that were used to generate these lightcurves. This was expressed with the average number of events as a function of phase, which was calculated using Eq. 5.114. The phase step was selected to match the temporal resolution of our simulation, i.e.  $1/50$  of the signal period. Under each p.d.f., we plotted the resulting integrated phasograms from 1 ks of data folded in 20 phase bins. At phase 0, the main peak of the Crab pulsar’s profile is clearly distinguishable, being  $\sim 5 \sigma$  above the background. However, the second peak, at  $\phi \approx 0.38$ , cannot be resolved from the background fluctuations. For PSR B1706–44, the main peak coincides with  $\phi = 0.4$  and has a broad profile with  $\delta \approx 0.3$ . This time, the signal excess at the peak position is only  $\sim 2.5 \sigma$ . The narrow profile in (c) was generated based on a unimodal p.d.f. with  $p = 0.31$  and a Gaussian source function centred on phase 0 with duty cycle  $\delta = 0.1$ . The resulting phasogram shows a clear excess of the signal, at the level of  $\sim 15 \sigma$ .

0.3. The background and signal event rates were kept the same as in the case of the Crab pulsar, and the exposure time was, again,  $T = 16.6$  min. The integrated profile is shown in Fig. 5.27b together with the average, phase-resolved event rate that arises from the p.d.f. (Eq. 5.113).

A third, fictitious signal was also simulated in order to provide a clear target for comparison tests regarding the sensitivity of the uniformity tests. More specifically, we chose to simulate a very narrow ( $\delta = 0.1$ ) and strong ( $p \approx 0.31$ ) peak centred on phase zero, which would lead to a detection at a high significance, with any test. The corresponding lightcurve is shown in Fig. 5.27c.

## 5.7.2 Uniformity Tests: Operation and Performance

### Probability Distributions

Once we had finalised the code for the Rayleigh and  $H$  tests, it was considered appropriate to investigate the consistency of the probability distributions for each test. In order to do this, we simulated a data set using a Poissonian generator, which contained  $\sim 10^5$  random timestamps. Using our code we generated  $M \sim 10^4$  values of each test statistic,  $Z$  ( $Z \equiv H$  or  $Z \equiv 2NR^2$  in our case), by folding the above data set with 900 independent frequency values. The range of values for each statistic was binned using 50 bins of equal widths ( $\Delta Z = \text{const}$ ). Since we wanted to calculate the probability of having a value of  $Z$  higher than that corresponding to each bin, we constructed a cumulative histogram of the number of  $Z$  values: for every bin,  $k$ , the number of values of  $Z$  contained in the bin, say  $M_k$ , equals the sum of all the values in the  $k + 1, k + 2, \dots, m$  bins, where  $m = 50$  in our case. Hence,

$$M_k = \sum_{i=k+1}^m M_i \quad (5.116)$$

Therefore, division of each bin's content by  $M$  gives the fraction of our sample that lies above a specific  $Z$ ; for  $M \rightarrow \infty$ , this should be equivalent to the probability of finding a value higher than  $Z$ . Of course our sample was much more limited, and therefore we can only use this statement as an approximation: thus,

$$pr(> Z|H_0) \approx \frac{M_k}{\sum_{i=1}^m M_i} \quad (5.117)$$

where the probability is calculated assuming uniformity. Furthermore, because each bin contains a countable number of  $Z$  values, we can calculate the error on this

probability value assuming Poissonian statistics. Hence, if the standard deviations for the bins are  $\sigma_k = \sqrt{M_k}$ , then

$$\sigma_{pr} = \frac{1}{M} \sigma_k = \frac{\sqrt{M_k}}{M} \quad (5.118)$$

Based on these expressions, the resulting probability distributions from our data set are those shown in Fig. 5.28. In the same figure, we have included the analytical functions of the probability distributions for the Rayleigh and  $H$  tests, as given in [401] and [393], respectively. The simulated distributions were consistent within statistical errors with the corresponding analytical functions.

### Parametric Curves from the Helene Method

The method of Helene for the calculation of upper limits assumes Poissonian or Gaussian p.d.f.s for the signal strengths (see section 5.5). Prior to using this method with H.E.S.S. data, we aimed at reproducing the parametric curves of Fig. 5.22, which would reassure us of the correct function of our code. Helene derived these plots based on the p.d.f. of equation Eq. 5.99, which in fact is of little use for Cherenkov astronomy, since the Gaussian approximation of Eq. 5.101 produces the same results for large event numbers, as it will be shown graphically.

Our code increments the values of the background,  $B$ , and upper limit,  $A$ , by customisable intervals, until it reaches the specified confidence level,  $\alpha$ ; this was done for a few values of the peak area counts,  $C$ . In order to directly compare our plots with Helene's, we assumed a background with negligible standard deviation and a  $(1 - \alpha) \cdot 100\% = 95\%$  C.L. Our resulting plots are shown in Fig. 5.29, where one can see that the curves match exactly those of Fig. 5.22.

In addition, we were able to produce the same parametric curves for the case where the underlying p.d.f. is the Gaussian approximation of Eq. 5.101. Although this function is only useful when  $C \gg 1$ , we reproduced curves for the same range of peak area counts as in the Poisson case, so that we can compare how effective the approximation becomes with increasing  $C$ . The results are shown in Fig. 5.30, where we have plotted both cases in the same graph. One can see that for  $C \leq 10$  the difference between the upper limit from the approximated curves and that from the exact, Poissonian solution is  $> 13\%$ . Moreover, for  $C = 1$  the error becomes  $> 1 \sigma$  for the entire range of background counts, if Poissonian statistics are assumed for the distribution of  $A$ . On the other hand, for  $C > 10$  the Gaussian curves become a

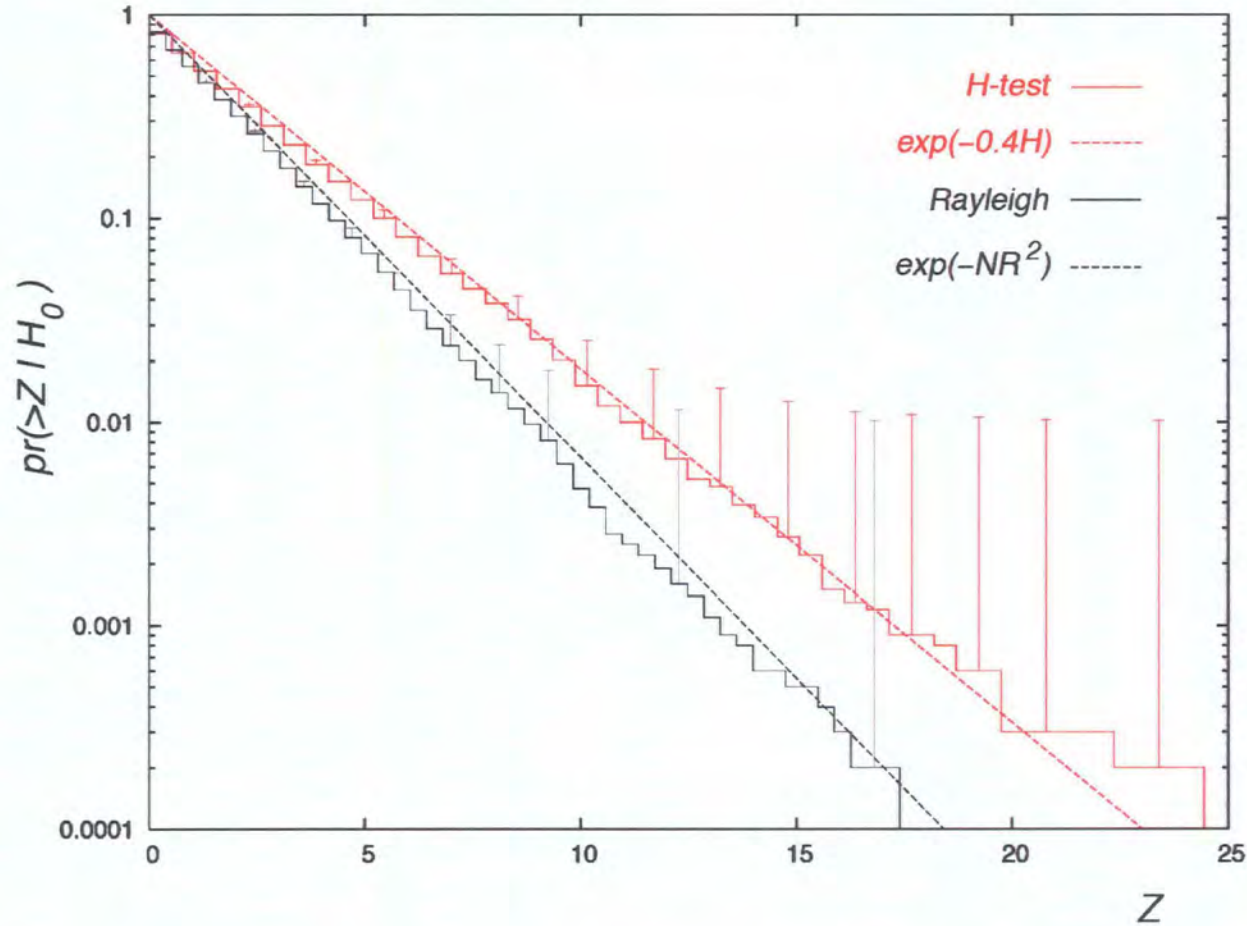


Figure 5.28: The resulting probability distributions of the Rayleigh ( $Z \equiv 2NR^2$ ) and  $H$  ( $Z \equiv H$ ) statistics, as were calculated with our analysis software. Both statistics were calculated from a simulated file containing  $N \sim 10^5$  random timestamps. A total of  $\sim 10^4$  independent frequencies were scanned, and the resulting values of  $H$  and  $2NR^2$  from each frequency were binned to construct the above histograms. The expected distributions for the  $H$  (red colour) and Rayleigh (black colour) statistics are drawn with dashed lines. At the highest values of the test statistics, i.e.  $Z > 15$ , the statistical errors become large due to the small sample in these bins.

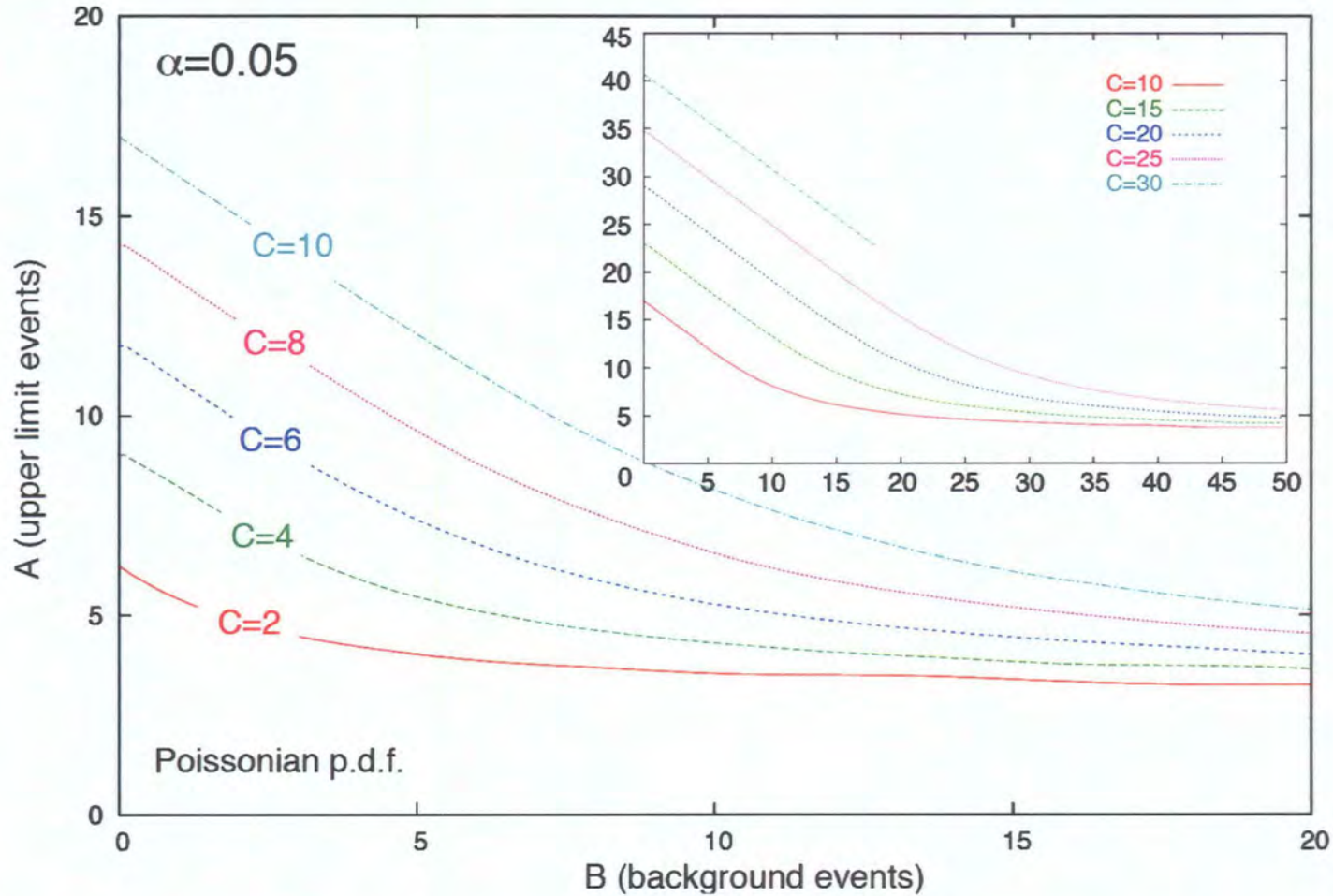


Figure 5.29: The parametric curves of the Helene method, which provide the 95% upper limit on the counts of the peak area ( $A$ ) as a function of the background counts ( $B$ ), for various values of the total counts in the peak area ( $C$ ). The standard deviation of the background was considered negligible. These plots were derived from our analysis code in order to verify its functionality. A comparison with Fig. 5.22, which contains the corresponding curves as were presented in Helene’s publication of the method, reveals a perfect match.

good approximation of the corresponding Poissonian ones, and the difference is well within  $1 \sigma$  for the whole examined range of  $B$ .

### Test sensitivity: $\chi^2$ -test versus $H$ -test

It is generally known that the  $\chi^2$ -test is more sensitive to narrow pulse profiles than other, more general tests for uniformity. The  $H$ -test, on the other hand, is considered a general test that performs well for various pulse shapes. We decided to compare the temporal and flux sensitivity between those two tests, using the simulated narrow pulse of Fig. 5.27c.

For the flux sensitivity comparison, we fixed the exposure time of the signal to 5 h and varied the signal strength as a percentage of the background. The background count rate was set to  $R_c = 7$  Hz, which is a typical cosmic ray rate after the application of the standard H.E.S.S. cuts. Based on that value, we produced 11 pulsed signals of gradually increasing pulsed fractions,  $p$ , in the 1–3% range; five of them are shown in Fig. 5.31. After having produced the simulated data sets, we proceeded by applying the  $\chi^2_{19}$  and  $H$  tests to the data and folding the timestamps with the chosen signal frequency:  $f = 29$  Hz in this case. The resulting probability values from each test were plotted against the fundamental scaling parameter  $p\sqrt{N}$  (see Fig. 5.32). On average, both tests showed a similar response to the different signal strengths, which follows a linear trend across the examined range. However, our small sample of data points exhibits a large spread which does not allow for a more detailed comparison between the flux sensitivities of each test.

Additionally, we simulated a number of data sets with exposure times in the  $10^4$ – $10^5$  s range, while fixing the pulsed fraction to 1% (see Fig. 5.33). As before, we applied the  $H$  and  $\chi^2_{19}$  tests to the data and plotted the resulting probabilities against the exposure time. Fig. 5.34 shows the resulting scatter plot with the individual probabilities for each data set and uniformity test. There is an evident increase of the average  $-\log pr(> Z|H_0)$  with exposure time, as expected, but no particular difference between the tests can be distinguished. It is also unsafe to conclude that the function which describes the variation of significance with exposure time has any particular form, since the data spread is large.

The above tests were based on parameters that are likely to be dealt with in real observations. Hence, the fluxes were chosen to be low — a few percent of the background — and the exposure time was limited to realistic values. (A 30-h exposure time corresponds to roughly 70 observation runs: an amount of data that



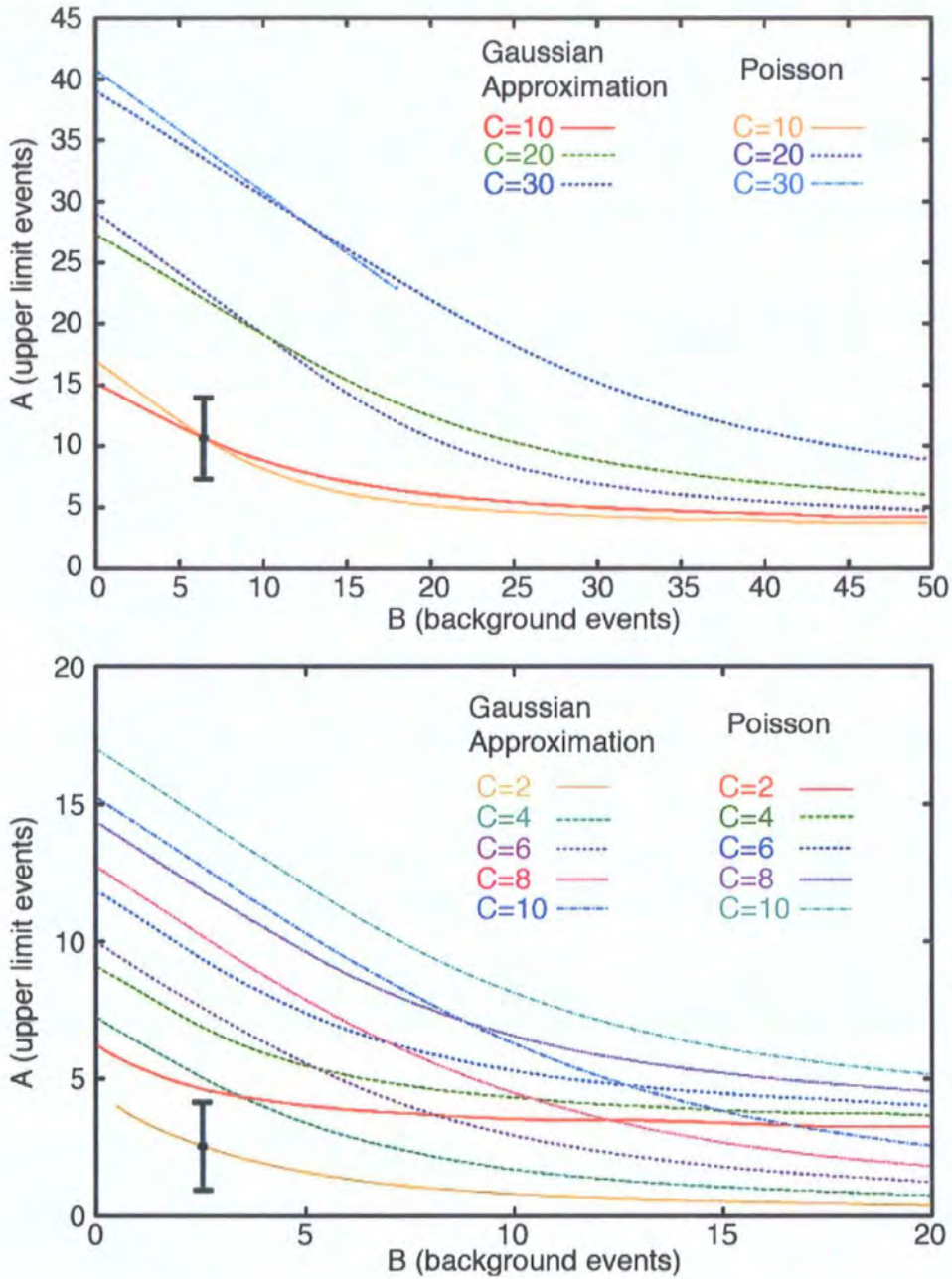


Figure 5.30: Plots of the 95% upper limit ( $A$ ) for the Poissonian and Gaussian cases of the Helene method, as a function of the background ( $B$ ). The curves are shown for different values of the peak area counts,  $C$ . For  $C \leq 10$  (bottom graph), the deviation between the two cases is evident. More specifically, one can see that for  $C = 1$  the difference remains larger than  $1 \sigma$  for the entire investigated range of background counts. Large values of  $C$  (i.e.  $C > 10$ , in the top graph) led to a close match between the curves derived from the two parent distributions. The error bars were calculated assuming Poissonian statistics for the upper limit counts.

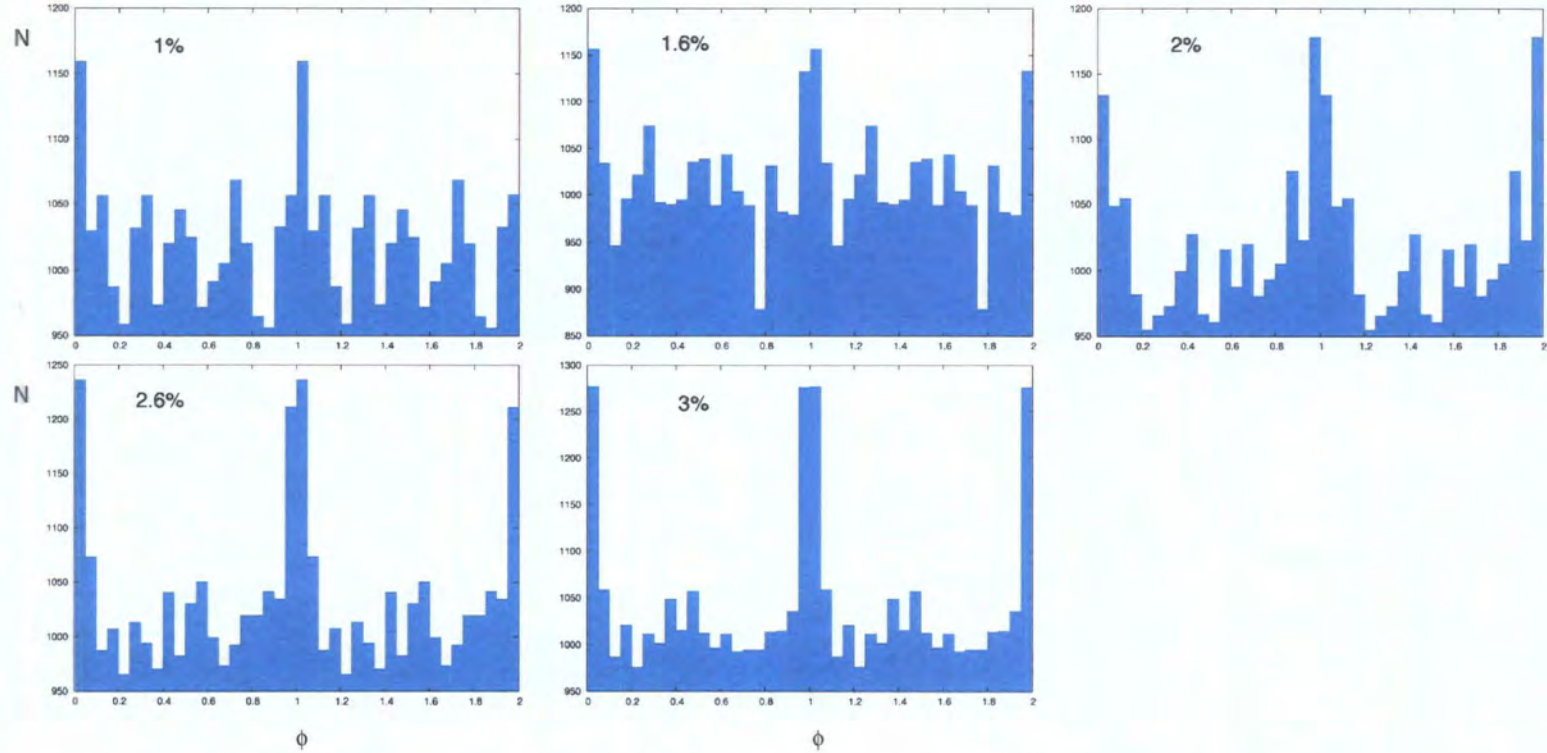


Figure 5.31: 5 of the 11 integrated pulse profiles that were used in the flux sensitivity tests. All profiles contain a simulated, pulsed component with 10% duty cycle and a Poissonian background with event rate equal to  $R_c = 7$  Hz. The phasograms have been constructed from 5-h data sets. In each case, the pulsed signal is centred on phase 0. The pulsed fraction is also shown with each phasogram.

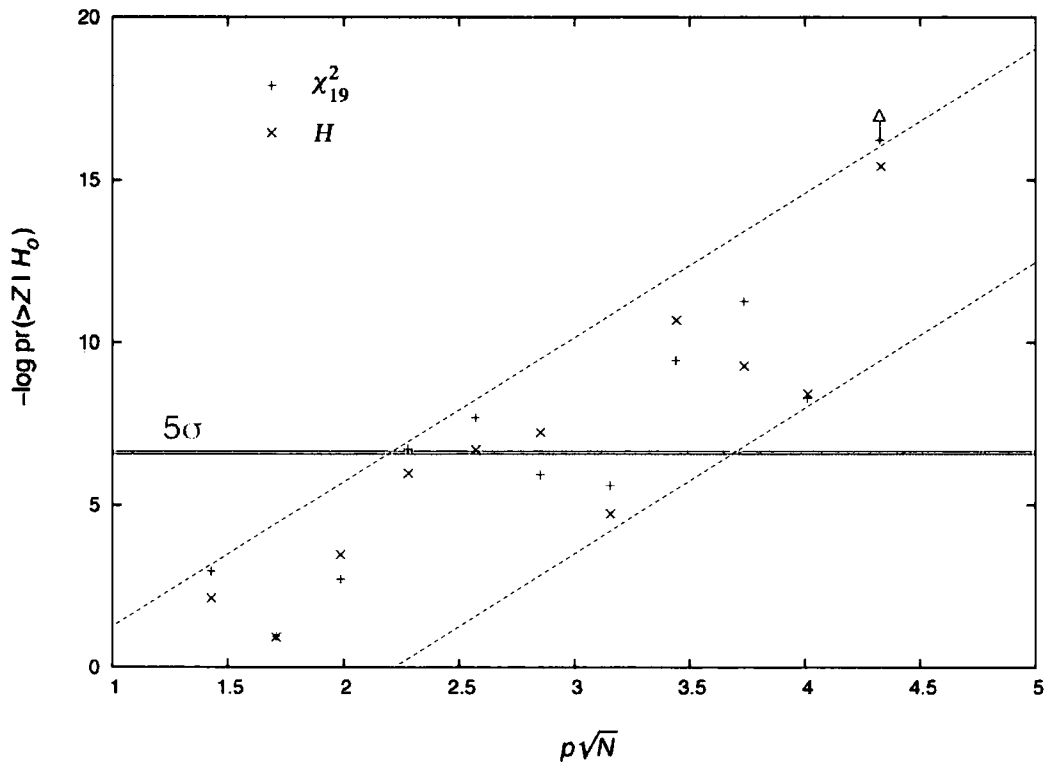


Figure 5.32: The resulting probabilities, under the  $H_0$ , from the application of the  $H$  (blue crosses) and  $\chi^2_{19}$  (red plus signs) tests to our simulated profiles, as a function of the fundamental scaling parameter. Each symbol represents the result from the corresponding uniformity test, which was derived using one of the simulated profiles (see Fig. 5.31). The general trend of the probabilities with increasing signal strength is emphasised with the dashed lines. The horizontal, grey line corresponds to the probability of accepting  $H_0$  for signals that are 5 Gaussian standard deviations above the background. Despite the large spread of the data points, both tests appear to have similar response to the variations of the signal strength. For the last data point from the  $\chi^2$ -test (profile with  $p = 0.03$ ), we were only able to state an upper limit on the probability value (arrow), which was  $< 10^{-16}$ .

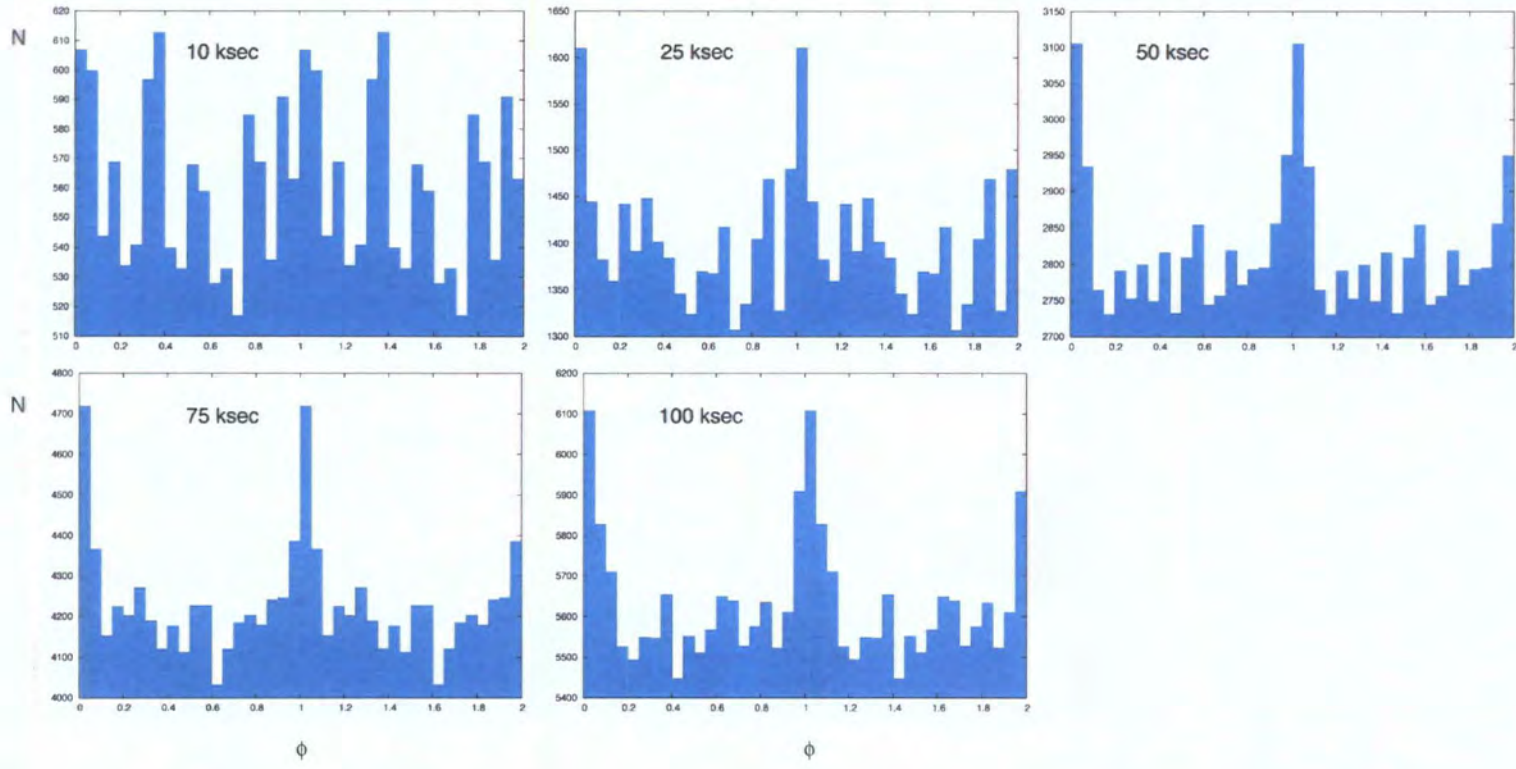


Figure 5.33: 5 of the 18 integrated profiles that were used in the temporal sensitivity tests. The exposure time of the data sets that were used to construct the phasograms is stated in kiloseconds. In all cases, the pulsed signal is centred on phase 0, and the pulsed fraction is fixed to 1%, with the background event rate being 7 Hz.

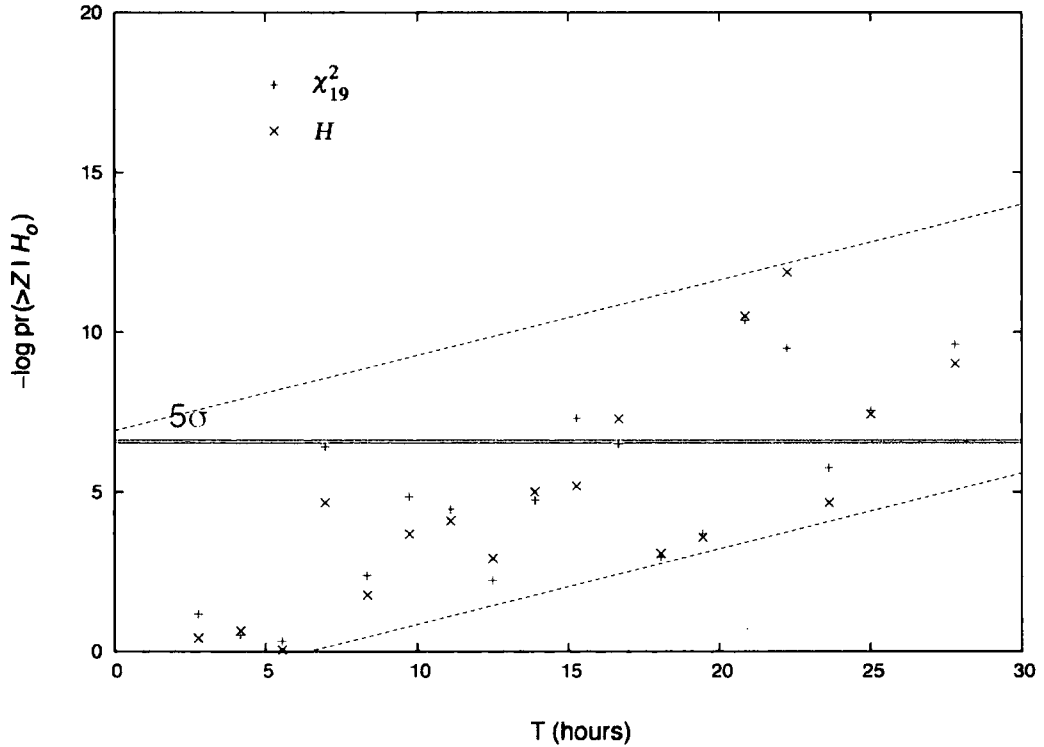


Figure 5.34: The resulting probabilities from the application of the  $H$  (blue crosses) and  $\chi_{19}^2$  (red plus signs) tests to our simulated profiles, as a function of the exposure time,  $T$ . The dashed lines have been included for visual reference of the average trend and do not necessarily imply a linear dependence of  $-\log pr(> Z|H_0)$  on  $T$ . It can be seen, however, that both tests performed similarly, on average. The horizontal grey line corresponds to the probability of accepting  $H_0$  for signals that are 5 Gaussian standard deviations above the background.

was only available for a few targets — e.g. the Crab and PSR B1706–44 — at the time of our analysis.) The drawback with such an approach is the large fluctuations that are inherent with marginally detectable signals.

Therefore, if one wants to investigate each test's behaviour as a function of either exposure time or flux, it is necessary to use strong but potentially unrealistic signals. In section 5.4.1 we derived the dependence of  $\chi^2$  on the pulsed fraction, as well as on the exposure time,  $T$  (Eq. 5.55). We have shown these dependencies graphically, using a number of simulated profiles which we generated by varying the pulsed fraction while keeping the exposure time fixed and, inversely, by varying the exposure time while keeping the pulsed fraction fixed.

For the first set of simulations, we chose 7 data sets with exposure times in the 0.5–25 ks range and fixed the pulsed fraction of the profiles to 10%. We then calculated the  $\chi^2_{19}/(19 \text{ df})$  values for each data set. According to Eq. 5.55, the  $\chi^2$  values should be a linear function of  $T$ . Indeed, as Fig. 5.35a shows, the data points were well-fitted with a straight line: the goodness-of-fit  $\chi^2$  was 1.13. Assuming the same holds for the  $H$ -test, we fitted a linear function to the derived  $H$  values from the same data sets (Fig. 5.35c). Hence, in both cases, we find a strong linear relation between the test statistic and the exposure time.

Also, in order to verify the dependence of  $\chi^2$  on the pulsed fraction, we simulated 7 data sets of 1-ks exposure time each, which contained pulses with  $p = 0.01$ – $0.5$ . By plotting the derived  $\chi^2$  values against  $p$ , we expected to see the quadratic dependence of Eq. 5.57, for small values of the pulsed fraction, and a polynomial behaviour, for the whole range of  $p$ ; fig. 5.35b and 5.35d show that this is the case for both  $\chi^2$  and  $H$  tests, respectively. In the  $\chi^2$  plot, data points corresponding to pulsed fractions up to  $p = 0.3$  were well-fitted with a parabolic function: the goodness-of-fit  $\chi^2$  value was 1.07. However, the entire range of values could not be fitted with a low-order polynomial, which agrees with the predictions of Eq. 5.56; and the same was also found true for the  $H$ -test plot.

### Test Application: Simulated Profiles

The EGRET pulse shapes for the Crab pulsar and PSR B1706–44 are similar to those of Fig. 5.27a and Fig. 5.27b. Since these pulsars were part of our analysis, it was considered interesting to compare the results from the application of the aforementioned tests to bimodal, Crab-like and broad, PSR B1706–44-like profiles.

We applied  $\chi^2_{19}$ , Rayleigh,  $H$  and  $C_m$  tests to the simulated Crab pulsar and

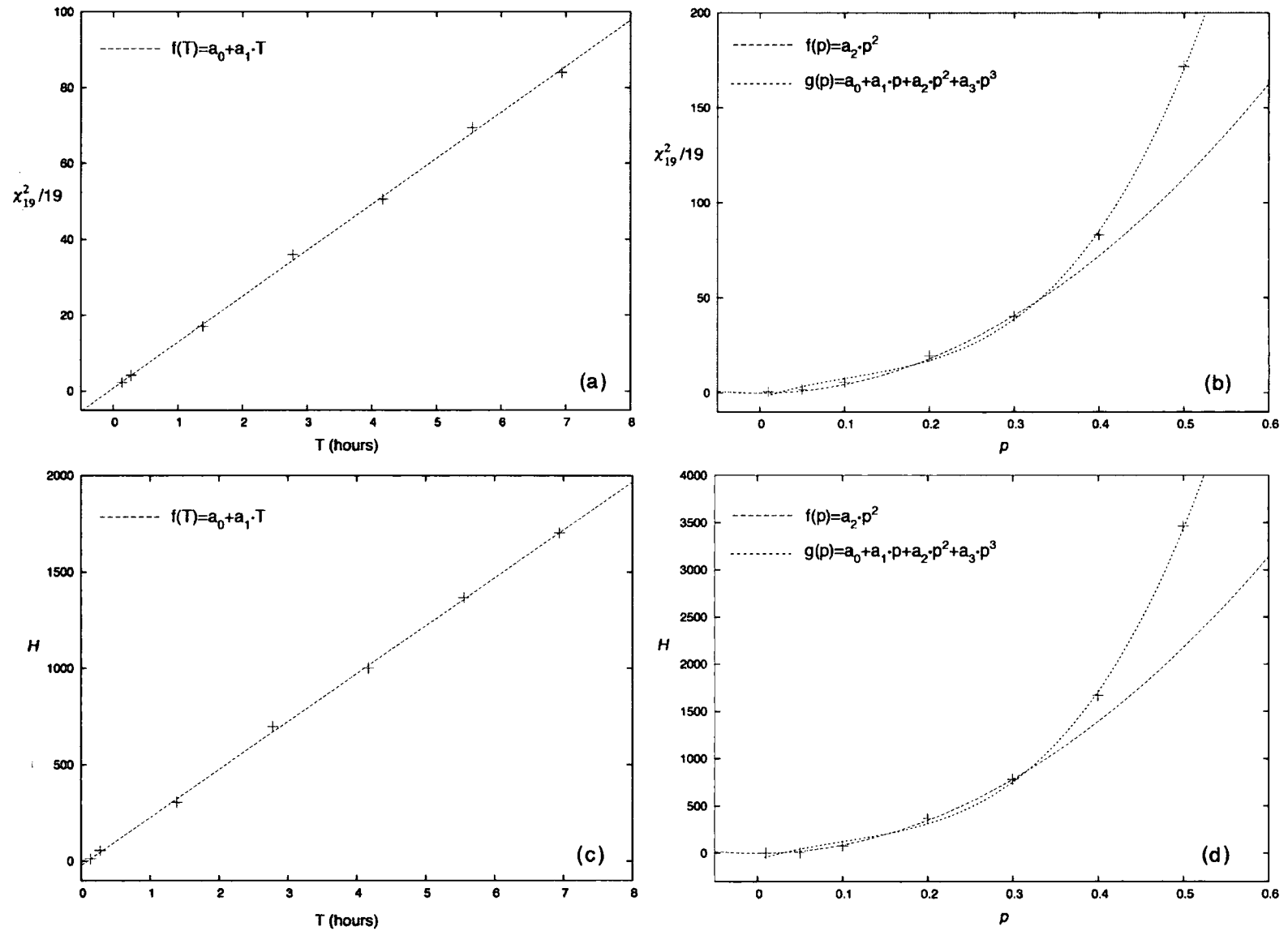


Figure 5.35: The dependencies of the  $H$  and  $\chi^2$  statistics on the exposure time,  $T$ , and the pulsed fraction,  $p$ , as were derived from our simulated data sets. The linear and quadratic functions for the former and latter cases are evident.

	$\chi^2_{19}$	$\text{NR}^2$	$H$	$C_m$
<b>Crab</b>	3.6 ( $1.3 \times 10^{-7}$ )	13.6 ( $1.2 \times 10^{-6}$ )	53 ( $1.3 \times 10^{-9}$ )	5.8 ( $3.3 \times 10^{-9}$ )
<b>PSR B1706–44</b>	1.7 (0.02)	9.7 ( $6.1 \times 10^{-5}$ )	19.9 ( $5.2 \times 10^{-4}$ )	4.3 ( $8.5 \times 10^{-6}$ )

Table 5.7: The results from the uniformity tests on the simulated Crab pulsar and PSR B1706–44 profiles of Fig 5.27a,b. The values in parentheses are the probabilities of accepting  $H_0$  with each test.

PSR B1706–44 data. The resulting statistics together with the corresponding probabilities are shown in Table 5.7.

The Crab pulsar’s profile was essentially detected by all tests, with the  $H$ -test producing the lowest probability. This is not a surprise, as the  $H$ -test is more sensitive than the rest when it comes to multi-modal profiles of unknown shape and position. In contrast, the Rayleigh test appears weak in comparison, mainly due to its lack of sensitivity for bimodal profiles with the peaks separated by  $180^\circ$  ( $137^\circ$  in this case). On the other hand, the faint and broad profile of PSR B1706–44 was harder to detect in the relatively large background, and both  $\chi^2$  and  $H$  tests produced insignificant probabilities. However, the Rayleigh test, which is sensitive to broad, sinusoidal profiles, managed to reject  $H_0$  to a  $3.8\text{-}\sigma$  level. In addition, the  $C_m$  test, whose power comes from the *a priori* knowledge of the pulse position, produced the most significant result, rejecting uniformity to a  $4.3\text{-}\sigma$  level.

### Test Application: Telescope Data

As well as testing our temporal analysis software with simulated data, we were also reassured of its correct function through applying it to telescope data. In the early days of H.E.S.S., when only the first telescope was operational, we discovered a strong, persistent Rayleigh power in the background data, from Crab observations. The strong periodicity was found at 1 Hz after scanning  $\approx 50$  IFSs, and the probability of the maximum Rayleigh power occurring by chance was  $\sim 10^{-38}$ . The resulting periodogram from the search is shown in Fig. 5.36; the phasogram of the folded events, at the frequency of the peak, is also shown in this figure. One can see that the reason for the large Rayleigh power is a dip in the data, or, in other words, a trigger-rate deficit, which occurs every second. The technical reason behind this deficit is the Central Processing Unit of the Data Acquisition System, which becomes busy on a regular basis in order to handle other operations [385].

A second application in conjunction with telescope data was the use of the  $H$ -



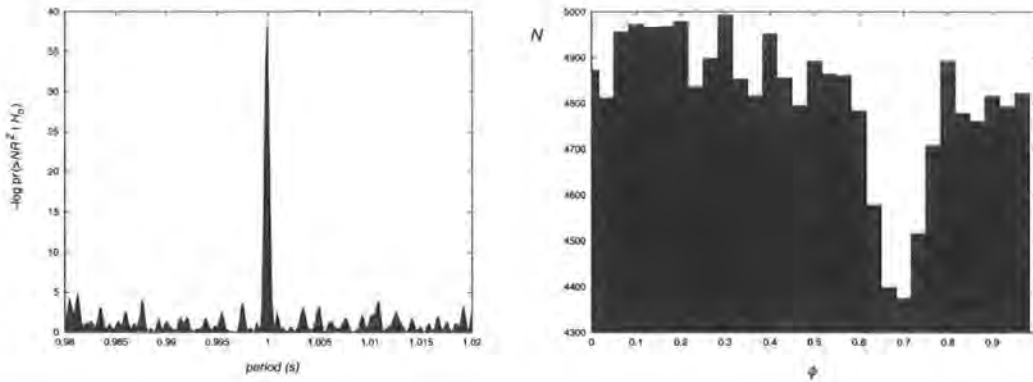


Figure 5.36: The plot on the left shows the resulting periodogram from our scan through  $\approx 50$  IFS. Each IFS was oversampled by a factor of 3, in order to produce a smoother plot. The probability of chance occurrence at the peak's frequency was found to be  $\sim 10^{-38}$  if all trials are accounted for. The phasogram on the right is the result of folding all the events in our data set with  $f = 1$  Hz. It shows that the reason behind the large peak is a trigger-rate deficit, which occurs periodically every second.

test as a pointer of the most probable frequency at which the flat-fielding device operates. More specifically, we analysed 75 flat-fielding runs, which were scanned for periodicities through two frequency ranges centred on 40 and 120 Hz: these frequency values were the preset hardware values for our two sets of flat-fielding runs. The frequencies which yielded the highest  $H$  value in each run were binned in 10 frequency steps. Fig. 5.37 shows the two histograms for 32–46 Hz and 108–130 Hz. There are two things to be noted for each histogram: first, about 50% of the data is distributed across the frequencies surrounding the highest bin; and, secondly, in both cases the majority of runs are concentrated within a single bin that corresponds to a different frequency than the preset.

We assume that the reason for the first is the communication delays between the flat-fielding device and the DAQ: the trigger signal is sent through the local network via ethernet, and hence the pulse frequency is dependent on how busy the network is. Due to the random nature of the network delays, the number of trigger signals per time interval (i.e. the trigger rate) fluctuates on a run-by-run basis by an amount that corresponds to the observed distribution of run frequencies.

Since the frequency fluctuations caused by the network's response are random, this means that the run frequencies should be uniformly distributed around a most

probable one: naturally, this is the preset frequency in the DAQ. However this is not observed, and both frequency distributions peak at a frequency significantly lower than the preset. It should be noted that the uncertainty in our frequency scan was  $\sim 10^{-3}$  Hz (1 IFS) and could not have been the reason behind the mismatch between the expected and most probable frequencies. Instead, we believe that this is an effect of the dead time that is inherent in the flat-fielding device's circuit. When the network is busy, it allows successive triggers to catch up with those delayed by the 'slow' network response. As a result, the triggers have to wait in the queue until they can be transmitted. Queued triggers are then sent almost simultaneously to the flat-fielding device, within time intervals that may well be  $\sim 1$  ms. This amount is comparable to the device's dead time [413], which practically rejects the incoming triggers, unable to respond to them. If several triggers are lost this way, the trigger rate will drop, and so will the frequency of the flat-fielding events. Otherwise, in less congested network conditions, although there might still be a higher trigger rate than the preset, the time intervals between successive events could be longer than the flat-fielding device's dead time, thus allowing the device to be triggered at a frequency that is higher than the preset.

It is important to note that no experimental work has been performed to verify the above, and so the validity of the explanations provided is uncertain. Nevertheless, our method was powerful enough to detect the *actual* frequency of operation and could potentially be used as a means for calibration of the process that controls the flat-fielding frequency: if, for example, it is found that the operation frequency of the flat-fielding device is systematically different to the one detected by our method, then one could in principle eliminate this error by reassigning the preset values of the control software to the actual ones.

### 5.7.3 Effective Area

Prior to calculating signal fluxes or flux upper limits, one has to know the effective area of the detector as a function of shower energy,  $A_{\text{eff}}(E)$  (see section 4.2.3). This function is calculated from simulations which generate a large number of showers with various energies and directions. The fraction of showers that results in a positive trigger defines  $A_{\text{eff}}(E)$  (see section 4.2.3). These showers are recorded in root files and are characterised, amongst others, by the source type which was used in the simulation: i.e.  $\gamma$ - or cosmic-ray source, or both. Moreover, Monte Carlo code can produce triggered events for a single H.E.S.S. telescope or the whole array (Phase

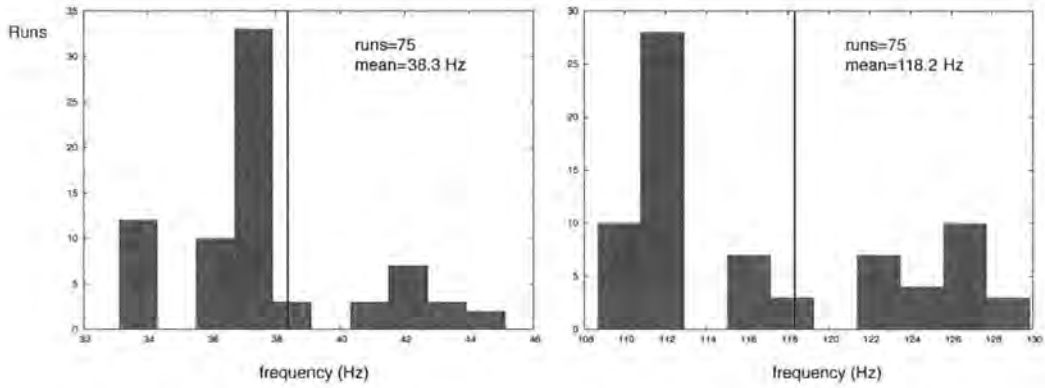


Figure 5.37: The resulting histograms from the 75 most probable frequencies, which were derived from application of the  $H$ -test to 75 flat-fielding runs. Two sets of flat-fielding data were examined: one, during which the device was operating at the preset frequency of 40 Hz, and the another, during which the preset frequency was 120 Hz. The resulting frequencies were binned in 10 frequency steps across the 32–46 Hz and 108–130 Hz ranges, respectively. One can clearly see that, in both cases, almost half of the runs are concentrated in a single bin, which is not however coincident with the preset frequency. In addition, the rest of the runs are almost uniformly distributed across the examined ranges. In both plots, the vertical, black line marks the position of the arithmetic mean, which was calculated from the sample of 75 frequencies.

I).

We used a H.E.S.S.-specific analysis package [384] that reads the Monte Carlo files that contain simulated  $\gamma$ -ray events. Each event is accompanied by an energy value and a set of Hillas parameters, so it is possible to apply cuts and calculate the effective area for the events that pass the cuts. Moreover, the files are categorised according to the Z.A. of the simulated source. In our case, we used the appropriate files, in order to match as closely as possible the Z.A.s — at culmination — of the three pulsars that we subsequently analysed: the closest Z.A.s available were those of  $50^\circ$ , which we used for the Crab pulsar and PSR B1259–63, and  $20^\circ$ , which we used for PSR B1706–44.

The software that we used divides the energy range of the simulated showers into a number of bins. For each bin, it calculates the fraction of the total showers, contained in the bin, that pass the cuts and produces a value for the effective area corresponding to this energy bin; this is done for a user-defined energy range. The resulting scatter plots should represent, within the stated errors, the  $A_{\text{eff}}(E)$  for a single telescope or the whole array. In our simulations, we aimed at reproducing the effective area for the low-energy cuts of Table 5.5, since those are the ones we used with real data. However, it was necessary to have an analytical expression for  $A_{\text{eff}}(E)$ , so that  $\gamma$ -ray fluxes or upper limits could be derived from Eq. 4.19, and energy thresholds could be defined from the maximum of the differential trigger rate. Therefore, we fitted the data points with up to fourth-order polynomial functions; the best fit was selected on the basis of the reduced  $\chi^2_{k-1}$  value, which was required to be as close to unity as possible, for the least deviations between the fit and the data points.

All the effective-area plots against energy, and the corresponding selected fits, are shown in Fig. 5.38. Each plot is the result of  $\sim 10^4$  simulated  $\gamma$  rays. For Z.A.= $20^\circ$  we fitted only single-telescope data, since that was the only available type of observation for PSR B1706–44 at the time.

#### 5.7.4 Energy versus Image Amplitude

The light content of a Cherenkov image is generally a function of shower energy, but it also depends on the *distance* parameter, which is an approximate measure of the distance between a shower's core location and the telescope. Mohanty *et al.* have investigated this dependency by simulating a large number of  $\gamma$ -ray showers whose *IA* and *distances* were fitted as a function of the shower energies [414]; the general

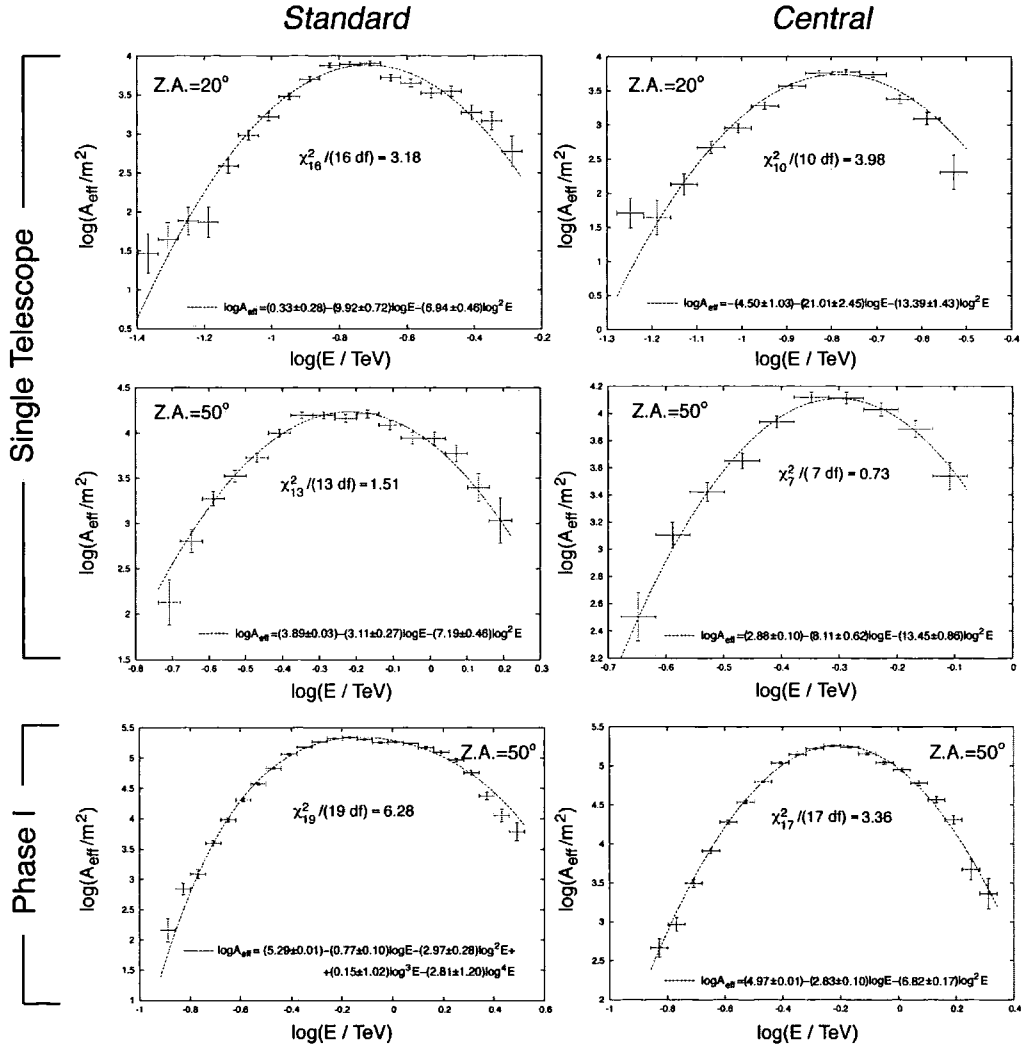


Figure 5.38: Effective area as a function of energy for single-telescope and stereo observations with the whole array (H.E.S.S. Phase I). Some  $10^4$  events were used for each plot. The left and right columns correspond to the effective areas after application of our low-energy cuts with 18 (standard) and 12.7 mrad (central) *distance* cuts, respectively (see also Table 5.5). The fits to the data provide an analytical function for flux calculations. The reduced  $\chi^2$  shown with each plot provides a measure for the goodness of the fit. The Monte Carlo files used were for Z.A.=50°, which corresponds to the Crab pulsar and PSR B1259–63 observations from the H.E.S.S. site, and Z.A.=20°, which corresponds to the Z.A. of PSR B1706–44 at culmination.

form of their polynomial fit was

$$\begin{aligned} \ln E = a_0 + a_1 \ln(IA) + a_2(\text{distance}) + a_3 \ln^2(IA) + \\ + a_4(\text{distance})^2 + a_5 \ln(IA) \cdot (\text{distance}) \end{aligned} \quad (5.119)$$

where  $a_{0-5}$  are the fit coefficients.

A similar approach would allow us to assign an energy range to our low-energy cuts and estimate the accuracy with which that can be done. Hence, we decided to analyse the same set of data as for the effective area and plot the Monte Carlo energy of the events as a function of  $IA$ . For this purpose, we used an analysis tool similar to the one for the effective area [384]. As before, the software applies a user-defined set of cuts to the data, which are then binned according to  $IA$ . The mean energy of all the events in each bin is then plotted together with its error value.

The available Monte Carlo files which were used for the  $E$ - $A_{\text{eff}}$  and  $E$ - $IA$  plots contained events with energies that were generated from a simulated source with a flat spectrum<sup>2</sup>, i.e. with  $\nu = 2$ . As will be seen in the following paragraph, we were interested in plotting  $E$ - $IA$  for different spectra. Instead of having to generate more Monte Carlo files for different  $\nu$ , it was possible — using the aforementioned analysis tool — to scale the energies of the existing events so that they correspond to the desired spectra: each event's energy was weighted accordingly using the formulation described below. It is worth noting that the effective-area calculations are not affected by the chosen spectra, since the former is defined as the ratio of positive triggers that pass the cuts over the total events per energy bin. Hence, the weights cancel out in this calculation.

In our calculations we decided to adopt a single power-law fit to the EGRET spectra for the Crab pulsar and PSR B1706–44 (see third column of Table 3.2). For PSR B1259–63 we do not have spectral information from EGRET observations, and therefore we arbitrarily assumed a spectral index equal to the median value of the 6 EGRET spectral indices (see Table 3.2): i.e.  $\nu = 1.76$ . Hence, we placed this pulsar's spectral slope in the middle of the available spectral-index distribution.

Considering the above arguments, the routine calculates the mean energy for each  $IA$  bin as follows: if  $E_{ij}$  are the Monte Carlo energies of the  $i$  events contained in each bin  $j$  — with the total events in the bin equal to  $N_j$  — and  $w_{ij}$  are the

---

<sup>2</sup>The characterisation as flat arises from the fact that the spectrum appears as a straight horizontal line when the quantity  $E^2(dN_\gamma/dE)$  is plotted against  $E$ .

corresponding weights for each event in that bin, then the weighted mean is given by

$$\langle E_j \rangle = \frac{\sum_{i=1}^{N_j} w_{ij} E_{ij}}{\sum_{i=1}^{N_j} w_{ij}} \quad (5.120)$$

where each event's energy is weighted by

$$w_{ij} = \frac{(E_{ij}/E_0)^{\nu'}}{(E_{ij}/E_0)^{\nu}} \quad (5.121)$$

In this expression,  $E_0$  is the normalisation energy of the differential power-law spectrum where the flux equals some value  $K$  (see Eq. 3.22). Since the mean energy in each bin is derived from a sample of  $N_j$  events, the error on the mean is the RMS spread of the sample divided by  $\sqrt{N_j}$ . This represents the  $1\text{-}\sigma$  confidence interval, which contains the true mean of the population. Hence,

$$\sigma_j = \frac{1}{N_j} \sqrt{\sum_i^{N_j} (E_{ij} - \langle E_j \rangle)^2} \quad (5.122)$$

Using these expressions with the chosen spectral indices for the three pulsars, we plotted the Monte Carlo energy as a function of  $IA$  and fitted a second order polynomial (see Fig. 5.39).

One obvious remark on the  $A_{\text{eff}}$  and  $IA$  plots is that the error bars in the stereo simulations are considerably smaller than those in the single-telescope ones: up to an order of magnitude. This can be explained in terms of the larger effective area of the stereo system, which allows for more triggered events,  $N_j$ , than the single telescope in the same energy range. Hence, since the statistical error is  $\sigma \propto \sqrt{N_j}/N_j$ , the determination of the mean energy or effective area is better defined for stereo systems.

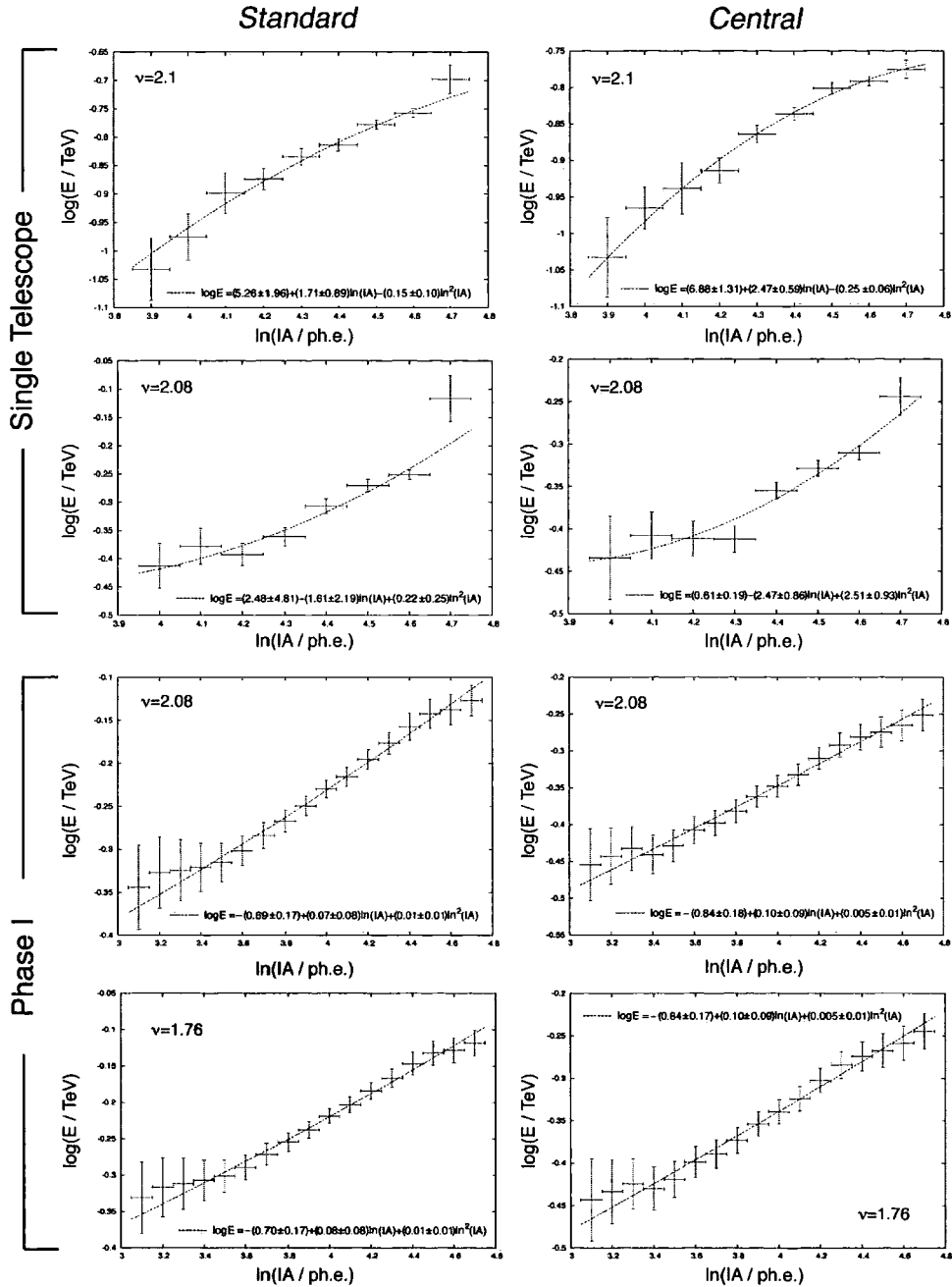


Figure 5.39: Monte Carlo energy as a function of *Image Amplitude* ( $IA$ ), derived from simulations of the Crab pulsar (assumed power-law index  $\nu = 2.08$ ), PSR B1706–44 ( $\nu = 2.1$ ) and PSR B1259–63 ( $\nu = 1.76$ ). The Crab data correspond to single-telescope and stereo (Phase I) simulations at  $50^\circ$  Z.A. For PSR B1706–44, single-telescope data at  $20^\circ$  Z.A. were used, and, finally, the PSR B1259–63 simulations correspond to Phase I observations at  $50^\circ$  Z.A. Only data that survived our low-energy cuts (see Table 5.5) were used in the above plots. The fits shown are second-order polynomials in  $IA$ .



## Chapter 6

# Observations and Results

### 6.1 Introduction

The current chapter presents the results that were obtained from the application of our low-energy cuts to data, which were collected with the H.E.S.S. telescopes from the directions of three pulsars: the Crab, PSR B1706–44 and PSR B1259–63. In contrast to the standard H.E.S.S. analysis, our low-energy analysis was largely based on the periodic nature of the signal rather than the nature of the events: i.e.  $\gamma$  rays or hadrons. As we have shown with simulations in the previous chapter, a periodic signal should stand out from a large background, given sufficient exposure time. This allowed us to lower the energy threshold of the data sets, but introduced a large background. Since, as was made clear earlier, the signal significance increases linearly with exposure time for a given pulse profile, we tried to maximise, in each case, the amount of data used in our analysis; and that, of course, required looser selection criteria than those used together with the standard cuts by the H.E.S.S. collaboration. However, we kept in mind that quantities like the trigger rate and the weather conditions are vital for a successful analysis. Runs with low trigger rates — possibly due to cloud formation in the overhead sky — were rejected, as these data are less likely to contain the desired low-energy events, which would be more susceptible to atmospheric attenuation than more luminous cosmic-ray events.

### 6.2 Pulsar Observations

In the period 2002–2005, H.E.S.S. collected data from 10 pulsars. The exposure times of the respective observations are shown in Table 6.1. The first three, the

Crab, Vela and PSR B1706–44, are the young  $\gamma$ -ray pulsars seen with EGRET, whereas PSR J0437–4715 and PSR J0737–3039A belong to binary systems. PSR B1259–63 has been extensively observed with H.E.S.S. during its periastron passage, which resulted in a detection of unpulsed emission that is thought to arise from the pulsar’s interaction with the companion star’s stellar wind. More about this pulsar is presented in section 6.3.3.

The last two pulsars on the list are of special interest: PSR J0437–4715 was discovered in 1992 during a southern sky survey for millisecond pulsars, and it is the closest known millisecond pulsar to date, at a distance of  $\approx 150$  pc [415]. It orbits a  $0.2-M_{\odot}$  helium white dwarf in a close circular orbit with a 5.7-d period. Its proximity makes PSR J0437–4715 a good candidate for a possible detection with H.E.S.S. As a supporting argument one can mention the Vela pulsar, which despite its average  $\gamma$ -ray efficiency, being the lowest amongst the high-energy pulsars (see Table 3.3), because of its short distance it is the brightest known  $\gamma$ -ray pulsar. Nevertheless, the high-energy  $\gamma$ -ray emission from PSR J0437–4715 has so far been only constrained by EGRET with upper limits [416]. On the other hand, the theoretical spectra predict that the pulsed emission from this object should be persistent up to a few tens of GeV [263]. H.E.S.S. is in a good position to investigate this case and find out whether the radiation extends to the experiment’s sensitivity range.

In addition, PSR J0737–3039A, which has been briefly observed with H.E.S.S., presents an interesting laboratory for studying high-energy phenomena. This pulsar is part of a highly relativistic, double neutron-star system (PSR J0737–3039A and B), which has been detected at radio frequencies [417]. The system demonstrates short eclipses between the neutron stars, which are accompanied by modulations on the flux and the pulse shapes. It is believed that the modulations are caused by the interaction of the eclipsed star’s radio emission with its companion’s magnetospheric plasma [418],[419]. The relative-to-us geometry of this system allows the observation of neutron star A through the light cylinder of neutron star B — which is naturally a much larger area than the star itself (see section 3.1.2). Therefore, it provides a unique opportunity to study the pulsar-emission properties before and during the eclipse, which could potentially unveil the magneto-ionic consistency of a pulsar’s magnetosphere.

In early 2005, H.E.S.S. extended the pulsar observations by investigating the young, rotation-powered PSR B1046–58, as well as by collecting additional data from PSR B1259–63 and PSR J0737–3039. PSR B1046–58 is a particularly in-

Pulsar	Total exposure time (h)		
	Single		Stereo (CTS)
	ON/OFF	wobble	
Crab	46.5	–	114
Vela	–	–	25.5
PSR B1706–44	19.5	44.5	4.5
PSR B1259–63	–	–	79
PSR B1046–58	–	–	1
PSR B1821–24	–	–	4
IC 443 (pulsar)	–	–	5.3
PSR J1638–4725	–	–	1
PSR J0437–4715	–	–	28.5
PSR J0737–3039A	0.5	–	5.5

Table 6.1: Distribution of exposure times amongst the various observation modes for the observed pulsars with H.E.S.S., in the period 2002–2005 [420].

interesting pulsar: it has a rotational period of 124 ms and a characteristic age of  $\log(\tau/y) = 4.3$ ; and given its distance of 3 kpc and its spin-down luminosity  $\dot{E} = 2.0 \times 10^{36}$  erg s<sup>-1</sup>, this pulsar is ranked 9<sup>th</sup> according to observability (see section 3.1). EGRET has detected  $\gamma$ -ray emission, above 100 MeV, from a source coincident with PSR B1046–58 (inside EGRET’s 95% C.L. contour), which was catalogued as the unidentified source 3EG J1048–5840 [14]. In the first analysis of the EGRET data, there were only reports for upper limits on the pulsed emission from 3EG J1048–5840 ( $F_{99\%}(> 100 \text{ MeV}) = 4.5 \times 10^{-7}$  cm<sup>2</sup> s<sup>-1</sup>), as well as a hint for pulsations above 1 GeV [421]. However, subsequent analysis presented arguments for a match between this source and PSR B1046–58 [422]. This analysis resulted in a marginal pulsed detection of 3–4  $\sigma$ , for energies  $> 400$  MeV, at the pulsar’s radio period. The inferred  $\gamma$ -ray flux was  $1.5 \times 10^{-4}$  MeV cm<sup>-2</sup> s<sup>-1</sup>, which implies a remarkable  $\gamma$ -ray conversion efficiency of 1.1%. This fact, together with the absence of an energy cut-off up to 10 GeV, makes this pulsar a good candidate for H.E.S.S.

H.E.S.S. also dedicated a few hours on the shell-type SNR IC 443 (G189.1+3.0): an SNR which is believed to host a supersonic pulsar [423]. The high velocity of the pulsar in this system causes the formation of a bow shock around it, which is the morphology expected when the pulsar catches up with the shock front ahead of it. The shape of the PWN can then be compared with the water ripples that form around a swan swimming across a lake; but the latter example is, of course, a 2-dimensional projection of the PWN’s shape.

The first indications that IC 443 may be powered by a pulsar came with *ASCA* observations, which showed that the bulk of the hard X-ray emission was being produced by a single, yet unresolved feature at the edge of the radio shell [424]. This X-ray source had a considerably harder spectrum than the rest of the SNR. Later on, Olbert *et al.* using *Chandra* observations showed that, if the X-ray point source (given the name CXOU J061705.3+222127) is assumed to be a young pulsar, the derived characteristics of the neutron star (i.e.  $\tau$ ,  $\dot{E}$ ,  $P$ ,  $B$ , etc.) support the hypothesis: the pulsar was born 30,000 y ago in a core-collapse supernova event and travelled ever since at a high velocity through the surrounding medium, forming a bow-shock PWN [423]. Based on the observed X-ray (and assuming a single power law across the soft and hard X-ray regime) the authors derived an X-ray luminosity which they connected with the pulsar's period and magnetic field (see Eq. 3.10). The values were close to those of other young pulsars. Also, the observability,  $\dot{E}/d^2$  was close to that of the EGRET  $\gamma$ -ray pulsars, insinuating that the nearby (yet outside the 95% confidence contour of EGRET) unidentified EGRET source 2EG J0618+2234 may be the one that powers IC 443.

The above results were recently confirmed by Gaensler *et al.*, who reprocessed the previous *Chandra* observations (2000 data) and also used further *Chandra* data from 2005 [425]. The data revealed a thermal X-ray component, directly produced from the compact source, which Gaensler *et al.* fitted with a blackbody spectrum; the resulting temperature was in agreement with that expected from a cooling 30,000-year-old neutron star.

Despite the aforementioned evidence, no pulsations have been detected either in radio or X-rays from the direction of IC 443. Nevertheless, this has been argued not to be an obstacle, since the pulsed emission could be obscured by the surrounding nebular emission (as in the case of Vela-like pulsars) [426]; or, indeed, the alignment is such that the pulsar beam does not intersect our line of sight [427]. In any case, the X-ray — and possibly HE  $\gamma$ -ray — source in IC 443 was worth investigating at VHE with H.E.S.S.

PSR B1821–24 was the first millisecond pulsar to have been found in a globular cluster: the M 28 [428]. It is the youngest millisecond pulsar known ( $\tau = 3 \times 10^7$  y) and the second brightest X-ray pulsar ( $\dot{E} = 2.2 \times 10^{36}$  erg s<sup>-1</sup>) whose emission arises from non-thermal processes in the outer magnetosphere — as opposed to thermal cooling of the surface [429],[430]. The hard X-ray spectrum of PSR B1821–24 has been detected with *RXTE* up to 20 keV [431]; and the equally hard spectral index

( $\nu = 1.13$  in 0.8–20 keV) — uncommon amongst the X-ray pulsars; exceptions are the Crab, PSR B0540–69 and PSR B1509–58 — reveals magnetospheric activity which could extend the emission to the  $\gamma$ -ray regime. However, *CGRO* has only reported upper limits from soft and hard  $\gamma$ -ray observations of this pulsar [432],[416]. Nevertheless, H.E.S.S., being a vastly more sensitive instrument than EGRET (see Fig. 5.9), will try to investigate whether this pulsar is capable of producing detectable VHE emission.

Finally, another candidate for VHE emission is the massive binary system involving the 764-ms pulsar PSR J1638–4725 and a  $20-M_{\odot}$  stellar companion [433]. This system is in many ways similar to the unique, so far, PSR B1259–63/SS 2883: the high-mass companion is likely to be a Be star, and it has a very long and eccentric orbit, with eccentricity  $e \approx 0.94$  and orbital period  $P = 5.3$  y. Moreover, PSR J1638–4725 exhibits radio eclipses around periastron (the most recent one occurred on 30 April 2005), which could be an indication of intense interaction between the pulsar wind and the stellar photosphere. And, thus, TeV emission produced in the same way as the one detected for PSR B1259–63/SS 2883 is plausible (see section 6.3.3).

Even more intriguing is the fact that the close proximity between the Be star and the pulsar around periastron may trigger an accretion phase of stellar material into the pulsar’s magnetosphere; it is believed that this phase is followed by thermal X-ray emission. If such scenario is proven to be true, then it will be the first time that a binary system is found, in which a pulsar transits from an accretion phase to rotation-powered radio emission and vice versa.

## 6.3 Three Pulsars Under the Microscope: Periodic Analysis and Upper Limits

### 6.3.1 The Crab Pulsar: Standard Candle?

The Crab pulsar has been in the centre of VHE observations since the early days of ground-based  $\gamma$ -ray astronomy. In 1972, Grindlay reported the results from 47 h of Crab observations with the Whipple telescope on Mt. Hopkins [94]. He used phasogram analysis to bin the events, and looked at the excess in the bins which were contemporaneous with radio data. An excess of  $3.5 \sigma$  for the main peak and  $5.5 \sigma$  for the second peak was found. The derived integral flux above 680 GeV

was  $1.25 \times 10^{-11} \text{ cm}^{-2} \text{ s}^{-1}$ . Ten years later, between 1982–1983, Dowthwaite *et al.* collected 103 h of Crab data with the Durham Mark 1 and 2 telescopes in Dugway [93]. Some  $1.5 \times 10^4$  events were binned using a contemporaneous MIT ephemeris and the resulting phasogram showed an excess of  $4 \sigma$ , at the main-peak position. In addition, an independent analysis of the same data set took place, which involved the temporal spread of the Cherenkov arrival times. This analysis showed that the events which were coincident with the main peak were more consistent with the source direction than those at other phases. This additional correlation decreased the probability of accepting  $H_0$  to  $6 \times 10^{-7}$ . The deduced time-averaged flux over the whole data set of 1982–1983 was  $F(> 1 \text{ TeV}) = (7.9 \pm 1.8) \times 10^{-12} \text{ cm}^{-2} \text{ s}^{-1}$ . Finally, the Tata Institute with their Pachmarhi Array of Cherenkov telescopes have also observed the Crab pulsar in the period 1992–1993 [434]: they reported a chance probability of  $3 \times 10^{-9}$  for the observed lightcurve, which showed emission at the position of the main and second peak, as well as the interpulse region in between.

Those pre-imaging experiments produced positive results that could potentially extend the Crab pulsar’s reputation as a standard candle to the VHE regime. However, more recent attempts with much more sensitive instruments have failed to reproduce any of the previous detections: H.E.G.R.A. observed this pulsar in the period 1996–1998, during which the total amount of Crab data collected was  $\approx 83$  h [289]. The observations were performed in stereo ON/OFF and wobble modes and the energy threshold of the data set was 1 TeV. No detectable pulsed emission was found in the data and the upper limits on the flux were derived using the Helene method as a percentage of the DC flux. Assuming only a main peak with 10% duty cycle the authors reported a  $3\text{-}\sigma$  ( $\sim 99.9\%$ ) upper limit equal to 3.3% of the DC flux above 1 TeV; and below 1 TeV the corresponding upper limit was 5.7%. Moreover, the Whipple 10-m Cherenkov detector, which had observed the Crab pulsar in 1994–1997, also did not find evidence of periodic emission [95]. They collected 73.4 h of data, which they binned into 25 phase steps per period. Application of a  $\chi^2$ -test to the folded data resulted in values consistent with uniformity. The upper limits on the flux were derived with the method of Helene, assuming two peak areas coincident with the EGRET profile. Above 250 GeV, which represents the data set with the least energetic events detectable with this experiment, the 99.9% integral flux upper limit was  $4.8 \times 10^{-12} \text{ cm}^{-2} \text{ s}^{-1}$ .

In addition, a very useful upper limit was calculated from 14 h of Crab observations with the CELESTE experiment [435]. The large collection area of this

solar-array experiment allowed the energy threshold to be lowered to 60 GeV, after the application of cuts. The data were searched for a periodic signal using the  $H$ -test and binning the events into 10-bin phasograms. No significant excess was observed in the bins that were contemporaneous with the main and secondary optical peaks; this was also verified with the  $H$ -test, which yielded  $H = 2.6$  [ $pr(> 2.6|H_0) \approx 0.35$ ]. Using the Helene method, an upper limit on the pulsed flux equal to  $F_{ul}(> 60 \pm 20 \text{ GeV}) = 7.5 \times 10^{-11} \text{ cm}^{-2} \text{ s}^{-1}$  was derived.

Finally, the MAGIC collaboration performed a sensitive, low-energy periodicity search on 10.5 h of Crab data collected between September and November 2004 [257]. Despite using a conservative trigger method in their data-taking — which resulted in higher energy thresholds and less sensitive  $\gamma$ /hadron discrimination — the estimated energy thresholds were the lowest reported from observations of the Crab pulsar with imaging Air Cherenkov experiments. After applying various periodicity tests, the results were consistent with uniformity, and upper limits above 90 and 150 GeV were derived using the  $H$ -test: these were equal to 2 and  $1.1 \times 10^{-10} \text{ cm}^{-2} \text{ s}^{-1}$ , respectively. In addition, their analysis set an upper limit to an assumed exponential cut-off in the Crab pulsar's spectrum above the EGRET range: the highest cut-off consistent with the derived upper limits was at 60 GeV.

A graphical comparison of all the above upper limits with the predicted model spectra has been given in Fig. 3.15.

### Independent H.E.S.S. Analysis

As mentioned earlier, H.E.S.S. collected a total of 143.5 h of data from the Crab in the period 2002–2004. A small fraction of these data, amounting to 4 h exposure time, was selected by the collaboration for periodic analysis [436]. All runs were recorded with the 3, available at the time, H.E.S.S. telescopes operating with a central trigger criterion. This analysis was performed on the events passing the H.E.S.S. standard cuts and, hence, was not optimised for the least energetic events. The generated phasograms from the folded events did not show any significant excess from the background, at the expected phase regions of the Crab pulsar's lightcurve [289]. Following the non-detection, upper limits on the integral flux were derived using Helene's method, with the peak area matching the double-peaked feature seen with EGRET. Table 6.2 shows the resulting upper limit values for two energy thresholds.

Crab pulsar		
	Exposure time	4 h
	Configuration	3 telescopes (CTS)
	Phase regions (peak area)	$[0.94, 0.04] \cup [0.32, 0.43]$
	$F_{\text{ul}}(> 560 \text{ GeV})$	$6.30 \times 10^{-12} \text{ cm}^{-2} \text{ s}^{-1}$
	$F_{\text{ul}}(> 1 \text{ TeV})$	$2.79 \times 10^{-12} \text{ cm}^{-2} \text{ s}^{-1}$

Table 6.2: (from [436]) The upper limits on the Crab pulsar’s integral flux above 560 GeV and 1 TeV from the Helene method. The calculations were based on a 4-h data set containing events that passed the cuts of the standard H.E.S.S. analysis. The phase regions where the pulsed emission is expected to occur are shown in square brackets.

### Low-Energy Analysis

Our Crab pulsar data consisted of 31 ON/OFF pairs from single-telescope observations, 1 wobble run from a 2-telescope stereo observation, and 9 wobble runs from 3-telescope stereo observations. The function of the CTS in stereo observations is likely to reject the least energetic events that cannot trigger more than one telescope. On the other hand, we expect the single-telescope runs to contain a larger fraction of those events. Hence, we decided to analyse the stereo runs separately from the single-telescope ones, in order to retain a pulsed fraction as large as possible in the data.

The total exposure time of the single-telescope set of runs was roughly 13 h and was collected from October 2002 ( $\approx 8.7 \times 10^7$  seconds since J2000) to January 2003 ( $\approx 9.5 \times 10^7$  seconds since J2000). The visibility plot of Crab for 2003 is shown in Fig. 6.1, where one can see that the Z.A. of observation was mainly between  $60^\circ$  and  $45^\circ$ . We applied our standard and central sets of low-energy cuts to the data set, which reduced the number of triggered events to  $\sim 7 \times 10^5$ . The remaining events were folded into phases using the Jodrell Bank monthly ephemeris, which provided valid values for the pulsar’s frequency and its derivatives for the whole set of runs. The uncertainty on the frequency values during each run, as given by Eq. 5.11, was consistently  $\leq 10^{-9}$  Hz, which is roughly 4 orders of magnitude smaller than the IFS for this data set. Hence, there was no need for a scan over more than one frequency. The ephemeris values used in the event folding of the TDB arrival times are shown in Fig. 6.3.

Having folded the data, we proceeded with the application of the four uniformity tests described earlier. A reduced  $\chi^2$  value was calculated after binning the phases



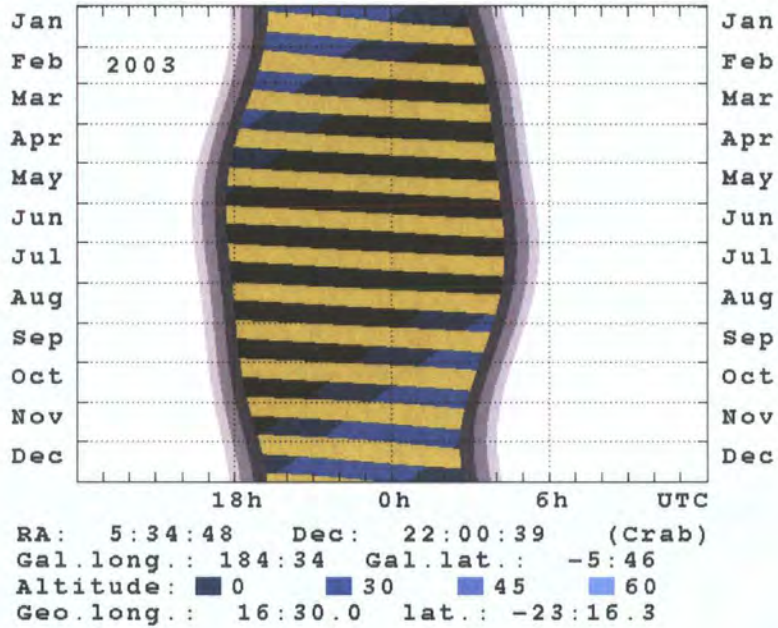


Figure 6.1: (from [325]) Visibility of the Crab nebula from the H.E.S.S. site in Namibia for 2003. The dates on the horizontal axis are given in UTC, starting at midnight. The white area around the coloured zones corresponds to sunlight, and the grey zones, to the various twilight definitions. The yellow bands across the coloured zones correspond to moonshine. The graduated blue colours correspond to the time periods when the Crab is above the given altitudes, as seen from Namibia. Finally, in the black area the object is below the horizon and, therefore, invisible. Our data were collected in the period from October 2002 to January 2003. The availability of the Crab in complete darkness and between  $60^\circ$  and  $45^\circ$  Z.A. for that period amounted to  $\approx 260$  h.

$t_0$ (seconds since J2000)	$f_0$ (Hz)	$\dot{f}_0$ (Hz s $^{-1}$ )	$\ddot{f}_0$ (Hz s $^{-2}$ )
8.791229019730e + 07	2.981324204859e + 01	-3.737779890888e - 10	3.760e - 20
9.076369039927e + 07	2.981217633077e + 01	-3.737610035258e - 10	-7.190e - 21
9.326935283174e + 07	2.981123985638e + 01	-3.737349983913e - 10	2.910e - 21
9.603407669784e + 07	2.981020663434e + 01	-3.736969891796e - 10	2.270e - 20
9.853949521970e + 07	2.980927040195e + 01	-3.736609940663e - 10	2.010e - 20
1.011312460713e + 08	2.980830199280e + 01	-3.736299988578e - 10	2.480e - 20
1.038093935529e + 08	2.980730136649e + 01	-3.736140044595e - 10	2.160e - 20
1.064012186531e + 08	2.980633305761e + 01	-3.735900064067e - 10	1.680e - 20
1.089931555990e + 08	2.980536478067e + 01	-3.735570067108e - 10	1.510e - 20
1.115852186882e + 08	2.980439651342e + 01	-3.735370100671e - 10	2.640e - 20
1.143502065903e + 08	2.980336376860e + 01	-3.734999985920e - 10	-7.280e - 21
1.169424502208e + 08	2.980239558512e + 01	-3.734839997635e - 10	4.710e - 21
1.196211042779e + 08	2.980139522676e + 01	-3.734389988378e - 10	3.820e - 21
1.222996903322e + 08	2.980039496992e + 01	-3.734139942144e - 10	1.180e - 20
1.248053539068e + 08	2.979945935180e + 01	-3.733799862085e - 10	2.490e - 20
1.274836835112e + 08	2.979845934181e + 01	-3.733639885892e - 10	2.360e - 20
1.301618906984e + 08	2.979745944462e + 01	-3.733339952908e - 10	1.620e - 20
1.330992064217e + 08	2.979636622974e + 01	-3.747929959617e - 10	6.290e - 19
1.354317893286e + 08	2.979549325001e + 01	-3.738790530924e - 10	2.520e - 19
1.380236168093e + 08	2.979452480279e + 01	-3.735380179343e - 10	4.680e - 20
1.406155568093e + 08	2.979355675696e + 01	-3.734420115232e - 10	2.600e - 20
1.432940272307e + 08	2.979255656250e + 01	-3.733970029822e - 10	8.000e - 21
1.459726133507e + 08	2.979155643223e + 01	-3.733590056751e - 10	3.040e - 20
1.489969005548e + 08	2.979042744526e + 01	-3.733319928130e - 10	7.150e - 20
1.512435110980e + 08	2.978958877152e + 01	-3.732949969234e - 10	9.890e - 21

Table 6.3: (from [357]) The Crab pulsar ephemeris values that were used in our analysis. These values correspond to the pulsar parameters at the SSB and were directly used with the event folding of our TDB timestamps.

Single telescope							
	$\chi^2_{19}/(19 \text{ df})$	Rayleigh	$H$ -test	$C_m$ test			
				main peak		second peak	
<b>Standard</b>	0.6417 (0.12)	0.03 (0.96)	0.06 (0.97)	$C_5$	$S_5$	$C_5$	$S_5$
				-0.24	-1.11	0.19	0.62
				main peak		second peak	
<b>Central</b>	1.009 (0.44)	0.41 (0.66)	0.82 (0.71)	$C_5$	$S_5$	$C_5$	$S_5$
				-0.48	-0.75	-0.63	1.2
Phase I							
	$\chi^2_{19}/(19 \text{ df})$	Rayleigh	$H$ -test	$C_m$ test			
				main peak		second peak	
<b>Standard</b>	1.43 (0.098)	1.52 (0.21)	3.04 (0.29)	$C_5$	$S_5$	$C_5$	$S_5$
				0.5	0.55	-0.48	0.51
				main peak		second peak	
<b>Central</b>	1.13 (0.30)	1.72 (0.17)	3.45 (0.25)	$C_5$	$S_5$	$C_5$	$S_5$
				1.86	-0.04	-1.10	-0.39

Table 6.4: The results from the application of four uniformity tests to Crab data. The tests were applied to events passing our two sets of low-energy cuts (see Table 5.5). For the  $\chi^2$ -test, the values shown are the reduced  $\chi^2$  with 19 df (Eq. 5.48). In the Rayleigh test column, the values are the Rayleigh powers for each data set. The  $H$ -test values were calculated from Eq. 5.87. For those three tests, we have included in parentheses the corresponding probability of accepting  $H_0$ . Finally, the  $C_5$  and  $S_5$  values, under the  $C_m$  test, are the sums of the cosine and sine trigonometric moments up to the fifth harmonic, respectively.

in 20 bins per period. The phasograms for both standard and central cuts are shown in Fig. 6.2, where we have also highlighted the EGRET profile's peak regions. The application of the  $C_m$  test required a central phase for the calculation of the trigonometric moments from equations 5.92 and 5.93: we chose  $\mu = 0$  and  $\mu = 0.38$ , which correspond to the two peaks of the EGRET profile. Furthermore, because each of the profile's peaks has  $\delta \approx 0.1$ , the selected number of harmonics according to Eq. 5.94 was set to  $m^* = 5$ . The resulting values from this test as well as from all the rest are shown in Table 6.4.

Furthermore, we analysed  $\approx 4.5$  h of stereoscopic data. The data were collected from October 2003 ( $\approx 1.2 \times 10^8$  seconds since J2000) to November 2003 ( $\approx 1.209 \times 10^8$  seconds since J2000). After the application of our cuts, the data were reduced to  $\sim 10^6$  events, which we folded into phases using the values of Table 6.3. The resulting

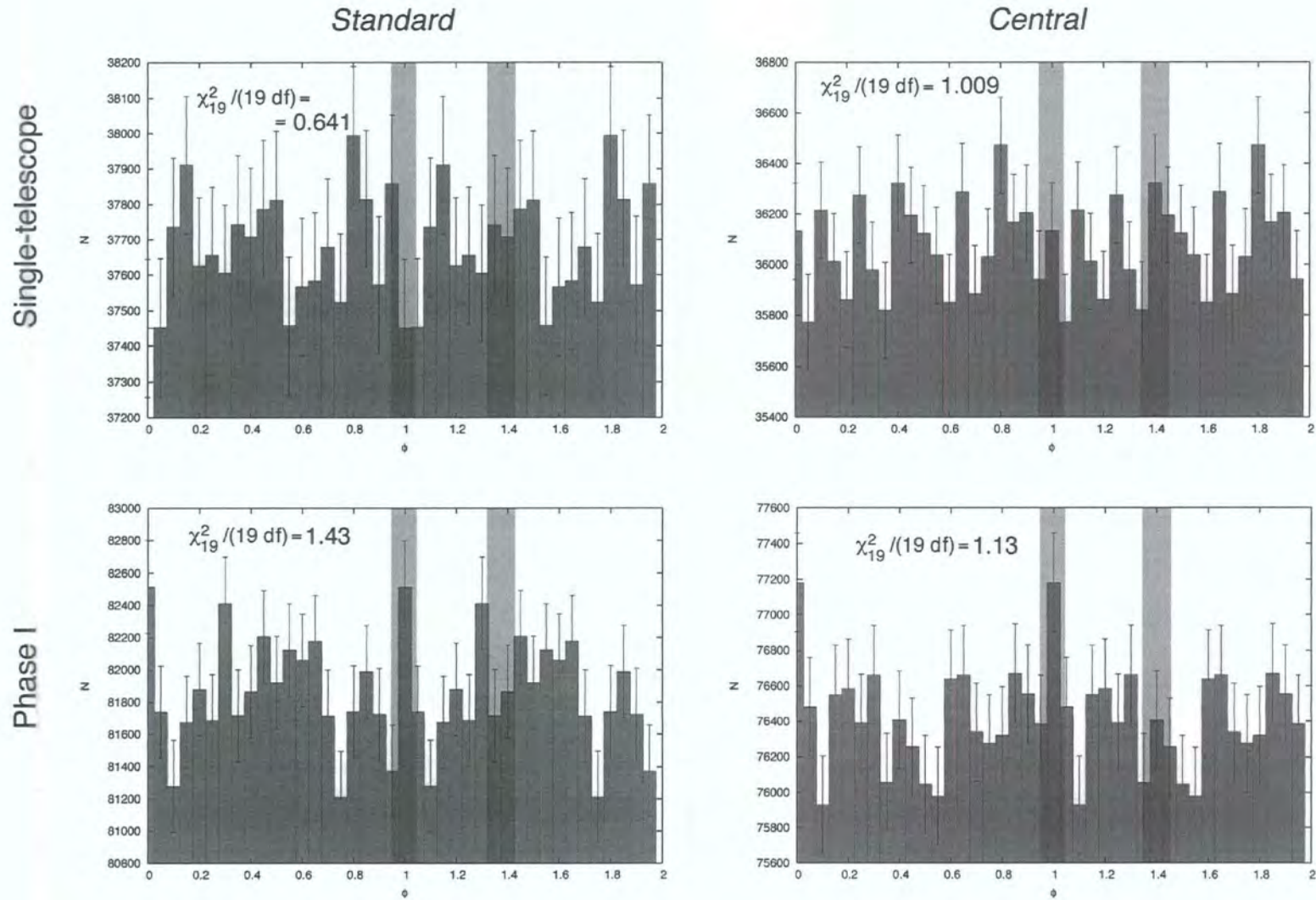


Figure 6.2: The phasograms of the folded events from the Crab that passed the standard and central low-energy cuts. The data were divided into single-telescope and stereo (Phase I) observations. The reduced  $\chi^2$  values show consistency with  $H_0$ , and moreover the phase ranges where EGRET observed pulsed emission (highlighted with light grey bands) do not show significant excess from the average.

phasograms are shown in Fig. 6.2. As in the single-telescope case, the errors on the frequency values for each telescope run were more than 4 orders of magnitude smaller than one IFS for the particular data set, so one can have confidence in the frequency values used in folding each event.

The event excess in the expected phase regions was not significant, as the phasograms show. This fact was also verified with the more sensitive tests for uniformity, which were run with the same parameters as in the single-telescope case. The resulting values from each test, accompanied by the probability of accepting  $H_0$ , are shown in Table 6.4. Although the probability values are consistent with the absence of pulsed emission in the data, one interesting remark can be made regarding the sensitivity of the  $C_m$  test in relation to well-localised peaks: despite its insignificant excess, the bin that is coincident with the main peak in the stereo data after the central cuts was still detected with  $\approx 2\text{-}\sigma$  significance by this test.

### 6.3.2 PSR B1706–44: A Young, Promising Candidate

As opposed to the Crab pulsar, the VHE radiation from PSR B1706–44 has been studied by only a few experiments, none of which reported a detection of pulsed emission. Amongst the southern experiments that had the opportunity to observe this pulsar is Durham’s Mark 6, which published a  $3\text{-}\sigma$  UL above 300 GeV, equal to  $4 \times 10^{-11} \text{ cm}^{-2} \text{ s}^{-1}$ , from  $\approx 9$  h of data [34]. CANGAROO has also observed PSR B1706–44 above 1 TeV, and the derived total integral flux was  $8 \times 10^{-12} \text{ cm}^{-2} \text{ s}^{-1}$ , which was however estimated to be mostly, if not entirely, steady.

#### Independent H.E.S.S. Analysis

H.E.S.S. is in a privileged geographic latitude with respect to the celestial position of PSR B1706–44. In 2003, this pulsar was available — during darkness — for observations from the H.E.S.S. site, for an equivalent exposure of  $\approx 270$  h, during which it was constantly below  $30^\circ$  Z.A. (see Fig. 6.3). 14.3 h of PSR B1706–44 data, collected from April to July 2003, were used by the collaboration for an independent-to-ours pulsed analysis [436],[92]. The energy threshold of the data set, after passing the standard set of H.E.S.S. cuts, was 500 GeV. In that data set, there was no evidence of pulsed emission, and an integral flux upper limit was derived at the 99.9% C.L using the method of Helene; its value was  $F_{\text{ul}}(> 500 \text{ GeV}) = 1.38 \times 10^{-12} \text{ cm}^{-2} \text{ s}^{-1}$ . Table 6.5 shows the results from this independent analysis, where it was

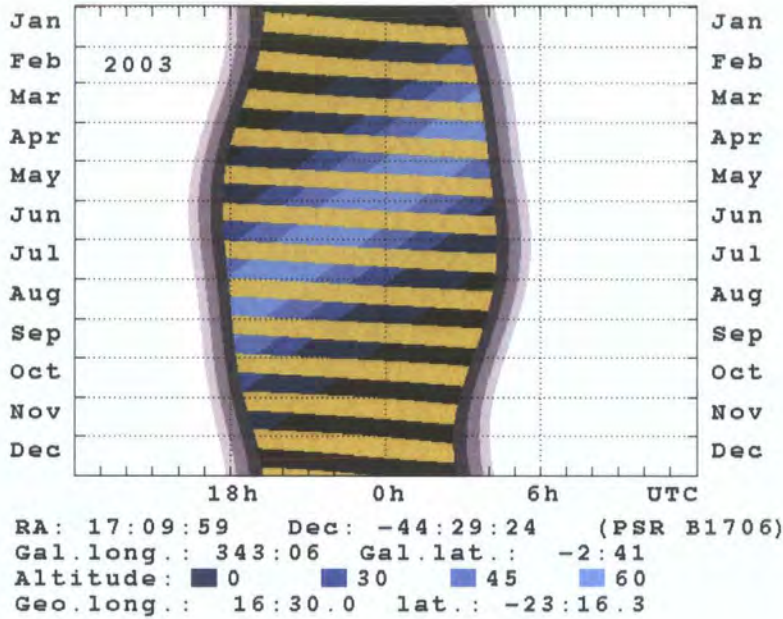


Figure 6.3: (from [325]) Visibility plot for PSR B1706–44 during 2003. From April to July 2003, H.E.S.S. collected  $\approx 65$  out of the available 230 h of data, during which period the pulsar was constantly below  $30^\circ$  Z.A.

assumed that the pulsed emission occurs in the same phase range as in EGRET data.

### Low-Energy Analysis

For the purpose of potential signal detection, we opted for the maximum available data set that satisfied some basic criteria: good weather conditions and a reasonably high trigger rate. For the latter we chose only runs with  $R_{\text{pre-cut}} > 150$  Hz, while the weather conditions were checked through the observation log that is available with each run; also, runs that were interrupted due to sunrise/moonrise were avoided. A set of 62 runs from the April–July 2003 period, which was equivalent to 28 h exposure time, was selected for our analysis. All data were taken with a single telescope operating in wobble mode.

The event folding was done using a GRO ephemeris from the Australian Pulsar Timing Archive [381]. Our data range covered the Modified Julian Dates from 52759 to 52823, which was inside the validity range of the GRO ephemeris line (i.e. 52659–

<b>PSR B1706–44</b>	
Exposure time	14.3 h
Configuration	Single telescope
Phase regions (peak area)	[0.25,0.55]
$F_{ul}(> 500 \text{ GeV})$	$1.38 \times 10^{-12} \text{ cm}^{-2} \text{ s}^{-1}$
$F_{ul}(> 1 \text{ TeV})$	$0.49 \times 10^{-12} \text{ cm}^{-2} \text{ s}^{-1}$

Table 6.5: (from [436]) The upper limits on PSR B1706–44’s integral flux above 500 GeV and 1 TeV, from the Helene method. The calculations were based on 14.3 h of single-telescope observations that contained events which passed the cuts of the standard H.E.S.S. analysis. The phase region where pulsed emission was seen with EGRET is shown in square brackets.

$t_0$ (seconds since J2000)	$f_0$ (Hz)	$\dot{f}_0$ (Hz s <sup>-1</sup> )	$\ddot{f}_0$ (Hz s <sup>-2</sup> )
1.061428817270e + 08	9.757929340737	-8.888919494204e - 12	1.05000e - 21

Table 6.6: (from [381]) The PSR B1706–44 ephemeris values that were used in our analysis. These values correspond to the pulsar parameters at the SSB and were directly used with the event folding of our TDB timestamps.

52887). The ephemeris values used in our analysis are shown in Table 6.6. The calculated uncertainty on the frequency was  $< 10^{-10}$  Hz throughout the whole data set, which is negligible compared to 1 IFS ( $\sim 10^{-5}$  Hz), and therefore no scanning in frequency was necessary. Table 6.7 shows how the 62 analysed runs were distributed in the observation period in which they were recorded: three batches containing a roughly equal number of runs can be distinguished.

After folding the arrival times of the events that passed the low-energy cuts into phases, we constructed the phasograms of Fig. 6.4. The resulting phasograms

Period (MJD)	No. of Runs	GRO Ephemeris	
		Validity range (MJD)	TDB epoch ( $t_0$ MJD)
52759–52772	19	52659–52887	52773.000000195
52782–52792	21		
52809–52823	22		

Table 6.7: This table shows how the 62 PSR B1706–44 runs were distributed across the observation period from 52759 to 52823 MJD: there is a clear grouping of roughly equal amount of data in three periods (columns 1 and 2). The last column shows the validity period and the TDB epoch that corresponds to the frequency values of the GRO ephemeris that were used together with these data.

	$\chi^2_{19}/(19 \text{ df})$	Rayleigh	$Z_2^2$	$H$ -test	$C_m$ test	
					$C_1$	$S_1$
<b>Standard</b>	1.842 (0.014)	0.79 (0.45)	6.7 (0.0012)	15.5 (0.0086)	0.47	1.16
<b>Central</b>	1.824 (0.015)	1.8 (0.16)	2 (0.13)	9.2 (0.091)	0.16	1.88

Table 6.8: The results from the application of five tests for uniformity to PSR B1706–44 data. The tests were applied to events passing our two sets of low-energy cuts (see Table 5.5). For the  $\chi^2$ -test, the values shown are the reduced  $\chi^2$  with 19 df (Eq. 5.48). In the Rayleigh-test column, the values are the Rayleigh powers for each data set. The  $Z_2^2$  statistic was calculated from Eq. 5.64, using  $m = 2$  harmonics. The  $H$ -test values were calculated from Eq. 5.87. For those four tests, we have included in parentheses the corresponding probability of accepting  $H_0$ . Finally, the  $C_1$  and  $S_1$  values under the  $C_m$  test are the sums of the cosine and sine trigonometric moments for the first harmonic, respectively.

from both standard and central cuts appear to fluctuate, in places, by  $\approx 4$  standard deviations, although the  $\chi^2$  values reject  $H_0$  only to a  $\approx 2\text{-}\sigma$  level. However, the latter depends on the sensitivity of the  $\chi^2$ -test, which is known to become low for wide profiles like the one expected for this pulsar. In addition, the fluctuations are not suggestive of a peak confined inside the EGRET peak area in GeV energies: i.e. inside the phase range  $\phi = 0.25\text{--}0.55$  [24]. In order to investigate the origin of these fluctuations, we applied the rest of the uniformity tests to the data: for the  $C_m$  test, specifically, we summed up the cosine and sine moments of the first harmonic only, which is the optimal choice for PSR B1706–44’s EGRET profile, since  $\delta = 0.3$ ; also, all phases were centred on  $\phi = 0.4$ . Our results are summarised in Table 6.8.

The resulting probabilities from the tests do not justify the rejection of  $H_0$ . The only notable values are those from the  $H$ -test, which assigned a significance of  $2.5 \sigma$  to the fluctuations, and the one from the  $Z_2^2$  test, which produced a  $3\text{-}\sigma$  significance. However, neither of these values are conclusive, especially since the rest of the probabilities are not significantly low.

### 6.3.3 PSR B1259–63: SS 2883’s Closest Companion

PSR B1259–63 is a  $\sim 48$ -ms radio pulsar revolving around a giant B2e star catalogued as SS 2883. Its orbit is considered highly eccentric ( $e = 0.87$ ), and as a result the pulsar reaches a distance of  $26R_\star$  ( $\sim 10^{26}$  cm) from its giant companion at periastron. Furthermore, the orbit is relatively long, with a period of  $\approx 3.4$  y. For VHE  $\gamma$ -ray astronomy, the interesting part of the orbit occurs at periastron,



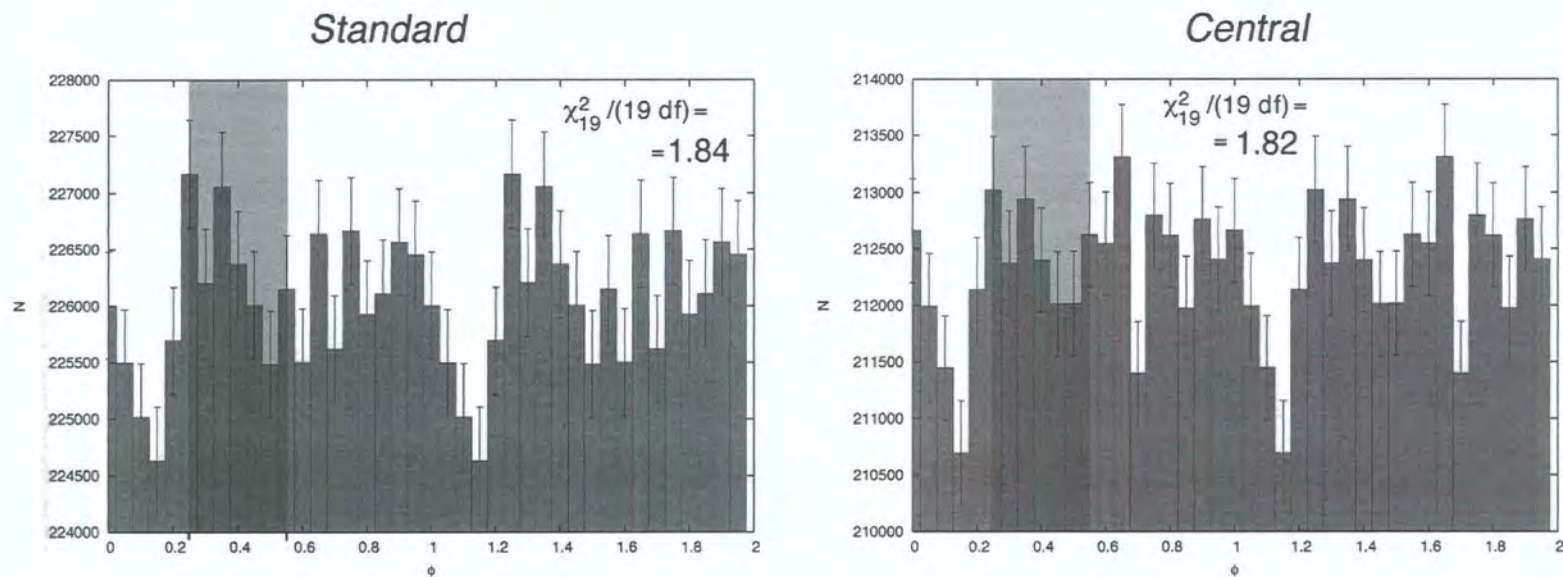


Figure 6.4: The phasograms of the folded events that passed our low-energy cuts (standard and central) from 28 h of PSR B1706–44 observations. The events were collected with single-telescope observations.

where the pulsar wind interacts with the intense photon field of the companion star's photosphere. Theoretical support for the high-energy interaction in this system has been given by a number of authors [437],[438],[439],[440]. The prediction of  $\gamma$ -ray lightcurves modulated with the system's period of revolution was the motivation for VHE experiments to try and detect such emission. However, the large southern declination of this system has not allowed northern observatories to study this pulsar. On the other hand, H.E.S.S. and CANGAROO are situated in appropriate locations that allow the observation of this source at  $40^\circ$  and  $32^\circ$  Z.A.s, respectively, during culmination.

H.E.S.S. observed the PSR B1259–63/SS 2883 system in early 2004, during the pulsar's periastron passage, when the  $\gamma$ -ray flux was expected to reach its peak value. This was a unique opportunity for H.E.S.S.: the system returns to this position only every 3.4 y, and, moreover, periastron observations with Cherenkov detectors are only possible every 6.8 y due to the Sun's relative position with respect to PSR B1259–63/SS 2883. Previous periastron passages have been studied with radio, optical and X-ray experiments [441],[442],[443],[444],[118]. From the H.E.S.S. site, PSR B1259–63/SS 2883 was visible at a Z.A. below  $45^\circ$  from January to July 2004; during that period the source was in darkness and available for observations below that angle, for a total of 300 h. Nevertheless, the total collected amount of data from this source that passed the quality criteria was 75 h. Fig. 6.5 shows graphically the available observation time below a specific Z.A., during which PSR B1259–63 was in darkness, as viewed from the H.E.S.S. site.

Fig. 6.6 shows the positions of PSR B1259–63 along its orbit, at the dates when H.E.S.S. observed the system. From a data set of a total of 50 h exposure time, the resulting signal significance was  $13.8 \sigma$  and the measured integral flux above 380 GeV was  $4 \times 10^{-12} \text{ cm}^{-2} \text{ s}^{-1}$  [117]. The measured flux from the individual observations of the data set is also shown in this figure: it can be seen that at the end of the March data set the integral flux reaches its maximum observed value of  $\sim 10^{-11} \text{ cm}^{-2} \text{ s}^{-1}$  above 380 GeV.

The predicted VHE emission from this binary system arises from inverse Compton upscattering of the low-energy photons of the B2e star by the relativistic electrons and positrons of the pulsar's wind. The latter are isotropised and accelerated in the termination shock of the wind, where the B2e star's particle outflow balances the pressure of the pulsar wind particle outflow. Type B2e stars are known to have anisotropic stellar winds, forming a thick disc around the star. In the case of the

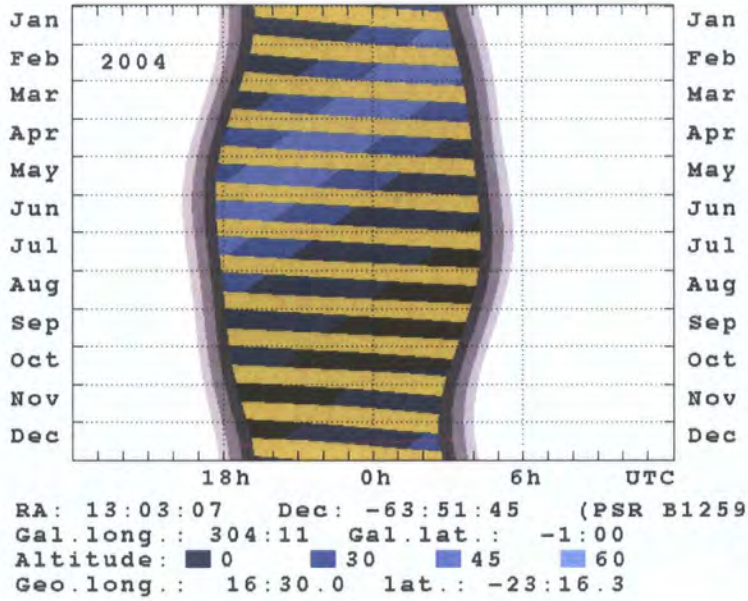


Figure 6.5: (from [325]) Visibility plot for the PSR B1259–63/SS 2883 system during 2004. It can be seen that from January to July, the source was available for observations from the H.E.S.S. site at a Z.A. below  $45^\circ$ . H.E.S.S. collected a total of 75 h of data during that period. In February, the pulsar was at the periastron position.

PSR B1259–63/SS 2883 system, the pulsar crosses the stellar-wind disc, through which most of the star’s mass outflow takes place, twice per revolution. At that time, synchrotron-emitting particles are accelerated as they cross the shock front and interact subsequently with the low-energy photons of the star. The observations with H.E.S.S. near periastron revealed the increased GeV–TeV flux at the predicted orbital positions, which is consistent with the above scenario.

### Low-energy Analysis

From all the above, it becomes evident that the  $\gamma$ -ray flux that was detected with H.E.S.S. is modulated with the orbital period, and that it can be considered steady over the time-scales of the pulsar’s period. In the context of our analysis, we were only interested in the periodic emission from the pulsar itself, which should, of course, if there, be persistent during the whole orbit. Previous observations of PSR B1259–63 have revealed pulsed emission only in radio frequencies [445]. Never-

theless, the wealth of available H.E.S.S. data from this object was a good reason to search for a pulsed signal in the VHE range. It was fortunate for us that H.E.S.S. observed PSR B1259–63 extensively, despite the different purpose of the observations, which were mainly motivated by the periastron passage, at first, and extended to mid-2004 due to the serendipitous discovery of HESS J1303–631 (read also section 1.6.2) [133].

We selected 25.5 h of stereoscopic observations that spanned from April 2004 (MJD 53108) to June 2004 (MJD 53172). After the application of our low-energy cuts, the event arrival times in Namibia were converted into TDB timestamps at the SSB, as usual. However, in the case of PSR B1259–63, an additional correction for the binary motion had to be applied. The following section describes the formulation behind this correction.

### Focus Correction

The event folding in the case of PSR B1259–63 observations requires additional information per event than that for isolated pulsars. Similarly to the barycentric correction of the event arrival times, which requires them to be transferred to the SSB, an additional correction is needed. Due to the pulsar’s velocity in its orbit around the B2e star, the pulsed signal is Doppler-shifted towards a higher or a lower frequency than the pulsar’s, depending on whether the pulsar is receding or approaching a stationary observer. Hence, unless one compensates for the frequency shift that corresponds to the different velocities of the pulsar during one orbit, a potential signal at the pulsar’s period of rotation will appear smeared. As in the case of the barycentric correction, a suitable reference frame which remains stationary with respect to SSB during the observation periods considered is the Binary System Barycentre (BSB), or, as is otherwise called, its *focus*. By adding or subtracting the appropriate time increment that is equal to the projected-in-the-observer’s-line-of-sight travel time of the signal, from the pulsar to the BSB, one can be confident that any pulsed events will be arriving at the SSB, at the pulsar’s frequency. The process of transferring the event arrival times from the pulsar’s accelerating reference frame to the BSB is called *focus correction*. This process will become clearer as we explain the formulation which was used in our focus-correction code.

Our calculations are based on the orbital configuration of Fig. 6.8, which the reader is referred to for an explanation of the different parameters used throughout our analysis. Starting from the position vector that connects the pulsar with the

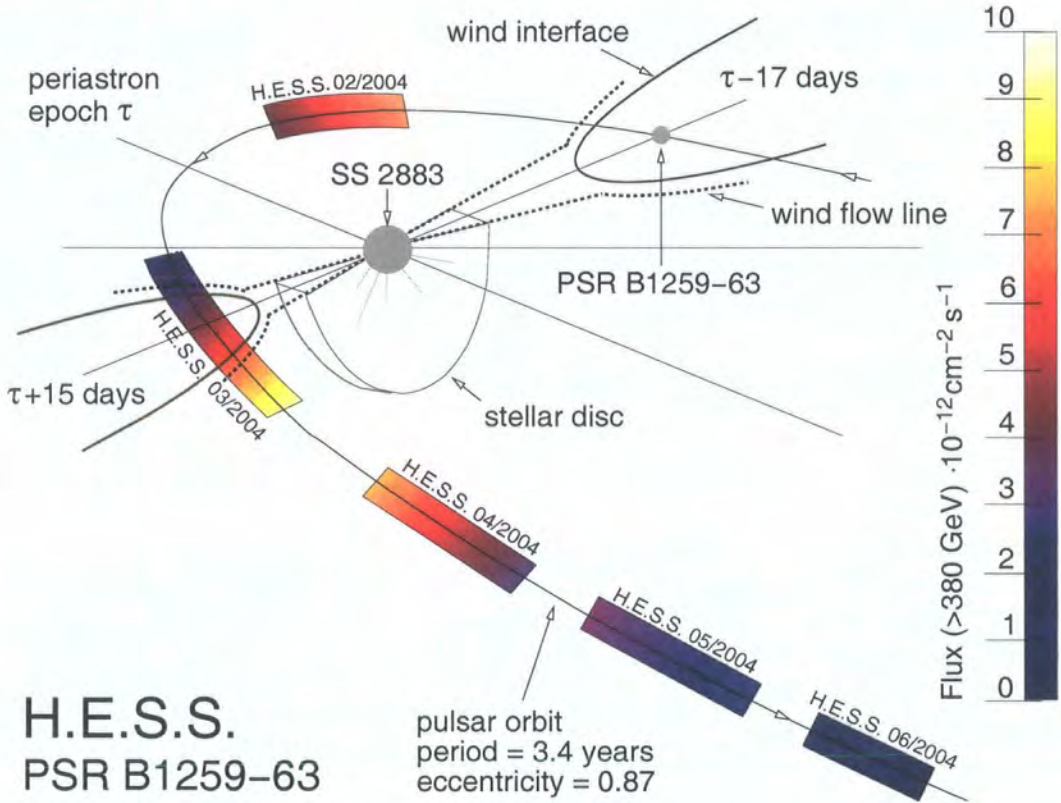


Figure 6.6: (from [117]) A schematic of PSR B1259-63's orbit around the B2e star SS 2883, at the time of the periastron passage that occurred in March 2004 (epoch  $\tau$ ). The observation periods before and after  $\tau$  are shown with the rectangular, graduated colour bands. The different colour gradient for each observation represents the variations of the measured integral flux value above 380 GeV. Each colour corresponds to a value on the vertical flux scale shown on right of this figure, in units of  $10^{-12} \text{ cm}^{-2} \text{ s}^{-1}$ . It can be seen that soon after periastron (March 2004), the flux reaches its maximum observed value of  $\sim 10^{-11} \text{ cm}^{-2} \text{ s}^{-1}$ .

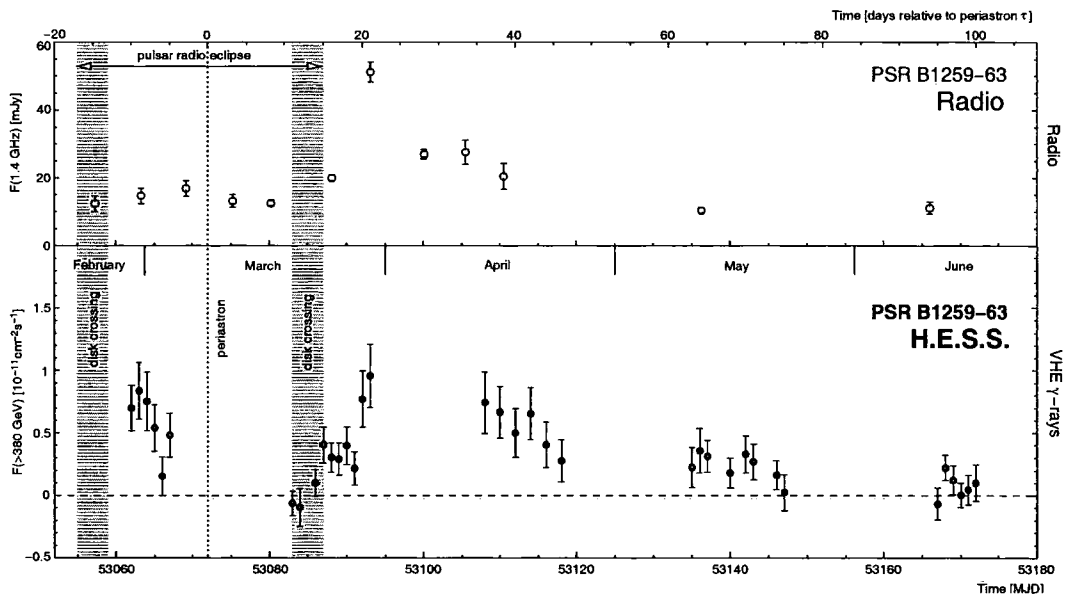


Figure 6.7: (from [117]) Radio (top) and VHE (bottom) lightcurves of the steady emission from the PSR B1259–63/SS 2883 system, around periastron. The top diagram shows the flux density of the transient radio emission, from observations at 1.4 GHz. The pulsed radio emission from PSR B1259–63 eclipsed during 53057–53088 MJD. The bottom plot shows the variation of the DC integral  $\gamma$ -ray flux above 380 GeV, during the same period, from observations with H.E.S.S. The passages of PSR B1259–63 through the stellar wind disk of SS 2883 are indicated with the grey bands, and the periastron position is shown with the dashed line.



P	1236.723319051 d
$a \sin i$	1296.3837509 light-seconds
$\omega$	$138^\circ.668020$
$e$	0.86990542
MJD <sub>II</sub>	48124.35237650

Table 6.9: (from [381]) The orbital parameters of the PSR B1259–63/SS 2883 system.

BSB, on the true orbital plane, we have [446]

$$\mathbf{r} = \frac{a(1 - e^2)}{1 + e \cos \nu} \hat{\mathbf{r}} \quad (6.1)$$

where  $a$  is the semi-major axis;  $e$ , the eccentricity;  $\nu$ , the true anomaly of the orbit, and  $\hat{\mathbf{r}}$  is the polar-radius unit vector.

The projection of  $\mathbf{r}$  perpendicular to the line-of-nodes is

$$\mathbf{r}_K = \frac{a(1 - e^2)}{1 + e \cos \nu} \sin(\nu + \omega) \hat{\mathbf{K}} \quad (6.2)$$

where  $\hat{\mathbf{K}}$  is the unit vector perpendicular to the line-of-nodes NN'.

Finally, the projection of  $\mathbf{r}_K$  along the line-of-sight gives the required amount of separation between the BSB and the pulsar companion: this is

$$r_z = a \sin i \frac{(1 - e^2)}{1 + e \cos \nu} \sin(\nu + \omega) \hat{\mathbf{z}} \quad (6.3)$$

where  $i$  is the inclination of the true orbit with respect to the line-of-sight, and  $\hat{\mathbf{z}}$  is the unit vector along the line-of-sight. Using the length of this vector as a function of time, we can correct the arrival times of the pulsed events to the BSB.

For spectroscopic binaries, the known parameters are  $a \sin i$ , the semi-major axis projection;  $\omega$ , the longitude of the periastron;  $P$ , the orbital period;  $e$ , the eccentricity of the orbit; and MJD<sub>II</sub>, the date of the periastron passage. These values are given in the ephemerides for binary pulsars; for the PSR B1259–63/SS 2883 system the corresponding values are shown in Table 6.9.

Based on these values we plotted the orbit of PSR B1259–63 which is shown in Fig. 6.9. The plot marks are 10 d apart in time, and the total data spans from MJD 53000 to 54300. The exposure time coverage of our set of analysed H.E.S.S. data, from April to June 2004, is also shown in the same plot.

Using Eq. 6.3, we calculated the time increment,  $\Delta t$ , that needs to be added to



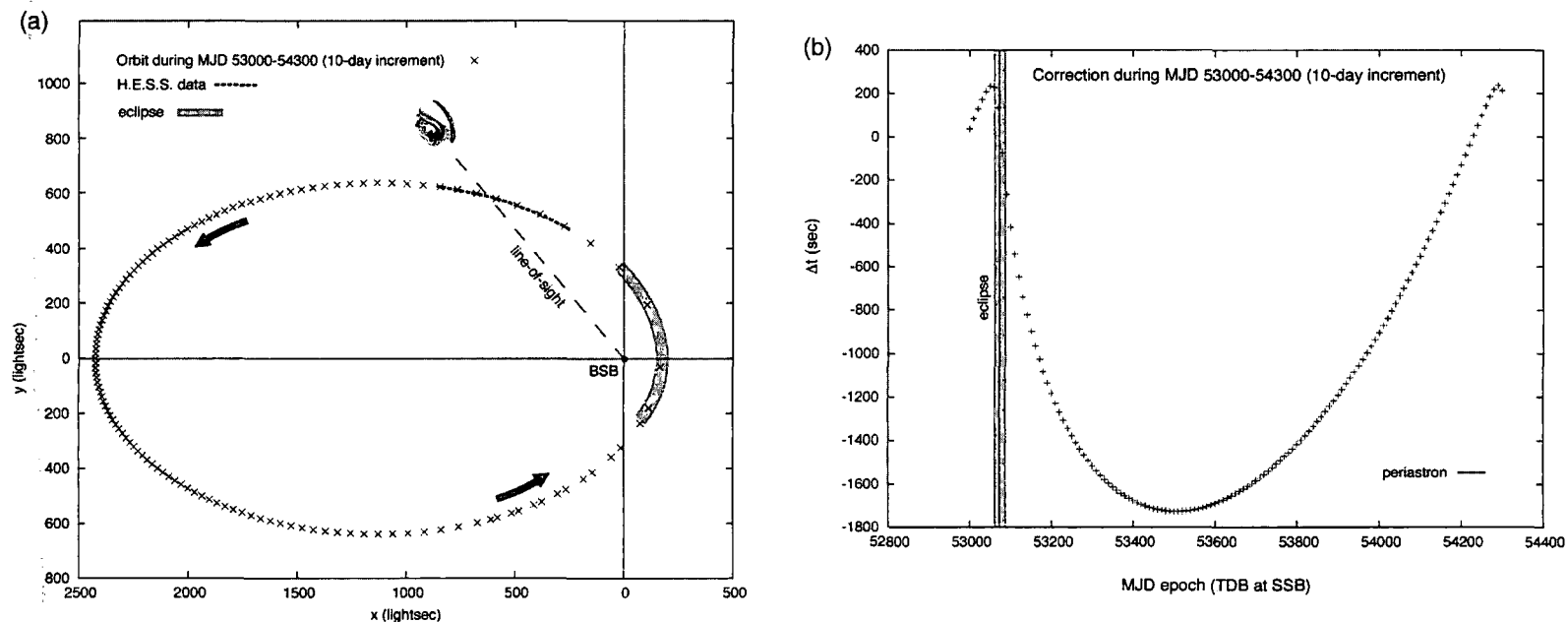


Figure 6.9: (a) The apparent orbit of PSR B1259-63 from MJD 53000 to 54300, as was calculated by substituting  $a$  with  $a \sin i$  in Eq. 6.1. Also shown with the dotted line is the H.E.S.S. data coverage of the orbit, which corresponds to the data from April to June 2004. The co-ordinate  $(x, y) \equiv (0, 0)$  corresponds to the BSB. (b) The variation of the time increment that has to be added to the TDB arrival times of the events at the SSB in order to correct for the binary motion, as a function of the event arrival time at the SSB (shown as MJD epoch). In both plots, the time interval between successive points is equal to 10 Julian days.

the event arrival times at the SSB, so that the resulting times are transferred to the BSB reference frame. Naturally, this correction is a function of time. We plotted  $\Delta t$  against the Modified Julian days, as they are measured at the SSB, in TDB format. The resulting plot for a full orbit is shown in Fig. 6.9.

In addition, we plotted  $\Delta t$  as a function of the pulsar's orbital position, expressed by the true anomaly,  $\nu$ . Based on this plot, which is shown in Fig. 6.10, one can deduce the following information: to begin with, the pulsar is at the true periastron when  $\nu = 0^\circ$ ; and when  $\Delta t = 0$  s, the pulsar is at one of the nodes. In this particular case, where  $\omega \approx 138^\circ$ , the pulsar crosses the ascending node N at a slower speed than the one with which it crosses the descending node N'. From the plot it can be seen that N is at  $\approx -138^\circ$  and N' at  $\approx 40^\circ$ . By adding  $90^\circ$  to these values, we can obtain the line-of-sight which is shown in Fig. 6.9. The observer's position can be located at either end of the line-of-sight, and for this system we were able to determine it based on the information about the eclipse of PSR B1259–63 by the B2e star, which lasted from MJD 53057 to 53088 [447].

The maximum separations from the plane where the BSB lies are  $\approx 1726$  light-seconds behind the star and  $\approx 235$  light-seconds in front of it. Finally, the maximum receding velocity is  $\approx 76 \text{ km s}^{-1}$ , and the maximum approaching velocity, towards the observer, is  $\approx 16 \text{ km s}^{-1}$ .

After applying the barycentric and focus corrections to the TDB timestamps, the latter were converted into phases using a valid GRO ephemeris supplied by ATNF [448]. The ephemeris values are shown in Table 6.10, and the validity range was from MJD 53099 to 53176. Throughout our set of PSR B1259–63 runs, the error on the frequency remained below  $5.4 \times 10^{-11}$  Hz, which is insignificant compared to the IFS for that particular set (1 IFS  $\sim 10^{-5}$  Hz).

In order to check visually for any significant excess at the pulsar period, we constructed 20-bin phasograms for the two sets that passed our low-energy cuts (see Fig. 6.12). In contrast to the other two pulsars we have studied, we did not have any information about PSR B1259–63's high-energy pulse profile from other observations. Therefore, we made the assumption that the radio profile of this pulsar is persistent in the VHE range too. In fact, PSR B1259–63's radio profile and the Crab pulsar's, which is persistent over the whole studied EM spectrum, have many things in common: a direct comparison between these two profiles is shown in Fig. 6.11, where one can see that in both cases there is a prominent main peak that is followed by a weaker second peak; also the separation between the peaks

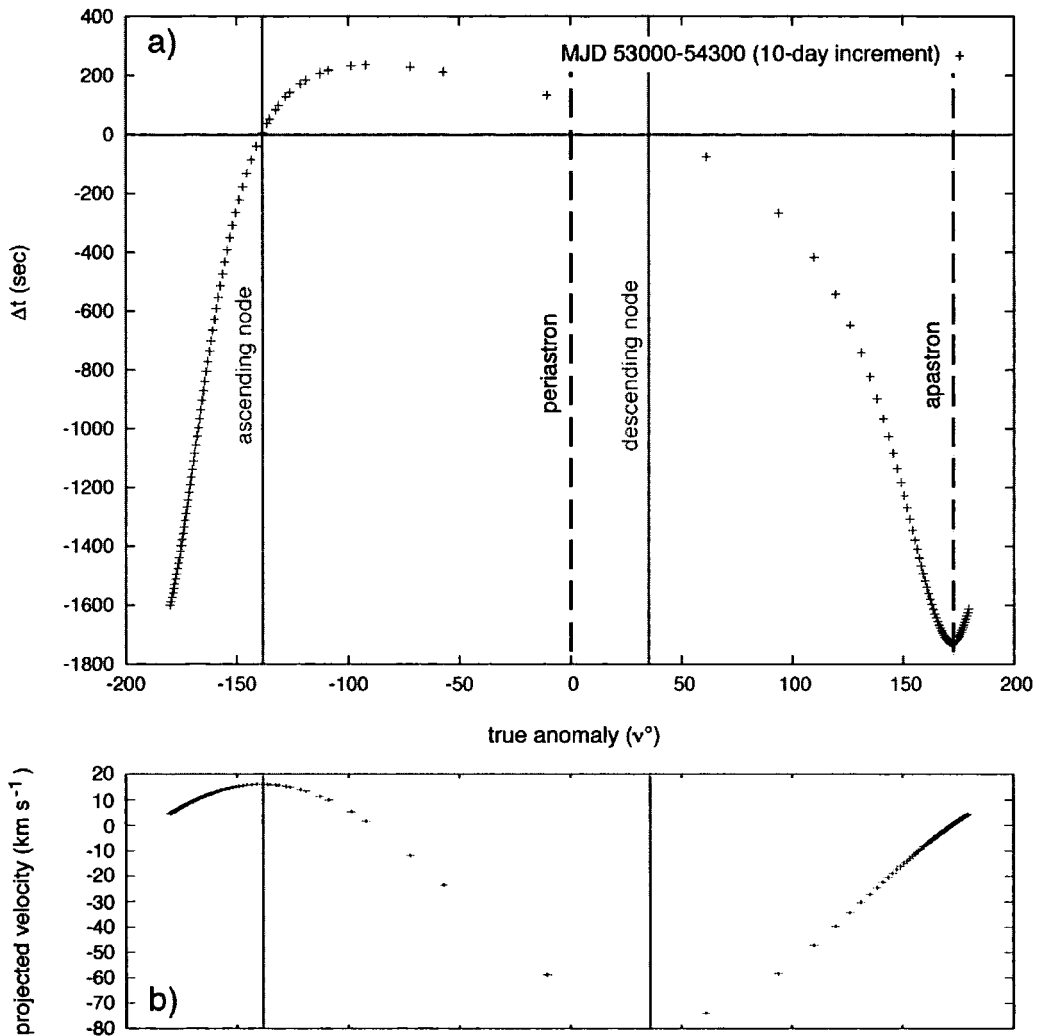


Figure 6.10: (a) The binary correction,  $\Delta t$ , as a function of the true anomaly,  $\nu$ , for a full orbit, in 10-d intervals. The dashed lines indicate the binary correction when the pulsar is at periastron or apastron. The binary correction when the pulsar crosses the ascending or descending node is zero. (b) A plot of the projected velocity of the pulsar along the line-of-sight. Both plots are drawn in the same scale with respect to  $\nu$ , to allow direct comparison.

$t_0$ (seconds since J2000)	$f_0$ (Hz)	$\dot{f}_0$ (Hz s <sup>-1</sup> )	$\ddot{f}_0$ (Hz s <sup>-2</sup> )
1.375923811339e + 08	20.93668485739	-1.001710712632e - 12	-1.87000e - 21

Table 6.10: (from [381]) The PSR B1259–63 ephemeris values that were used in our analysis.

	$\chi^2_{19}/(19 \text{ df})$	Rayleigh	$H$ -test	$C_m$ test			
				main peak		second peak	
<b>Standard</b>	1.285 (0.18)	0.04 (0.95)	0.09 (0.96)	$C_2$	$S_2$	$C_2$	$S_2$
				1.19	0.17	-0.2	1.1
<b>Central</b>	1.42 (0.1)	0.61 (0.54)	1.22 (0.61)	$C_2$	$S_2$	$C_2$	$S_2$
				1.53	0.12	-0.66	0.41

Table 6.11: The results from the application of four tests for uniformity to PSR B1259–63 data. The tests were applied to events passing our two sets of low-energy cuts (see Table 5.5). For the  $\chi^2$ -test the values shown are the reduced  $\chi^2$  with 19 df (Eq. 5.48). In the Rayleigh test column, the values are the Rayleigh powers for each data set. The  $H$ -test values were calculated from Eq. 5.87. For those three tests, we have included in parentheses the corresponding probability of accepting  $H_0$ . Finally, the  $C_2$  and  $S_2$  values, under the  $C_m$  test, are the sums of the cosine and sine trigonometric moments up to the second harmonic, respectively.

is roughly half a period for both profiles; on the other hand, it is clear that PSR B1258–63’s profile contains broader peaks, with  $\delta \approx 0.2$ .

Neither of the two phasograms showed significant fluctuations above the mean, which was also confirmed by the low  $\chi^2_{19}/(19 \text{ df})$  values (see Fig. 6.12). Also, the rest of the tests did not result in significant probability values (see Table 6.11). Specifically for the  $C_m$  test, we chose to sum the moments up to  $m = 2$ . In addition, our search with this test was centred on  $\phi = 0$  for the main radio peak and  $\phi = 0.4$  for the second peak. Despite the fact that most EGRET  $\gamma$ -ray lightcurves tend to have broader components than their radio counterparts, in the case of PSR B1259–63, we decided to assume the same duty cycle as in the radio profile, i.e.  $\delta = 0.2$ . Under that assumption, the only notable result was that from the  $C_2$  test on the main peak, after the central cuts; but the probability was only  $\sim 10^{-2}$ . Also, it can be seen that in the corresponding phasogram there is one other bin ( $\phi \approx 0.65$ ) which also shows the same excess, as well as many others that have comparable excess within the statistical errors shown.

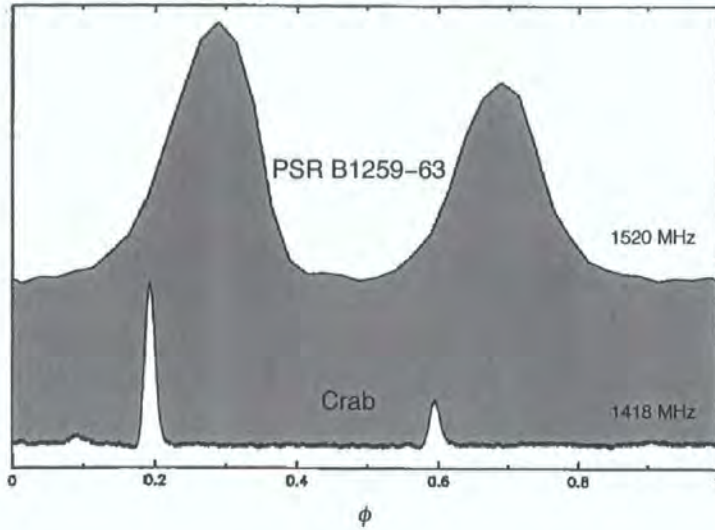


Figure 6.11: The radio profiles of PSR B1259–63 [449] and of the Crab pulsar [450], at 1520 and 1418 MHz, respectively. Despite the broader peaks in PSR B1259–63’s profile, the two lightcurves are similar, as they both have two components separated by half a cycle. Also, the first component is more prominent in both profiles.

### Event Ghosting

Prior to our main analysis of PSR B1259–63 data, we selected one of the first runs produced from February observations of this object. The purpose for this limited analysis was purely to test our focus correction algorithms with real data. However, the application of the  $H$ -test to the  $\sim 10^5$  events contained in that run resulted in a surprisingly low probability, which was of the order of  $10^{-20}$ . In order to investigate the reason behind this value, we decided to divide the run into 200-s segments and run the  $H$ -test again on each segment. The variation of  $-\log[\text{pr}(> H|H_0)]$  across the whole run is shown with the step histogram of Fig. 6.13: it can be seen that two segments resulted in probability values as low as  $10^{-100}$ . By isolating these segments, it was discovered that they contained sequences of repetitive timestamps: i.e. with  $\Delta t < 1 \mu\text{s}$ . These events had, of course, identical phases and were detected as signal by the  $H$ -test.

We simulated the above situation by injecting  $10^3$  identical timestamps — which corresponds to the number of repetitive events found in the PSR B1259–63 run — into a file containing  $10^5$  random events. Subsequently, we folded the events with a random frequency and ran the  $H$ -test at that frequency: the resulting probability

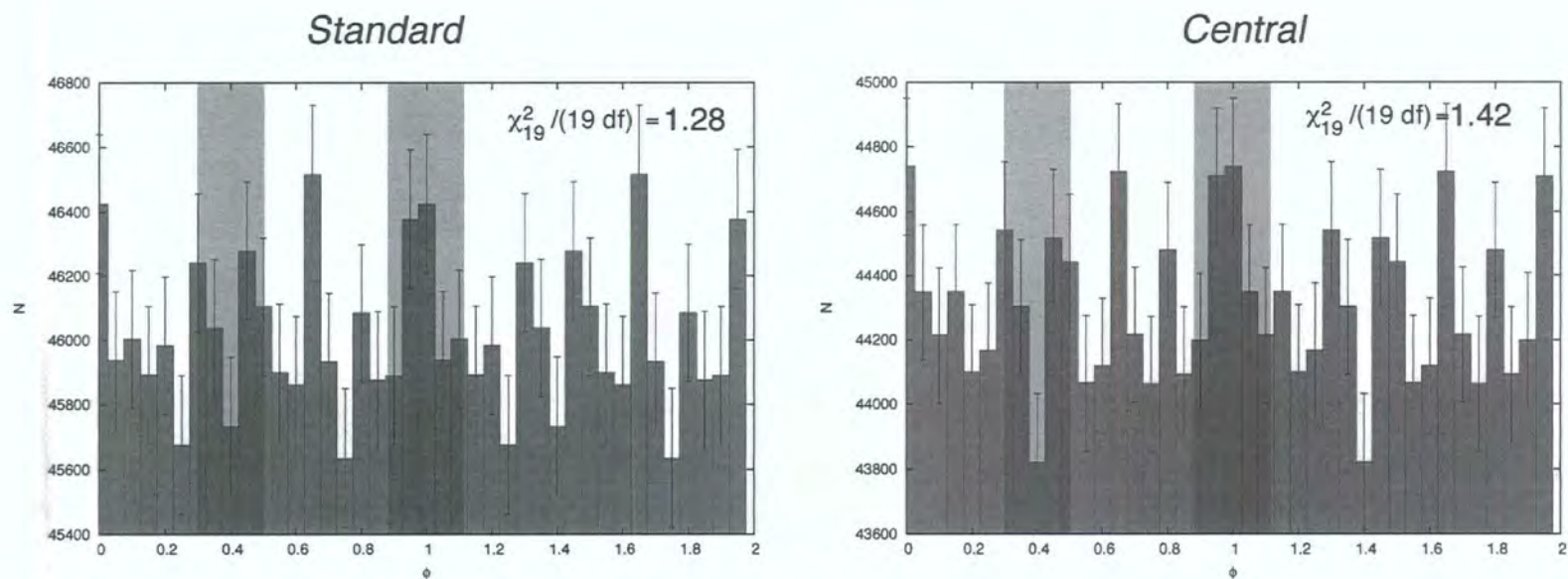


Figure 6.12: The resulting phasograms for PSR B1259–63 after binning the  $\sim 10^7$  events that passed the standard and central low-energy cuts. The shaded areas cover the phase ranges of the two peaks that were seen in radio observations of this pulsar. A notable excess in our data is that at the main radio peak position, after the central cuts. However, there are many other bins with comparable excess: i.e. within  $1\sigma$ .

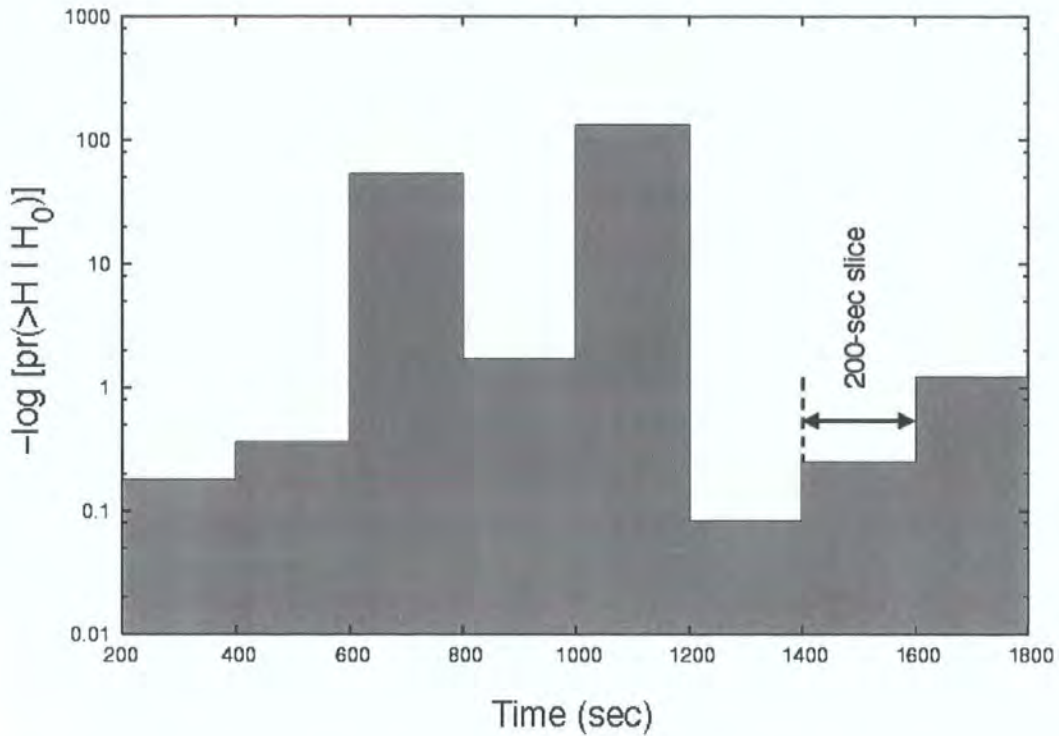


Figure 6.13: This histogram shows the variation of the probability values, as were calculated with the  $H$ -test, across one run of PSR B1259–63. The length of the run was split into 8 contiguous segments that were in chronological order. It can be seen that two segments resulted in abnormally low probabilities.

from the test was  $\sim 10^{-15}$ . Moreover, we isolated a fraction of the simulated data set that corresponds to one 200-s segment ( $\sim 10^4$  events), in which we included the same  $10^3$  identical timestamps, as before. After running the  $H$ -test again, we got  $-\log[pr(> H|H_0)] \approx 114$ , which showed that the injected events were responsible for the abnormal  $pr$ -levels. However, it should be mentioned that the test detected the artificial nature of the signal, since the optimal harmonics at which the above probabilities were found were  $m = 19$  and  $20$ . It is unlikely that the Hart rule would detect a strong power that is due to a real source, at such high harmonics. In general, real sources are likely to be detected up to the 5<sup>th</sup> harmonic [400]. An interesting remark with regards to the performance of the Rayleigh test is that it failed to produce significant probabilities in the above simulations. This shows the lack of sensitivity of this test to narrow signals: like the one in this extreme case, where  $\delta = 0$ .

### 6.3.4 Upper Limits on the Flux

For the calculation of flux upper limits (hereafter ULs), we used Eq. 4.19, 4.20, 4.21 and Eq. 4.22, combined with the expressions for the UL on the counts from the aforementioned tests for uniformity as well as from the Helene method. Clearly, this route requires knowledge of the source's differential flux spectrum,  $dN_\gamma/dE$ , which had to be assumed. In other words, we used a model-dependent approach for the calculation of ULs. Other approaches are also possible, and in the context of the H.E.S.S. experiment, the reader can find out more about such work in [256].

The present work assumes a simple power-law spectrum for the investigated pulsars: for the Crab and PSR B1706–44, the spectral index can be adopted from the corresponding EGRET observations; and as mentioned in section 5.7.4, an index of 1.76 has been assumed for PSR B1259–63. However, one can see, for example, that the EGRET power law for the Crab pulsar is inconsistent beyond 60 GeV, since it conflicts with the CELESTE UL at that energy (see Fig. 6.14). On the other hand, the super-exponential (SE) fit to the EGRET data by de Jager *et al.*, with a cut-off at 30 GeV, is compatible with all present measurements in the VHE range. Therefore, one could in principle assume such a spectrum and derive the ULs. Unfortunately, the implementation of SE cut-offs in combination with the H.E.S.S. effective areas results in very low event rates above the H.E.S.S. threshold ( $\sim 100$  GeV), as Fig. 6.14 shows. Hence, the resulting ULs become very large compared to the spectra which they are tested against. The exact values will be mentioned later, but one can see in this figure that the Crab rate for a SE spectrum is roughly 10 orders of magnitude lower than that from the EGRET power law, above 60 GeV. On the other hand, the SE spectrum of PSR B1706–44, with  $E_c = 40$  GeV, results in a more comparable  $\gamma$ -ray rate, yet still 4 orders of magnitude lower than its EGRET counterpart, above 40 GeV. Hence, we have decided to calculate the ULs based predominantly on the single power-law fits to the EGRET data, although some of the SE ULs will be mentioned for comparison. This way, the UL values become more constraining on the Outer Gap and Polar Cap models.

There is, however, one parameter which is improved with the choice of SE spectra, and that is the energy threshold. It is clear in Fig. 6.14 that the peak of the  $dR/dE$  function is shifted towards lower energies for the SE case. This is clearly beneficial, as we expect a steep increase of the pulsed flux towards the lower GeV range, for all  $\gamma$ -ray pulsars. Hence, provided the resulting UL values are comparable with the predicted fluxes, a low-energy UL can be the decisive factor for rejecting



either model.

Finally, for the Crab pulsar and PSR B1706–44, we decided to derive ULs based on a simple exponential (EXP) spectrum, given by Eq. 3.22 with  $b = 1$ . This solution represents a middle ground between the optimistic power-law spectrum, which allows detectable fluxes well inside H.E.S.S.’s sensitivity range ( $\gtrsim 100$  GeV) and the conservative super-exponential spectrum, which predicts that the emission should diminish well below that range.

### The Choice of Energy Thresholds

The calculation of upper limits on the integral flux is usually performed for all events with energies above the energy threshold of a particular data set. Typically, this threshold, say  $E_{\text{th}}$ , equals the energy at which the differential rate becomes maximum. Fig. 6.15 shows that such a decision is justified, since  $dR/dE$  is quenched rapidly below  $E_{\text{th}} = 235$  GeV. Our specific low-energy analysis, however, required a different definition for the energy threshold. It is clear in our  $dR/dE$  plots that there is a significant number of events per energy interval below the maximum differential rate<sup>1</sup>. Therefore, an important decision had to be made concerning the energy, which would represent best the threshold for each of our data sets. Based on the shape of the differential-rate function, whose low-energy tail resembles a Gaussian, we arbitrarily set the energy threshold equal to the value,  $E'_{\text{th}}$ , for which the differential rate becomes  $1/e$  of its maximum value. More specifically,  $E'_{\text{th}}$  was defined by

$$\frac{dR(E'_{\text{th}} < E_{\text{th}})}{dE} = \frac{1}{e} \cdot \frac{dR(E_{\text{th}})}{dE} \quad (6.4)$$

Fig. 6.16 shows the derived differential-rate functions for the three pulsars that were analysed. Clearly, the choice of  $E_{\text{th}}$  as the energy that corresponds to the maximum differential rate ignores a large fraction of the low-energy events in the calculation of integral ULs above the threshold; and in the case of the Crab pulsar and PSR B1259–63, this fraction is  $\approx 25\%$ ; but for PSR B1706–44 it is roughly as high as  $35\%$ . By setting the energy threshold to the value that corresponds to  $(1/e)dR/dE$ , the fraction of events below  $E'_{\text{th}}$  drops below  $5\%$  in all studied cases. Our choice not only selects the energy above which nearly all events lie — after all, that is the definition of the energy threshold — but most importantly, the derived

<sup>1</sup>Prior to directly comparing Fig. 6.14 with Fig. 6.15, note the logarithmic scale in the former plots.

$E'_{\text{th}} \pm \Delta E$ (GeV)	Crab pulsar		PSR B1706–44	PSR B1259–63
	<i>Single</i>	<i>Phase I</i>		
<b>standard</b>	$242 \pm 35$	$232 \pm 51$	$75 \pm 12$	$248 \pm 52$
<b>central</b>	$272 \pm 42$	$242 \pm 39$	$90 \pm 12$	$254 \pm 40$
<b>H.E.S.S.</b>	$300 \pm 60$		$100 \pm 20$	$300 \pm 60$

Table 6.12: The energy thresholds,  $E'_{\text{th}}$ , of our data sets after the low-energy cuts, and the equivalent energy thresholds — calculated for the same Z.A. — after the standard H.E.S.S. cuts. All thresholds have been defined as the energy that corresponds to the  $1/e$  of the maximum differential rate for the respective data set. The statistical errors ( $\Delta E$ ) after the low-energy cuts have been calculated for the lowest simulated energy above the threshold (see text for explanation).

ULs based on those thresholds are more representative of our low-energy sample. Ultimately, these events are at the focus of our analysis and are expected to occupy a large fraction of the data sets after the standard and central cuts. The selected energy thresholds from the above definition are shown in Table 6.12.

### Errors on the Energy Threshold

In addition to determining the energy threshold for each data set, a statistical error that would state the accuracy of our UL positions on a flux diagram had to be calculated. The usefulness of such error values can be appreciated if we recall the plots of Fig. 3.14: in those plots, two Outer Gap scenarios, the thick and thin Outer Gap, are tested against data points from observations of Geminga and PSR B1055–52. However, the relatively large error bars prevent the data from being constraining on either scenario. In the context of our analysis, the derived ULs were tested against the Outer Gap and Polar Cap predictions for each object. In order for these to be constraining, apart from being at an adequately low energy,  $E_0$ , the error on this energy,  $\Delta E$ , should be sufficiently small. Ideally, the magnitude of this error should allow us to be confident as to whether our observations reject a hypothesis in favour of another or cannot discriminate between the various models. For example, the UL value from CELESTE (see Fig. 6.17) clearly places a constraint on the Outer Gap model, in the energy range  $E_0 = 60 \pm 20$  GeV. However, this is only true because of the small error bar, which confidently restricts the flux below the one predicted by this model, across the whole  $\Delta E$ . Had the error been larger, we would have been unsure of the validity of the model and the usefulness of this UL would have been much less.

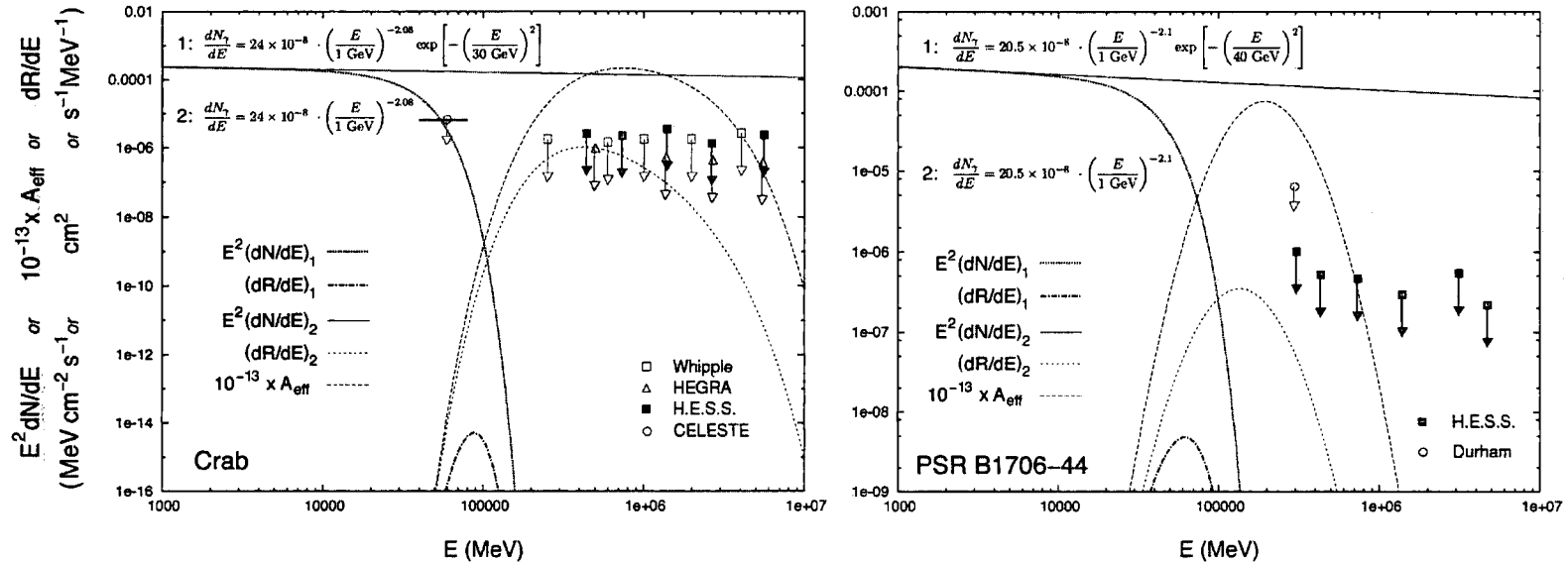


Figure 6.14: Plots of the differential event rate,  $dR/dE$ , from a single power-law spectrum (2) and from a super-exponential spectrum (1). The value of  $dR/dE$  has been derived from the multiplication of the effective-area function (dashed line), which was scaled down in order to fit in this plot, and the differential flux spectrum,  $dN/dE$ . The resulting function from both spectra is shown for the case of the Crab pulsar and PSR B1706-44 and after the application of our standard low-energy cuts. In the case of the former, it can be seen that the event rate,  $R$ , from the super-exponential spectrum is roughly 10 orders of magnitude lower than that from the power-law spectrum. The upper limits on the pulsed flux from various experiments are shown for direct comparison between the modelled spectra and the experimental sensitivity of VHE detectors.

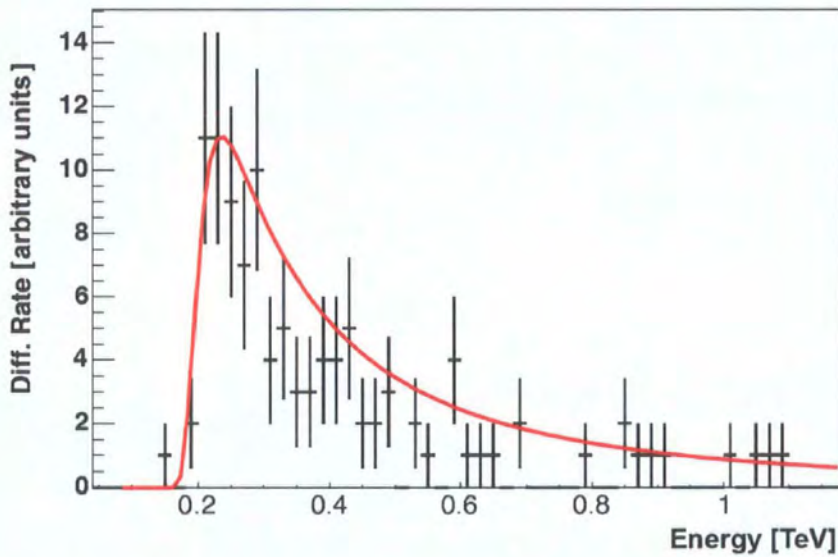


Figure 6.15: (from [256]) The typical shape of a differential-rate plot,  $dR/dE$ , after the application of standard H.E.S.S. cuts. In this figure, the black data points were derived from observations of the Vela pulsar. The solid, red line is the result of Monte Carlo simulations of the same source (Z.A.= $30^\circ$ ), where a spectral index  $\nu = 2.76$  was assumed. It can be seen that below the energy where  $dR/dE$  becomes maximum, the differential rate diminishes rapidly. Hence, an energy threshold equal to that energy — in this case  $E_{\text{th}} = 235$  GeV — is justified.

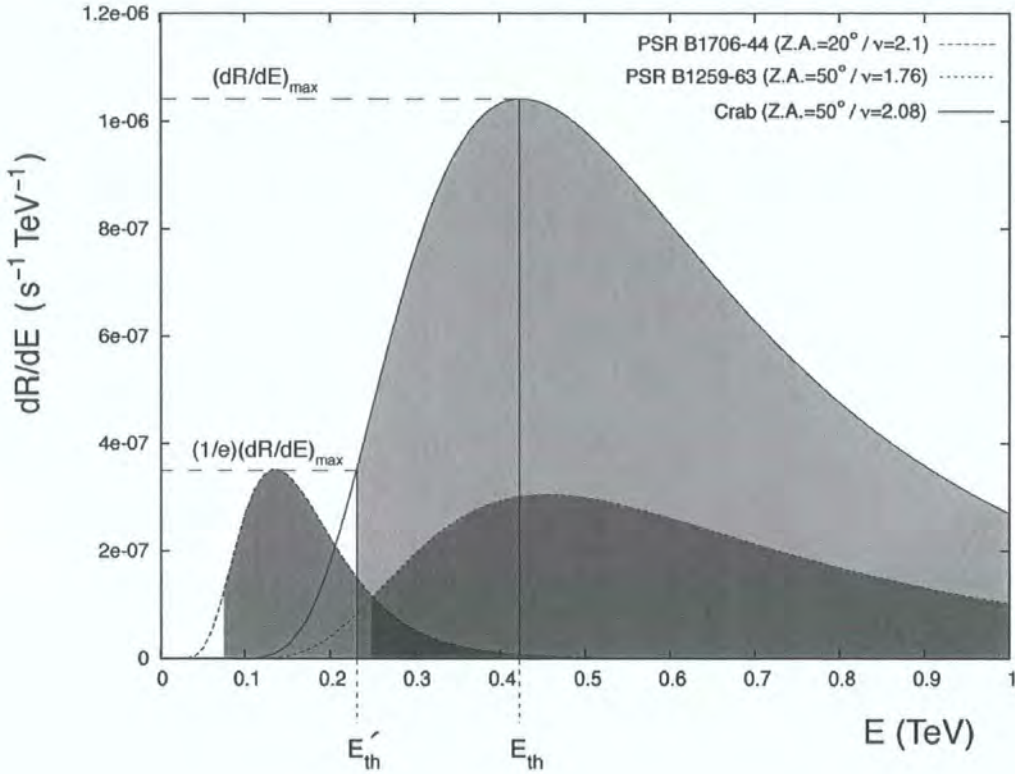


Figure 6.16: The differential-rate plots for the Crab pulsar, PSR B1706–44 and PSR B1259–63, derived from Monte Carlo simulations. The assumed spectral indices and Z.A.s are shown for each pulsar. All plots correspond to the standard low-energy cuts. For PSR B1259–63, we did not have available information from high-energy observations, so the normalisation flux at 1 GeV was given an arbitrary value. The shaded area in all plots corresponds to the energy region above our chosen energy threshold,  $E'_{th}$ , which contains  $> 95\%$  of the total events. It can be seen that for all three cases, the classical definition of  $E_{th}$ , i.e.  $dR(E_{th})/dE \geq dR(E)/dE \forall E \geq 0$ , neglects a large fraction of event energies: those with  $E < E_{th}$ . Hence, we set the energy threshold to the value that corresponds to  $(1/e)(dR/dE)_{max}$ , which includes nearly all event energies.

In our analysis, the statistical errors on the energy were estimated with Monte Carlo simulations. The errorbars that represent them can be seen in the  $\log E$ - $\ln IA$  plots of Fig. 5.39. Note, however, that our low-energy thresholds for the three pulsars do not correspond to any data points: in most cases, the  $\sim 10^5$  simulated  $\gamma$  rays were not enough to result in a significant number of triggers<sup>2</sup> below 350 GeV. The exception is the small-Z.A. simulations for PSR B1706–44, for which the Monte Carlo energy was as low as 90 GeV. As a consequence, we decided to use the error on the data point with the *lowest* energy, in each case, as the uncertainty on the energy threshold for each data set. One should be aware, of course, that these values represent lower limits, and that it is likely that, in the case of the Crab pulsar and PSR B1259–63, the actual error is larger. Our decided error values for each data set are shown beside the energy threshold values in Table 6.12.

### Crab pulsar

Our ULs for the Crab pulsar were based on the morphology of the EGRET profile (phase range  $[0.94,0.04] \cup [0.32,0.44]$ ), our simulated effective areas and the assumed power-law spectrum (spectral index  $\nu = 2.08$ ). The integral ULs above each data set's energy threshold, from all uniformity tests, are shown in Table 6.13. In addition, we calculated the ULs on the differential flux at the energy threshold. These were compared with previous work with other experiments, as well as with the ULs after the standard H.E.S.S. cuts for the Crab pulsar. We placed the corresponding values in the plot of Fig. 6.17, which also shows the spectra from the Outer Gap and Polar Cap model: it can be seen that our upper limits are well shifted towards the low energies with respect to the rest; also our low-energy thresholds are competitive with those from Whipple, which is expected to perform better for the Crab because of the experiment's advantageous geographical location with respect to this pulsar's celestial position.

A notable property of our calculated differential flux ULs is their clear separation in three groups: the group with the lowest upper limits, with an average value of  $\langle E'_{\text{th}}{}^2 [dN(E'_{\text{th}})/dE]_{\text{ul}}^{3\sigma} \rangle = 3.17 \times 10^{-6} \text{ MeV cm}^{-2} \text{ s}^{-1}$ , consists of ULs produced with the  $C_m$  test, which shows again increased sensitivity compared to the rest of the tests; this was found true independently of the type of data that was analysed: i.e. single-telescope or stereo. This test's high sensitivity can be justified by the

---

<sup>2</sup>The acceptance condition in the binning code required at least 4 event triggers in an energy bin.

fact that it searches for emission at a specific frequency and phase, and hence it ‘burns’ fewer degrees of freedom compared to the rest of the tests, which only fix the frequency of emission.

Otherwise, the rest of the tests produced ULs that were lower in the case of stereo data ( $\langle E'_{\text{th}}{}^2 [dN(E'_{\text{th}})/dE]_{\text{ul}}^{3\sigma} \rangle = 5.3 \times 10^{-5} \text{ MeV cm}^{-2} \text{ s}^{-1}$ ) than in the case of single-telescope data ( $\langle E'_{\text{th}}{}^2 [dN(E'_{\text{th}})/dE]_{\text{ul}}^{3\sigma} \rangle = 1.91 \times 10^{-4} \text{ MeV cm}^{-2} \text{ s}^{-1}$ ). The gap between these two groups of ULs could be attributed to the different exposure of the data sets, which is inversely proportional to the flux UL (see Eq. 4.21 and Eq. 4.22). For the single-telescope data set after the standard low-energy cuts, the exposure was  $1.26 \times 10^{12} \text{ cm}^2 \text{ s}$ , whereas the corresponding value for the stereo data was  $4.7 \times 10^{12} \text{ cm}^2 \text{ s}$ , which is a factor 4 higher. That explains the amount of separation between the two groups of ULs, which is of the same magnitude. The energy-threshold difference between stereo and single-telescope data has a less important effect on the flux UL values: the former is comparable to the statistical uncertainties, and hence the threshold can be considered the same in either case. Finally, it is worth noting that, with the exception of 3 single-telescope ULs, all our values are inconsistent with the single power-law assumption in the investigated energy regime.

The bottom rows of Table 6.13 present the integral ULs for an EXP and SE spectrum. Despite the much-desired low-energy thresholds associated with these spectra, being as low as 53 GeV, the corresponding ULs are at least 2 orders of magnitude larger than those based on a single power-law. Clearly, such ULs cannot place any constraints on the models.

At this point, we would like to draw attention to the UL on the pulsed fraction, which we obtained using the method of Helene; see the last column of Table 6.13. These percentages should not be directly compared with relative ULs reported elsewhere: e.g. [289]. They represent the UL on the pulsed emission as a fraction of the total events after cuts, whose nature is unknown. It is possible that a percentage of those events came from the plerionic DC emission of the Crab nebula, but their characterisation could only be performed via the standard H.E.S.S. cuts, which reject nearly all hadronic events; and in our case, the majority of the  $N \sim 10^6$  events in the cut data sets are almost certainly of hadronic nature.

The percentage of DC emission in our data can be roughly estimated based on the differential spectrum of the DC emission from the Crab nebula and the effective-area function after our low-energy cuts. Then, the  $\gamma$ -ray rate can be calculated from

Eq. 4.20 by integrating over all events with energies above the corresponding energy threshold for this data set ( $E'_{\text{th}} = 232$  GeV). Using the expression for  $A_{\text{eff}}(E)$ , from H.E.S.S. Phase I simulations after the standard low-energy cuts, we obtain  $R_{\gamma} \approx 7.9$  ph min $^{-1}$ . So, for an exposure time of  $T = 4.5$  h, the number of DC  $\gamma$  rays is  $N_{\gamma} \approx 2100$ , which suggests a  $\gamma$ -ray fraction equal to  $N_{\gamma}/N \approx 0.2\%$ . Hence, considering the derived pulsed fractions from our analysis, the UL on the number of pulsed  $\gamma$  rays relative to the DC emission becomes  $N_{\gamma}/N_{\gamma} \approx p_{\text{ul}}(N/N_{\gamma}) = 0.0019(10^6/2100) \approx 90\%$  of the DC  $\gamma$  rays. Clearly, this number is an order of magnitude larger than most reported ULs. However, one has to bear in mind that the nature of our analysis, whose purpose was to retain the least energetic events regardless of the amount of background, led to large data sets, and, as a consequence, large ULs.

### PSR B1706–44

The ULs for PSR B1706–44 were expected to be the most interesting of all three pulsars studied: the small Z.A. of observation means that  $A_{\text{eff}}$  remains substantial down to  $\approx 40$  GeV (see Fig. 5.38); also, the relatively soft spectral index ( $\nu = 2.1$ ) of the assumed power-law fit from EGRET observations means that the expected number of events during the exposure time ( $T = 28$  h) of our observations should be high. All these were expected to conspire towards a low-energy and low-flux UL (see equations 4.21 and 4.22). On the other hand, the upper limit on the number of pulsed events at a specific level of significance — as calculated with the uniformity tests — is expected to be large for this pulsar: this is because of the large duty cycle ( $\delta = 0.3$ ) and the large number of events in our data set ( $N \sim 5 \times 10^6$ ). The effect of these two parameters on the UL can be made clear if we consider, for example, the Helene method. A  $3\text{-}\sigma$ , say, upper limit means that the number of pulsed events in the peak area would have had to be less or equal to 3 background standard deviations, in order not to have been detected to that significance level. Since the Poissonian standard deviations are  $\sqrt{N}$ , the corresponding  $3\text{-}\sigma$  UL is also large. Moreover, the larger the duty cycle the wider the peak area, which means that a higher number of pulsed events is needed for the signal to stand out against the background, to the requested significance level.

Unfortunately, our expectations were only partially fulfilled. Despite the low-energy thresholds of our ULs, all being below 100 GeV, the flux values were up to 3 orders of magnitude larger than previously calculated upper limits above 100



			Rayleigh	$H$ -test	$C_5$ test		Helene ( $p_{ul}\%$ )	
					main peak	second peak		
power law	Phase I	Single	$F_{ul}^{3\sigma}(> 242 \text{ GeV; std}) (\times 10^{-10} \text{ cm}^{-2} \text{ s}^{-1})$	6.68	4.53	0.10	0.12	6.39 (0.28)
			$F_{ul}^{3\sigma}(> 272 \text{ GeV; ctl}) (\times 10^{-10} \text{ cm}^{-2} \text{ s}^{-1})$	8.94	6.70	0.12	0.12	7.79 (0.26)
			$F_{ul}^{3\sigma}(> 232 \text{ GeV; std}) (\times 10^{-10} \text{ cm}^{-2} \text{ s}^{-1})$	1.94	1.73	0.12	0.084	1.8 (0.19)
			$F_{ul}^{3\sigma}(> 242 \text{ GeV; ctl}) (\times 10^{-10} \text{ cm}^{-2} \text{ s}^{-1})$	2.41	2.20	0.20	0.079	2.38 (0.20)
EXP	Phase I	Single	$F_{ul}^{3\sigma}(> 114 \text{ GeV; std}) (\times 10^{-10} \text{ cm}^{-2} \text{ s}^{-1})$	$1.15 \times 10^3$	784	17.8	20.6	–
			$F_{ul}^{3\sigma}(> 130 \text{ GeV; std}) (\times 10^{-10} \text{ cm}^{-2} \text{ s}^{-1})$	194	173	11.8	8.46	–
SE	Phase I	Single	$F_{ul}^{3\sigma}(> 53 \text{ GeV; std}) (\times 10^{-5} \text{ cm}^{-2} \text{ s}^{-1})$	212	144	3.2	3.8	–
			$F_{ul}^{3\sigma}(> 72 \text{ GeV; std}) (\times 10^{-5} \text{ cm}^{-2} \text{ s}^{-1})$	74.3	66.6	4.53	3.24	–

Table 6.13: The calculated upper limits on the integral pulsed flux of the Crab pulsar, from single-telescope and stereo (Phase I) observations. All ULs were calculated to a  $3\text{-}\sigma$  or 99.95% C.L. The values that were derived from data passing the standard low-energy cuts are denoted by “std”, whereas those derived from the central low-energy cuts are denoted by “ctl”. For the Helene UL, the pulsed emission was assumed to be contained in the phase range  $[0.94,0.04] \cup [0.32,0.44]$ . For the UL from the  $C_5$  test, the event phases were centred on  $\phi = 0$  and  $\phi = 0.38$ , for the main and second peak, respectively. The power-law upper limits are based on a single power law with  $\nu = 2.08$ , whereas the EXP and SE cases correspond to the assumption of the same power law but with an exponential and super-exponential cut-off at  $E_c = 30 \text{ GeV}$ , respectively.

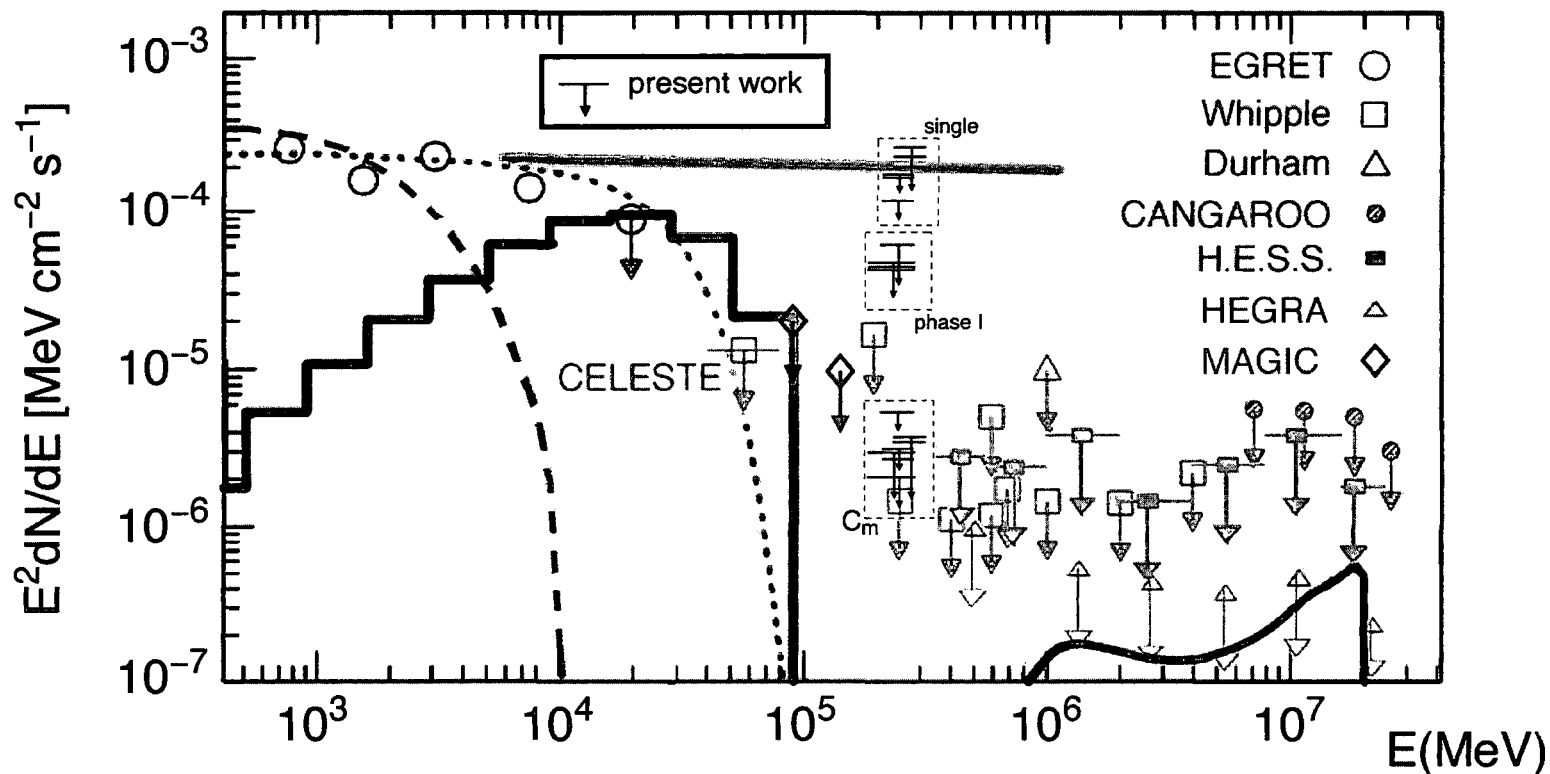


Figure 6.17: The derived ULs on the differential pulsed flux of the Crab pulsar, from the various statistical tests, after the application of our low-energy cuts. Both single-telescope and stereo data (Phase I) have been analysed prior to calculating these values. The predicted Outer Gap (thick solid line) and Polar Cap (dashed line) spectra are shown for comparison. The single power-law fit to the EGRET data ( $\nu = 2.08$ ) in the energy range of our ULs is shown as a thick, grey line. The grey, dotted line corresponds to the same power law, but with a super-exponential (SE) cut-off at  $E_c = 30$  GeV. Previous ULs from H.E.S.S. and other experiments that were shown earlier in this thesis have been dimmed out. Our calculated ULs can be divided into three groups which we have highlighted with dashed rectangles. The bottom group consists of ULs from the  $C_m$  test with both single and stereo data. This test, which appears as the most sensitive, constrained the differential flux below  $10^{-5}$  MeV cm $^{-2}$  s $^{-1}$ . Furthermore, the stereo data (middle group) resulted in lower flux ULs under the  $H$ , Rayleigh and Helene tests compared to those from the single-telescope analysis (top group).

GeV. Table 6.14 and Fig. 6.18 contain our UL results for the integral and differential pulsed flux, respectively. The differential flux ULs can be directly compared with those previously reported with H.E.S.S. and with those from Durham. As seen in Fig. 6.18, these are both above 200 GeV. In the context of our analysis, only the ULs from the  $C_m$  test have comparable fluxes to these other results. In particular, they are incompatible with the exponential spectrum shown, which predicts higher fluxes at the corresponding UL energies. Moreover, the lowest UL value calculated for PSR B1706–44, at 75 GeV, seems to marginally constrain the SE fit model by de Jager *et al.* Otherwise, the Polar Cap and Outer Gap spectra are both consistent with all our values. Finally, a single power-law spectrum for PSR B1706–44 is inconsistent with the  $C_m$  test ULs, but cannot be ruled out by the rest of our values.

In addition to the power-law ULs, we calculated the UL values from the Rayleigh,  $H$  and  $C_m$  tests, under the assumption of a power-law fit with an EXP and a SE cut-off at 40 GeV. Once again, despite the very low energy threshold of the SE ULs (41 GeV), the corresponding flux value is not comparable to the spectra under test; see bottom row of Table 6.14. The exception in this case is the UL from the  $C_m$  test, which appears in Fig 6.18, next to the top energy bin of EGRET. It is worth noting that the ULs on the integral flux, based on the simple exponential spectrum, are only an order of magnitude higher than those based on a power law. In particular, the UL on the differential flux at 56 GeV is marginally consistent with the predicted flux at the same energy, from a SE spectrum. However, the same upper limit seems incompatible with an EXP spectrum, although the error may have been underestimated, since it corresponds to such a low energy (see section 6.3.4).

### PSR B1259–63

The ULs for PSR B1259–63 were the lowest in flux of the three cases studied (see Table 6.15). This can be explained, in part, by the hard spectrum assumed, which introduced a high event rate above the energy threshold (see Fig. 6.16). However, the upper limit on the pulsed fraction,  $p_{ul}$ , is the highest derived from our study, but still consistent with the large duty cycle of the profile’s components, which is twice that of the Crab pulsar. Unfortunately, due to the lack of pulsed detection in  $\gamma$  rays and theoretical modelling for the pulsed  $\gamma$ -ray emission from this pulsar, we were unable to provide a direct comparison between our upper limits and other work. Nevertheless, one could compare the recently derived TeV spectrum of the steady IC emission, detected near periastron, with our results [117]. The index of

		Rayleigh	$H$ -test	$C_1$ test	Helene ( $p_{\text{ul}}\%$ )
power law	$F_{\text{ul}}^{3\sigma}(> 75 \text{ GeV}; \text{std}) (\times 10^{-10} \text{ cm}^{-2} \text{ s}^{-1})$	16.7	38.7	0.35	25.6 (0.19)
	$F_{\text{ul}}^{3\sigma}(> 90 \text{ GeV}; \text{ctl}) (\times 10^{-10} \text{ cm}^{-2} \text{ s}^{-1})$	22.8	46.4	0.44	28.7 (0.16)
EXP	$F_{\text{ul}}^{3\sigma}(> 56 \text{ GeV}; \text{std}) (\times 10^{-10} \text{ cm}^{-2} \text{ s}^{-1})$	60.8	141	1.29	–
SE	$F_{\text{ul}}^{3\sigma}(> 41 \text{ GeV}; \text{std}) (\times 10^{-5} \text{ cm}^{-2} \text{ s}^{-1})$	79.3	184	1.68	–

Table 6.14: The calculated upper limits on the integral pulsed flux of PSR B1706–44, from single-telescope observations. All ULs were calculated to a  $3\text{-}\sigma$  or 99.95% C.L. The values that were derived from data passing the standard low-energy cuts are denoted by “std”, whereas those derived from the central low-energy cuts are denoted by “ctl”. For the Helene UL, the pulsed emission was assumed to be contained in the phase range [0.25,0.55]. For the UL from the  $C_1$  test, the event phases were centred on  $\phi = 0.4$ . The power-law upper limits are based on a single power law with  $\nu = 2.1$ , whereas the EXP and SE cases correspond to the assumption of the same power law but with an exponential and super-exponential cut-off at  $E_c = 40$  GeV, respectively.

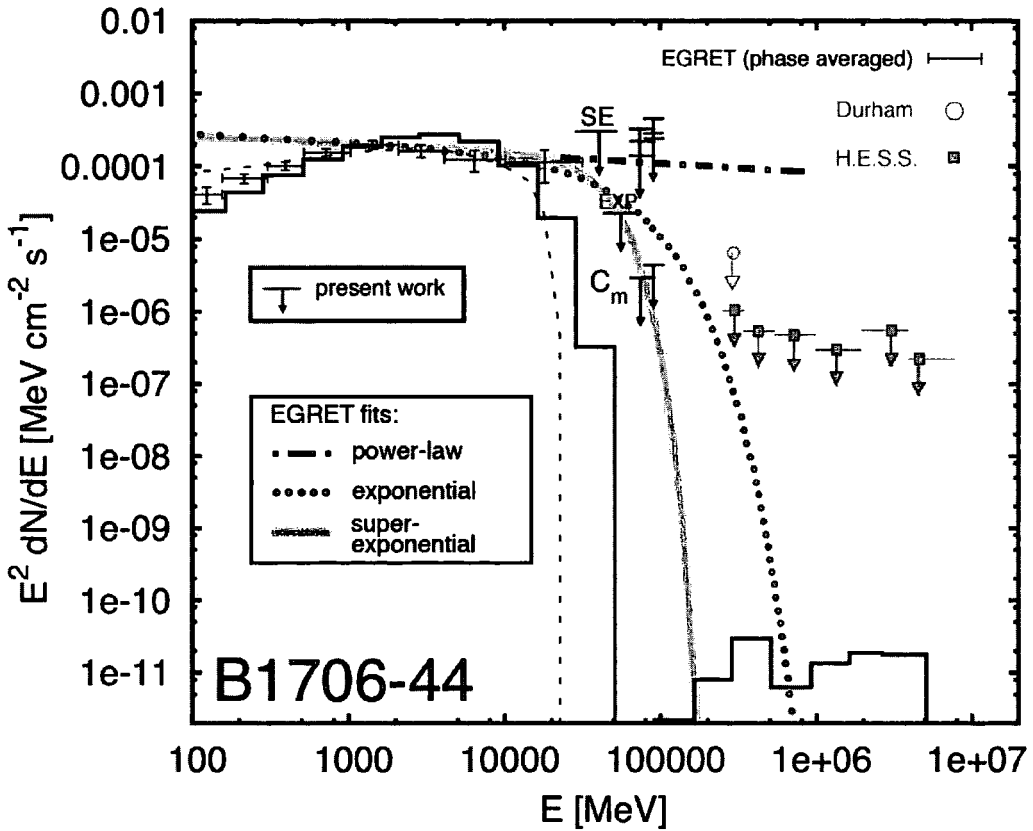


Figure 6.18: The derived ULs on the differential pulsed flux of PSR B1706–44, from the various statistical tests, after the application of our low-energy cuts. All values correspond to single-telescope data. The predicted Outer Gap (thick solid line) and Polar Cap (dashed line) spectra are shown for comparison. The dashed–dotted line in the energy range of our ULs represents a single power-law fit to the EGRET data, with  $\nu = 2.1$ . The grey, solid and dotted lines correspond to the same power law, but with a super-exponential (SE) and exponential cut-offs at  $E_c = 40$  GeV, respectively. Previous ULs from H.E.S.S. and Durham that were shown earlier in this thesis have been dimmed out. Our calculated ULs are clearly lower in energy than those from previous investigations. However, due to the large background involved with our analysis, they are also up to 3 orders of magnitude larger. As in the case of the Crab pulsar, the  $C_m$  test produced the lowest ULs compared to other tests. The UL at 40 GeV, labelled SE, has been calculated from the  $C_m$  test assuming the super-exponential spectrum shown. Finally, the UL at 56 GeV, labelled EXP, has been derived from the same power-law spectrum as above, with an exponential cut-off at 40 GeV.

this spectrum,  $\nu_{\text{DC}} = 2.7$ , is roughly a unit softer than that assumed in our pulsed analysis. This is however expected, as the hypothesised astrophysical mechanism that produces the steady TeV emission is clearly different to that of the pulsed emission, as described earlier. However, the synchrotron-emitting electrons that interact with the B2e star's photon field are likely to be responsible for both the pulsed  $\gamma$  rays, as well as the detected TeV emission. Hence, in terms of energy flux, it would be interesting to compare the percentage of the pulsar's power that goes into pulsed  $\gamma$  rays, with that which is responsible for the observed TeV emission. Fig. 6.19 shows the ULs on the differential pulsed flux and compares them with the TeV spectrum, which was constructed from partially overlapping observations with those used in our analysis.

A direct comparison between our results and the DC spectrum implies, of course, that this spectrum extends down to our low-energy thresholds. Under this assumption, we have integrated the differential spectrum above our low-energy threshold ( $\sim 250$  GeV), which resulted in  $F(> 250 \text{ GeV}) = 8.07^{+1.46}_{-1.67} \times 10^{-12} \text{ cm}^{-2} \text{ s}^{-1}$ . Ultimately, our ULs place constraints on the flux of the pulsed emission, which vary in this energy range from  $\approx 3.5\%$  of the detected TeV flux to as much as 10 times higher than that. It seems unlikely that, if such emission existed at such levels, it would not have been detected with H.E.S.S. However, one has to bear in mind that the instrument's sensitivity declines rapidly with decreasing energy threshold.

### 6.3.5 Upper Limits on the Cut-off Energy of Exponential and Super-Exponential Spectra

Most of our calculated ULs on the flux were consistent with the corresponding EXP and SE spectra with cut-offs at tens of GeV. In the case of PSR B1706–44, our lowest UL values are incompatible with an EXP fit to the EGRET data. However, the rest of our results permit the spectral cut-offs to be at a higher energy. Consequently, one can set a  $3\text{-}\sigma$  UL on the cut-off energy,  $E_c^{3\sigma}$ , by constraining the integral flux of an assumed SE spectrum above the energy threshold,  $E'_{\text{th}}$ , with our single power-law ULs. In addition, the differential flux of the SE spectrum at  $E'_{\text{th}}$  must be consistent with the corresponding ULs. These conditions translate into the mathematical expressions below (based on Eq. 3.22):

$$K \cdot \int_{E'_{\text{th}}}^{\infty} \left( \frac{E}{1000 \text{ MeV}} \right)^{-\nu} \exp \left[ - \left( \frac{E}{E_c} \right)^b \right] dE \leq F_{\text{ul}}^{3\sigma} (> E'_{\text{th}}) \quad (6.5)$$

		Rayleigh	$H$ -test	$C_2$ test		Helene ( $p_{ul}\%$ )
				main peak	second peak	
power law	$F_{ul}^{3\sigma}(> 248 \text{ GeV}; \text{std}) (\times 10^{-10} \text{ cm}^{-2} \text{ s}^{-1})$	0.26	0.24	$4.94 \times 10^{-3}$	$3.3 \times 10^{-3}$	0.45 (0.47)
	$F_{ul}^{3\sigma}(> 254 \text{ GeV}; \text{ctl}) (\times 10^{-10} \text{ cm}^{-2} \text{ s}^{-1})$	0.35	0.39	$7.3 \times 10^{-3}$	$3.76 \times 10^{-3}$	0.62 (0.48)

Table 6.15: The calculated upper limits on the integral pulsed flux of PSR B1259–63 from stereo observations. All ULs were calculated to a  $3\text{-}\sigma$  or 99.95% C.L. The values that were derived from data passing the standard cuts are denoted by “std”, whereas those derived from the central image cuts are denoted by “ctl”. For the Helene UL, the pulsed emission was assumed to be contained in the phase range  $[0.88, 0.11] \cup [0.30, 0.50]$ . For the UL from the  $C_2$  test, the event phases were centred on  $\phi = 0$  and  $\phi = 0.4$ , for the main and second peak, respectively. All upper limits are based on a single power law with  $\nu = 1.76$ .

		Rayleigh	$H$ -test	$C_2$ test		Helene
				main peak	second peak	
power law	$(248 \text{ GeV})^2 [dN(248 \text{ GeV}; \text{std})/dE]_{\text{ul}}^{3\sigma} (\times 10^{-6} \text{ MeV cm}^{-2} \text{ s}^{-1})$	4.9	4.63	0.092	0.062	8.62
	$(254 \text{ GeV})^2 [dN(254 \text{ GeV}; \text{ctl})/dE]_{\text{ul}}^{3\sigma} (\times 10^{-6} \text{ MeV cm}^{-2} \text{ s}^{-1})$	6.9	7.54	0.14	0.072	12.04

Table 6.16: Upper limits on the differential energy flux  $E'_{\text{th}}{}^2 [dN(E'_{\text{th}})/dE]_{\text{ul}}^{3\sigma}$  of PSR B1259–63, at the respective energy thresholds of our data sets,  $E'_{\text{th}}$ , after the standard (“std”) and central (“ctl”) cuts. All ULs were calculated to a  $3\text{-}\sigma$  or 99.95% C.L.



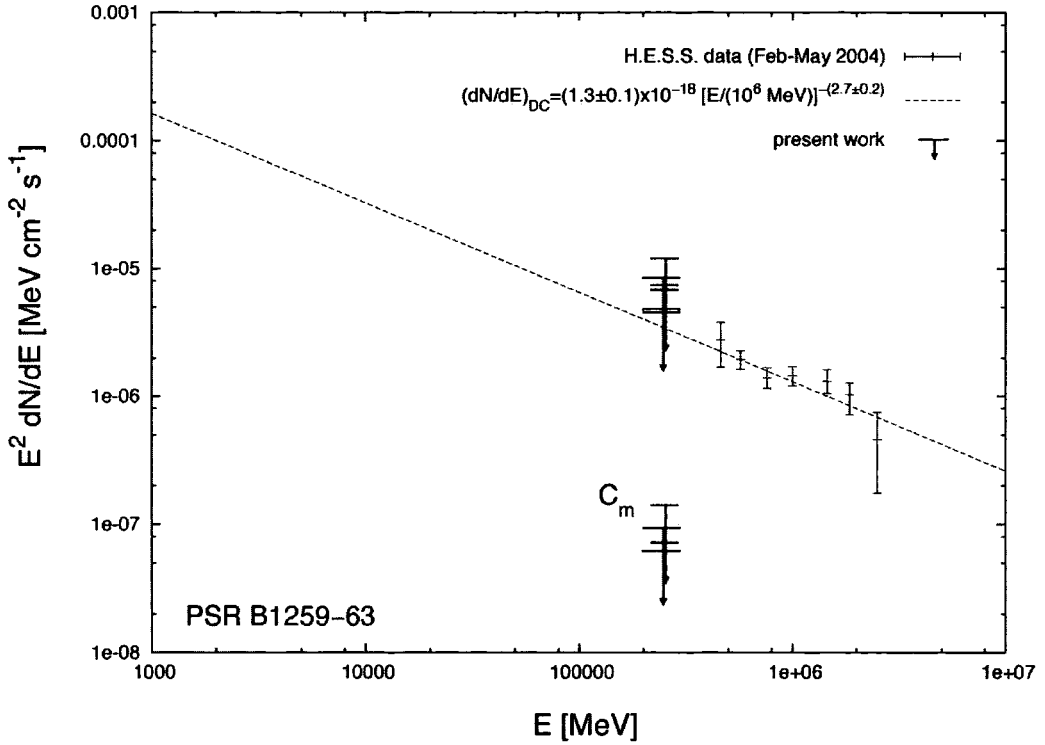


Figure 6.19: The derived ULs on the pulsed emission of PSR B1259-63 from data taken in the period April-June 2004. Only data that passed the standard and central low-energy cuts were used for the calculations. These ULs assume a single power-law spectrum for the pulsed emission, with  $\nu = 1.76$ . The lowest group of ULs shown has been derived with the  $C_m$  test, which systematically produces the lowest UL values, as it assumes that the emission occurs at a specific phase. In this plot, we have also included the DC spectrum from TeV  $\gamma$  rays produced by the PSR B1259-63/SS 2883 system, as it was derived from H.E.S.S. observations during the period from February to May 2004 [117]. Here, the fit to the data has been extended to lower energies in order to directly compare it with our ULs.

$$K \cdot \left( \frac{E'_{\text{th}}}{1000 \text{ MeV}} \right)^{-\nu} \exp \left[ - \left( \frac{E'_{\text{th}}}{E_c} \right)^b \right] \leq \left[ \frac{dN}{dE}(E'_{\text{th}}) \right]_{\text{ul}}^{3\sigma} \quad (6.6)$$

where  $K$  is the normalisation flux at 1 GeV, and  $\nu$  is the spectral index of the EGRET power law (see Table 3.2). Depending on the desired spectral shape, one can choose  $b = 1$  or  $b = 2$  for a simple exponential or super-exponential cut-off at  $E_c$ , respectively.

A similar calculation of ULs on the EXP cut-off energy has already been done for the Crab and Vela pulsars as well as for PSR B1706–44, by F. Schmidt [256], who applied the H.E.S.S. standard cuts to the data (see Eq. 3.22). In our analysis, the flux ULs were derived from various data sets using a number of different statistical tools. For the above calculation, we selected only the most constraining ULs above each energy threshold: in all cases this corresponds to the results from the  $C_m$  test. Our results are shown in Tables 6.17 and 6.18, where we have included the values of  $E_c^{3\sigma}$  from the integral and differential flux constraints. The final column of this table shows the tightest constraint of the two, which coincides with the one imposed by the ULs on the differential flux. A notable result is that of PSR B1706–44 for an EXP cut-off. As mentioned earlier, the derived ULs from the  $C_m$  test reject the simple exponential model. This resulted in the ULs on  $E_c$  to coincide with EGRET's top energy bin, where pulsed emission has been detected up to  $20 \pm 10$  GeV without showing a spectral break [24].

	$K$ ( $\text{cm}^{-2} \text{s}^{-1} \text{MeV}^{-1}$ )	$\nu$	$E'_{\text{th}}$ (GeV)	$E_c^{3\sigma}(F_{\text{ul}}^{3\sigma})$ (GeV)	$E_c^{3\sigma}([dN/dE]_{\text{ul}}^{3\sigma})$	$E_{c(\text{min})}^{3\sigma}(1\sigma \text{ C.L.})$
Crab pulsar	$24 \times 10^{-11}$	2.08	$242 \pm 39$	$85 \pm 18$	$56 \pm 14$	$56 \pm 14$
			$232 \pm 51$	$82 \pm 24$	$54 \pm 19$	$54 \pm 19$
			$272 \pm 42$	$112 \pm 24$	$140 \pm 28$	$72 \pm 18$
PSR B1706–44	$20.5 \times 10^{-11}$	2.1	$75 \pm 12$	$30 \pm 7$	$20 \pm 5$	$20 \pm 5$
			$90 \pm 12$	$42 \pm 8$	$26 \pm 6$	$26 \pm 6$

Table 6.17:  $3\text{-}\sigma$  ULs on the EXP cut-off energy for the Crab pulsar and PSR B1706–44 (last column). The derived values correspond to the minimum cut-off energy that satisfies equations 6.5 (column 5) and 6.6 (column 6) with  $b = 1$ . The selected ULs are given to a  $1\text{-}\sigma$  C.L. All values of  $E_c^{3\sigma}$  have been derived based on a power-law fit to the EGRET data, with spectral index  $\nu$ , a normalisation flux at 1 GeV equal to  $K$ , and an unknown EXP cut-off energy,  $E_c$ . Then, the value of  $E_c$  was constrained independently by our  $3\text{-}\sigma$  ULs on the integral and differential flux. Within  $1\text{-}\sigma$  statistical error, the derived value of  $E_c^{3\sigma}$  can be said to satisfy both ULs. Note that both derived ULs for PSR B1706–44 are incompatible with EGRET’s top energy bin, at  $20 \pm 10$  GeV, where emission *has* been observed.

	$K$ ( $\text{cm}^{-2} \text{s}^{-1} \text{MeV}^{-1}$ )	$\nu$	$E'_{\text{th}}$ (GeV)	$E_c^{3\sigma}(F_{\text{ul}}^{3\sigma})$ (GeV)	$E_c^{3\sigma}([dN/dE]_{\text{ul}}^{3\sigma})$	$E_{c(\text{min})}^{3\sigma}(1\sigma \text{ C.L.})$
Crab pulsar	$24 \times 10^{-11}$	2.08	$242 \pm 39$	$156 \pm 30$	$117 \pm 24$	$117 \pm 24$
			$232 \pm 51$	$150 \pm 39$	$112 \pm 31$	$112 \pm 31$
			$272 \pm 42$	$193 \pm 35$	$140 \pm 28$	$140 \pm 28$
PSR B1706–44	$20.5 \times 10^{-11}$	2.1	$75 \pm 12$	$53 \pm 10$	$38 \pm 8$	$38 \pm 8$
			$90 \pm 12$	$69 \pm 11$	$49 \pm 8$	$49 \pm 8$

Table 6.18:  $3\text{-}\sigma$  ULs on the SE cut-off energy for the Crab pulsar and PSR B1706–44 (last column). The derived values correspond to the minimum cut-off energy that satisfies equations 6.5 (column 5) and 6.6 (column 6) with  $b = 2$ . The selected ULs are given to a  $1\text{-}\sigma$  C.L. All values of  $E_c^{3\sigma}$  have been derived based on a power-law fit to the EGRET data, with spectral index  $\nu$ , a normalisation flux at 1 GeV equal to  $K$ , and an unknown SE cut-off energy,  $E_c$ . Then, the value of  $E_c$  was constrained independently by our  $3\text{-}\sigma$  ULs on the integral and differential flux. Within  $1\text{-}\sigma$  statistical error, the derived value of  $E_c^{3\sigma}$  can be said to satisfy both ULs.

## Chapter 7

# Summary and Future of H.E.S.S. Pulsar Observations

### 7.1 Summary of Results

We have searched for pulsed emission in the VHE range from two EGRET pulsars, the Crab and PSR B1706–44, that are known to emit GeV  $\gamma$  rays modulated with their respective radio frequencies. In addition, we applied the same statistical methods to the case of PSR B1259–63, which is a radio pulsar that has not been detected pulsing at higher energies. Our work aimed at the analysis of the least energetic showers detectable with H.E.S.S., from observations of the above pulsars. This approach was motivated both by the EGRET observations, which showed that pulsar emission extends up to at least 20 GeV, but also by preceding theoretical work, which predicts that the corresponding spectra die out somewhere below 100 GeV, where the sensitivity of H.E.S.S. is at least 100 times lower than that at  $\sim 1$  TeV. In order to probe the low-energy capabilities of the instrument, we had to abandon the standard H.E.S.S. event selection, which is optimised for energies above 500 GeV. Instead, we used a set of looser selection criteria that retained all events below  $\sim 200$  GeV, while rejecting most of them at higher energies. As a result, our data contained  $\sim 10^3$  times larger background than that in the standard analysis. However, it was shown that the application of tests for phase uniformity, together with tight constraints on the phases where the pulsed emission is expected to occur, can lead to the detection of periodic emission in a large background. Hence, we applied 4 tests for uniformity to our low-energy data sets: namely a  $\chi^2$ , a Rayleigh, a  $H$  and

a  $C_m$  test.

Our analysis did not discover any significant deviations from the background for any of the pulsars. It is worth mentioning, however, that in the case of the Crab pulsar, the  $C_5$  test produced a  $\approx 2\text{-}\sigma$  result at the main peak position of the radio profile. Furthermore, a  $3\text{-}\sigma$  deviation was found in PSR B1706–44 data when we searched with a  $Z_2^2$  test (a Rayleigh test with 2 harmonics). Despite these indications for possible presence of pulsed emission, in neither case could we confirm these fluctuations with other tests, and  $H_0$  could not be rejected with confidence.

Consequently, our efforts concentrated on the estimation of the maximum allowed  $\gamma$ -ray flux by the statistics, which would lead to the resulting non-detection, given the exposure of each data set. Hence, we calculated ULs on the flux to a  $3\text{-}\sigma$  (or 99.95%) confidence level, based on the analysed data sets. Our primary objectives were to place constraints on the Outer Gap and Polar Cap models, which provide a clear prediction with regards to the GeV spectra of the pulsed emission from EGRET pulsars. Such predictions were not available for PSR B1259–53, and we were forced to use the derived spectrum from the detection of unpulsed (steady) emission, as a reference.

Although we did not manage to constrain the predictions of the two main astrophysical models, Polar Cap and Outer Gap, our ULs are at the *lowest* energies reported yet, for the sources we investigated with H.E.S.S., above EGRET’s energy range. In the cases of the Crab pulsar and PSR B1706–44, our values reject the scenario of a single power-law spectrum that extends from the EGRET range to the investigated VHE range. Moreover, this is the *first* time that ULs based on exponential and super-exponential spectra are being derived with the use of the popular  $H$  and Rayleigh tests, but also with the recently introduced  $C_m$  test. In one instance, that of PSR B1706–44, our lowest ULs on the flux rule out completely a simple exponential cut-off above the EGRET observations and are marginally consistent with the super-exponential cut-off hypothesised by de Jager *et al.* Moreover, we produced the first quantitative estimates of the maximum allowed cut-off energy by our ULs for both exponential and super-exponential spectral decays, for all three pulsars discussed here. In the case of the Crab pulsar, these energies are in the unexplored energy region above EGRET’s top energy bin, so a spectral break has not been observed, yet. However, the maximum cut-off energy for PSR B1706–44 assuming an exponential decay coincides with EGRET’s top bin, where such spectral behaviour has not been seen; hence, we are forced to accept that the spectrum

must exhibit a steeper decline above  $20 \pm 10$  GeV, which allows it to possibly be super-exponential.

In Fig. 7.1 we compare the sensitivity of our periodicity searches, for each of the three pulsars studied herein, with that of H.E.S.S. Phase I. Note that the sensitivity curve for H.E.S.S. corresponds to the minimum required integral flux for a  $5\text{-}\sigma$  detection of an overhead steady source, after 50 h exposure time; and the steady source is assumed with a spectral index equal to the Crab's DC spectrum ( $\nu \approx 2.59$ ). The equivalent sensitivity ranges for pulsar emission have been derived for the same detection level and exposure time, but with the Z.A.s and assumed spectra varying with object type. Furthermore, the height and width of the coloured areas, for the three pulsars, correspond to the range of test sensitivities and the uncertainty in the determination of the threshold energy for each case, respectively. It is important to note that these results do not represent the general performance of the aforementioned uniformity tests but were based on the resulting event rates from our cut data sets. Hence, a different selection criteria would alter the above picture.

## 7.2 A Brighter Future: H.E.S.S. Phase II

A significant, reproducible detection of pulsed VHE  $\gamma$ -ray emission is yet to be achieved by modern Cherenkov experiments. Despite their superior sensitivity to present satellite observatories, they have not been able to close the energy gap that separates them from space-borne observations. If one looks at the Outer Gap predictions for Vela and PSR B1706–44 (Fig. 5.9), it becomes clear that the integral flux across the 10-GeV neighbourhood drops by roughly 5 orders of magnitude from EGRET's top energy bin to 50 GeV. However, even the minimum sensitivity stated for H.E.S.S., at 100 GeV, is 3 orders of magnitude higher than EGRET's and enough to detect this component in a matter of days, had the detector's threshold been as low as  $\sim 30$  GeV. Clearly, the Cherenkov experiments are not lacking the required sensitivity, but rather the low energy thresholds that would allow them to intercept the pulsed emission below the sharp cut-offs predicted by the models. We have already mentioned that the main agents for lowering the energy threshold are:

- **Large reflective area**, which allows for a similarly large percentage of a faint shower's light pool to be recorded and, hence, increases the detector's efficiency at low energies.

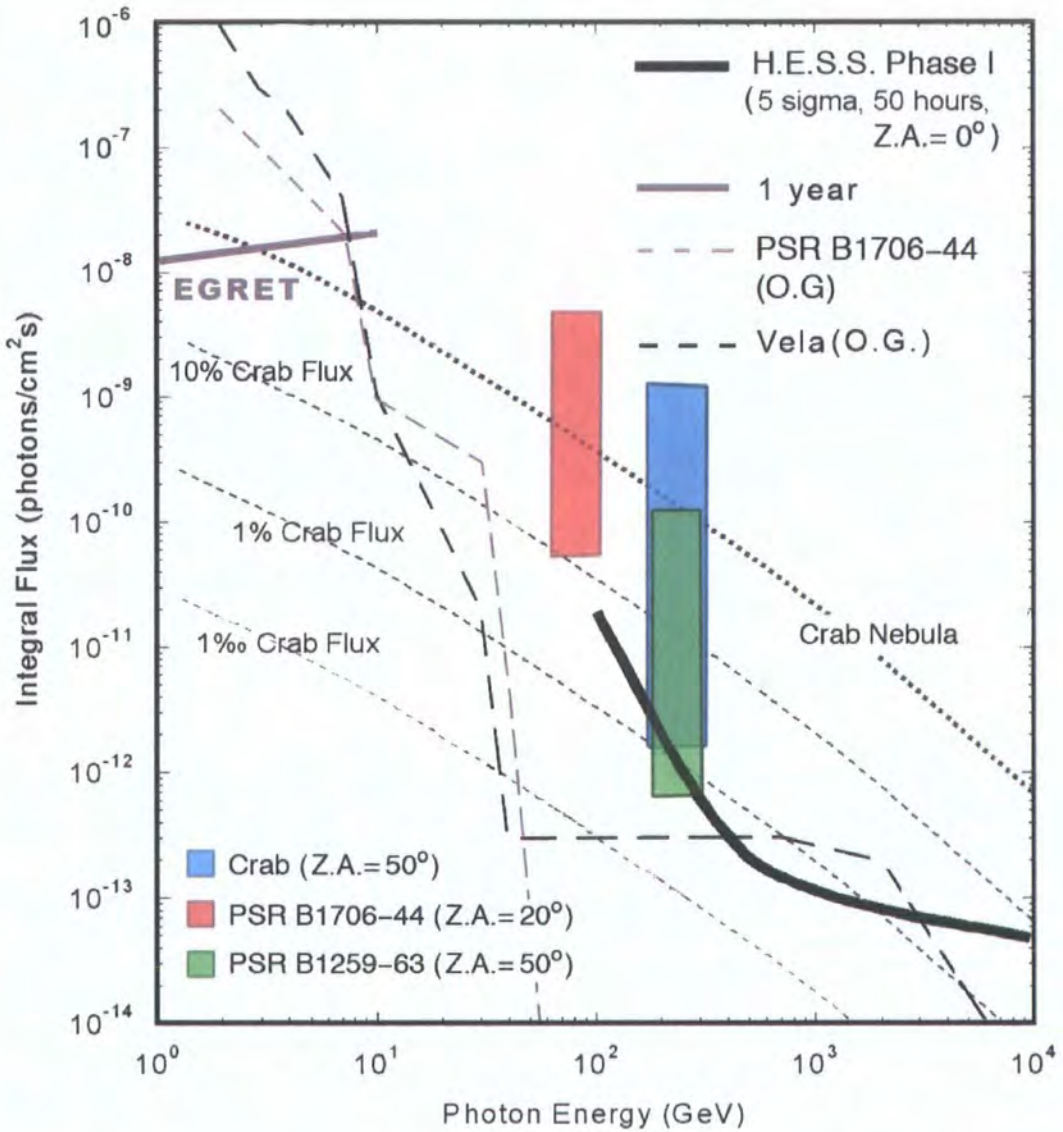


Figure 7.1: The sensitivity of our periodicity searches (red, green and blue bands) compared with that of H.E.S.S. for steady overhead sources (solid, black line). Also shown is the sensitivity of EGRET for 1-y observations of steady sources. In this plot, the sensitivity is expressed as the minimum integral flux above a specific energy, which is required in order to achieve a 5- $\sigma$  detection after 50 h exposure time. The H.E.S.S. sensitivity has been derived under the assumption of a power-law spectrum with spectral index  $\nu = 2.59$  and an effective-area function corresponding to 0° Z.A. The sensitivity ranges from our work were calculated assuming power-law spectra with  $\nu = 2.08, 2.1$  and  $1.76$ , for the Crab pulsar, PSR B1706-44 and PSR B1259-63, respectively, as well as the Z.A.s shown. The vertical spread of the sensitivity for each pulsar represents the results from the various uniformity tests applied, whereas the horizontal spread is due to the uncertainty in the determination of the threshold energies. Finally, the dotted and dashed contours show the flux levels (100, 1 and 0.1%) of Crab's nebular (DC) emission, above a specific energy.



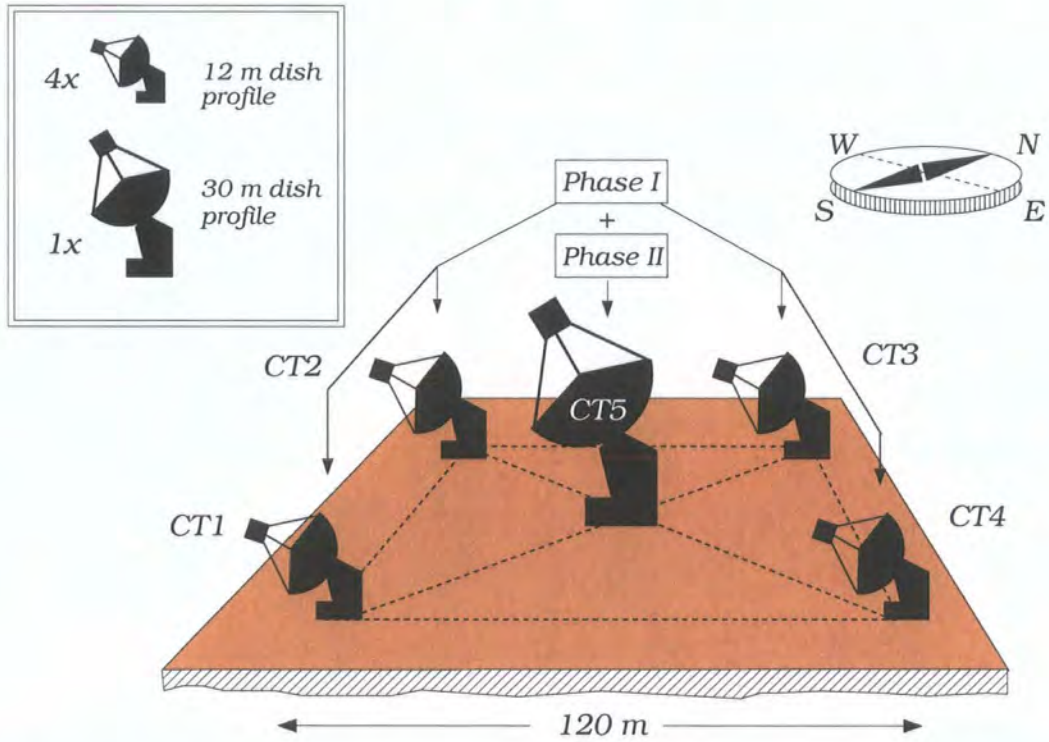


Figure 7.2: The telescope arrangement of H.E.S.S. Phase I and II. The 4 currently operating telescopes of Phase I, CT1–CT4, are arranged in a square formation with 120-m side length. Each telescope dish is 12-m wide (flat-to-flat). The next phase of the H.E.S.S. experiment, Phase II, will include an additional 30-m telescope, CT5, which will be placed in the centre of the current arrangement.

- **Efficient background rejection**, which allows for telescope operation in the energy region where a single telescope would normally suffer from NSB contamination.

These two criteria are the building blocks of the next H.E.S.S. phase, namely H.E.S.S. Phase II. The final configuration of H.E.S.S. Phase II is still under discussion, but it is very likely to be composed of an additional  $\approx 28$ -m telescope, nicknamed “large telescope”, placed in the centre of the current telescope formation (see Fig. 7.2) [451].

In H.E.S.S. Phase II, the mirror design is likely to change drastically from that of Phase I. Although a final decision on the design has not been made yet, it has been proposed to increase the number of mirrors for the large telescope fourfold, and make

	Phase I	Phase II — <i>proposed in 2004</i> (large telescope only)
Number of mirrors (total area)	382 (108 m <sup>2</sup> )	1,600 (600 m <sup>2</sup> )
Material	Aluminised Glass	Aluminium ( $\approx 60\%$ lighter)
Profile	Circular	Hexagonal
Diameter (cm)	60	100
Weight (kg)	11	6.6
Reflectivity (300–600 nm)	$> 80\%$	$\approx 90\%$

Table 7.1: (from [331] and [452]) Comparison between the basic properties of the H.E.S.S. Phase I mirrors and that proposed for the H.E.S.S. Phase II in 2004.

the profile hexagonal instead of circular, which will allow closer packing between the mirrors and, thus, increase the amount of collected light on the camera (by  $\approx 25\%$ ) for equivalent dish areas. For the mirrors of Phase I, this design was proven to be costly, since the process of shaping spherical, glass mirrors into hexagons is more complex. However, the new mirrors of Phase II are likely to be made of aluminium sheets that are easier to cut and have further advantages: including e.g. better weather endurance (see Table 7.1). Aluminium mirrors are constructed by vacuum-pressing the sheets on a spherical mould and then gluing them on honeycomb filler and lightweight bases [452]. Hence, they will be a lot lighter and cheaper than glass mirrors. Also, their high-reflectivity surface, optimised for Cherenkov light (300–600 nm), is expected to reflect  $\approx 90\%$  of the light back to the camera. A comparison between the Phase I mirror design and that proposed in 2004 for H.E.S.S. Phase II is presented in Table 7.1.

However, the design of the Phase II reflector will not follow the Davies–Cotton design of the Phase I telescopes. For such a telescope, which aims at even lower energy thresholds, timing is everything. At low energy thresholds, the number of triggers that one gets from the faint Cherenkov showers is comparable to the number of accidental NSB triggers (see Fig. 4.9). The magnitude of the latter can be appreciated if one considers its enormous flux which is  $\sim 10^8 \text{ cm}^{-2} \text{ s}^{-1}$  in the 300–600 nm range [51]. As was explained in section 4.3.1, a Davies–Cotton design with small spherical mirrors and a spherical dish radius of  $\approx 15 \text{ m}$  introduces a time spread to the Cherenkov photons that arrive at the camera plane, due to the asynchronous dish surface; the size of the spread is comparable to the duration of a Cherenkov event: i.e.  $\Delta\tau_w \approx 2 \text{ ns}$ . Therefore, one can use time windows  $\tau_w \approx 16 \text{ ns}$

that will allow the total Cherenkov light to be recorded, while including the least possible amount of NSB (see section 4.2). Nevertheless, a Phase II spherical reflector, which is roughly twice as wide, will have substantially longer delays between photons reflected on the edge of the dish and those reflected on the centre. Ray-tracing simulations of incident 10-GeV  $\gamma$  rays reflected on such dish have shown that the time spread introduced is up to 11 ns [453]. Unavoidably, longer integration times would then have to be used in order to collect all the light from the Cherenkov events. Clearly, this would introduce an unnecessarily large amount of NSB with every event, which would lower the signal-to-noise ratio and increase the energy threshold (see Eq. 4.15). In order to fulfil the low-energy expectations from the large Phase II detector, the timing has to be improved. Therefore, the current decision for Phase II is the implementation of an isochronous parabolic dish instead of a spherical one. Identical ray-tracing simulations to those above were applied to a 20-m reflector and showed that the improvement is by  $\approx 4.5$  times, which reduces the delays to a maximum of  $\approx 2.5$  ns.

The large telescope will be used in coincidence mode together with the rest of the H.E.S.S. telescopes, which will slightly increase the instrument's overall sensitivity compared to Phase I, at the same energies (Fig. 7.4). However, the power of H.E.S.S. Phase II lies in single-telescope observations that will lower the energy threshold of the observations below 50 GeV (see Fig. 7.3). The increased sensitivity and the extension towards lower energies in H.E.S.S. Phase II observations will consequently increase the trigger rate of the system. (In the energy range of interest, below 100 GeV, the cosmic electrons and positrons contribute equally as much to the total Cherenkov events as the proton background; see Fig. 4.11.) In particular, single-telescope observations with the 28-m telescope alone are expected to result in trigger rates of  $\approx 5$  kHz. Such high rates cannot be sustained by the DAQ and have to be constrained using additional trigger criteria. Hence, apart from the standard pixel and sector thresholds (Level 1 trigger), a more complex trigger condition (Level 2 trigger) will be implemented. Although the final decision has not been made yet, the possibilities for the Level 2-trigger conditions consider a pixel-clustering criterion: more specifically, images which are formed by  $n$  separate clusters of  $k$  adjacent pixels will be considered only if  $n$  is sufficiently low, say 1 or 2; that imposes a constraint on scattered images, which are likely to originate from hadrons. The resulting trigger rates from simulations are  $< 3$  kHz for single large-telescope observations below 50 GeV. There have been many discussions on

the decision for the Level 2 trigger throughout the H.E.S.S. collaboration; and the reader can find some preliminary information in [451],[390].

The energy regime of H.E.S.S. Phase II will overlap with that of *GLAST* in the GeV range, thus bridging space-borne and ground-based experiments. Parallel observation of steady sources will allow for inter-calibration of both experiments: H.E.S.S. will use *GLAST* data to estimate its systematic errors (NSB noise), and *GLAST* will estimate its statistical errors (low event numbers) using H.E.S.S. data (Fig. 7.5).

### 7.2.1 H.E.S.S. Phase II Detection Rates

The large telescope of H.E.S.S. Phase II, operating in single-telescope mode, is certain to close the gap between EGRET and Cherenkov observations. Moreover, its effective area will be 6 orders of magnitude larger than EGRET's, which implies similarly higher detection rates. To quantify this, we performed some preliminary calculations based on the predicted effective-area functions for the large telescope (Fig. 7.7) and the SE spectra for the EGRET pulsars by de Jager *et al* [238]. Using our estimated detection rates for pulsed emission, we then proceeded with the calculation of the minimum required exposure time for a  $5\text{-}\sigma$  detection with a  $\chi^2_{19}$ -test (Eq. 5.58). For each pulsar, we adopted the standard value for the duty cycle,  $\delta$ , as it was given in the respective discovery publication (see Table 3.3). The background rate was fixed to 1 kHz, which seems rather high compared to that of present observations (typically below  $\sim 200$  Hz), but one has to consider the much-higher expected trigger rate for Phase II: the large telescope, operating in stand-alone mode, will not benefit from stereoscopic reconstruction that rejects most of the background; and the Hillas parametrisation will be similarly poor at the lowest energies detectable, as it was in our analysis (see Fig. 7.6). Hence, the full set of cuts might not be applicable, which will result in data rates not significantly lower than those before cuts.

Table 7.2 presents the resulting detection rates and the minimum required exposure times for a detection. In this table, the estimated  $\gamma$ -ray rates for H.E.S.S. Phase II, above 10 GeV, are compared with the EGRET detection rates above 100 MeV. In nearly all cases, the latter were approximated by  $F_\gamma(> 100/\text{MeV}) \times A_{\text{eff}}$ , where the effective area was assumed constant and equal to  $A_{\text{eff}} = 10^3 \text{ cm}^2$ . A first remark can be made about the detection rates of H.E.S.S. Phase II, which are  $\sim 100$  times higher than EGRET's. The exception in this case is the Geminga pulsar, whose

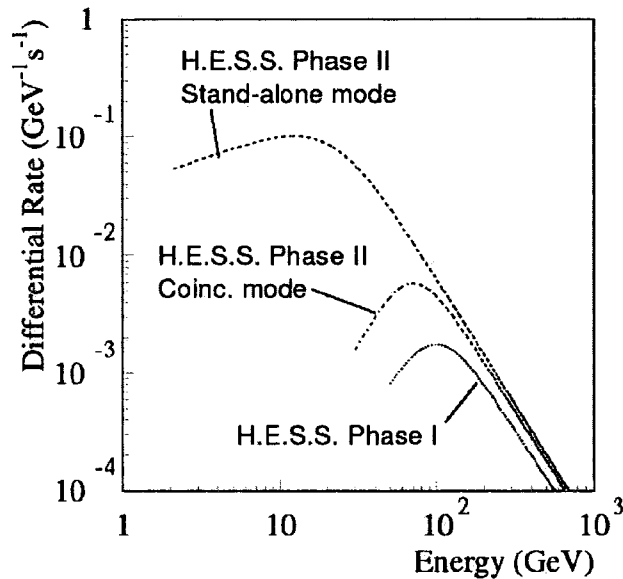


Figure 7.3: (from [390]) Predicted energy thresholds — defined as the peak of differential rates — for H.E.S.S. Phase I and H.E.S.S. Phase II, in stereo and single-telescope modes. It can be seen that stand-alone observations with the large telescope of Phase II involve substantially higher trigger rates than their stereo counterparts. Moreover, fainter (lower-energy) events can be detected with a single-telescope configuration, with a larger fraction of them being below the maximum differential rate than in stereo mode. However, there are significant advantages to be gained from stereoscopic observations with H.E.S.S., which are not evident in this plot. The telescope separation allows to record the same shower from different viewpoints on the ground, which provides better spatial resolution and better determination of the  $\gamma$ -ray energy. Consequently, VHE observations become more accurate with stereoscopy, and sources of VHE emission are better resolved on the sky maps.

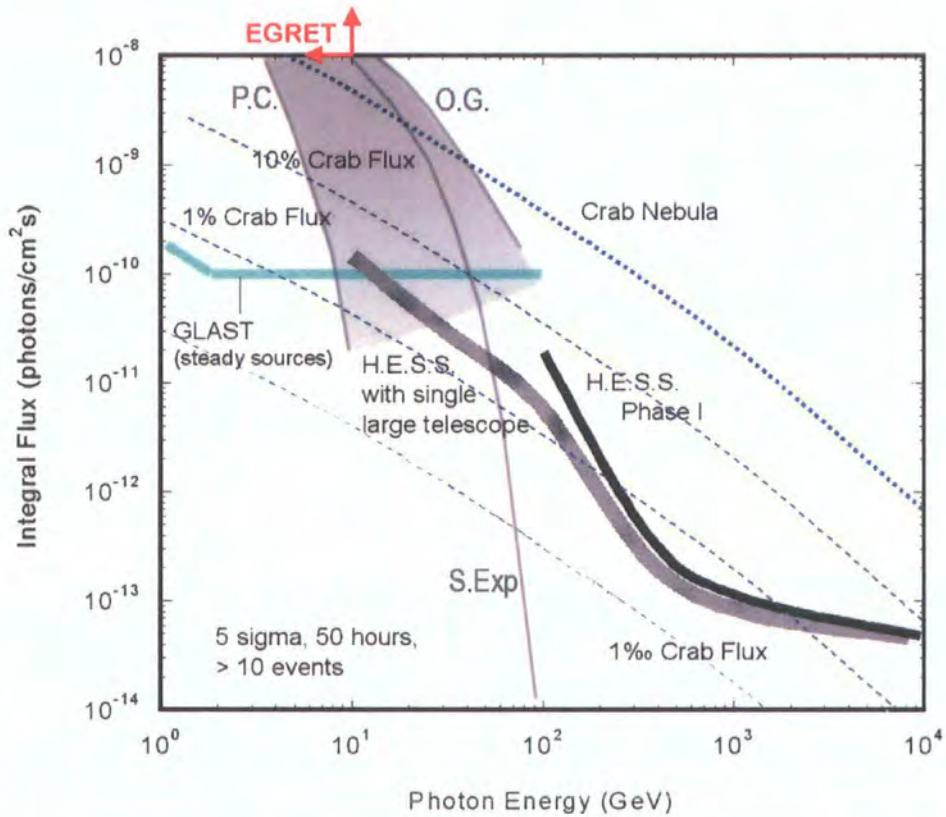


Figure 7.4: (from [390]) Predicted sensitivity of H.E.S.S. Phase II (stand-alone mode) and *GLAST* (steady sources) compared with that of H.E.S.S. Phase I. The calculated integral fluxes were based on 50-h data sets, which gave  $5\sigma$  and contained more than 10 events. The grey-shaded section in this plot represents the spectral range of the theoretical predictions for the Crab pulsar. The low-energy boundary of this section is defined by the steep Polar Cap spectra, whereas the high-energy boundary corresponds to the gentler Outer Gap spectra. The spectrum in between represents Crab pulsar's super-exponential model spectrum. The dotted lines running across this figure represent the 100, 10, 1 and 0.1% flux levels of the Crab nebular emission. EGRET's sensitivity range is outside the scale shown, and the arrows have been used to mark the position of its top energy bin.

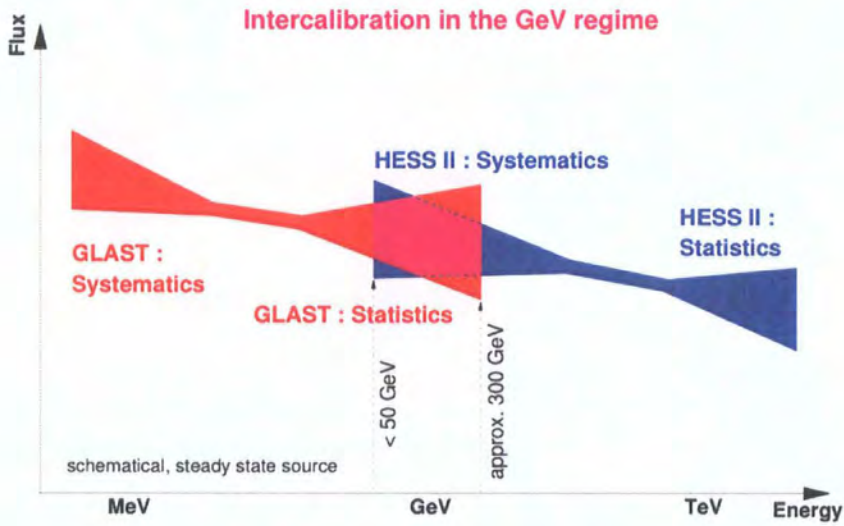


Figure 7.5: (from [390]) The overlap of *GLAST* and H.E.S.S. Phase II observations in the GeV range could help towards the estimation of the corresponding statistical and systematic errors, respectively. The low-energy tail of both experiments is dominated by systematic errors inherent with the detectors: *GLAST*'s angular resolution degrades and H.E.S.S. suffers from increased NSB noise. On the other hand, at the highest energies of each experiment's regime, the statistical errors dominate and the number of detectable events decreases.

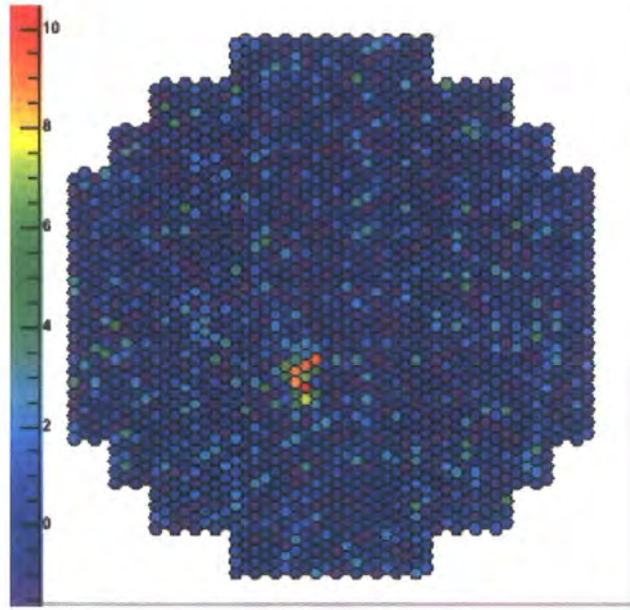


Figure 7.6: (from [454]) A simulated 20-GeV event as it is expected to appear on the camera plane of the large telescope of H.E.S.S. Phase II. The vertical, colour-graduated scale corresponds to the significance of the signal-excess levels above the background. Such low-energy events will be detectable with H.E.S.S. Phase II, but their Hillas parametrisation will be limited due to their low ph.e. content. Analysis methods similar to ours could then be used to recognise their periodic nature that has already been detected at these energies with EGRET.



spectral cut-off is already evident in the EGRET range and was assumed here to be at 5 GeV, which is below the predicted threshold of the large telescope. In addition, Geminga's low altitude above the horizon conspires towards the miniscule event rate shown here, although surprisingly not beyond comparison to EGRET's, which is only 10 times higher. On the other hand, PSR B1706–44 manages to produce 1,000 times higher pulsed  $\gamma$ -ray rate, which is mainly attributed to the combination of relatively high cut-off energy (40 GeV) and low Z.A. — and hence a significant effective area below the cut-off. In general, we found that only 3 EGRET pulsars are detectable within the detector's lifetime: upon completion of H.E.S.S. Phase II, PSR B1706–44 and Vela will be detected in a matter of hours, whereas the Crab pulsar, in tens of hours of observation. The rest of the EGRET pulsars are either too weak as  $\gamma$ -ray emitters (i.e. PSR B1055–52) or their large Z.A.s at culmination places their integral flux — above the detector's threshold — below the telescope's sensitivity.

The present work has provided a methodology towards the extraction and possible detection of the least energetic  $\gamma$  rays observed with H.E.S.S. Our analysis techniques can be easily applied to data from H.E.S.S. Phase II; doing so will help us recognise the pulsed emission seen with EGRET below 20 GeV and connect the results from space-borne observations with those from the ground. Nevertheless, there is room for improvement. The next section discusses these possibilities.

## 7.3 Potential Improvements on the Present Analysis Methods

### 7.3.1 Introduction

Our approach towards focusing on the lowest energies in the H.E.S.S. pulsar data and then extracting a possible periodic signal utilised very sensitive tests for uniformity, as well as a number of event-selection criteria. Nevertheless, certain features of the analysis can be made even more sensitive to sparse, low-energy events. In this section we will focus on two aspects of our search for GeV pulsations, which can be significantly improved upon: (a) the choice of a statistical test which would detect faint, low-signal-to-noise pulses and define their properties accurately; and (b) the process of selecting a *size* cut, which would increase the signal-to-noise ratio at low energy thresholds.

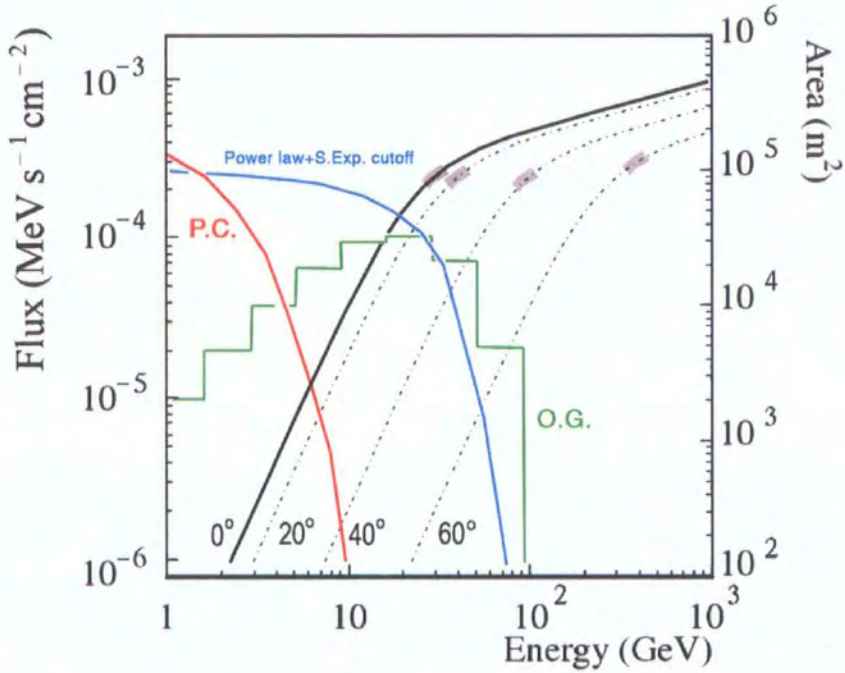


Figure 7.7: The predicted effective area of H.E.S.S. Phase II (stand-alone mode) as a function of energy, for *overhead* sources (solid black line) [455]. The effective-area functions for larger Z.A.s (dashed-dotted lines) were assumed to scale with Z.A. in the same way as for a single telescope of the current array [384]. The grey-shaded areas correspond to the energy threshold's position for each Z.A. The overlaid spectra are the Polar Cap (P.C.) and Outer Gap (O.G.) predictions for the Crab pulsar; and the blue line represents a power-law fit to EGRET data from the Crab pulsar, with a super-exponential cut-off at 30 GeV.

Pulsar	$R_{\gamma}^{\text{Phase II}}(> 10 \text{ GeV})$ (Hz)	$R_{\gamma}^{\text{EGRET}}(> 100 \text{ MeV})$ (Hz)	$\geq T(5\sigma)$
Crab	0.2	$3 \times 10^{-3}$	40 h
Vela	1	0.01	$\sim 1$ h
PSR B1706–44	2	$10^{-3}$	$\sim 1$ h
PSR B1951+32	$9 \times 10^{-3}$	$10^{-4}$	–
Geminga	$2 \times 10^{-4}$	$4 \times 10^{-3}$	–
PSR B1055–52	0.04	$2 \times 10^{-4}$	–

Table 7.2: Estimated detection rates above 10 GeV, from future observations of EGRET pulsars with the large telescope of H.E.S.S. Phase II. The calculations were based on the predicted SE spectra by de Jager *et al.* and the simulated effective areas of Fig. 7.7. The third column presents the resulting event rates above 100 MeV, from EGRET observations of the same sources: the latter were calculated under the assumption of a constant effective area (i.e.  $10^3 \text{ cm}^2$ ) and are based on the reported integral fluxes above 100 MeV. The last column contains the minimum required exposure times for a  $5\text{-}\sigma$  detection of these sources, which were derived from the rates of column 2 using Eq. 5.58, with the background rate fixed to 1 kHz. For the last three pulsars, the required exposure time exceeds  $\sim 1,000$  h of observation, and hence they qualified as undetectable (denoted by “–”), within the detector’s lifetime.

### 7.3.2 Improving the Statistics

The analysis presented in this thesis followed the so-called *frequentist* approach: we used tests like the  $\chi^2$ , the  $H$ -test, etc. Although the procedures based on this approach have been particularly popular in the analysis of astronomical data, it has a number of disadvantages — albeit also a few advantages. These disadvantages can be eliminated by using a fundamentally different notion of the meaning of *probability*, which leads to a more sensitive and accurate search and characterisation of a periodic signal: *Bayesian inference*. A qualitative description of each method and the differences between the frequentist and Bayesian approach are presented in the following paragraphs (for an extensive comparison, the reader is referred to [456]).

#### Frequentist Methods

We saw in section 5.4 that tests for uniformity use statistics ( $Z$ ) which are a measure of how close to uniformity the investigated data set is. Then, the probability of having a certain value of a statistic is given under the assumption of uniformity (the null hypothesis,  $H_0$ ). Therefore, the probability is denoted as  $pr(Z|H_0)$ : i.e. assuming uniformity holds for that data set, what is the probability of  $Z$  to occur in

such a data set. In order to assess  $pr(Z)$  correctly, the probability distribution of the entire population of  $Z$  values must be known; and, of course, that requires a search through an infinite number of periods (or frequencies). In other words, in the frequentist view, probability is the relative frequency with which  $Z$  occurs in a hypothetical, infinite ensemble of independent trials (or experiments).

### Bayesian Inference

On the other hand, the Bayesian approach uses probability to review the plausibility of the assumptions themselves, based on the available information (which could be the number of periods searched) rather than an imaginary infinite set of repetitions. Bayesian methods directly compare the probability of a hypothesis, say  $H_1$ , with that of another, say  $H_2$ , based on the *available* data set, say  $D$ . Then, by calculating the quantities  $pr(H_1|D)$  and  $pr(H_2|D)$ , they assess the viability of a model over another. The degree to which a model, say the  $H_1$ , is better (i.e. matches the observed data better) than another, say the  $H_2$ , is quantified by how much higher  $pr(H_1|D)$  is, compared to  $pr(H_2|D)$ . In a sense, the Bayesian approach makes a direct comparison — via the corresponding probabilities — between the various investigated hypotheses. But there is also another feature of Bayesian tests that is automatically incorporated in the probability calculations: Occam's razor. This well-known principle states that amongst the plausible hypotheses bearing equal probabilities, those that are simpler (i.e. involve fewer free parameters) are preferred. We briefly expand on that statement in the following paragraph, where the key differences between frequentist and Bayesian tests are summarised.

### Summary of the Main Differences between the Two Methods

It has been made clear that the key difference between Bayesian and frequentist methods is that the former considers the probabilities of alternative hypotheses, while using only the available information from observations, whereas the latter does the opposite: it assumes one particular hypothesis (e.g.  $H_0$ ) and compares the probability of the observed data set (e.g.  $D_1$ ), given the truth of  $H_0$  (i.e.  $pr(D_1|H_0)$ ), with those of a number of hypothetical data sets — which were never observed — consistent with  $H_0$ . Given that the only real information we have comes from our observations, the Bayesian approach is more intuitive: we are uncertain of which hypothesis is most realistic given the available data; hence, we try different models

and decide for the one that fits best our observations. On the other hand, frequentist methods reject a hypothesis over not more probable hypotheses — which is the Bayesian approach — but over the results of alternative data sets consistent with the hypothesis in question.

An integral part of the frequentist analyses is the user’s choice of various tools towards the best characterisation of the observed data: e.g. the user has to decide amongst a variety of kernel estimators (the Histogram Estimator, the Fourier Series Estimator, etc.) and try to draw conclusions from the *maximum* test statistic associated with a particular value of the frequency (see section 5.4). Also, in some cases, this involves a user’s choice of the free parameters of the problem (e.g. the number of bins across one period or the central phase on which the analysis is focused). A few of these parameters are sometimes irrelevant to the test’s purpose, which may be revolving around the question, “Is there a significant signal in the data?” Then, these parameters are characterised as *nuisance parameters*. Frequentist tests depend on the user to set those *a priori*, although it has to be said that there *is* a certain number of tests which incorporate an optimisation of the nuisance parameters prior to testing (e.g. *H*-test). All of the above naturally lead to a number of solutions instead of a single one, and it is up to the user to select the best based on the associated outcome probabilities.

On the other hand, Bayesian inference automatically incorporates the best statistics to be used in order to extract the maximum information from the data, and provides a single solution to a problem. A good example of how it does it can be given if one assumes a stepwise model for a pulsar’s lightcurve, like the one realised in the Gregory–Loredo (GL) method [457]. In such a model, the shape of a lightcurve is fully described using  $m - 1$  bins (see section 5.4.1), plus the average data rate, the frequency and the phase: i.e.  $m + 2$  parameters. Virtually any pulse shape can be described using such a model. What Bayesian methods do is to calculate the probability associated with a particular model, based on the *average* values — over the respective ranges — of all those parameters. To be more precise, the probability of the tested periodic model is divided by the equivalent probability of a constant, flat lightcurve. This ratio is the basic tool with which Bayesian methods evaluate the plausibility of various models; and Occam’s razor arises from the averaging. Furthermore, since the averaging procedure is not sensitive to the number of examined periods, for example, but only to the limits of the period range, it can seamlessly incorporate any additional information (e.g. the allowed range of phases, periods,

etc.) in the search.

The authors of the GL method argued in their publication that their approach managed to produce a significant detection of PSR B0540–69 from *ROSAT* X-ray data, where a Fast Fourier Transform (FFT) failed to detect a signal [458]; Epoch Folding (EF) was successfully used to detect the signal as well. Although this example seems to give an advantage to methods utilising stepwise functions for describing the lightcurve, it has been reported elsewhere that tests relying on smooth functions to model the signal are more sensitive than those using binning [459]. However, the same critical analysis showed that sensitivity increases for tests that match the signal’s properties closely: for example, a Rayleigh test performs better for broad, sinusoidal profiles.

Upon detection of a signal, the next step of interest is signal characterisation: i.e. the determination of the signal’s frequency and shape. Following their method, Gregory and Loredó used the *ROSAT* data set to compare the precision with which a Bayesian method was capable of determining the frequency and position of the peak with that from an EF ( $\chi^2$ ) procedure [458]. Note that those two methods have a common property: both tests bin the data across one period using  $m$  bins. The results from the simulations are clearly represented by the respective p.d.f.s of the frequencies searched (see Fig. 7.8a): the GL method produced a much narrower p.d.f. with approximately two-orders-of-magnitude better determination — at FWHM — of the most likely frequency.

Most importantly, for strong signals where the pulse is evident, the signal characterisation under Bayesian methods improves dramatically with increasing pulsed-photon rate. Again, a comparison of the GL method with EF shows that by increasing the pulsed-photon rate in the data set from one-quarter its original value to one-half, and then to its original value, the p.d.f. describing the most probable frequencies under the GL method becomes substantially narrower than the corresponding p.d.f. under the  $\chi^2$ -test (see Fig. 7.8b,c).

Perhaps the remaining task in signal characterisation is to determine the shape of the lightcurve. In EF this is simply done by selecting a set number of bins and plotting the binned data. The Bayesian approach is rather more complicated: it utilises the p.d.f. of the signal’s strength at each instant. Since this function is time-dependent, it will depend on the frequency and phase but also on the number of bins,  $m$ , associated with the chosen model. In other words, the *shape function*, as it is called, will depend on all the  $m + 2$  parameters of the model but not the average

data rate — which does not affect the lightcurve’s shape. The optimum number of bins ( $m$ ) corresponding to a model ( $H_m$ ) that has been chosen to represent the signal is derived by finding the maximum of  $pr(m|H_m)$  across a range of  $m$  values, where  $pr(m|H_m)$  is the Bayesian probability for that model after averaging over frequency and phase.

In itself, the shape function is so complicated that it is virtually impossible to use it, as is, for the shape estimation. Instead, what GL did was to plot its mean and standard deviation as a function of time. Hence, in the GL analysis, the lightcurve is represented by a  $1-\sigma$  confidence interval around the mean signal intensity (see Fig. 7.9).

Finally, a factor which has become less important in the recent years is computational speed. Unlike Fourier-based tests like the Rayleigh and  $H$  tests, which do not depend on stepwise functions for the calculation of their respective statistics, the main computational burden of the GL and EF methods is binning. That makes the former class of tests, which is based on smooth functions, faster on average — although this advantage is removed with the search over 20 harmonics with an  $H$ -test, for example. However, the GL method is more resource-demanding compared to EF, since it has to consider (average over) a wider range of frequencies and bin numbers; this makes it more cumbersome. In contrast, the GL method removes, via the Occam’s razor, the necessity for exploring complex models, and therefore insignificant peaks in the noise are not considered, which saves computational time.

### **The relevance to VHE pulsar observations**

But what impact would the use of a Bayesian approach, like Gregory and Loredo’s, make on the analysis of current and future VHE pulsar data? As a first point, an improvement in sensitivity could come from the use of Bayesian methods with regards to narrow, multi-component profiles like those of the Crab pulsar, the Vela pulsar and Geminga: the freedom of fitting the data with model-lightcurves of arbitrary shape (various values of  $m$ ) means that the GL method will be sensitive to weak signals whose energy is spread over many harmonics. An equally powerful frequentist tool, in the form of the  $H$ -test, would also be capable of detecting such profiles — although the versatility of the GL method at incorporating previous information (e.g. the allowed phase range, number of harmonics, etc.) will make it more sensitive to expected profile shapes, like those observed in lower energies with EGRET.

Future observations with H.E.S.S. Phase II will collect data at energies where pulsar fluxes are much higher compared to those predicted by the models in the energy range explored with H.E.S.S. Phase I. Therefore, as was shown in the previous section, the detection of such signals will be a matter of hours and signal characterisation will become the next important task. As mentioned above, the GL method outperforms the frequentist tests for strong signals and is able to resolve the shape of the lightcurves with an accuracy that becomes rapidly better with increasing photon numbers. An estimate of the improvement on the currently available EGRET GeV profiles can be given based on the predicted pulsed-photon rates with H.E.S.S. Phase II (see section 7.2.1). According to Table 7.2, the detection rates will increase on average 100-fold. Assuming a linear improvement with increasing detection rate that follows that of Fig. 7.8, a frequency resolution that is 150 times higher can be expected. This is indeed a remarkable improvement which will allow us to achieve EGRET’s resolution in 150 times shorter exposure time ( $\sim$  days).

A class of sources for which we have little information about their properties is the sample of pulsar candidates amongst the unidentified EGRET sources. Upon detection, these will greatly benefit from a Bayesian approach, which will allow the determination of their precise frequency at very high energies — something that EGRET was not able to achieve due to low statistics. Given the accurate ephemeris values, the data will be folded with high precision, and thus the lack of pulse smearing (see Fig. 5.26) will lead to well-defined pulse shapes.

Finally, having Occam’s razor embedded in the calculation of probabilities means that, by using the GL method, the analysis will not be sensitive to artificial signals composed of many harmonics — like the one we described in section 5.7.2. Of course, all of the above require a software implementation that, in the most general case, will scan over a wide range of frequencies, phases and bin numbers for each of the tested models: clearly a heavy computational strain; but, as computer power increases, Bayesian methods will also increase their practicality and will become as fast as frequentist tests are now.

### 7.3.3 Optimising the Image Amplitude Cut: The $Q$ -factor

Our choice of cuts was largely influenced by the standard H.E.S.S. analysis, which aims at exploring sub-TeV–TeV DC signals. In an effort to restrict our sample to the lowest energies detectable and be rid of the background at energies above those we were interested in, we chose to place an upper limit on the *size* parameter



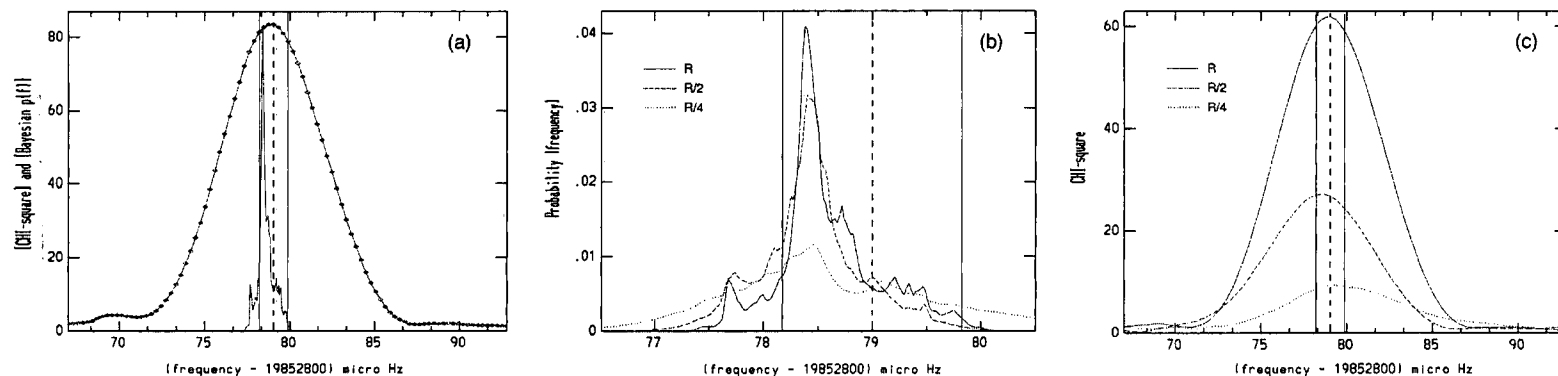


Figure 7.8: (from [458]) (a) Probability density plots around the most likely frequency in X-ray data from PSR B0540–69: the p.d.f. shown with diamonds connected with a solid line represents the strongest peak in a search in period with a  $\chi^2_4$ -test; and that drawn with a solid line represents the strongest peak from the analysis of the same data set but with a GL method. The latter p.d.f. is approximately two orders of magnitude narrower at the FWHM, which reveals that the GL method is more precise at extracting the signal’s properties. (b),(c) The dependence of the p.d.f. around the most likely frequency of PSR B0540–69 on the detection rate, as was found with (b) the GL method and (c) a  $\chi^2$ -test: the dotted line was derived from the data set of PSR B0540–69, after considering only every fourth X-ray event (one-quarter the original rate); the dashed line corresponds to the same data set but after skipping only every second event; finally, the solid line corresponds to the original data rate. In all three plots, the vertical, dashed line at  $79 \mu\text{Hz}$  indicates the measured frequency of PSR B0540–69 from *ROSAT* observations [460]; the  $1-\sigma$  error ( $\pm 0.8 \mu\text{Hz}$ ) is also shown with thinner, solid lines on each side of the *ROSAT* frequency.

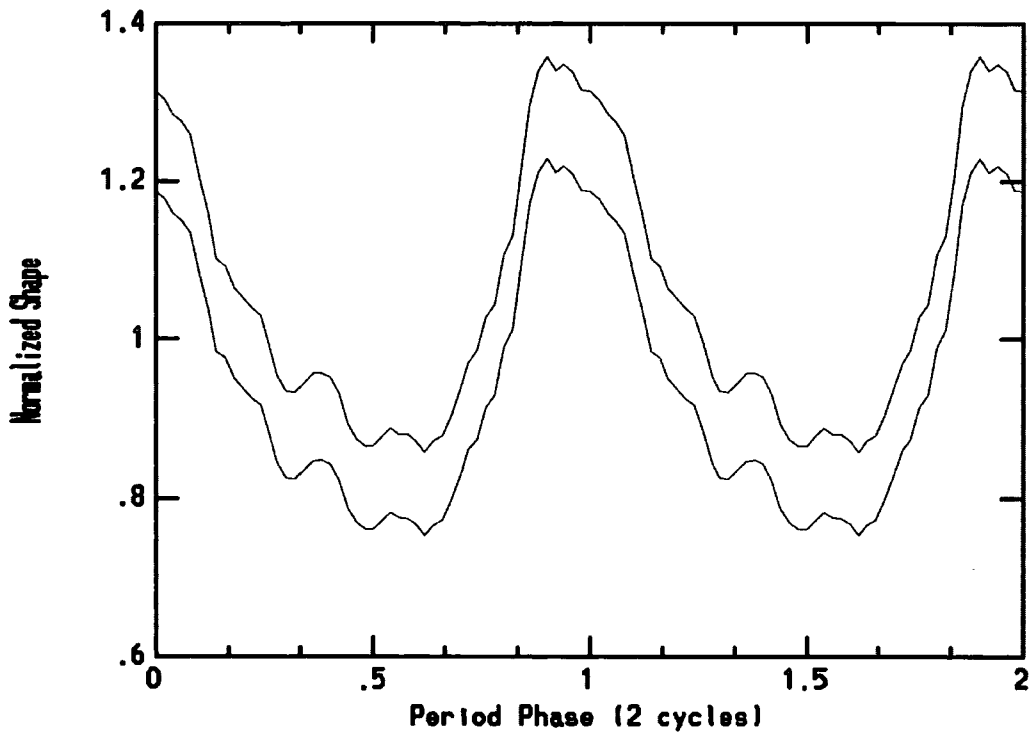


Figure 7.9: (from [458]) The lightcurve of PSR B0540–69, as was calculated using the GL method and setting the number of bins to  $m = 12$ . The two lines enclose the  $\pm 1\text{-}\sigma$  confidence interval, inside which the true lightcurve lies.

equal to the lower limit of the standard H.E.S.S. analysis (i.e.  $S_0 = 100$  ph.e.; see section 5.3.4). This way, we stood a better chance of extracting a weak, low-energy pulsed signal at a detectable signal-to-noise ratio. Despite having a solid basis, our approach lacked the optimisation which could further enhance a potential signal hidden in the large background.

It was shown in section 4.2.5 that an appropriate cut on the *distance* of simulated events leads to a roughly linear trend between the *Image Amplitude* or *size* and the event energy. Thus, as has been the case throughout the present thesis, a *size* cut is a straightforward way of sampling events with particular energies. The question is *which size* cut produces the highest signal-to-noise ratio. A simple solution to this problem is to construct a quantity that is maximised when the optimal *size* cut is applied: the *Q-factor*. Given a particular data set, the *Q-factor* is equal to the number of standard deviations of the pulsed  $\gamma$ -ray signal above the background, after the application of cuts, divided by the number of standard deviations of the signal in the same data set, before cuts. Strictly speaking, the significance of the signal in an uncut data set would almost certainly be zero, due to the large background involved. Therefore, using a data set to which loose cuts have been applied as the ‘uncut’, reference data set is more useful. Such a choice may well be the selection criterion used in the present work.

Based on the above definition of the *Q-factor*, we may now write its mathematical form as a function of the signal significance as is calculated with tests for uniformity. In general, the outcome probability in those tests is a function of the fundamental scaling parameter,  $p\sqrt{N} = N_\gamma/\sqrt{N}$  (see section 5.4). Hence, the *Q-factor* can be written as

$$Q_i = \frac{n\sigma_i}{n\sigma_0} = \frac{s(N_{\gamma(i)}/\sqrt{N_i})}{s(N_{\gamma(0)}/\sqrt{N_0})} \quad (7.1)$$

where  $s(N_\gamma/\sqrt{N})$  is a function of the scaling parameter that gives the signal significance; its exact form depends on the test for uniformity that has been used to detect the signal. Here, the quantities with index 0 correspond to the values associated with the reference data set, and those with index  $i$  (where  $i = 0, 1, 2 \dots$ ), to those of other possible data sets. By definition,  $Q_0 = 1$ .

For the purpose of optimising the energy range, the independent variable on which the *Q-factor* depends will be the event *size*, and more specifically the upper limit of the *size* cut. The lower limit is set to zero, since we are interested in the

lowest energies possible. The existence of a maximum  $Q$ -factor can be justified as follows:

In the VHE range, cosmic-ray background spectra are generally described by power laws (see e.g. Fig. 4.11). Also, the results of this thesis showed — at least for the pulsars studied herein — that pulsar spectra must exhibit steep cut-offs somewhere above EGRET's range; and there are indications that these may well be super-exponential (see section 6.3.4). In addition, it was explained in section 4.2.3 that the detection rate across an energy range is the result of convolving the effective-area function with the source's spectrum and integrating across the energy range of interest. Of course, the overall rate will be composed of both background and pulsed events. But, as opposed to the quickly diminishing pulsed spectra in the GeV range, the simple power laws of the background events contribute significantly up to TeV energies. Hence, one can enhance the signal-to-noise by constraining the event sample below an *optimal* energy, which should be high enough as to have significant effective area to allow the events to trigger the telescope but, also, be sufficiently low as to leave out most of the unwanted high-energy background.

Fig. 7.10a presents a plot of a typical background power-law spectrum with spectral index  $\nu'$ , a power-law spectrum (index  $\nu$ ) with a super-exponential cut-off at  $E_c$ , and an effective-area function with a steep threshold behaviour at low energies. It should be noted that the background flux is in general many orders of magnitude higher than that of  $\gamma$ -ray sources (see section 4.1.2), but for display purposes the former has been scaled down. Three choices of *size* cuts are shown — corresponding to three energies — with maximum values  $S1(E_1)$ ,  $S2(E_2)$  and  $S0(E_0)$ ; the latter of the three is used as the reference cut that we aim at optimising. The resulting differential-rate functions after convolving the background and the source spectrum with the effective area is shown in Fig. 7.10b with red and blue lines, respectively. The limited extent of the pulsed differential rate compared to the background rate is evident: the former is constrained both by the decline of the effective area, at the low-energy end, and by the steep spectral cut-off, at the high-energy end. The loose cut at  $E_0$  practically allows the entire pulsed differential-rate function to be integrated but also an extensive part of the background differential rate. Hence, the scaling parameter ( $\propto 1/N_c$ ) is expected to be small. Since we chose

$S_0(E_0)$  to be the reference *size* cut,  $Q_0$  will be 1. However, an even looser cut with  $size > S_0$  would introduce further background events and thus lead to a smaller  $Q$ -factor. Similarly, the lowest cut, at  $E_1$ , leaves out a considerable part of the pulsed differential-rate function, which results in a small data rate. Ultimately, as this cut is further lowered, the data rate will diminish to zero due to lack of telescope sensitivity. As a result, the sensitivity of the uniformity tests will also decline, which will lead to  $Q = 0$ . Therefore, it becomes clear that there exists an optimal energy, say  $E_2$ , which leads to the maximum value of the  $Q$ -factor. A qualitative curve describing the behaviour of  $Q$  as a function of the maximum *size*, across the arbitrary energy range of Fig. 7.10b, has been drawn to the same scale in Fig. 7.10c. The three selected *size* values  $S_1(E_1)$ ,  $S_2(E_2)$  and  $S_0(E_0)$  have been connected with the corresponding points of the  $Q$ -factor's curve. The *size* cut  $S_2(E_2)$  results in the maximum value of  $Q$ , i.e.  $Q_2 = Q_{\max}$ , and it is therefore the optimal choice.

The best way of determining the optimal  $Q$ -factor for a specific observation is through simulations. One could simulate a large number of periodic air showers, whose energies are distributed according to the theoretical super-exponential spectra, and hadronic background showers, whose energies follow the observed power-law spectra. Then, by running the appropriate code that simulates the detector, data sets of triggered showers sorted by Z.A. can be generated. Finally, the application of various *size* cuts (together with a distance cut which will remove undesirable, remote high-energy showers) and subsequent calculation of the  $Q$ -factor will indicate the most appropriate cut prior to analysing real data.

## 7.4 Beyond H.E.S.S.

Another interesting prospect for  $\gamma$ -ray astronomy is the 5@5 experiment [461]. It is based on the simple idea of placing several large, 20-m diameter Cherenkov detectors, which will be able to observe stereoscopically the  $\gamma$ -ray sky, at 5 km altitude. This way, the detectors will be able to directly observe Cherenkov light from the shower maxima which will be only a few km above the experiment. At 5 km altitude, the photon density generated by 5-GeV showers ( $\approx 1 \text{ ph m}^{-2}$ ) is roughly 10 times higher than at sea-level [1], which means that such low-energy showers will be easily detectable given an efficient background rejection technique. So, this system will combine the power of stereoscopic reconstruction with high-altitude observations,

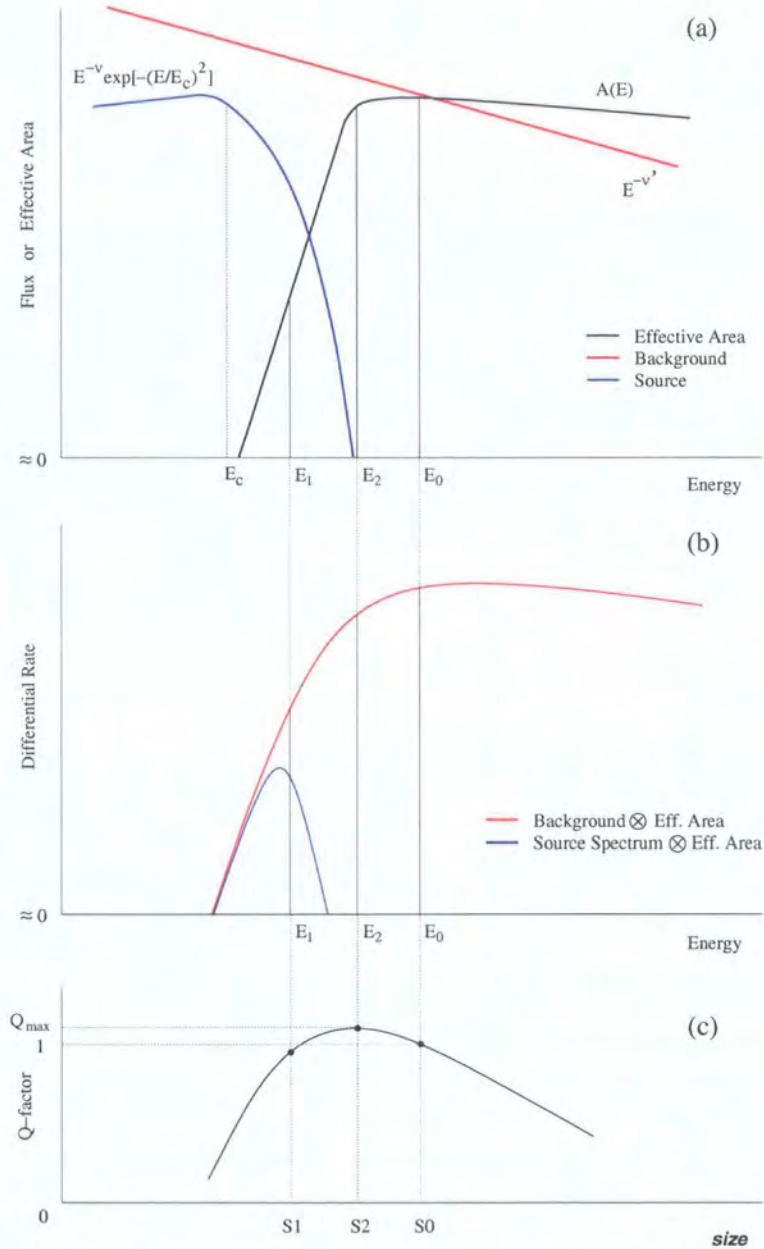


Figure 7.10: (a) The typical shapes of two flux spectra and an effective-area function: a power-law spectrum, with index  $\nu'$ , corresponding to background emission (red line); a  $\gamma$ -ray spectrum (spectral index  $\nu$ ) with a super-exponential cut-off at  $E_c$  (blue line), as is predicted by theoretical models of pulsar high-energy emission; and, finally, a typical effective-area function with a step decline below  $\approx E_2$ . (b) The resulting differential-rate functions from the convolution of the background (red line) and source (blue line) spectra with the effective area. (c) The variation of the  $Q$ -factor for three *size* cuts,  $\leq S_1$ ,  $\leq S_2$  and  $\leq S_0$ , corresponding to three different energy ranges,  $\leq E_1$ ,  $\leq E_2$  and  $\leq E_0$ .  $S_0$  is the reference cut, for which  $Q_0$  is by definition equal to 1 (see text).

in order to achieve the minimum energy threshold of 2–3 GeV, below which the secondary electrons from pair production stop emitting Cherenkov radiation.

# Bibliography

- [1] T. C. Weekes. *Very high energy gamma-ray astronomy*. Bristol, UK: The Institute of Physics Publishing, 2003.
- [2] J. Woodfill for NASA. *Space Educators' Handbook* [online], 2004. Available from: <http://www.jsc.nasa.gov/er/seh/> [accessed 18 March 2006].
- [3] T. Yoshida *et al.* BESS-polar experiment. *Advances in Space Research*, 33(10):1755, 2004.
- [4] E. S. Seo *et al.* Cosmic-ray energetics and mass (CREAM) balloon project. *Advances in Space Research*, 33(10):1777, 2004.
- [5] D. J. Thompson *et al.* Gamma Radiation from PSR B1055–52. *ApJ*, 516(1):297, 1999.
- [6] J. Lochner for NASA. *Imagine the Universe Science* [online], 2004. Available from: <http://imagine.gsfc.nasa.gov/docs/science/> [accessed 18 March 2006].
- [7] Naval Research Laboratory. *NRL Compton Telescopes* [online], 2000. Available from: <http://heseweb.nrl.navy.mil/gamma/detector/compton/compton.htm> [accessed 18 March 2006].
- [8] R. Hillier. *Gamma ray astronomy*. Oxford, UK: Clarendon Press, 1984.
- [9] W. Kraushaar *et al.* Explorer XI Experiment on Cosmic Gamma Rays. *ApJ*, 141(2):845, 1965.
- [10] J. Clear *et al.* A detailed analysis of the high energy gamma-ray emission from the Crab pulsar and nebula. *A&A*, 174(1–2):85, 1987.
- [11] C. von Montigny *et al.* Multiwavelength Observations of 3C 273 in 1993–1995. *ApJ*, 483(1):161, 1997.



- [12] European Space Agency. *ESA Science & Technology: Galactic* [online], 2000. Available from: <http://sci.esa.int/> [accessed 18 March 2006].
- [13] G. Kanbach *et al.* The project EGRET (Energetic Gamma-Ray Experiment Telescope) on NASA's Gamma-Ray Observatory (GRO). *Space Sci. Rev.*, 49(1-2):69, 1988.
- [14] R. C. Hartman *et al.* The third EGRET catalog of high-energy gamma-ray sources. *ApJS*, 123(1):79, 1999.
- [15] D. F. Torres, Y. M. Butt, and F. Camilo. Recently discovered pulsars and unidentified EGRET sources. *ApJ*, 560(2):L155, 2001.
- [16] R. Diehl. The COMPTEL experiment on the NASA Gamma-Ray Observatory. *Space Sci. Rev.*, 49(1-2):85, 1988.
- [17] V. Schoenfelder *et al.* COMPTEL overview: achievements and expectations. *A&AS*, 120:C13, 1996.
- [18] A. M. Soderberg *et al.* The sub-energetic  $\gamma$ -ray burst GRB 031203 as a cosmic analogue to the nearby GRB 980425. *Nature*, 430(7000):648, 2004.
- [19] F. Lebrun *et al.* Compact sources as the origin of the soft  $\gamma$ -ray emission of the Milky Way. *Nature*, 428(6980):293, 2004.
- [20] N. Gehrels *et al.* The Swift Gamma-Ray Burst mission. *ApJ*, 611(2):1005, 2004.
- [21] National Aeronautics and Space Agency. *Official NASA GLAST Website* [online], 2005. Available from: <http://glast.gsfc.nasa.gov/> [accessed 18 March 2006].
- [22] P. L. Nolan *et al.* Observations of the Crab pulsar and nebula by the EGRET telescope on the Compton Gamma-Ray Observatory. *ApJ*, 409(2):697, 1993.
- [23] G. Kanbach *et al.* EGRET observations of the Vela pulsar, PSR0833-45. *A&A*, 289(3):855, 1994.
- [24] D. J. Thompson *et al.* EGRET observations of high-energy gamma radiation from PSR B1706-44. *ApJ*, 465(pt 1):385, 1996.

- [25] P. V. Ramanamurthy *et al.* EGRET detection of pulsed gamma radiation from PSR B1951+32. *ApJ*, 447(2):L109, 1995.
- [26] H. A. Mayer-Hasselwander *et al.* High-energy gamma radiation from Geminga observed by EGRET. *ApJ*, 421(1):276, 1994.
- [27] A. Konopelko. Future Pulsar Observations with H.E.S.S. In *Proceedings of the 270. WE-Heraeus Seminar: Neutron Stars, Pulsars, and Supernova Remnants, Physikzentrum Bad Honnef, Germany, 2002*, W. Becker, H. Lesch and J. Trümper (eds.), page 105. Munich, Germany: Max-Planck-Institut für extraterrestrische Physik, 2002.
- [28] O. C. de Jager *et al.* Gamma-ray observations of the crab nebula: a study of the synchro-Compton spectrum. *ApJ*, 457(pt 1):253, 1996.
- [29] J. V. Jelley and N. A. Porter. Čerenkov radiation from the night sky, and its application to  $\gamma$ -ray astronomy. *Quarterly Journal of the Royal Astronomical Society*, 4:275, 1963.
- [30] W. Galbraith and J. V. Jelley. Light pulses from the night sky associated with cosmic rays. *Nature*, 171:349, 1953.
- [31] A.E. Chudakov, V.I. Dadykin, N.M. Zatsepin, and N.M. Nestrova. A search for photons with energy  $10^{13}$  eV from local sources of cosmic radiation. In *Proceedings of the P.N. Lebedev Phys. Inst., Moscow, USSR, 1964*, volume 26, page 99. English Translation: Consultants Bureau, 1965.
- [32] A. M. Hillas *et al.* The spectrum of TeV gamma rays from the Crab nebula. *ApJ*, 503(2):744, 1998.
- [33] Very High Energy Gamma Ray Group. *Very High Energy Gamma Ray Group, Department of Physics, University of Durham* [online], 2005. Available from: <http://www.dur.ac.uk/~dph0www4/> [accessed 18 March 2006].
- [34] P. M. Chadwick *et al.* TeV gamma rays from PSR 1706–44. *Astroparticle Physics*, 9(2):131, 1998.
- [35] T. C. Weekes *et al.* VERITAS: The Very Energetic Radiation Imaging Telescope Array System. *Astroparticle Physics*, 17(2):221, 2002.

- [36] J. Holder *et al.* Status and performance of the first VERITAS telescope. In *Proceedings of the 29th International Cosmic Ray Conference, Pune, India, 2005*, B. Sripathi Acharya, S. Gupta, P. Jagadeesan, A. Jain, S. Karthikeyan, S. Morris and S. Tonwar (eds.), volume 5, page 379. Mumbai, India: Tata Institute of Fundamental Research, 2005.
- [37] G. Maier for the VERITAS collaboration. Monte Carlo studies of the first VERITAS telescope. In *Proceedings of the 29th International Cosmic Ray Conference, Pune, India, 2005*, B. Sripathi Acharya, S. Gupta, P. Jagadeesan, A. Jain, S. Karthikeyan, S. Morris and S. Tonwar (eds.), volume 5, page 395. Mumbai, India: Tata Institute of Fundamental Research, 2005.
- [38] F. Krennrich *et al.* Observation of VHE gamma-emission from the Crab nebula with the prototype of the HEGRA Air Cherenkov telescope array. In *Proceedings of the 23rd International Cosmic Ray Conference, Calgary, Canada, 1993*, R. B. Hicks, D. A. Leahy and D. Venkatesan (eds.), volume 1, page 251. Calgary, Canada: Department of Physics and Astronomy, The University of Calgary, 1993.
- [39] F. A. Aharonian *et al.* Evidence for TeV gamma ray emission from Cassiopeia A. *A&A*, 370(1):112, 2001.
- [40] S. A. Dazeley *et al.* Recent results from the CANGAROO project. In *Proceedings of the 160th colloquium of the International Astronomical Union: Pulsars: Problems and Progress, Sydney, Australia, 1996*, S. Johnston, M. A. Walker and M. Bailes (eds.), volume 105, page 363. San Francisco, CA: Astronomical Society of the Pacific, 1996.
- [41] R. Enomoto *et al.* Design study of CANGAROO-III, stereoscopic imaging atmospheric Cherenkov telescopes for sub-TeV  $\gamma$ -ray detection. *Astroparticle Physics*, 16(3):235, 2002.
- [42] K. Nishijima *et al.* Status of the CANGAROO-III project. In *Proceedings of the 29th International Cosmic Ray Conference, Pune, India, 2005*, B. Sripathi Acharya, S. Gupta, P. Jagadeesan, A. Jain, S. Karthikeyan, S. Morris and S. Tonwar (eds.), volume 5, page 327. Mumbai, India: Tata Institute of Fundamental Research, 2005.

- [43] T. Yoshikoshi *et al.* Performance of the Imaging Atmospheric Cherenkov Telescope system of CANGAROO-III. In *Proceedings of the 29th International Cosmic Ray Conference, Pune, India, 2005*, B. Sripathi Acharya, S. Gupta, P. Jagadeesan, A. Jain, S. Karthikeyan, S. Morris and S. Tonwar (eds.), volume 5, page 343. Mumbai, India: Tata Institute of Fundamental Research, 2005.
- [44] A. K. Konopelko. The Monte Carlo studies on the performance of the H.E.S.S. array (Phase I). *H.E.S.S. Internal Documents* [online], 2000. Available from: <http://www.mpi-hd.mpg.de/hfm/HESS/intern/> [accessed 18 March 2006][restricted access].
- [45] A. Konopelko for the H.E.S.S. collaboration. H.E.S.S. (High Energy Stereoscopic System). Presentation (slides) in the GAMMA Multiwavelength Workshop, Adler, Chicago, 2002.
- [46] S. Gillessen for the H.E.S.S. collaboration. Arcsecond level pointing of the H.E.S.S. telescopes. In *Proceedings of the 28th International Cosmic Ray Conference, Tsukuba, Japan, 2003*, G. Kajita, Y. Asaoka, A. Kawachi, Y. Matsumura and M. Sasaki (eds.), page 2899. Tokyo, Japan: Universal Academy Press, 2003.
- [47] P. Vincent and the H.E.S.S. collaboration. HESS phase II experiment. In *Proceedings of the SF2A-2004: Semaine de l'Astrophysique Francaise, Paris, France, 2004*, F. Combes, D. Barret, T. Contini, F. Meynadier and L. Pagani (eds.), page 407. Les Ulis, France: EdP-Sciences, Conference Series, 2004.
- [48] E. Lorenz. Status of the 17 m MAGIC telescope. *New Astronomy Review*, 48(5-6):339, 2004.
- [49] E. Lorenz and M. Martinez. High energy astrophysics: The MAGIC telescope. *Astronomy and Geophysics*, 46(6):21, 2005.
- [50] A. Moralejo *et al.* The MAGIC telescope for gamma-ray astronomy above 30 GeV. *Chinese Journal of Astronomy and Astrophysics*, 3:531, 2003.
- [51] D. Ferenc for the MAGIC collaboration. MAGIC  $\gamma$ -ray observatory. Presentation (slides) in the 5th International Conference on Ring Imaging Cherenkov Counters (RICH 2004), Playa del Carmen, Mexico, 2004.

- [52] D. A. Smith *et al.* CELESTE: a large heliostat array for gamma ray astronomy. *Nuclear Physics B Proceedings Supplements*, 54(3):362, 1997.
- [53] D. A. Williams *et al.* Astrophysics around 100 GeV with STACEE. *New Astronomy Review*, 48(5–6):359, 2004.
- [54] R. A. Ong *et al.* A new atmospheric Cherenkov detector using the heliostats of Solar Two. In *Proceedings of the International Workshop Towards a Major Atmospheric Cherenkov Detector-IV for TeV Astro/Particle Physics, Padova, Italy, 1995*, M. Cresti (ed.), page 261. Piazzola sul Brenta, Italy: Papergraf, 1996.
- [55] S. W. Cui and C. T. Yan. A wide sky survey for TeV  $\gamma$ -ray sources by using the Tibet-III air shower array. In *Proceedings of the 28th International Cosmic Ray Conference, Tsukuba, Japan, 2003*, G. Kajita, Y. Asaoka, A. Kawachi, Y. Matsubara and M. Sasaki (eds.), page 2315. Tokyo, Japan: Universal Academy Press, 2003.
- [56] G. Walker and D. Kieda. Whipple telescope observations of potential TeV  $\gamma$ -ray sources found by the Tibet air shower array. *New Astronomy Review*, 48(5–6):477, 2004.
- [57] A. J. Smith for the MILAGRO collaboration. Detection of diffuse gamma-ray emission from the Cygnus region with the Milagro gamma-ray observatory. In *Proceedings of the 29th International Cosmic Ray Conference, Pune, India, 2005*, B. Sripathi Acharya, S. Gupta, P. Jagadeesan, A. Jain, S. Karthikeyan, S. Morris and S. Tonwar (eds.), volume 4, page 271. Mumbai, India: Tata Institute of Fundamental Research, 2005.
- [58] A. I. Mincer. *Allen Mincer's Home Page* [online], 2004. Available from: <http://www.physics.nyu.edu/~am3> [accessed 18 March 2006].
- [59] C. Winkler *et al.* The INTEGRAL mission. *A&A*, 411(1):L1, 2003.
- [60] H. Kubo *et al.* Status of the CANGAROO-III project. *New Astronomy Review*, 48(5–6):323, 2004.
- [61] J. A. Hinton. The status of the HESS project. *New Astronomy Review*, 48(5–6):331, 2004.

- [62] E. Blaufuss. Results from the Milagro gamma-ray observatory. *New Astronomy Review*, 48(5–6):513, 2004.
- [63] N. Ito *et al.* GRAPES III : A new large EAS experiment at Ooty. In *Proceedings of the 25th International Cosmic Ray Conference, Durban, SA, 1997*, M. S. Potgieter *et al.* (eds.), volume 7, page 225. Potchefstroom, SA: Wesprint, Space Research Unit, 1997.
- [64] A. Aloisio *et al.* The ARGO-YBJ experiment in Tibet. *Il Nuovo Cimento C*, 24(0405):739, 2001.
- [65] M. Ohnishi *et al.* Performance of the Tibet-III air shower array. In *Proceedings of the 28th International Cosmic Ray Conference, Tsukuba, Japan, 2003*, G. Kajita, Y. Asaoka, A. Kawachi, Y. Matsubara and M. Sasaki (eds.), page 3019. Tokyo, Japan: Universal Academy Press, 2003.
- [66] T. C. Weekes *et al.* Observation of TeV gamma rays from the Crab nebula using the atmospheric Čerenkov imaging technique. *ApJ*, 342(pt 1):379, 1989.
- [67] F. A. Aharonian *et al.* Discovery of extended VHE gamma-ray emission from the asymmetric pulsar wind nebula in MSH 15-52 with HESS. *A&A*, 435(1):L17, 2005.
- [68] T. Sako *et al.* Very High Energy gamma-ray observations of PSR B1509–58 with the CANGAROO 3.8 meter telescope. *ApJ*, 537(1):422, 2000.
- [69] F. A. Aharonian *et al.* The H.E.S.S. survey of the inner galaxy in very high energy gamma rays. *ApJ*, 636(2):777, 2006.
- [70] F. A. Aharonian *et al.* A possible association of the new VHE  $\gamma$ -ray source HESS J1825–137 with the pulsar wind nebula G18.0–0.7. *A&A*, 442(3):L25, 2005.
- [71] T. Yoshikoshi *et al.* Very High Energy gamma rays from the Vela pulsar direction. *ApJ*, 487(1):L65, 1997.
- [72] D. C.-J. Bock and V. V. Gvaramadze. Some arguments in support of the association of PSR B1706–44 with the supernova remnant G343.1–2.3. In *Proceedings of the ASP Conf. Ser. 271: Neutron Stars in Supernova Remnants, Boston, MA, 2001*, P. O. Slane and B. M. Gaensler (eds.), volume 271, page 49. San Francisco, CA: Astronomical Society of the Pacific, 2002.

- [73] F. A. Aharonian *et al.* High-energy particle acceleration in the shell of a supernova remnant. *Nature*, 432(7013):75, 2004.
- [74] F. A. Aharonian, H. Krawczynski, G. Pühlhofer, G. P. Rowell, and the HEGRA collaboration. Search for TeV gamma rays from supernova remnants Cas A and Tycho with the HEGRA stereoscopic system of atmospheric Cherenkov telescopes. *BAAS*, 32(3):1239, 2000.
- [75] H. Muraishi *et al.* Evidence for TeV gamma-ray emission from the shell type SNR RX J1713.7–3946. *A&A*, 354:L57, 2000.
- [76] R. Enomoto *et al.* The acceleration of cosmic-ray protons in the supernova remnant RX J1713.7–3946. *Nature*, 416(6883):823, 2002.
- [77] H. Katagiri *et al.* Detection of gamma rays around 1 TeV from RX J0852.0–4622 by CANGAROO-II. *ApJ*, 619(2):L163, 2005.
- [78] F. A. Aharonian *et al.* Detection of TeV  $\gamma$ -ray emission from the shell-type supernova remnant RX J0852.0–4622 with HESS. *A&A*, 437(1):L7, 2005.
- [79] P. Slane *et al.* RX J0852.0–4622: another nonthermal shell-type supernova remnant (G266.2–1.2). *ApJ*, 548(2):814, 2001.
- [80] S. Mereghetti. The X-ray sources at the center of the supernova remnant RX J0852.0–4622. *ApJ*, 548(2):L213, 2001.
- [81] G. G. Pavlov, D. Sanwal, B. Kızıltan, and G. P. Garmire. The compact central object in the RX J0852.0–4622 supernova remnant. *ApJ*, 559(2):L131, 2001.
- [82] T. Tanimori *et al.* Recent status of the analyses for stereoscopic observations with the CANGAROO-III telescopes. In *Proceedings of the 29th International Cosmic Ray Conference, Pune, India, 2005*, B. Sripathi Acharya, S. Gupta, P. Jagadeesan, A. Jain, S. Karthikeyan, S. Morris and S. Tonwar (eds.), volume 4, page 215. Mumbai, India: Tata Institute of Fundamental Research, 2005.
- [83] F. A. Aharonian *et al.* Upper limits to the SN 1006 multi-TeV gamma-ray flux from HESS observations. *A&A*, 437(1):135, 2005.
- [84] V. Vitale and the HEGRA collaboration. Observation of VHE gamma rays from the remnant of SN 1006 with HEGRA CT1. In *Proceedings of the 28th International Cosmic Ray Conference, Tsukuba, Japan, 2003*, G. Kajita, Y.

- Asaoka, A. Kawachi, Y. Matsubara and M. Sasaki (eds.), page 2389. Tokyo, Japan: Universal Academy Press, 2003.
- [85] T. Tanimori. Detection of TeV gamma rays from SN 1006. In *Proceedings of the IAU Symposium 188: The Hot Universe, Kyoto, Japan, 1997*, K. Koyama, S. Kitamoto and M. Itoh (eds.), page 121. Dordrecht, The Netherlands: Kluwer Academy Press, 1998.
- [86] S. Hara and the CANGAROO collaboration. Observation of TeV gamma rays from NE-rim of SN 1006 with CANGAROO-II 10m telescope. In *Proceedings of the 27th International Cosmic Ray Conference, Hamburg, Germany, 2001*, K. H. Kampert *et al.* (eds.), page 2455, 2001.
- [87] F. A. Aharonian *et al.* A new population of Very High Energy gamma-ray sources in the Milky Way. *Science*, 307(5717):1938, 2005.
- [88] J. Albert *et al.* MAGIC observations of Very High Energy  $\gamma$ -rays from HESS J1813-178. *ApJ*, 637(1):L41, 2006.
- [89] T. N. LaRosa, N. E. Kassim, T. J. W. Lazio, and S. D. Hyman. A wide-field 90 centimeter VLA image of the Galactic center region. *AJ*, 119(1):207, 2000.
- [90] F. A. Aharonian *et al.* A search for TeV gamma-ray emission from SNRs, pulsars and unidentified GeV sources in the Galactic plane in the longitude range between  $-2$  deg and 85 deg. *A&A*, 395(3):803, 2002.
- [91] F. A. Aharonian *et al.* Very high energy gamma rays from the composite SNR G0.9+0.1. *A&A*, 432(2):L25, 2005.
- [92] F. A. Aharonian *et al.* Search for TeV emission from the region around PSR B1706-44 with the HESS experiment. *A&A*, 432(1):L9, 2005.
- [93] J. C. Dowthwaite *et al.* Evidence for pulsed 1000 GeV gamma-rays from the Crab pulsar. *ApJ*, 286:L35, 1984.
- [94] J. E. Grindlay. Detection of pulsed gamma rays of  $\sim 10^{12}$  eV from the pulsar in the Crab nebula. *ApJ*, 174:L9, 1972.
- [95] R. W. Lessard *et al.* Search for pulsed TeV gamma-ray emission from the Crab pulsar. *ApJ*, 531(2):942, 2000.



- [96] B. W. Stappers, B. M. Gaensler, V. M. Kaspi, M. van der Klis, and W. H. G. Lewin. An X-ray nebula associated with the millisecond pulsar B1957+20. *Science*, 299(5611):1372, 2003.
- [97] L. Kuiper *et al.* The likely detection of pulsed high-energy gamma -ray emission from millisecond pulsar PSR J0218+4232. *A&A*, 359(6):615, 2000.
- [98] M. S. Longair. *High energy astrophysics. Vol.2: Stars, the galaxy and the interstellar medium.* Cambridge, UK: Cambridge University Press, second edition, 1994.
- [99] R. Giacconi, H. Gursky, E. Kellogg, E. Schreier, and H. Tananbaum. Discovery of periodic X-ray pulsations in Centaurus X-3 from UHURU. *ApJ*, 167:L67, 1971.
- [100] E. Schreier *et al.* Evidence for the binary nature of Centaurus X-3 from UHURU X-ray observations. *ApJ*, 172:L79, 1972.
- [101] A. Carramiñana, P. M. Chadwick, and N. A. Dipper *et al.* *Timing Neutron Stars*, H. Ögelman and E. P. J. van den Heuvel (eds.). Dordrecht, The Netherlands: Kluwer Academic Press, 1989.
- [102] R. A. North *et al.* TeV gamma-ray observations of Cen X-3. In *Proceedings of the 21st International Cosmic Ray Conference, Adelaide, Australia, 1990*, R. J. Protheroe (ed.), volume 2, page 275. Northfield, South Australia: The University of Adelaide, Graphic Services, 1990.
- [103] A. M. Atoyan *et al.* Very High Energy gamma-rays from Centaurus X-3: indications and implications. *A&A*, 383(3):864, 2002.
- [104] E. P. J. van den Heuvel and C. de Loore. The nature of X-ray binaries III. Evolution of massive close binaries with one collapsed component, with a possible application to Cygnus X3. *A&A*, 25(1):387, 1973.
- [105] M. H. van Kerkwijk, T. R. Geballe, D. L. King, M. van der Klis, and J. van Paradijs. The Wolf-Rayet counterpart of Cygnus X-3. *A&A*, 314(6):521, 1996.
- [106] B. M. Vladimirsky, A. A. Stepanian, and V. P. Fomin. High-energy gamma-ray outburst in the direction of the X-ray source Cyg X-3. In *Proceedings of the*

- 13th International Cosmic Ray Conference, Denver, CO, 1973*, R. L. Chas-son (ed.), volume 1, page 456. Boulder, CO: University of Denver, Colorado Associated University Press, 1973.
- [107] S. Danaher, D. J. Fegan, N. A. Porter, and T. C. Weekes. Gamma-ray obser- vations of Cygnus X-3 at energies of 10 to the 12th eV. *Nature*, 289(5798):568, 1981.
- [108] R. C. Lamb, C. P. Godfrey, W. A. Wheaton, and T. Tumer. Cygnus X-3 observed at photon energies above 500 GeV. *Nature*, 296(5857):543, 1982.
- [109] J. C. Dowthwaite *et al.* Ultra high energy gamma rays from Cygnus X3. *A&A*, 126(1):1, 1983.
- [110] P. M. Chadwick, N. A. Dipper, J. C. Dowthwaite, A. I. Gibson, and A. B. Harrison. A 12.6-ms pulsar in Cygnus X-3. *Nature*, 318(6047):642, 1985.
- [111] A. A. Gregory, J. R. Patterson, M. D. Roberts, N. I. Smith, and G. J. Thorn- ton. Observations of Cygnus X-3 near 100 TeV using the low elevation atmo- spheric Cherenkov technique. *A&A*, 237(2):L5, 1990.
- [112] D. J. Fegan *et al.* Search for a 12.59 ms pulsar in Cygnus X-3. *A&A*, 211(1):L1, 1989.
- [113] M. Mori *et al.* Cygnus X-3 and EGRET gamma-ray observations. *ApJ*, 476(2):842, 1997.
- [114] A. M. Atoyan and F. A. Aharonian. Modelling of the non-thermal flares in the Galactic microquasar GRS 1915+105. *MNRAS*, 302(2):253, 1999.
- [115] F. A. Aharonian *et al.* Discovery of Very High Energy gamma rays associated with an X-ray binary. *Science*, 309(5735):746, 2005.
- [116] M. Tavani and J. Arons. Theory of high-energy emission from the Pulsar/Be star system PSR 1259–63. I. Radiation mechanisms and interaction geometry. *ApJ*, 477(1):439, 1997.
- [117] F. A. Aharonian *et al.* Discovery of the binary pulsar PSR B1259-63 in very- high-energy gamma rays around periastron with HESS. *A&A*, 442(1):1, 2005.
- [118] M. Tavani *et al.* Hard X-ray emission from the pulsar system PSR B1259–63 near periastron. *BAAS*, 26:1485, 1994.

- [119] S. Johnston, R. N. Manchester, A. G. Lyne, L. Nicastro, and J. Spyromilio. Radio and optical observations of the PSR:B1259–63 / SS:2883 Be-star binary system. *MNRAS*, 268(2):430, 1994.
- [120] R. P. Olling and M. R. Merrifield. Luminous and dark matter in the Milky Way. *MNRAS*, 326(1):164, 2001.
- [121] J. Ellis, J. L. Feng, A. Ferstl, K. T. Matchev, and K. A. Olive. Prospects for detecting supersymmetric dark matter at Post-LEP benchmark points. *European Physical Journal C*, 24(2):311, 2002.
- [122] A. M. Ghez, B. L. Klein, M. Morris, and E. E. Becklin. High proper-motion stars in the vicinity of Sagittarius A\*: evidence for a supermassive black hole at the center of our galaxy. *ApJ*, 509(2):678, 1998.
- [123] P. Gondolo and J. Silk. Dark matter annihilation at the Galactic center. *Phys. Rev. Lett.*, 83(9):1719, 1999.
- [124] J. Albert *et al.* Observation of gamma rays from the Galactic center with the MAGIC telescope. *ApJ*, 638(2):L101, 2006.
- [125] D. Elsässer and K. Mannheim. Supersymmetric Dark Matter and the Extragalactic Gamma Ray Background. *Physical Review Letters*, 94(17):171302, 2005.
- [126] F. A. Aharonian *et al.* Very high energy gamma rays from the direction of Sagittarius A\*. *A&A*, 425(1):L13, 2004.
- [127] R. Schödel *et al.* A star in a 15.2-year orbit around the supermassive black hole at the centre of the Milky Way. *Nature*, 419(6908):694, 2002.
- [128] K. Kosack *et al.* TeV gamma-ray observations of the Galactic center. *ApJ*, 608(2):L97, 2004.
- [129] K. Tsuchiya *et al.* Detection of sub-TeV gamma rays from the Galactic center direction by CANGAROO-II. *ApJ*, 606(2):L115, 2004.
- [130] T. C. Weekes. Status of VHE astronomy c. 2000. In *Proceedings of the High Energy Gamma-Ray Astronomy International Symposium, Heidelberg, Germany, 2001*, F. A. Aharonian and H. J. Völk (eds.), volume 558, page 15. Melville, NY: American Institute of Physics, 2001.

- [131] M. Martinez. VHE gamma-ray astronomy: observations. Presentation (slides) in Topics in Astroparticle and Underground Physics (TAUP), Zaragoza, Spain, 2005.
- [132] R. Atkins *et al.* Evidence for TeV gamma-ray emission from a region of the Galactic plane. *Physical Review Letters*, 95(25):251103, 2005.
- [133] F. A. Aharonian *et al.* Serendipitous discovery of the unidentified extended TeV  $\gamma$ -ray source HESS J1303-631. *A&A*, 439(3):1013, 2005.
- [134] F. A. Aharonian *et al.* An unidentified TeV source in the vicinity of Cygnus OB2. *A&A*, 393(2):L37, 2002.
- [135] M. J. Lang *et al.* A new TeV source confirmed in Whipple archival data: TeV J2032+41. *Ap&SS*, 297(1-4):345, 2005.
- [136] F. A. Aharonian *et al.* A search for very high energy  $\gamma$ -ray emission from the starburst galaxy NGC 253 with HESS. *A&A*, 442(1):177, 2005.
- [137] H. J. Volk, F. A. Aharonian, and D. Breitschwerdt. The nonthermal energy content and gamma-ray emission of starburst galaxies and clusters of galaxies. *Space Science Reviews*, 75(1-2):279, 1996.
- [138] C. Itoh *et al.* Detection of diffuse TeV gamma-ray emission from the nearby starburst galaxy NGC 253. *A&A*, 396(1):L1, 2002.
- [139] C. Itoh *et al.* Evidence of TeV gamma-ray emission from the nearby starburst galaxy NGC 253. *A&A*, 402(2):443, 2003.
- [140] R. Enomoto, T. Yoshida, S. Yanagita, and C. Itoh. Constraints on Cold Dark Matter in the gamma-ray halo of NGC 253. *ApJ*, 596(1):216, 2003.
- [141] A. Konopelko *et al.* Effectiveness of TeV gamma-ray observations at large zenith angles with a stereoscopic system of imaging atmospheric Čerenkov telescopes. *Journal of Physics G: Nuclear and Particle Physics*, 25(9):1989, 1999.
- [142] M. Punch *et al.* Detection of TeV photons from the active galaxy Markarian 421. *Nature*, 358(6386):477, 1992.
- [143] J. Quinn *et al.* Detection of gamma rays with  $E > 300$  GeV from Markarian 501. *ApJ*, 456(2):L83, 1996.

- [144] F. A. Aharonian *et al.* Measurement of the flux, spectrum, and variability of TeV  $\gamma$ -rays from Mkn 501 during a state of high activity. *A&A*, 327(1):L5, 1997.
- [145] J. Holder *et al.* Detection of TeV gamma rays from the BL Lacertae object 1ES 1959+650 with the Whipple 10 meter telescope. *ApJ*, 583(1):L9, 2003.
- [146] D. Horan *et al.* Detection of the BL Lacertae object H1426+428 at TeV gamma-ray energies. *ApJ*, 571(2):753, 2002.
- [147] J. Albert *et al.* Observation of Very High Energy gamma-ray emission from the Active Galactic Nucleus 1ES 1959+650 using the MAGIC telescope. *ApJ*, 639(2):761, 2006.
- [148] F. A. Aharonian *et al.* Observations of selected AGN with HESS. *A&A*, 441(2):465, 2005.
- [149] D. J. Macomb *et al.* Multiwavelength observations of Markarian 421 during a TeV/X-Ray flare. *ApJ*, 449:L99, 1995.
- [150] R. Remillard, H. G. Boerst, and N. Goetting. High energy outburst in BL Lac object Mkn 421. *The Astronomer's Telegram*, 65:1, 2001.
- [151] L. M. Boone *et al.* STACEE Observations of Markarian 421 during an Extended Gamma-Ray Outburst. *ApJ*, 579(1):L5, 2002.
- [152] F. A. Aharonian *et al.* Observations of Mkn 421 in 2004 with HESS at large zenith angles. *A&A*, 437(1):95, 2005.
- [153] M. Błażejowski *et al.* A multiwavelength view of the TeV blazar Markarian 421: correlated variability, flaring, and spectral evolution. *ApJ*, 630(1):130, 2005.
- [154] F. A. Aharonian *et al.* The temporal characteristics of the TeV  $\gamma$ -emission from Mkn 501 in 1997. II. Results from HEGRA CT1 and CT2. *A&A*, 349(3):29, 1999.
- [155] P. M. Chadwick *et al.* Very High Energy gamma rays from PKS 2155-304. *ApJ*, 513(1):161, 1999.
- [156] F. A. Aharonian *et al.* H.E.S.S. observations of PKS 2155-304. *A&A*, 430(3):865, 2005.

- [157] F. A. Aharonian *et al.* Discovery of VHE gamma rays from PKS 2005–489. *A&A*, 436(2):L17, 2005.
- [158] G. Ghisellini. Extreme blazars. *Astroparticle Physics*, 11(1–2):11, 1999.
- [159] L. Costamante and G. Ghisellini. TeV candidate BL Lac objects. *A&A*, 384(1):56, 2002.
- [160] S. Pita *et al.* and the H.E.S.S. collaboration. Discovery of Very High Energy gamma - ray emission from the extreme BL Lac object H2356-309 with H.E.S.S. Submitted to *A&A* (arXiv:astro-ph/0602435), 2006.
- [161] J. E. Grindlay, H. F. Helmken, R. H. Brown, J. Davis, and L. R. Allen. Evidence for the detection of gamma rays from Centaurus A at gamma-ray energies above 300 GeV. *ApJ*, 197(2):L9, 1975.
- [162] A. Carramiñana *et al.* An upper limit to 300 GeV gamma ray emission from Centaurus A. *A&A*, 228(2):327, 1990.
- [163] G. P. Rowell *et al.* TeV observations of Centaurus A. *Astroparticle Physics*, 11(1–2):217, 1999.
- [164] P. M. Chadwick *et al.* A search for Very High Energy gamma rays from Active Galactic Nuclei visible from the southern hemisphere. *ApJ*, 521(2):547, 1999.
- [165] M. Beilicke for the H.E.S.S. collaboration. Observation of the giant radio galaxy M 87 at TeV energies with H.E.S.S. Cherenkov telescopes. In *Proceedings of the 29th International Cosmic Ray Conference, Pune, India, 2005*, B. Sripathi Acharya, S. Gupta, P. Jagadeesan, A. Jain, S. Karthikeyan, S. Morris and S. Tonwar (eds.), volume 4, page 299. Mumbai, India: Tata Institute of Fundamental Research, 2005.
- [166] F. A. Aharonian *et al.* Is the giant radio galaxy M 87 a TeV gamma-ray emitter? *A&A*, 403(1):L1, 2003.
- [167] M. Tluczykont *et al.* Discovery of  $> 160$  GeV  $\gamma$  rays from 1ES 1101–232 ( $z = 0.186$ ) with H.E.S.S. In *Proceedings of the 29th International Cosmic Ray Conference, Pune, India, 2005*, B. Sripathi Acharya, S. Gupta, P. Jagadeesan, A. Jain, S. Karthikeyan, S. Morris and S. Tonwar (eds.), volume 4, page 291. Mumbai, India: Tata Institute of Fundamental Research, 2005.

- [168] F. A. Aharonian *et al.* Evidence for VHE  $\gamma$ -ray emission from the distant BL Lac PG 1553+113. *A&A*, 448(2):L19, 2006.
- [169] W. C. Keel. *Active Galaxies and Quasars — Mkn 421 across the Spectrum* [online], 2002. Available from: <http://www.astr.ua.edu/keel/agn/mkn421.html> [accessed 18 March 2006].
- [170] F. A. Aharonian *et al.* Resolving the Extragalactic Background Light with gamma-ray spectra from distant blazars. Submitted to *Nature* (arXiv:astro-ph/0508073), 2006.
- [171] S. V. Godambe *et al.* Very High Energy gamma-ray and near infrared observations of 1ES2344+514 with TACTIC and MIRO telescopes. In *Proceedings of the 29th International Cosmic Ray Conference, Pune, India, 2005*, B. Sripathi Acharya, S. Gupta, P. Jagadeesan, A. Jain, S. Karthikeyan, S. Morris and S. Tonwar (eds.), volume 4, page 347. Mumbai, India: Tata Institute of Fundamental Research, 2005.
- [172] R. Atkins *et al.* Evidence for TEV Emission from GRB 970417A. *ApJ*, 533(2):L119, 2000.
- [173] M. H. Salamon and F. W. Stecker. Absorption of high-energy gamma rays by interactions with extragalactic starlight photons at high redshifts and the High-Energy gamma-ray background. *ApJ*, 493(2):547, 1998.
- [174] J. R. Primack, J. S. Bullock, R. S. Somerville, and D. MacMinn. Probing galaxy formation with TeV gamma ray absorption. *Astroparticle Physics*, 11(1-2):93, 1999.
- [175] M. G. Hauser *et al.* The COBE diffuse infrared background experiment search for the cosmic infrared background. I. Limits and detections. *ApJ*, 508(1):25, 1998.
- [176] R. A. Shafer, J. C. Mather, D. J. Fixsen, S. Brodd, and K. A. Jensen. The COBE / FIRAS final deliveries II: The correlations and caveats relating Galactic emission and the far infrared background. *BAAS*, 29(5):1360, 1997.
- [177] C. L. Bennett, J. C. Mather, D. J. Fixsen, G. Hinshaw, and E. L. Wright. The COBE-FIRAS far-IR spectral survey of the Galaxy. *BAAS*, 25:1463, 1993.

- [178] T. Stanev and A. Franceschini. Constraints on the extragalactic infrared background from gamma-ray observations of Mrk 501. *ApJ*, 494(2):L159, 1998.
- [179] E. Dwek and F. Krennrich. Simultaneous constraints on the spectrum of the Extragalactic Background Light and the intrinsic TeV spectra of Markarian 421, Markarian 501, and H1426+428. *ApJ*, 618(2):657, 2005.
- [180] F. Krennrich *et al.* Cutoff in the TeV energy spectrum of Markarian 421 during strong flares in 2001. *ApJ*, 560(1):L45, 2001.
- [181] F. W. Samuelson *et al.* The TeV spectrum of Markarian 501. *ApJ*, 501(1):L17, 1998.
- [182] F. Krennrich *et al.* Measurement of the multi-TeV gamma-ray flare spectra of Markarian 421 and Markarian 501. *ApJ*, 511(1):149, 1999.
- [183] P. P. Kronberg. Intergalactic Magnetism - Time Trials Test the Field. *Nature*, 374(6521):404, 1995.
- [184] A. G. Lyne and F. Graham-Smith. *Pulsar Astronomy*, A. King, D. Lin, S. Maran, J. Pringle and M. Ward (eds.). Cambridge, UK and New York, NY: Cambridge University Press (Cambridge Astrophysics Series, No. 16), 1990.
- [185] J. D. Jackson. *Classical Electrodynamics*. New York, NY: Wiley, 1962.
- [186] P. J. Duke. *Synchrotron Radiation*. Oxford, UK: Oxford University Press, 2000.
- [187] A. Fassò and J. Poirier. Spatial and energy distribution of muons in  $\gamma$ -induced air showers. *Phys. Rev. D*, 63(3):036002, 2001.
- [188] G. F. Krymskii and S. I. Petukhov. Acceleration of charged particles in the shell of a supernova. *Vsesoiuznaia Konferentsiia Kosmicheskim Lucham Yerevan Armenian SSR Aademiai Nauk SSSR Izvestiia Seriia Fizicheskaia*, 43:2480, 1979.
- [189] P. O. Lagage and C. J. Cesarsky. The maximum energy of cosmic rays accelerated by supernova shocks. *A&A*, 125(2):249, 1983.
- [190] K. Greisen. End to the cosmic-ray spectrum? *Phys. Rev. Lett.*, 16(17):748, 1966.



- [191] G. T. Zatsepin and V. A. Kuzmin. Upper limit of the spectrum of cosmic rays. *Soviet Phys.- JEPT Lett.*, 4:78, 1966.
- [192] M. Takeda *et al.* Extension of the cosmic-ray energy spectrum beyond the predicted Greisen-Zatsepin-Kuz'min cutoff. *Phys. Rev. Lett.*, 81(6):1163, 1998.
- [193] T. K. Gaisser. *Cosmic Rays and Particle Physics*. Cambridge, UK and New York, NY: Cambridge University Press, 1990.
- [194] W. I. Axford, E. Leer, and G. Skadron. The acceleration of cosmic rays by shock waves. In *Proceedings of the 15th International Cosmic Ray Conference, Plovdiv, Bulgaria, 1977*, C. Ya. Christov *et al.* (eds.), volume 11, page 132. Sofia, Bulgaria: Institute for Nuclear Research, Bulgarian Academy of Sciences, 1977.
- [195] G. F. Krymskii. A regular mechanism for the acceleration of charged particles on the front of a shock wave. *Akademiia Nauk SSSR Doklady*, 234:1306, 1977.
- [196] A. R. Bell. The acceleration of cosmic rays in shock fronts. *MNRAS*, 182:147, 1978.
- [197] R. D. Blandford and J. P. Ostriker. Particle acceleration by astrophysical shocks. *ApJ*, 221:L29, 1978.
- [198] G. G. Fazio. Gamma radiation from celestial objects. *A&A Rev.*, 5:481, 1967.
- [199] M. Fatuzzo and F. Melia. A kinship between the EGRET supernova remnants and Sagittarius A East. *ApJ*, 596(2):1035, 2003.
- [200] W. Bednarek and M. Bartosik. Gamma-rays from the pulsar wind nebulae. *A&A*, 405(2):689, 2003.
- [201] A. H. Compton. The spectrum of scattered X-rays. *Physical Review*, 22(5):409, 1923.
- [202] T. Erber. High-energy electromagnetic conversion processes in intense magnetic fields. *Rev. Mod. Phys.*, 38(4):626, 1966.
- [203] A. K. Harding, M. G. Baring, and P. L. Gonthier. Photon-splitting cascades in gamma-ray pulsars and the spectrum of PSR 1509–58. *ApJ*, 476(pt 1):246, 1997.

- [204] K. A. van Riper. Stellar core collapse. II - Inner core bounce and shock propagation. *ApJ*, 257(pt 2):793, 1982.
- [205] S. Hannestad. *Aspects of Neutrino Physics in the Early Universe*. PhD thesis, University of Aarhus, Denmark, 1997.
- [206] S. Chandrasekhar. The maximum mass of ideal white dwarfs. *ApJ*, 74:81, 1931.
- [207] F. H. Shu. *Physical Universe: Introduction to Astronomy*. New York, NY: University Science Books, 1982.
- [208] L. Biermann. Über den ursprung der magnetfelder auf sternem und im interstellaren raum. *Zeitschrift für Naturforschung*, 5a:65, 1950.
- [209] J. MacDonald and D. J. Mullan. Magnetic fields in massive stars: dynamics and origin. *MNRAS*, 348(2):702, 2004.
- [210] W. Baade and F. Zwicky. On Super-novae. *PNAS*, 20(5):254, 1934.
- [211] A. Hewish, S. J. Bell, J. D. Pilkington, P. F. Scott, and R. A. Collins. Observation of a rapidly pulsating radio source. *Nature*, 217(5130):709, 1968.
- [212] J. H. Jeans. *Astronomy and Cosmogony*. Cambridge, UK: The University Press, 1928.
- [213] F. Hoyle, J. V. Narlikar, and J. A. Wheeler. Electromagnetic waves from very dense stars. *Nature*, 203(4948):914, 1964.
- [214] J. M. Fierro. *Observations of Spin-Powered Pulsars with the EGRET Gamma-ray Telescope*. PhD thesis, Stanford University, CA, 1995.
- [215] P. Goldreich and W. H. Julian. Pulsar electrodynamics. *ApJ*, 157(2):869, 1969.
- [216] D. W. Richards and J. M. Comella. The period of pulsar NP0532. *Nature*, 222(5193):551, 1969.
- [217] F. C. Michel. Relativistic stellar-wind torques. *ApJ*, 158(2):727, 1969.
- [218] J. P. Ostriker and J. E. Gunn. On the nature of pulsars. I. Theory. *ApJ*, 157(3):1395, 1969.

- [219] O. K. Guseinov and I. M. Iusifov. General track of pulsar evolution. *Ap&SS*, 94(2):249, 1983.
- [220] A. G. Lyne, R. S. Pritchard, and F. Graham-Smith. Twenty-three years of Crab pulsar rotational history. *MNRAS*, 265(4):1003, 1993.
- [221] A. G. Lyne, R. S. Pritchard, F. Graham-Smith, and F. Camilo. Very low braking index for the Vela pulsar. *Nature*, 381(6582):497, 1996.
- [222] V. M. Kaspi, R. N. Manchester, B. Siegman, S. Johnston, and A. G. Lyne. On the spin-down of PSR B1509–58. *ApJ*, 422(2):L83, 1994.
- [223] R. N. Manchester and B. A. Peterson. A braking index for PSR 0540–69. *ApJ*, 342:L23, 1989.
- [224] Students for the Exploration and Development of Space. *SEDS Messier Database* [online], 2004. Available from: <http://www.seds.org/messier/> [accessed 18 March 2006].
- [225] D. Bhattacharya and C. S. Shukre. Has the Crab pulsar magnetic field grown after its birth? *Journal of Astrophysics and Astronomy*, 6(4):233, 1985.
- [226] J. Hester *et al.* *Chandra::Photo Album::Crab Nebula Movie* [online], 2002. Available from: <http://chandra.harvard.edu/photo/2002/0052/> [accessed 18 March 2006].
- [227] A. J. Faulkner *et al.* The Parkes multibeam pulsar survey - V. Finding binary and millisecond pulsars. *MNRAS*, 355(1):147, 2004.
- [228] L. Zhang and K. S. Cheng. The gamma-ray conversion efficiency of rotation-powered pulsars. *MNRAS*, 294(1):L177, 1998.
- [229] B. Rudak and J. Dyks. The efficiency of gamma-ray emission from pulsars. *MNRAS*, 295(2):337, 1998.
- [230] P. A. Sturrock. A model of pulsars. *ApJ*, 164(3):529, 1971.
- [231] M. A. Ruderman and P. G. Sutherland. Theory of pulsars - Polar caps, sparks, and coherent microwave radiation. *ApJ*, 196(pt 1):51, 1975.
- [232] J. K. Daugherty and A. K. Harding. Electromagnetic cascades in pulsars. *ApJ*, 252(pt 1):337, 1982.

- [233] J. S. Shklovsky. *Supernovae*. London, UK: Wiley, 1968.
- [234] P. B. Jones. Density-functional calculations of the cohesive energy of condensed matter in very strong magnetic fields. *Phys. Rev. Lett.*, 55(12):1338, 1985.
- [235] A. K. Harding. Galactic gamma-ray emission from pulsars. *ApJ*, 247(pt 1):639, 1981.
- [236] J. K. Daugherty and A. K. Harding. Gamma-ray pulsars: emission from extended polar cap cascades. *ApJ*, 458(pt 1):278, 1996.
- [237] H. I. Nel and O. C. de Jager. Gamma-ray pulsars: Polar Cap or Outer Gap emission? *Ap&SS*, 230(1-2):299, 1995.
- [238] O. C. de Jager, A. Konopelko, B. C. Raubenheimer, and B. Visser. Prospects of observing pulsed radiation from gamma-ray pulsars with H.E.S.S. In *Proceedings of the High Energy Gamma-Ray Astronomy International Symposium, Heidelberg, Germany, 2000*, F. A. Aharonian and H. J. Völk (eds.), volume 558, page 613. Melville, NY: American Institute of Physics, 2001.
- [239] V. Radhakrishnan and D. J. Cooke. Magnetic poles and the polarization structure of pulsar radiation. *Astrophys. Lett.*, 3:225, 1969.
- [240] J. M. Rankin. Toward an empirical theory of pulsar emission - part two - on the spectral behavior of component width. *ApJ*, 274(1):359, 1983.
- [241] A. G. Lyne and R. N. Manchester. The shape of pulsar radio beams. *MNRAS*, 234:477, 1988.
- [242] A. K. Harding and J. K. Daugherty. Pulse profiles and spectra of gamma ray pulsars in the polar cap model. *Advances in Space Research*, 21(1-2):251, 1998.
- [243] K. S. Cheng, C. Ho, and M. Ruderman. Energetic radiation from rapidly spinning pulsars. I - Outer magnetosphere gaps. II - Vela and Crab. *ApJ*, 300(pt 1):500, 1986.
- [244] J. Krause-Polstorff and F. C. Michel. Pulsar space charging. *A&A*, 144(1):72, 1985.
- [245] F. C. Michel. Vacuum gaps in pulsar magnetospheres. *ApJ*, 227(pt 1):579, 1979.

- [246] I. A. Rylov. On the electron CAP shape of a rotating neutron star with a strong magnetic field. *Ap&SS*, 51(1):59, 1977.
- [247] K. S. Cheng, C. Ho, and M. Ruderman. Energetic radiation from rapidly spinning pulsars. II. Vela and Crab. *ApJ*, 300(2):522, 1986.
- [248] P. N. Bhat *et al.* Pulsed high energy gamma rays from Vela pulsar. *A&A*, 81(1-2):L3, 1980.
- [249] J. Chiang and R. W. Romani. Gamma radiation from pulsar magnetospheric gaps. *ApJ*, 400(2):629, 1992.
- [250] R. W. Romani. Gamma-ray pulsars: radiation processes in the outer magnetosphere. *ApJ*, 470(1):469, 1996.
- [251] L. Zhang and K. S. Cheng. High-energy radiation from rapidly spinning pulsars with thick outer gaps. *ApJ*, 487(1):370, 1997.
- [252] K. Hirotani and S. Shibata. Electrodynamic structure of an Outer Gap accelerator: location of the gap and the gamma-ray emission from the Crab pulsar. *ApJ*, 558(1):216, 2001.
- [253] K. Hirotani and S. Shibata. One-dimensional electric field structure of an outer gap accelerator - III. Location of the gap and the gamma-ray spectrum. *MNRAS*, 325(3):1228, 2001.
- [254] K. Hirotani and S. Shibata. Gamma-ray emission from an Outer Gap accelerator: constraints on magnetospheric current, magnetic inclination, and distance for PSR B1055-52. *ApJ*, 564(1):369, 2002.
- [255] A. K. Harding and A. G. Muslimov. High energy emission from the Polar Cap: the Slot Gap revisited. In *Proceedings of Pulsars, AXPs and SGRs Observed with BeppoSAX and Other Observatories, Marsala, Sicily, 2002*, G. Cusumano, E. Massaro and T. Mineo (eds.), page 121. Rome, Italy: Aracne Editrice, 2003.
- [256] F. Schmidt. Search for Pulsed TeV  $\gamma$ -ray Emission from Pulsars with H.E.S.S. Master's thesis, Humboldt-Universität zu Berlin, Berlin, Germany, 2005.

- [257] M. López for the MAGIC collaboration. Search for pulsed VHE gamma ray emission from the Crab pulsar. In *Proceedings of the 29th International Cosmic Ray Conference, Pune, India, 2005*, B. Sripathi Acharya, S. Gupta, P. Jagadeesan, A. Jain, S. Karthikeyan, S. Morris and S. Tonwar (eds.), volume 4, page 243. Mumbai, India: Tata Institute of Fundamental Research, 2005.
- [258] J. Dyks and B. Rudak. Two-pole caustic model for high-energy light curves of pulsars. *ApJ*, 598(2):1201, 2003.
- [259] M. G. Higgins and R. N. Henriksen. The Deutsch field gamma-ray pulsar. I - The model basics. *MNRAS*, 292:934, 1997.
- [260] W.-W. Tian and D. Leahy. Candidates for pulsar/supernova remnant associations. *Progress in Astronomy*, 22(4):308, 2004.
- [261] L. Nicastro *et al.* BeppoSAX observation of PSR B1937+21. *A&A*, 413(3):1065, 2004.
- [262] D. Bhattacharya. The origin of millisecond pulsars. In *Proceedings of the 160th colloquium of the International Astronomical Union: Pulsars: Problems and Progress, Sydney, Australia, 1996*, S. Johnston, M. A. Walker and M. Bailes (eds.), volume 105, page 547. San Francisco, CA: Astronomical Society of the Pacific, 1996.
- [263] L. Zhang and K. S. Cheng. X-ray and gamma-ray emission from millisecond pulsars. *A&A*, 398(2):639, 2003.
- [264] E. P. J. van den Heuvel and P. T. J. Bonsdema. Formation of a single millisecond pulsar by the coalescence of a neutron star and a massive white dwarf. *A&A*, 139(1):L16, 1984.
- [265] A. G. Lyne *et al.* The Parkes Southern Pulsar Survey - II. Final results and population analysis. *MNRAS*, 295(4):743, 1998.
- [266] R. N. Manchester. Radio pulsar surveys - wide and deep. In *Proceedings of the XXI Symposium on Relativistic Astrophysics: Texas in Tuscany, Florence, Italy, 2002*, R. Bandiera, R. Maiolino and F. Mannucci (eds.), page 305. Singapore: World Scientific Publishing, 2003.
- [267] M. Vivekanand, R. Narayan, and V. Radhakrishnan. On selection effects in pulsar searches. *Journal of Astrophysics and Astronomy*, 3(3):237, 1982.

- [268] V. Kalogera *et al.* The cosmic coalescence rates for double neutron star binaries. *ApJ*, 601(2):L179, 2004.
- [269] D. J. Thompson. Gamma ray pulsars: observations. In *Proceedings of the High Energy Gamma-Ray Astronomy International Symposium, Heidelberg, Germany, 2001*, F. A. Aharonian and H. J. Völk (eds.), volume 558, page 103. Melville, NY: American Institute of Physics, 2001.
- [270] C. Kouveliotou. Magnetars. *PNAS*, 96(10):5351, 1999.
- [271] C. Thompson and R. C. Duncan. The Soft Gamma Repeaters as very strongly magnetized neutron stars. II. Quiescent neutrino, X-ray, and Alfvén wave emission. *ApJ*, 473(1):322, 1996.
- [272] A. S. Fruchter, D. R. Stinebring, and J. H. Taylor. A millisecond pulsar in an eclipsing binary. *Nature*, 333(6170):237, 1988.
- [273] A. G. Lyne, S. Johnston, R. N. Manchester, L. Staveley-Smith, and N. D'Amico. An eclipsing millisecond pulsar in the globular cluster Terzan 5. *Nature*, 347(6294):650, 1990.
- [274] R. A. Hulse and J. H. Taylor. Discovery of a pulsar in a binary system. *ApJ*, 195(pt 2):L51, 1975.
- [275] M. Burgay *et al.* An increased estimate of the merger rate of double neutron stars from observations of a highly relativistic system. *Nature*, 426(6966):531, 2003.
- [276] D. Vincent. *General Relativity* [online], 2003. Available from: [http://scholar.uwinnipeg.ca/courses/38/4500.6-001/Cosmology/general\\_relativity.htm](http://scholar.uwinnipeg.ca/courses/38/4500.6-001/Cosmology/general_relativity.htm) [accessed 18 March 2006].
- [277] K. Bennett *et al.* COS-B observations of pulsed gamma-ray emission from PSR 0531 plus 21 and PSR 0833–45. *A&A*, 61(2):279, 1977.
- [278] R. Mukherjee *et al.* On the nature of the unidentified EGRET sources: Are they Geminga-like pulsars? *ApJ*, 441(2):L61, 1995.
- [279] D. J. Thompson. *Cosmic Gamma-Ray Sources*, K. S. Cheng and G. E. Romero (eds.), chapter 7, page 150. Dordrecht, The Netherlands: Kluwer Academic Press, 2004.

- [280] H. O. Vats *et al.* A possible detection of radio pulses from Geminga at 103 MHz. *MNRAS*, 302(4):L65, 1999.
- [281] D. J. Thompson, C. E. Fichtel, R. C. Hartman, D. A. Kniffen, and R. C. Lamb. Final SAS-2 gamma-ray results on sources in the galactic anticenter region. *ApJ*, 213(pt 1):252, 1977.
- [282] K. Bennett *et al.* COS-B observations of localised high-energy gamma-ray emission from the anticentre region of the galactic disc. *A&A*, 56(3):469, 1977.
- [283] G. F. Bignami, P. A. Caraveo, and R. C. Lamb. An identification for ‘Geminga’ (2CG 195+04) 1E 0630+178 - A unique object in the error box of the high-energy gamma-ray source. *ApJ*, 272(pt 2):L9, 1983.
- [284] G. F. Bignami, P. A. Caraveo, J. A. Paul, L. Salotti, and L. Vigroux. A deep optical study of the field of 1E 0630 + 178. *ApJ*, 319(pt 1):358, 1987.
- [285] D. L. Bertsch *et al.* Pulsed high-energy gamma-radiation from Geminga (1E0630 + 178). *Nature*, 357(6376):306, 1992.
- [286] G. F. Bignami and P. A. Caraveo. Geminga - New period old gamma-rays. *Nature*, 357(6376):287, 1992.
- [287] J. R. Mattox *et al.* SAS 2 observation of pulsed high-energy gamma radiation from Geminga. *ApJ*, 401(1):L23, 1992.
- [288] J. R. Mattox, J. P. Halpern, and P. A. Caraveo. Timing the Geminga pulsar with EGRET data. *A&AS*, 120:C77, 1996.
- [289] J. M. Fierro, P. F. Michelson, P. L. Nolan, and D. J. Thompson. Phase-resolved studies of the high-energy gamma-ray emission from the Crab, Geminga, and Vela pulsars. *ApJ*, 494(2):734, 1998.
- [290] L. Zhang and K. S. Cheng. Gamma-ray pulsars: the pulse profiles and phase-resolved spectra of Geminga. *MNRAS*, 320(4):477, 2001.
- [291] E. V. Gotthelf, J. P. Halpern, and R. Dodson. Detection of pulsed X-ray emission from PSR B1706–44. *ApJ*, 567(2):L125, 2002.
- [292] J. P. Finley *et al.* A broadband X-ray study of the young neutron star PSR B1706–44. *ApJ*, 493(2):884, 1998.



- [293] R. Dodson and K. Golap. On the association of G343.1–2.3 and PSR B1706–44. *MNRAS*, 334(1):L1, 2002.
- [294] L. Nicastro, S. Johnston, and B. Koribalski. Evidence against the association of PSR B1706–44 with SNR G343.1–2.3. *A&A*, 306(1):L49, 1996.
- [295] F. Schmidt (Humboldt–Universität zu Berlin, Berlin, Germany). Private communication, 2004.
- [296] K. Hirotani (Max-Planck-Institut für Kernphysik, Heidelberg, Germany). Private communication, 2004.
- [297] D. J. Thompson, C. E. Fichtel, D. A. Kniffen, and H. B. Ögelman. SAS-2 high-energy gamma-ray observations of the Vela pulsar. II. *ApJ*, 214(pt 2):L17, 1977.
- [298] K. Bennett *et al.* Pulsar studies with COMPTEL. *ApJS*, 90(2):823, 1994.
- [299] H. Ögelman, J. P. Finley, and H. U. Zimmerman. Pulsed X-rays from the Vela pulsar. *Nature*, 361(6408):136, 1993.
- [300] P. M. Chadwick *et al.* Very High Energy gamma rays from young pulsars and supernova remnants in the southern hemisphere. *ApJ*, 537(1):414, 2000.
- [301] A. Konopelko *et al.* for the HEGRA collaboration. Detection of gamma rays above 1 TeV from the Crab nebula by the second HEGRA imaging atmospheric Cherenkov telescope at La Palma. *Astroparticle Physics*, 4(3):199, 1996.
- [302] B. S. Acharya, M. V. S. Rao, K. Sivaprasad, B. V. Sreekantan, and P. R. Vishwanath. First simultaneous detection of PeV energy burst from the Crab nebula. *Nature*, 347(6291):364, 1990.
- [303] M. F. Cawley *et al.* Detection of TeV gamma rays from the Crab nebula using the atmospheric Cherenkov imaging technique. *Irish Astronomical Journal*, 19:51, 1989.
- [304] A. F. Cheng and M. A. Ruderman. A Crab pulsar model - X-ray, optical, and radio emission. *ApJ*, 216(pt 1):865, 1977.
- [305] H. Ögelman and J. P. Finley. ROSAT observations of pulsed soft X-ray emission from PSR 1055–52. *ApJ*, 413(1):L31, 1993.

- [306] J. A. Combi, G. E. Romero, and I. N. Azcarate. A non-thermal radio source detected towards PSR 1055–52. *Ap&SS*, 250(1):1, 1997.
- [307] J. H. Taylor and J. M. Cordes. Pulsar distances and the Galactic distribution of free electrons. *ApJ*, 411(2):674, 1993.
- [308] S. R. Kulkarni, T. C. Clifton, D. C. Backer, R. S. Foster, and A. S. Fruchter. A fast pulsar in radio nebula CTB80. *Nature*, 331(6151):50, 1988.
- [309] K. Hirotani. Gamma-ray emissions from pulsars: spectra of the TeV fluxes from Outer Gap accelerators. *ApJ*, 549(1):495, 2001.
- [310] L. Kuiper *et al.* COMPTEL detection of pulsed gamma -ray emission from PSR B1509–58 up to at least 10 MeV. *A&A*, 351(6):119, 1999.
- [311] C. W. Akerlof *et al.* Search for TeV gamma-rays from Geminga. *A&A*, 274(1):L17, 1993.
- [312] T. Kifune *et al.* Very high energy gamma rays from PSR 1706–44. *ApJ*, 438(2):L91, 1995.
- [313] P. M. Chadwick *et al.* Flux limits for TeV emission from pulsars. In *Proceedings of the GeV–TeV Gamma Ray Astrophysics Workshop: Towards a major atmospheric Cherenkov detector VI, Snowbird, Utah, 1999*, B. L. Dingus, M. H. Salamon and D. B. Kieda (eds.), volume 515, page 276. Melville, NY: American Institute of Physics, 2000.
- [314] R. Srinivasan *et al.* Very High Energy observations of PSR B1951+32. *ApJ*, 489(1):170, 1997.
- [315] W. Becker, N. Kawai, W. Brinkmann, and R. Mignani. The putative pulsar-wind nebulae of the three musketeers PSR B1055–52, B0656+14 and Geminga revisited. *A&A*, 352(6):532, 1999.
- [316] D. Sanwal, G. G. Pavlov, and V. E. Zavlin. The Pulsar Wind Nebula of the Geminga pulsar. Submitted to *ApJ*(arXiv:astro-ph/0511364), 2005.
- [317] N. Kawai, K. Tamura, and Y. Saito. ASCA observations of pulsars and their surroundings. *Advances in Space Research*, 21(1–2):213, 1998.
- [318] P. V. Ramanamurthy *et al.* A long-term study of high-energy gamma-ray emission from the Vela, Geminga, and Crab Pulsars. *ApJ*, 450(2):791, 1995.

- [319] I. Frank and Ig. Tamm. Coherent visible radiation of fast electrons passing through matter. *C.R. Acad. Sci. USSR*, 14(3):109, 1937.
- [320] M. V. S. Rao and B. V. Sreekantan. *Extensive Air Showers*. Singapore and River Edge, NJ: World Scientific, 1998.
- [321] S. Schlenker. Simulation Study of the H.E.S.S. Camera Trigger Rate. Master's thesis, Humboldt-Universität zu Berlin, Berlin, Germany, 2001.
- [322] K. Bernlöhr. *Konrad Bernlöhr* [online]. Available from: <http://www.mpi-hd.mpg.de/hfm/~bernlöhr> [accessed 18 March 2006][restricted access].
- [323] T. C. Weekes. The Atmospheric Cherenkov Technique in Very High Energy gamma-ray astronomy. *Space Sci. Rev.*, 75(1-2):1, 1996.
- [324] F. A. Aharonian *et al.* Calibration of cameras of the H.E.S.S. detector. *Astroparticle Physics*, 22(2):109, 2004.
- [325] K. Bernlöhr. *H.E.S.S. Internal Web Pages: Visibility of Astronomical Objects* [online]. Available from: [http://www.mpi-hd.mpg.de/hfm/HESS/intern/hess\\_internal.htm](http://www.mpi-hd.mpg.de/hfm/HESS/intern/hess_internal.htm) [accessed 18 March 2006][restricted access].
- [326] S. W. Barwick *et al.* The energy spectra and relative abundances of electrons and positrons in the Galactic cosmic radiation. *ApJ*, 498(2):779, 1998.
- [327] J. Nishimura *et al.* Emulsion chamber observations of primary cosmic-ray electrons in the energy range 30-1000 GeV. *ApJ*, 238(pt 1):394, 1980.
- [328] K.-K. Tang. The energy spectrum of electrons and cosmic-ray confinement: A new measurement and its interpretation. *ApJ*, 278(pt 1):881, 1984.
- [329] R. L. Golden *et al.* A measurement of the absolute flux of cosmic-ray electrons. *ApJ*, 287(pt 1):622, 1984.
- [330] R. L. Golden *et al.* Observations of cosmic-ray electrons and positrons using an imaging calorimeter. *ApJ*, 436(2):769, 1994.
- [331] W. Hofmann. *H.E.S.S. Telescopes* [online], 2004. Available from: [http://www.mpi-hd.mpg.de/hfm/HESS/public/telescope/hn\\_telescopes.htm](http://www.mpi-hd.mpg.de/hfm/HESS/public/telescope/hn_telescopes.htm) [accessed 18 March 2006].

- [332] A. M. Hillas. Čerenkov light images of EAS produced by primary gamma. In *Proceedings of the 19th International Cosmic Ray Conference, La Jolla, CA, 1985*, F. C. Jones *et al.* (eds.), volume 3, page 445. Goddard Space Flight Center, Greenbelt, MD: NASA Conference publication No. 2376, 1985.
- [333] A. Konopelko *et al.* for the H.E.S.S. collaboration. Study of the performance of a single, stand-alone H.E.S.S. telescope: Monte Carlo simulations and data. In *Proceedings of the 28th International Cosmic Ray Conference, Tsukuba, Japan, 2003*, G. Kajita, Y. Asaoka, A. Kawachi, Y. Matsubara and M. Sasaki (eds.), page 2903. Tokyo, Japan: Universal Academy Press, 2003.
- [334] C. Masterson for the H.E.S.S. collaboration. Observation of Galactic  $\gamma$ -ray TeV sources with H.E.S.S. In *Proceedings of the 28th International Cosmic Ray Conference, Tsukuba, Japan, 2003*, G. Kajita, Y. Asaoka, A. Kawachi, Y. Matsubara and M. Sasaki (eds.), page 2323. Tokyo, Japan: Universal Academy Press, 2003.
- [335] S. Funk *et al.* The trigger system of the H.E.S.S. telescope array. *Astroparticle Physics*, 22(3–4):285, 2004.
- [336] W. Hoffman. Trigger strategies for the H.E.S.S. CT array, v.2. *H.E.S.S. Internal Documents* [online], 1998. Available from: <http://www.mpi-hd.mpg.de/hfm/HESS/intern/> [accessed 18 March 2006][restricted access].
- [337] D. Berge. Development of an algorithm for the shower reconstruction with the H.E.S.S. telescope system. Master's thesis, Humboldt–Universität zu Berlin, Berlin, Germany, 2002.
- [338] F. A. Aharonian *et al.* H.E.S.S. letter of intent. *MPIK Report, MPIK H-V11* [online], 1997. Available from: <http://www.mpi-hd.mpg.de/hfm/HESS/public/> [accessed 18 March 2006].
- [339] M. Sarazin. Environmental conditions on potential observatories. *Gamsberg Astroclimatological Summary Report (ESO-MPIA)* [online], 1995. Available from: <http://www.eso.org/gen-fac/pubs/astclim/espas/gamsberg/> [accessed 18 March 2006].
- [340] University of Namibia. *University of Namibia — The H.E.S.S. project* [online], 2005. Available from: <http://www.unam.na/research/hess/> [accessed 18 March 2006].

- [341] K. Bernlöhr *et al.* The optical system of the H.E.S.S. imaging atmospheric Cherenkov telescopes. Part I: layout and components of the system. *Astroparticle Physics*, 20(2):111, 2003.
- [342] J.M. Davies and E.S. Cotton. Design of the quartermaster solar furnace. *J. Solar Energy Sci. and Eng.*, 1(2-3):16, 1957.
- [343] D.J. Fegan.  $\gamma$ /hadron separation at TeV energies. *J. Phys. G: Nucl. Part. Phys.*, 23(9):1013, 1997.
- [344] F. A. Aharonian *et al.* Conceptual design of the system telescopes. *H.E.S.S. Project Documentation: Appendix B* [online], 1997. Available from: [http://www.mpi-hd.mpg.de/hfm/HESS/public/hn\\_project.htm](http://www.mpi-hd.mpg.de/hfm/HESS/public/hn_project.htm) [accessed 18 March 2006].
- [345] J. Quinn and the VERITAS collaboration. VERITAS: The Very Energetic Radiation Imaging Telescope Array System. In *Proceedings of the 27th International Cosmic Ray Conference, Hamburg, Germany, 2001*, K. H. Kampert *et al.* (eds.), page 2781. Katlenburg-Lindau, Germany: Copernicus Gesellschaft, 2001.
- [346] R. Cornils *et al.* The optical system of the H.E.S.S. imaging atmospheric Cherenkov telescopes. Part II: mirror alignment and point spread function. *Astroparticle Physics*, 20(2):129, 2003.
- [347] P. Vincent *et al.* for the H.E.S.S. collaboration. Performance of the H.E.S.S. cameras. In *Proceedings of the 28th International Cosmic Ray Conference, Tsukuba, Japan, 2003*, G. Kajita, Y. Asaoka, A. Kawachi, Y. Matsubara and M. Sasaki (eds.), page 2887. Tokyo, Japan: Universal Academy Press, 2003.
- [348] N. Leroy *et al.* for the H.E.S.S. collaboration. Calibration results for the first two H.E.S.S. array telescopes. In *Proceedings of the 28th International Cosmic Ray Conference, Tsukuba, Japan, 2003*, G. Kajita, Y. Asaoka, A. Kawachi, Y. Matsubara and M. Sasaki (eds.), page 2895. Tokyo, Japan: Universal Academy Press, 2003.
- [349] A. Noutsos *et al.* for the H.E.S.S. collaboration. A novel alternative to UV-lasers used in flat-fielding VHE  $\gamma$ -ray telescopes. In *Proceedings of the 28th International Cosmic Ray Conference, Tsukuba, Japan, 2003*, G. Kajita, Y.

- Asaoka, A. Kawachi, Y. Matsubara and M. Sasaki (eds.), page 2975. Tokyo, Japan: Universal Academy Press, 2003.
- [350] HERO Electronics. *HERO* [online], 2005. Available from: <http://www.heroelec.co.uk/> [accessed 18 March 2006].
- [351] S. Schlenker *et al.* for the H.E.S.S. collaboration. The central Data Acquisition system of the H.E.S.S. telescope system. In *Proceedings of the 28th International Cosmic Ray Conference, Tsukuba, Japan, 2003*, G. Kajita, Y. Asaoka, A. Kawachi, Y. Matsubara and M. Sasaki (eds.), page 2891. Tokyo, Japan: Universal Academy Press, 2003.
- [352] K.-M. Aye *et al.* for the H.E.S.S. collaboration. Atmospheric monitoring for the H.E.S.S. project. In *Proceedings of the 28th International Cosmic Ray Conference, Tsukuba, Japan, 2003*, G. Kajita, Y. Asaoka, A. Kawachi, Y. Matsubara and M. Sasaki (eds.), page 2879. Tokyo, Japan: Universal Academy Press, 2003.
- [353] K.-M. Aye *et al.* for the H.E.S.S. collaboration. Implications of LIDAR observations at the H.E.S.S. site in Namibia for energy calibration of the Atmospheric Cherenkov Telescopes. In *Proceedings of the 28th International Cosmic Ray Conference, Tsukuba, Japan, 2003*, G. Kajita, Y. Asaoka, A. Kawachi, Y. Matsubara and M. Sasaki (eds.), page 2883. Tokyo, Japan: Universal Academy Press, 2003.
- [354] K.-M. Aye *et al.* for the H.E.S.S. collaboration. Implications of LIDAR observations at the H.E.S.S. site in Namibia for energy calibration of the Atmospheric Cherenkov Telescopes. Presentation (poster) in the 28th International Cosmic Ray Conference, Tsukuba, Japan, 2003.
- [355] D. Jansen. *Greenhouse gases* [online], 1999. Available from: [http://www.ou.nl/open/dja/Klimaat/System/greenhouse\\_gases.htm](http://www.ou.nl/open/dja/Klimaat/System/greenhouse_gases.htm) [accessed 18 March 2006].
- [356] K.-M. Aye *et al.* for the H.E.S.S. collaboration. Atmospheric monitoring for the H.E.S.S. project. Presentation (poster) in the 28th International Cosmic Ray Conference, Tsukuba, Japan, 2003.
- [357] A. G. Lyne and M. Roberts. *Jodrell Bank Crab Pulsar Monthly Ephemeris* [online], 2005. Available from: <http://www.jb.man.ac.uk/~pulsar/crab.html> [accessed 18 March 2006].

- [358] C. Franzen, S. Gillessen, G. Hermann, and J. Hinton for the H.E.S.S. collaboration. Optical observations of the Crab pulsar using the first H.E.S.S. Cherenkov telescope. In *Proceedings of the 28th International Cosmic Ray Conference, Tsukuba, Japan, 2003*, G. Kajita, Y. Asaoka, A. Kawachi, Y. Matsubara and M. Sasaki (eds.), page 2987. Tokyo, Japan: Universal Academy Press, 2003.
- [359] C. Straubmeier, G. Kanbach, and F. Schrey. OPTIMA: A photon counting high-speed photometer. *Experimental Astronomy*, 11(3):157, 2001.
- [360] R. Le Gallou. A transmissometer for H.E.S.S. Presentation (slides) in the H.E.S.S. collaboration meeting, Durham, UK, 2004.
- [361] W. Carnuth. Verification of Klett's method by comparison of lidar and transmissometer measurements. In *Proceedings of the Atmospheric Propagation in the UV, Visible, IR, and MM-Wave Region and Related Systems Aspects, 1990*, F. E. Niles, M. G. Heaps, R. C. Shirkey, L. D. Duncan and M. A. Seagraves (eds.), page 12. Neuilly Sur Seine, France: North Atlantic Treaty Organization, Advisory Group for Aerospace Research and Development (AGARD), 1990.
- [362] L. R. Bissonnette, G. J. Kunz, and K. Weiss-Wrana. Comparison of lidar and transmissometer measurements. *Optical Engineering*, 36(1):131, 1997.
- [363] J. L. Gaumet and A. Petitpa. Lidar-transmissometer visibility comparisons over slant and horizontal paths. *Journal of Applied Meteorology*, 21(5):683, 1982.
- [364] M.A. Mostafá for the Pierre Auger collaboration. Atmospheric monitoring for the Pierre Auger fluorescence detector. In *Proceedings of the 28th International Cosmic Ray Conference, Tsukuba, Japan, 2003*, G. Kajita, Y. Asaoka, A. Kawachi, Y. Matsubara and M. Sasaki (eds.), page 465. Tokyo, Japan: Universal Academy Press, 2003.
- [365] D. Horns. Observations with the ROTSE-III telescope on the H.E.S.S. site. *H.E.S.S. Internal Documents* [online], 2002. Available from: <http://www.mpi-hd.mpg.de/hfm/HESS/intern/> [accessed 18 March 2006][restricted access].
- [366] D. Horns. Status of ROTSE 3c. Presentation (slides) in the H.E.S.S. collaboration meeting, Durham, UK, 2004.

- [367] M. Hauser, K. Möllenhoff, Pühlhofer, L. Schöffner, and S. Wagner. Status of ATOM H.E.S.S. Presentation (slides) in the H.E.S.S. collaboration meeting, Durham, UK, 2004.
- [368] G. Pühlhofer. Background estimation, excess counts and significance determination when using a relative acceptance correction. *H.E.S.S. Internal Documents* [online], 2004. Available from: <http://www.mpi-hd.mpg.de/hfm/HESS/intern/> [accessed 18 March 2006][restricted access].
- [369] G. Pühlhofer for the HEGRA collaboration. Scans of the TeV  $\gamma$ -ray sky with the HEGRA system of Cherenkov telescopes. In *Proceedings of the 28th International Cosmic Ray Conference, Tsukuba, Japan, 2003*, G. Kajita, Y. Asaoka, A. Kawachi, Y. Matsubara and M. Sasaki (eds.), page 2319. Tokyo, Japan: Universal Academy Press, 2003.
- [370] R. Brun and F. Rademakers. The ROOT System Home Page [online], 1995. Available from: <http://root.cern.ch> [accessed 18 March 2006].
- [371] S. Allen. *Timescales* [online], 2005. Available from: <http://www.ucolick.org/~sla/leapsecs/timescales.html> [accessed 18 March 2006].
- [372] S. Aoki *et al.* The new definition of universal time. *A&A*, 105(2):359, 1982.
- [373] IERS Global Geophysical Fluids Centre (GGFC). *Special Bureau for the Core (SBC)* [online], 2005. Available from: <http://www.astro.oma.be/SBC/main.html> [accessed 18 March 2006].
- [374] IERS Central Bureau. Leap seconds announcements in UTC. *IERS Bulletin C* [online], 2005. Available from: <http://www.iers.org/iers/products/eop/> [accessed 18 March 2006].
- [375] R. Fisher. *Astronomical Times* [online], 1996. Available from: <http://www.cv.nrao.edu/~rfisher/Ephemerides/times.html> [accessed 18 March 2006].
- [376] R. L. Graham, D. E. Knuth, and O. Patashnik. *Concrete Mathematics: A Foundation for Computer Science*, chapter 3, page 67. Reading, MA: Addison-Wesley, second edition, 1994.
- [377] P. R. Bevington and D. K. Robinson. *Data Reduction and Error Analysis for the Physical Sciences*. Boston, MA: McGraw-Hill, third edition, 2003.



- [378] D. Morin. Week 84: Poisson and Gaussian. *Weekly Problems* [online], 2004. Available from: <http://www.physics.harvard.edu/academics/undergrad/probweek/sol84.pdf> [accessed 18 March 2006].
- [379] D. Manchester and D. Nice. *Tempo* [online], 2000. Available from: <http://pulsar.princeton.edu/tempo/> [accessed 18 March 2006].
- [380] E. M. Standish. Orientation of the JPL ephemerides, DE 200/LE 200, to the dynamical equinox of J 2000. *A&A*, 114(2):297, 1982.
- [381] Commonwealth Scientific and Industrial Research Organisation (CSIRO). *Australian Pulsar Timing Data Archive* [online], 2004. Available from: <http://www.atnf.csiro.au/research/pulsar/archive/> [accessed 18 March 2006].
- [382] A. Konopelko (Humboldt–Universität zu Berlin, Berlin, Germany), F. Breitling (Humboldt–Universität zu Berlin, Berlin, Germany), and F. Schmidt (Humboldt–Universität zu Berlin, Berlin, Germany). Private communication, 2004.
- [383] F. A. Aharonian *et al.* The energy spectrum of TeV gamma rays from the Crab nebula as measured by the HEGRA system of imaging Air Čerenkov telescopes. *ApJ*, 539(1):317, 2000.
- [384] W. Benbow (Max-Planck-Institut für Kernphysik, Heidelberg, Germany). Private communication, 2004.
- [385] M. Beilicke (Institut für Experimentalphysik, Universität Hamburg, Hamburg, Germany). Private communication, 2003.
- [386] F. Breitling (Humboldt–Universität zu Berlin, Berlin, Germany). Private communication, 2004.
- [387] U. S. Naval Observatory and Royal Greenwich Observatory. *The Astronomical Almanac for the Year 2003*. Washington, DC: U.S. Government Printing Office (USGPO) and London, UK: The Stationery Office, 2001.
- [388] STASYS Ltd. *WGS 84: World Geodetic System 1984* [online], 2005. Available from: <http://www.wgs84.com/> [accessed 18 March 2006].
- [389] D. T. Sandwell. Reference Earth Model — WGS84. *University of San Diego, CA: Geodynamics SIO 234 Syllabus* [online], 2002. Available from:

- <http://topex.ucsd.edu/geodynamics/14gravity1.2.pdf> [accessed 18 March 2006].
- [390] M. Tluczykont for the H.E.S.S. collaboration. Status and future of the H.E.S.S. experiment. Presentation (poster) in the Joint Symposium on GeV-TeV Astrophysics in the GLAST Era, Stanford, CA, 2004.
- [391] R. Mukherjee *et al.* Studies of AGN using the STACEE detector. In *Proceedings of the 26th International Cosmic Ray Conference, Salt Lake City, Utah, 1999*, D. Kieda *et al.* (eds.), volume 3, page 362. Melville, NY: American Institute of Physics, 2000.
- [392] R. J. Beran. Asymptotic theory of a class of tests for uniformity of a circular distribution. *Ann. Math. Stat.*, 40(4):1196, 1969.
- [393] O. C. de Jager, B. C. Raubenheimer, and J. W. H. Swanepoel. A powerful test for weak periodic signals with unknown light curve shape in sparse data. *A&A*, 221(1):180, 1989.
- [394] O. C. de Jager, B. C. Raubenheimer, and J. W. H. Swanepoel. Kernel density estimations applied to gamma ray light curves. *A&A*, 170(1):187, 1986.
- [395] K. Torii *et al.* ASCA detection of pulsed X-ray emission from PSR J0631+1036. *ApJ*, 551(2):L151, 2001.
- [396] S. Yancopoulos, T. T. Hamilton, and D. J. Helfand. The detection of pulsed X-ray emission from a nearby radio pulsar. *ApJ*, 429(2):832, 1994.
- [397] D. A. Leahy *et al.* On searches for pulsed emission with application to four globular cluster X-ray sources - NGC 1851, 6441, 6624, and 6712. *ApJ*, 266(pt 1):160, 1983.
- [398] D. A. Leahy, R. F. Elsner, and M. C. Weisskopf. On searches for periodic pulsed emission - The Rayleigh test compared to epoch folding. *ApJ*, 272(pt 1):256, 1983.
- [399] R. Buccheri *et al.* Search for pulsed gamma-ray emission from radio pulsars in the COS-B data. *A&A*, 128(1):245, 1983.
- [400] O. C. de Jager. *The Analysis and Interpretation of VHE ( $E_\gamma > 1$  TeV)  $\gamma$ -ray Measurements*. PhD thesis, Potchefstroom University, SA, 1987.

- [401] K. T. S. Brazier. Confidence intervals from the Rayleigh test. *MNRAS*, 268(3):709, 1994.
- [402] J. D. Hart. On the choice of a truncation point in Fourier Series Density Estimation. *JSCS*, 21(2):95, 1985.
- [403] O. C. de Jager. On periodicity tests and flux limit calculations for gamma-ray pulsars. *ApJ*, 436(1):239, 1994.
- [404] O. C. de Jager (Unit for Space Physics, North-West University, Potchefstroom, SA). Private communication, 2004.
- [405] O. Helene. Upper limit of peak area. *Nuclear Instruments & Methods in Physics Research*, 212(1-3):319, 1983.
- [406] W. T. Eadie, D. Drijard, and F. E. James. *Statistical Methods in Experimental Physics*. Amsterdam: North-Holland, 1971.
- [407] J. Spanier and K. B. Oldham. *An Atlas of Functions*, S. Tamburrino (ed.), chapter 40, page 385. USA: Hemisphere Publishing Corporation, 1987.
- [408] U. Schwanke (Humboldt-Universität zu Berlin, Berlin, Germany) and T. Lohse (Humboldt-Universität zu Berlin, Berlin, Germany). Private communication, 2004.
- [409] G. J. Feldman and R. D. Cousins. Unified approach to the classical statistical analysis of small signals. *Phys. Rev. D*, 57(7):3873, 1998.
- [410] J. Neyman. Outline of a theory of statistical estimation based on the classical theory of probability. *Phil. Trans. R. Soc. London, A* 236(767):333, 1937.
- [411] A. Fog. *Pseudo random number generators* [online], 2005. Available from: <http://www.agner.org/random/> [accessed 18 March 2006].
- [412] M. Matsumoto and T. Nishimura. Mersenne Twister: A 623-dimensionally equidistributed uniform pseudo-random number generator. *ACM Transactions on Modeling and Computer Simulation (TOMACS)*, 8(1):3, 1998.
- [413] R. Le Gallou (University of Durham, Durham, UK). Private communication, 2006.

- [414] G. Mohanty *et al.* Measurement of TeV gamma-ray spectra with the Cherenkov imaging technique. *Astroparticle Physics*, 9(1):15, 1998.
- [415] S. Johnston *et al.* Discovery of a very bright, nearby binary millisecond pulsar. *Nature*, 361(6413):613, 1993.
- [416] J. M. Fierro *et al.* EGRET high-energy  $\gamma$ -ray pulsar studies. II. Individual millisecond pulsars. *ApJ*, 447(2):807, 1995.
- [417] A. G. Lyne *et al.* A double-pulsar system: a rare laboratory for relativistic gravity and plasma physics. *Science*, 303(5661):1153, 2004.
- [418] M. Lyutikov. On the nature of eclipses in binary pulsar J0737-3039. *MNRAS*, 353(4):1095, 2004.
- [419] J. Arons, D. C. Backer, A. Spitkovsky, and V. M. Kaspi. Probing relativistic winds: the case of PSR J0737-3039 A and B. In *Proceedings of the ASP Conf. Ser. 328: Binary Radio Pulsars, Aspen, CO, 2004*, F. A. Rasio and I. H. Stairs (eds.), page 95. San Francisco, CA: Astronomical Society of the Pacific, 2005.
- [420] K. Bernlöhner. *H.E.S.S. Internal Web Pages: Run List Tool* [online]. Available from: [http://www.mpi-hd.mpg.de/hfm/HESS/intern/hess\\_internal.htm](http://www.mpi-hd.mpg.de/hfm/HESS/intern/hess_internal.htm) [accessed 18 March 2006][restricted access].
- [421] D. J. Thompson *et al.* EGRET high-energy gamma-ray pulsar studies. 1: Young spin-powered pulsars. *ApJ*, 436(1):229, 1994.
- [422] V. M. Kaspi *et al.* High-energy gamma-ray observations of two young, energetic radio pulsars. *ApJ*, 528(1):445, 2000.
- [423] C. M. Olbert, C. R. Clearfield, N. E. Williams, J. W. Keohane, and D. A. Frail. A bow shock nebula around a compact X-ray source in the supernova remnant IC 443. *ApJ*, 554(2):L205, 2001.
- [424] J. W. Keohane, R. Petre, E. V. Gotthelf, M. Ozaki, and K. Koyama. A possible site of cosmic ray acceleration in the supernova remnant IC 443. *ApJ*, 484(1):350, 1997.
- [425] B. M. Gaensler *et al.* The X-ray structure of the pulsar bow shock G189.22 +2.90 in the supernova remnant IC 443. Submitted to *ApJ*(arXiv:astro-ph/0601304), 2006.

- [426] W. Becker and J. Trümper. The X-ray luminosity of rotation-powered neutron stars. *A&A*, 326(6):682, 1997.
- [427] D. R. Lorimer, A. G. Lyne, and F. Camilo. A search for pulsars in supernova remnants. *A&A*, 331(6):1002, 1998.
- [428] A. G. Lyne, A. Brinklow, J. Middleditch, S. R. Kulkarni, and D. C. Backer. The discovery of a millisecond pulsar in the globular cluster M28. *Nature*, 328(6129):399, 1987.
- [429] Y. Saito *et al.* Detection of magnetospheric X-ray pulsation from millisecond pulsar PSR B1821-24. *ApJ*, 477(1):L37, 1997.
- [430] W. Becker *et al.* Chandra X-ray observatory observations of the globular cluster M28 and its millisecond pulsar PSR B1821-24. *ApJ*, 594(2):798, 2003.
- [431] L. Kuiper, W. Hermsen, and B. Stappers. Chandra and RXTE studies of the X-ray/ $\gamma$ -ray millisecond pulsar PSR J0218+4232. *Advances in Space Research*, 33(4):507, 2004.
- [432] P. C. Schroeder *et al.* OSSE upper limits to pulsar gamma-ray emission. *ApJ*, 450(2):784, 1995.
- [433] M. McLaughlin. Periastron observations of a massive eclipsing pulsar binary system. In *Chandra Proposal ID #06408206*, available from: <http://acis.mit.edu/cgi-bin/get-obsid?id=06261>, page 1643, 2004.
- [434] P. R. Vishwanath *et al.* Evidence for persistent emission of TeV gamma-rays from Crab and Geminga pulsars. *BASI*, 23:474, 1995.
- [435] M. de Naurois *et al.* Measurement of the Crab flux above 60 GeV with the CELESTE Čerenkov telescope. *ApJ*, 566(1):343, 2002.
- [436] F. Schmidt *et al.* and the H.E.S.S. collaboration. Search for pulsed TeV gamma-ray emission from young pulsars with H.E.S.S. In *Proceedings of the High Energy Gamma-Ray Astronomy International Symposium, Heidelberg, Germany, 2004*, F. A. Aharonian and H. J. Völk (eds.), page 377. Melville, NY: American Institute of Physics, 2005.
- [437] J. G. Kirk, L. Ball, and O. Skjaeraasen. Inverse Compton emission of TeV gamma rays from PSR B1259-63. *Astroparticle Physics*, 10(1):31, 1999.

- [438] L. Ball and J. G. Kirk. Probing pulsar winds using inverse compton scattering. *Astroparticle Physics*, 12(4):335, 2000.
- [439] L. Ball and J. Dodd. Shock geometry and inverse Compton emission from the wind of a binary pulsar. *PASA*, 18(1):98, 2001.
- [440] K. Murata, H. Tamaki, H. Maki, and N. Shibazaki. X-ray and  $\gamma$ -ray emission from the PSR B1259–63/Be star system. *Advances in Space Research*, 33(4):601, 2004.
- [441] S. Johnston, R. N. Manchester, A. G. Lyne, N. D’Amico, M. Bailes, B. M. Gaensler, and L. Nicastro. Radio observations of PSR B1259–63 around periastron. *MNRAS*, 279(3):1026, 1996.
- [442] N. M. McClure-Griffiths, S. Johnston, D. R. Stinebring, and L. Nicastro. Diffractive scintillation of the pulsar PSR B1259–63. *ApJ*, 492(1):L49, 1998.
- [443] N. Wex, S. Johnston, R. N. Manchester, A. G. Lyne, B. W. Stappers, and M. Bailes. Timing models for the long orbital period binary pulsar PSR B1259–63. *MNRAS*, 298(4):997, 1998.
- [444] S. Johnston, R. N. Manchester, A. G. Lyne, L. Nicastro, and J. Spyromilio. Radio and optical observations of the PSR:B1259–63 / SS:2883 Be-star binary system. *MNRAS*, 268(2):430, 1994.
- [445] S. Johnston, A. G. Lyne, R. N. Manchester, D. A. Kniffen, N. D’Amico, J. Lim, and M. Ashworth. A high-frequency survey of the southern Galactic plane for pulsars. *MNRAS*, 255:401, 1992.
- [446] J. Meeus. *Astronomical Algorithms*. Richmond, VA: Willmann–Bell, second edition, 1998.
- [447] S. Johnston, L. Ball, N. Wang, and R. N. Manchester. Radio observations of PSR B1259–63 through the 2004 periastron passage. *MNRAS*, 358(3):1069, 2005.
- [448] R. N. Manchester (Australia Telescope National Facility, New South Wales, Australia). Private communication, 2004.
- [449] S. Johnston *et al.* PSR 1259–63 - A binary radio pulsar with a Be star companion. *ApJ*, 387(pt 2):L37, 1992.

